Wind turbine airfoil catalogue

Bertagnolio, F.; Sørensen, Niels N.; Johansen, Jeppe; Fuglsang, P.

Publication date:
2001

Document Version
Publisher's PDF, also known as Version of record

Risø–R–1280(EN)

Wind Turbine Airfoil Catalogue

Franck Bertagnolio, Niels Sørensen, Jeppe Johansen and Peter Fuglsang

Risø National Laboratory, Roskilde, Denmark
August 2001

Abstract The aim of this work is two-sided. Firstly, experimental results obtained for numerous sets of airfoil measurements (mainly intended for wind turbine applications) are collected and compared with computational results from the 2D Navier-Stokes solver EllipSys2D, as well as results from the panel method code XFOIL. Secondly, we are interested in validating the code EllipSys2D and finding out for which airfoils it does not perform well compared to the experiments, as well as why, when it does so. The airfoils are classified according to the agreement between the numerical results and experimental data. A study correlating the available data and this classification is performed. It is found that transition modelling is to a large extent responsible for the poor quality of the computational results for most of the considered airfoils. The transition model mechanism that leads to these discrepancies is identified. Some advices are given for elaborating future airfoil design processes that would involve the numerical code EllipSys2D in particular, and transition modelling in general.

ISBN 87–550–2910–8
ISBN 87–550–2911–6(Internet)
ISSN 0106–2840

Print: Pitney Bowes Management Services Danmark A/S · 2001

Contents

1 Introduction

The aim of this report is to provide a catalogue of results for a wide range of wind turbine airfoils. These results are obtained from numerical simulations with the 2D incompressible Navier-Stokes solver EllipSys2D (see [18, 19, 22] for a detailed description of the numerical code). They are compared with experimental data, when these are available. The results are also compared with the XFOIL code, which is based on a panel method combined with a viscous boundary layer formulation [9].

This work has several objectives. Firstly, it will permit to qualitatively evaluate the computational code EllipSys2D and its performances. Secondly, by comparing the results obtained for the wide range of airfoils, on one hand it will be possible to give a better idea of the difficulties that can be faced when simulating certain types of airfoil, and on the other hand to identify the airfoil types that can be correctly simulated by the numerical model. Finally, it will provide a database of airfoil characteristics, that can be used in wind turbine design.

In each of the sections where experimental and computational results are reported, there is a short introductory text describing the experimental facilities, as well as some relevant informations about the computations.

Several airfoils can be included in the same section if they were experimentally measured during the same campaign. Measurements for some of the NACA wing sections were obtained in the VELUX wind tunnel [11], whereas others were collected from the book by Abbott and von Doenhoff [1]. In the present report, the former ones are distinguished from the latter by adding (V) at the end of their respective airfoil names whenever necessary (e.g. NACA 63-215 was obtained from [1], and NACA 63-215(V) was measured in the VELUX wind tunnel).

The meshes that were used for computations are not drawn for every single airfoil. However, the one used for the NACA 63-215 in section 2 is depicted. The general aspect of all the meshes used herein is very similar, the only difference in the mesh generation being the airfoil shape. All meshes were generated with the grid generator HypGrid2D [23].

The XFOIL code is used in its standard version with 120 panels distributed on the airfoil surface. The viscous boundary layer and wake options are activated. The Reynolds number is set to the same value as in the Navier-Stokes computations. An Orr-Sommerfeld transition criterion is used to simulate free transition. However, for cases where the experiment has been performed with a device triggering transition, fixed transition is enforced at the same chordwise location.

The report is organized as follows. In sections 2 to 11, the experimental and computational data are reported for the numerous airfoils. In section 12, the results are analysed by classifying the airfoils according to agreements or discrepancies between experiments and computations. Then, conclusions are drawn regarding the performances of the numerical code EllipSys2D. The main conclusions of this work are reported in the last section 13. Additional airfoils will progressively be included in the appendices in future releases of this report.

2 NACA Wing Sections

This section is dedicated to the computation of several airfoils of the NACA wing section family. The computational data obtained with EllipSys2D will be compared to the measurements performed at NASA in a low-turbulence pressure tunnel [26]. These measurements are reported in the book by Abbott and von Doenhoff [1].

Three sub-families of NACA wing sections are investigated: NACA 63, NACA 64 and NACA 65. They differ from each other by the chordwise position of minimum pressure. Then, a third digit indicates the design lift coefficient. The airfoils can finally be distinguished by their thickness, which is given by the last 2 digits. Among the numerous possibilities in the different families, only the following airfoils are considered:

- NACA 63-215, NACA 63-218, NACA 63-221
- NACA 63-415, NACA 63-418, NACA 63-421
- NACA 64-415, NACA 64-421
- NACA 65-415, NACA 65-421

It must be noted that most of these airfoils are used on wind turbines.

For all the cases that are presented in this section, the Reynolds number of the experiment (and the computations) was $Re = 3.0 \times 10^6$.

2.1 Method

C-meshes were used for all the computations with 384 cells in the direction along the airfoil, 256 of them being on the airfoil, and 64 cells in the direction away from the airfoil. The non-dimensional height of the cell at the airfoil was 1×10^{-5}. Further refinements of the grid didn't significantly improve the results.

The mesh used for the NACA 63-215 airfoil, and details of regions of interest, are displayed on Figures 1-2-3-4. As it can be seen, the mesh lines were extended in the wake of the trailing edge in order to stabilize the computations.

The computations were performed with the SUDS-scheme for convective terms. The $k - \omega$ SST turbulence model by Menter was used for the turbulent viscosity [16]. The transition model by Michel [17] was used for simulating the free transition, together with the empirical function given by Chen and Thyson [8] for modelling the turbulence intermittency. Numerical results were obtained with stationary computations.

2.2 Results

Results are presented as lift, drag and pitching moment coefficients as function of angle of attack, and also pressure and skin friction distributions at various angles are shown.

There was an overall good agreement between the experimental data and the computational results. However, for some of the airfoils, there exists a shift in the angle of attack between experiments and computations in the linear region, where simulations were expected to perform well. This shift can be observed on the lift curve for the following airfoils: NACA 63-215, NACA 63-221, NACA 63-418, NACA 65-415, NACA 65-421, on Figures 6-18-30-54-60, respectively. Moreover, similar results were found using the panel method XFOIL. In order to assess that the numerical code was not responsible for these discrepancies, an experiment that was performed with the same airfoil as NACA 63-215 in another wind tunnel was considered in section 3.

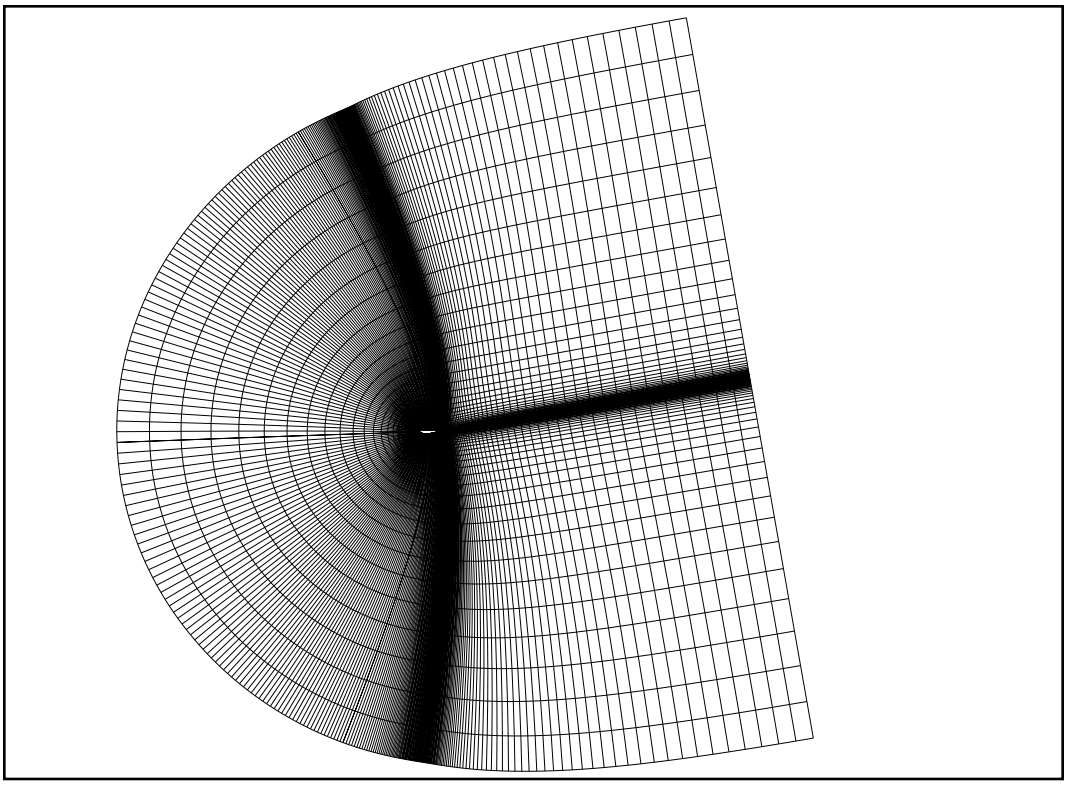

Figure 1. Mesh around the NACA 63-215 airfoil - Full view

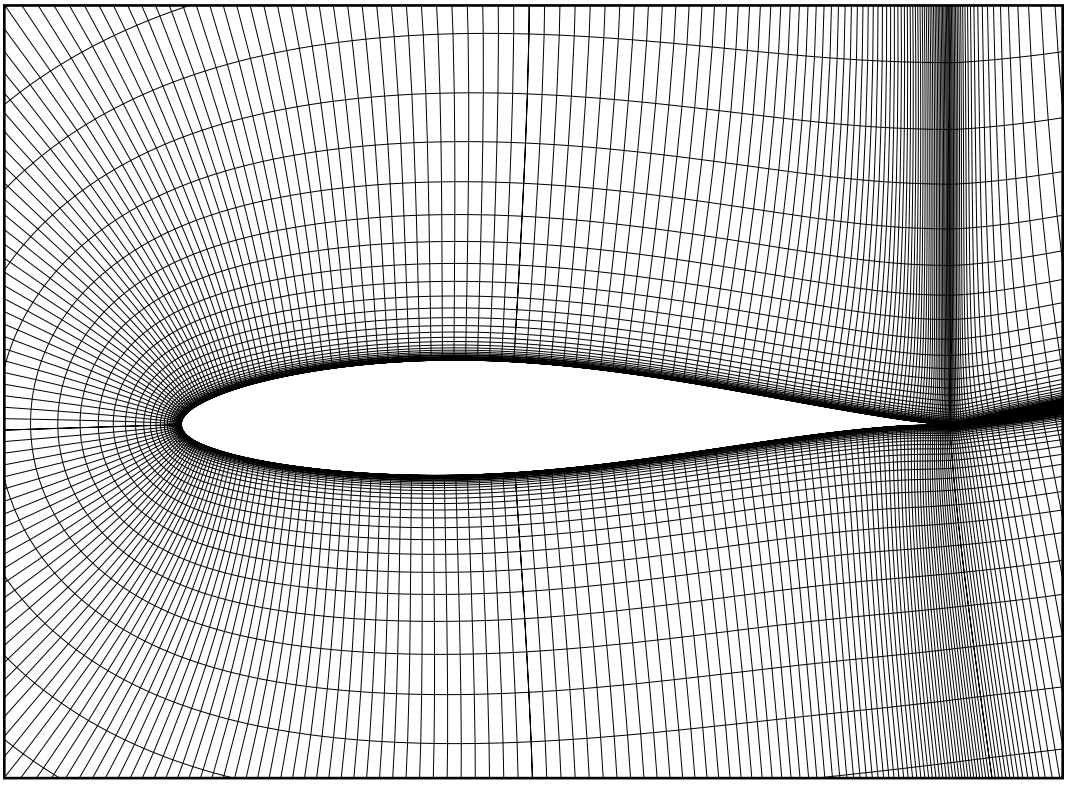

Figure 2. Mesh around the NACA 63-215 airfoil - Closer view of the airfoil

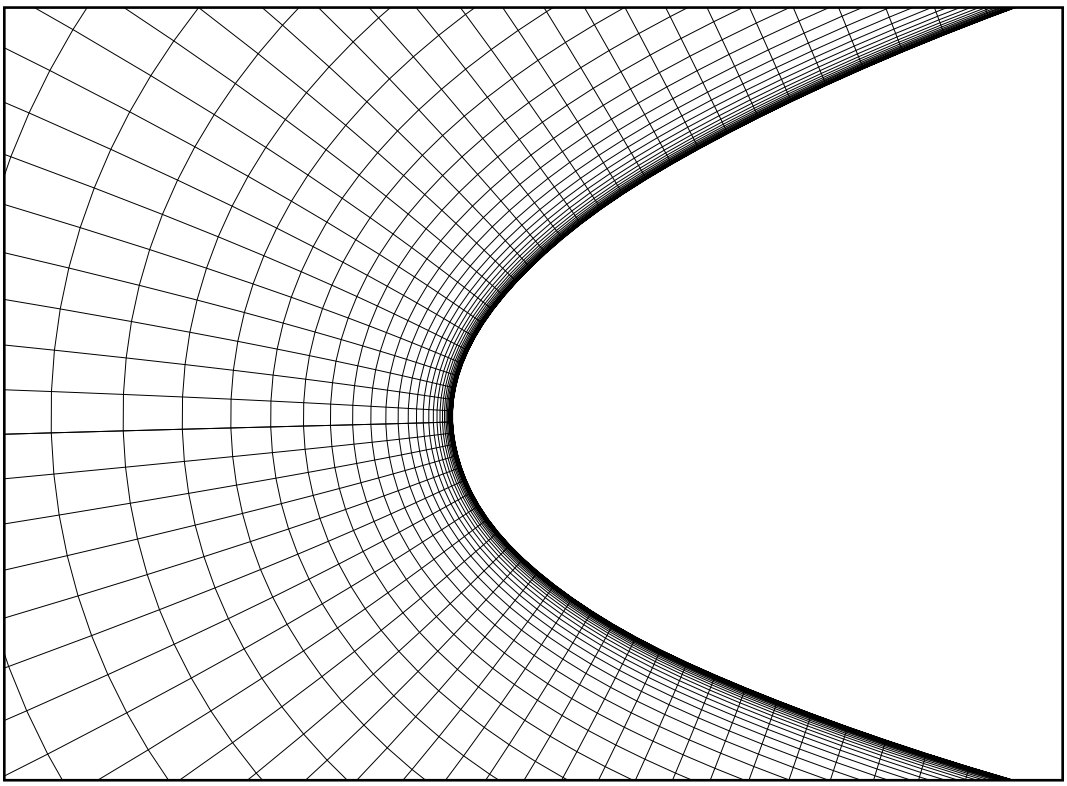

Figure 3. Mesh around the NACA 63-215 airfoil - Closer view of the leading edge

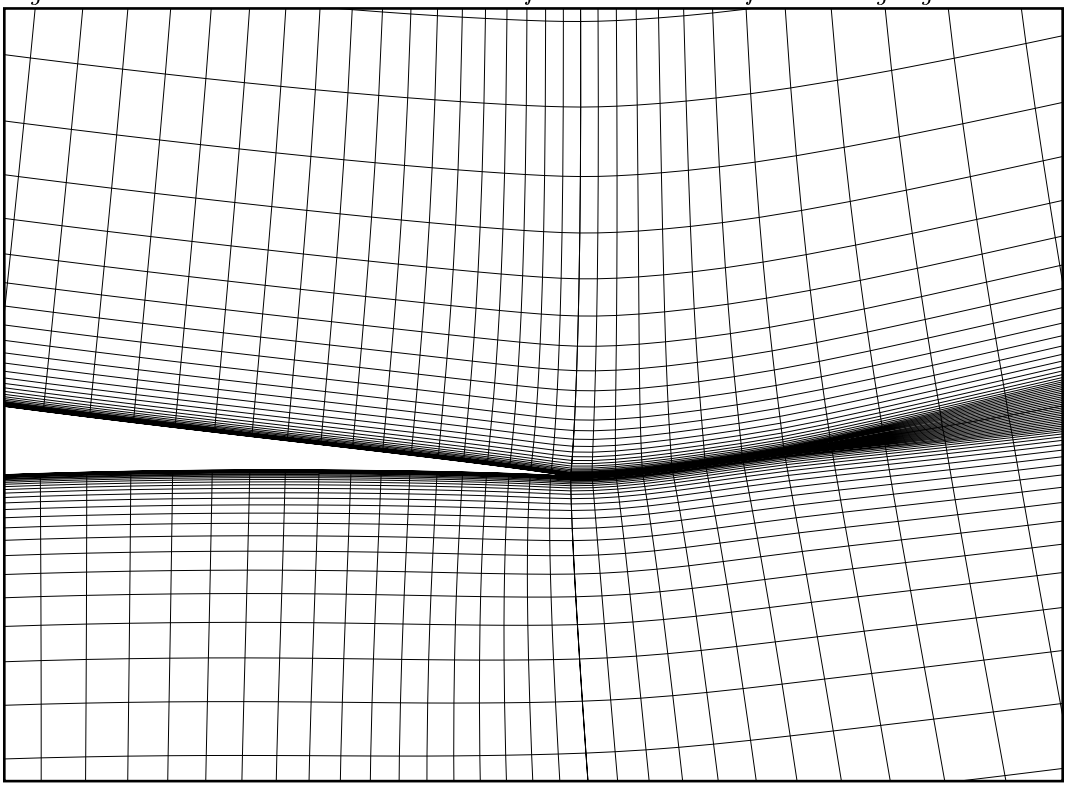

Figure 4. Mesh around the NACA 63-215 airfoil - Closer view of the trailing edge

NACA 63-215

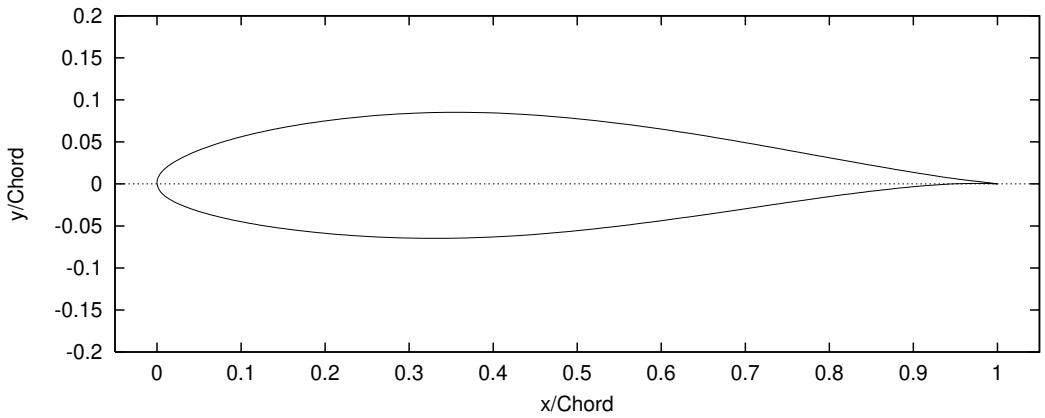

Figure 5. NACA 63-215 Airfoil

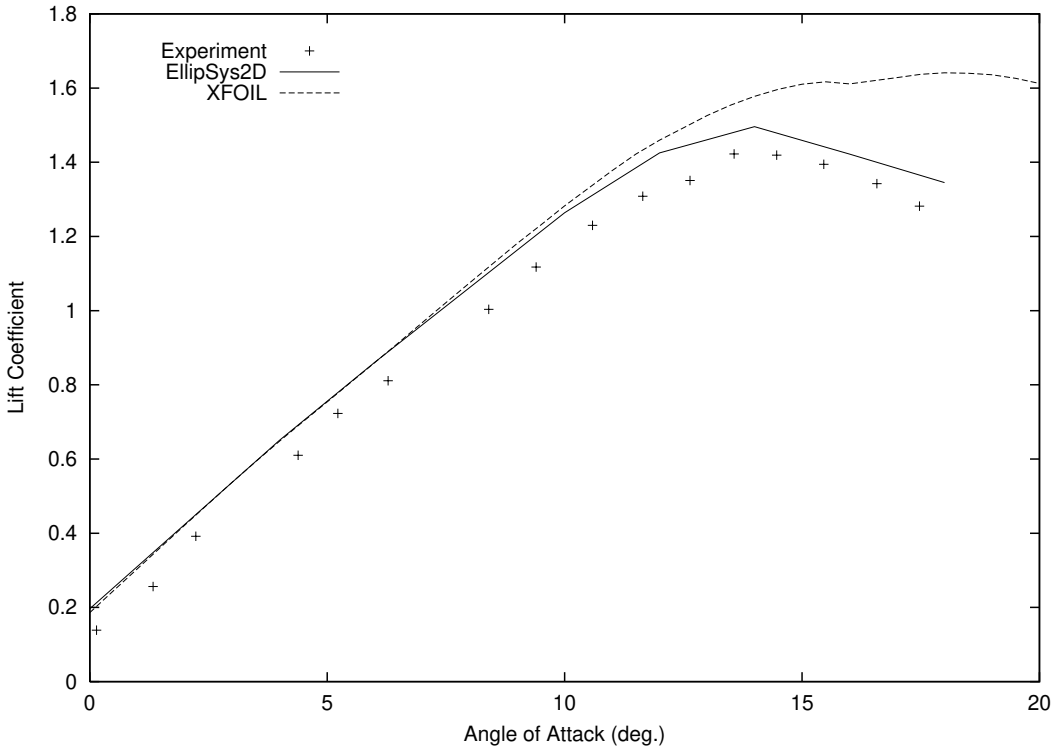

Figure 6. Lift Coefficient Curve (NACA 63-215, Experiment [1])

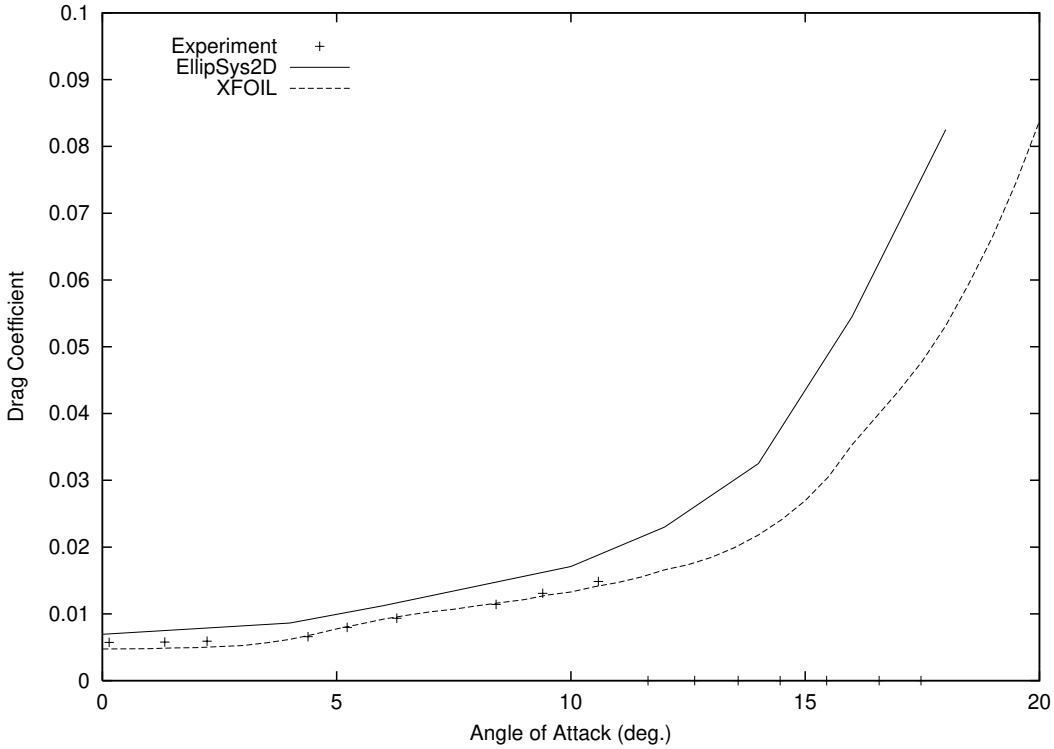

Figure 7. Drag Coefficient Curve (NACA 63-215, Experiment [1])

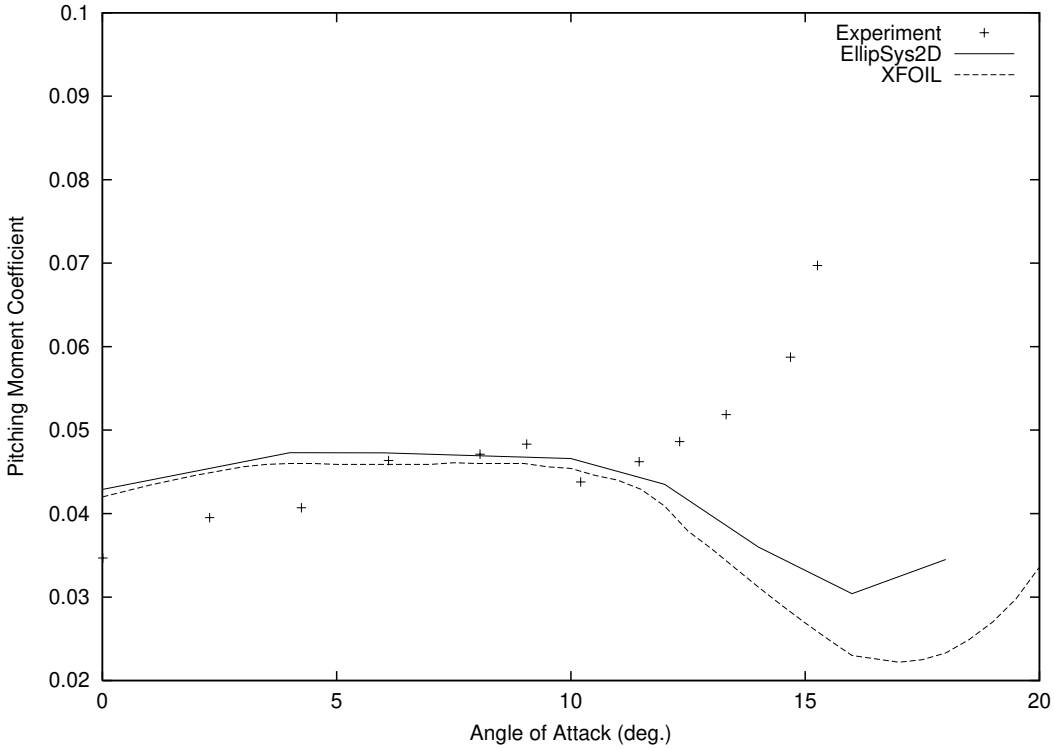

Figure 8. Pitching Moment Coefficient Curve (NACA 63-215, Experiment [1])

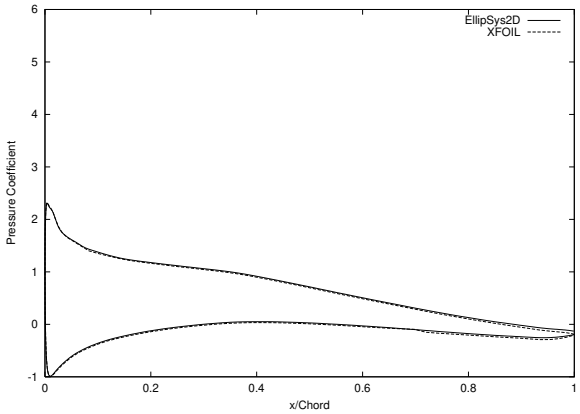

(a) $\alpha = 6^o$

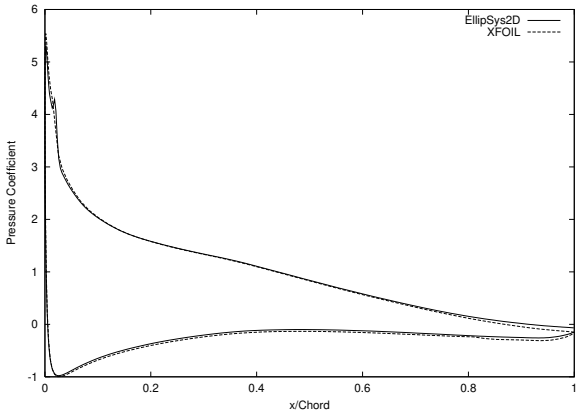

(b) $\alpha = 10^o$

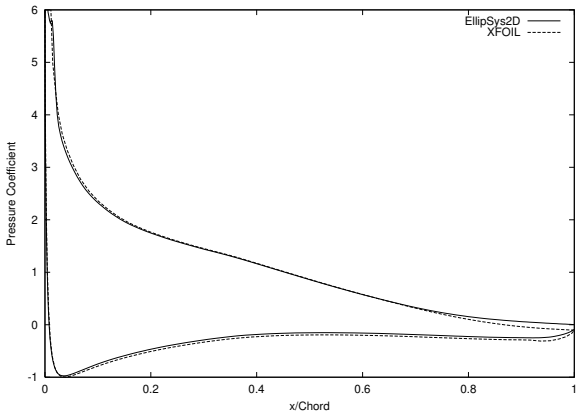

(c) $\alpha = 12^o$

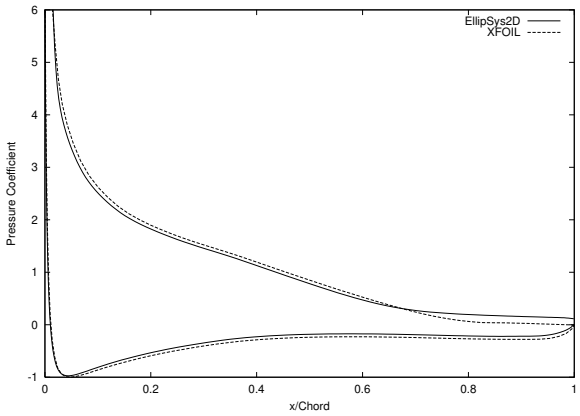

(d) $\alpha = 14^o$

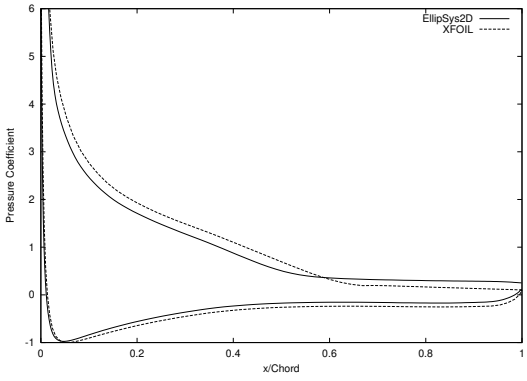

(e) $\alpha = 16^o$

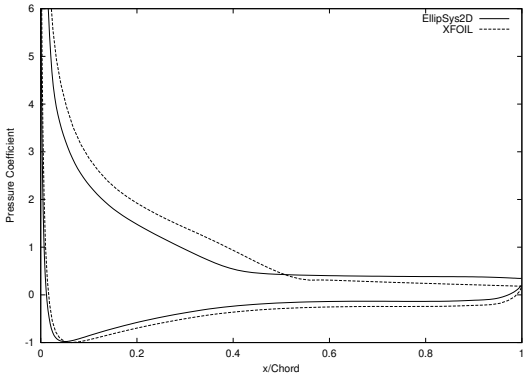

(f) $\alpha = 18^o$

Figure 9. Pressure Coefficient Distributions (NACA 63-215)

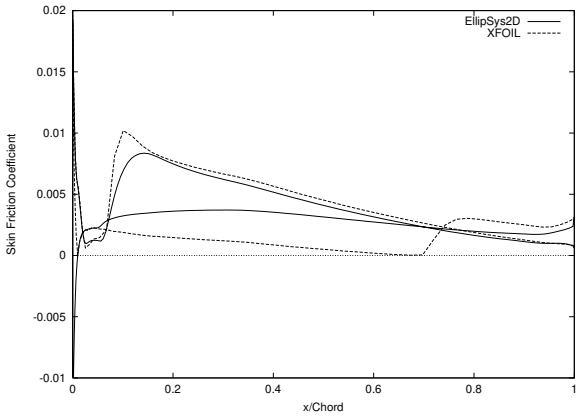

(a) $\alpha = 6^o$

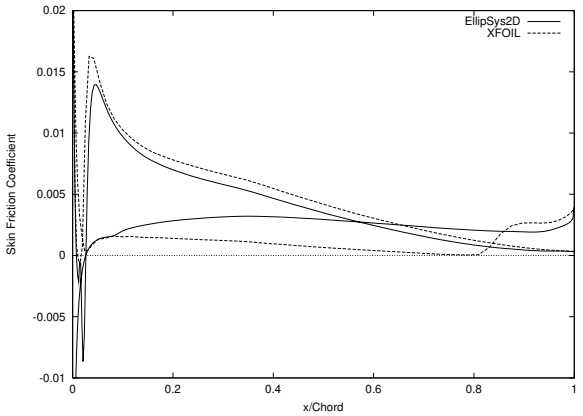

(b) $\alpha = 10^o$

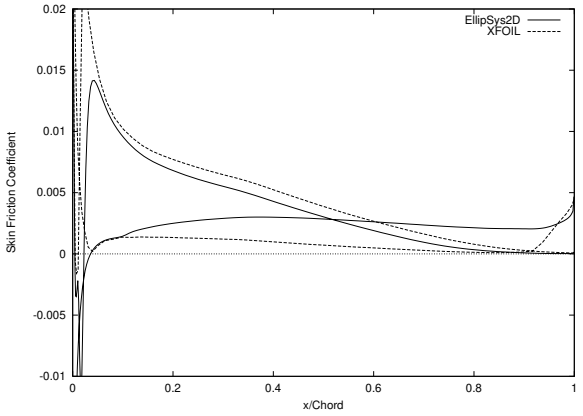

(c) $\alpha = 12^o$

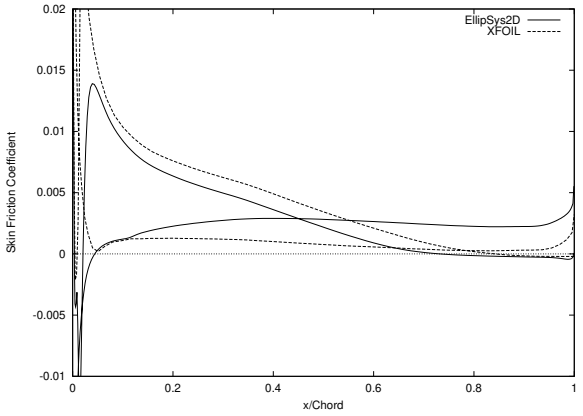

(d) $\alpha = 14^o$

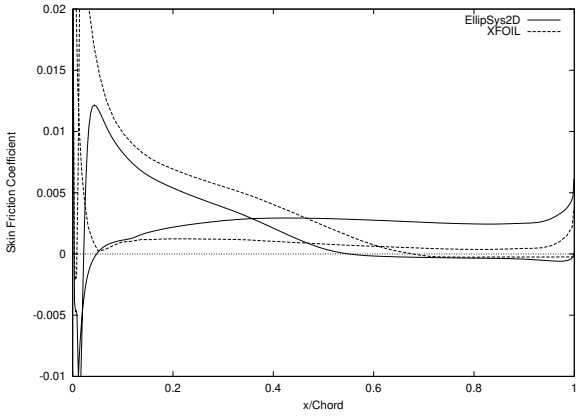

(e) $\alpha = 16^o$

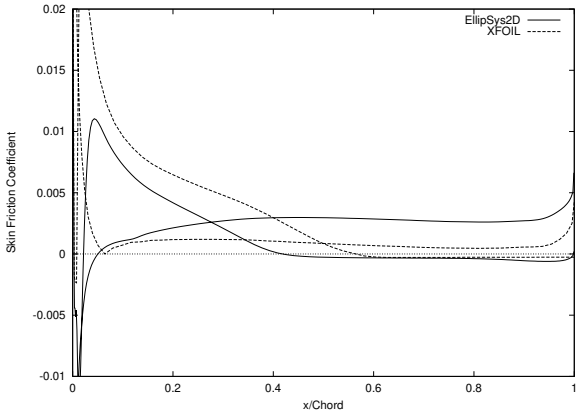

(f) $\alpha = 18^o$

Figure 10. Skin Friction Coefficient Distributions (NACA 63-215)

NACA 63-218

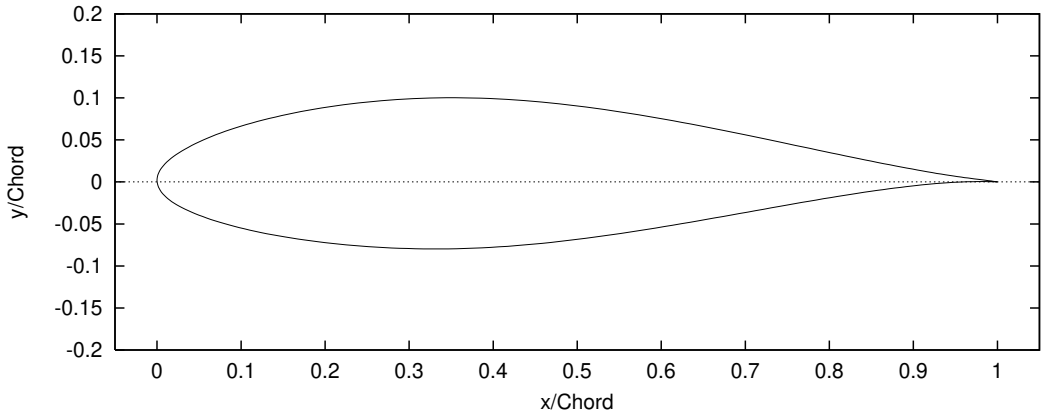

Figure 11. NACA 63-218 Airfoil

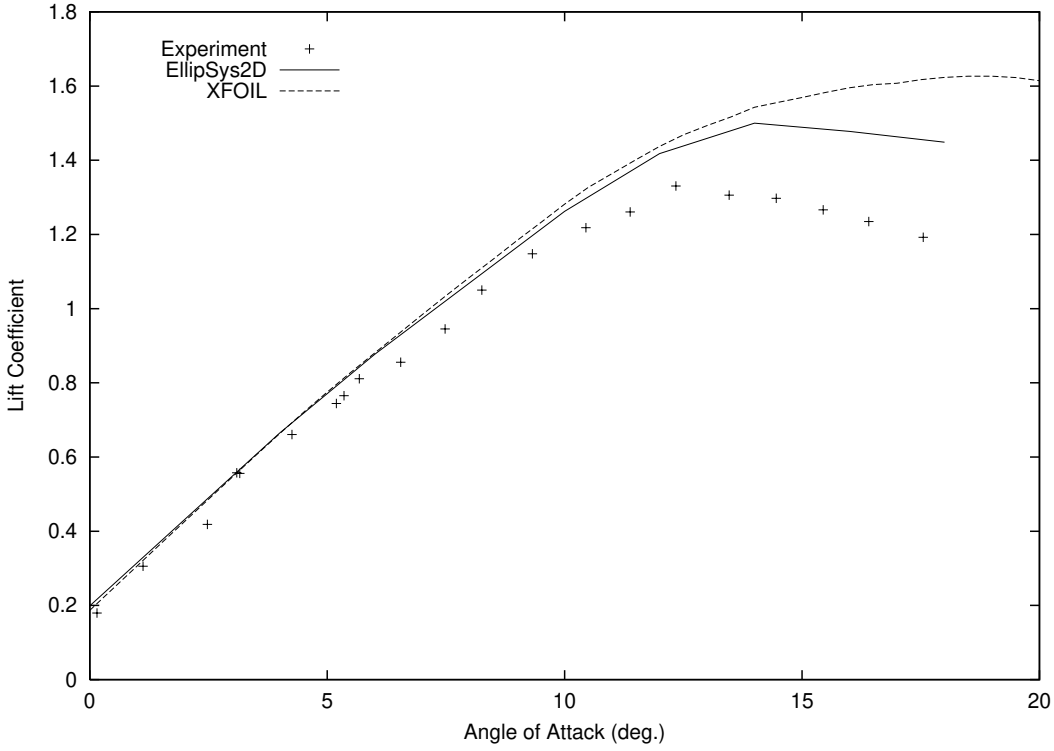

Figure 12. Lift Coefficient Curve (NACA 63-218, Experiment [1])

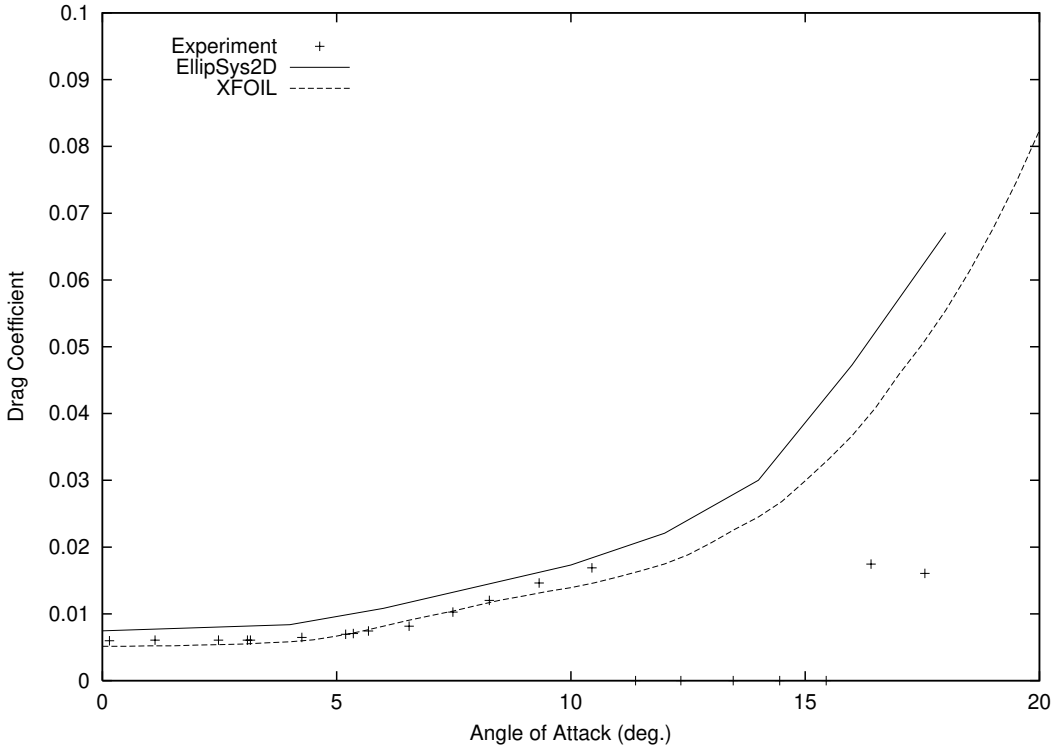

Figure 13. Drag Coefficient Curve (NACA 63-218, Experiment [1])

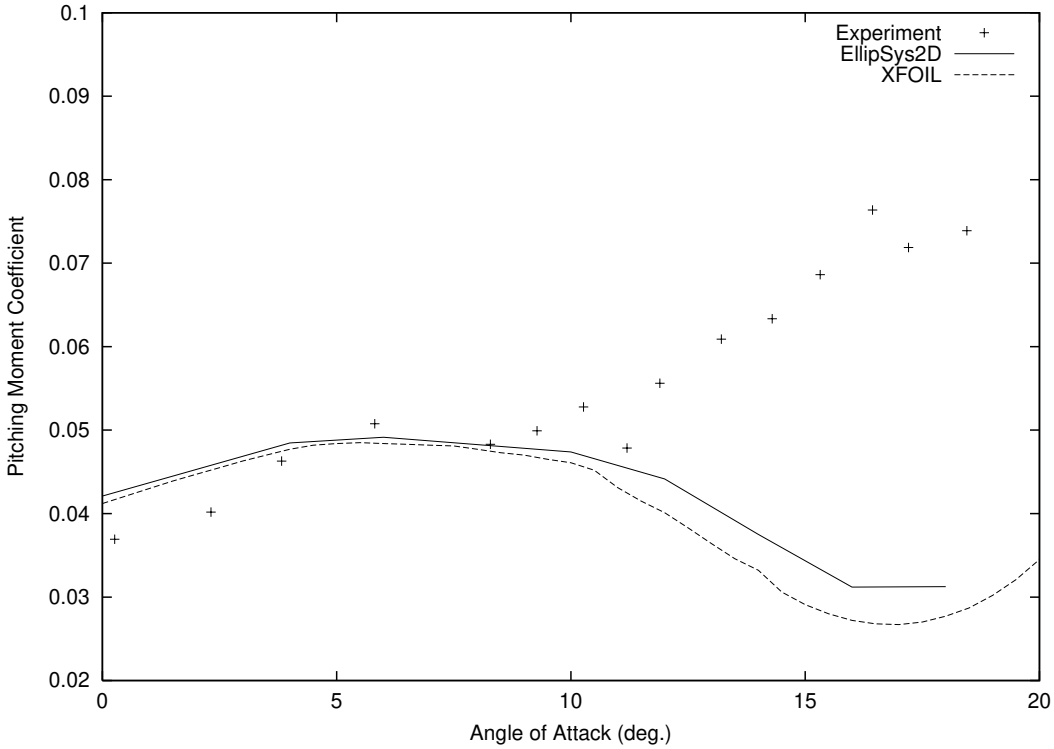

Figure 14. Pitching Moment Coefficient Curve (NACA 63-218, Experiment [1])

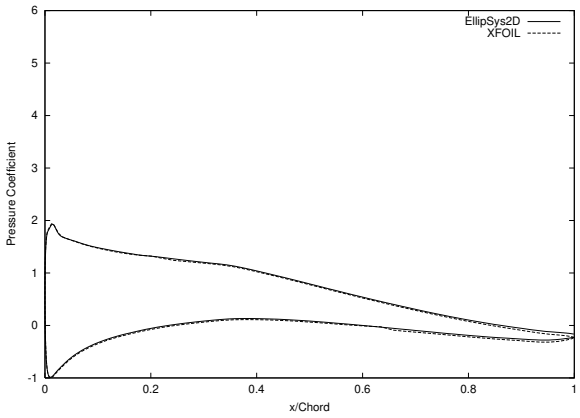

(a) $\alpha = 6^o$

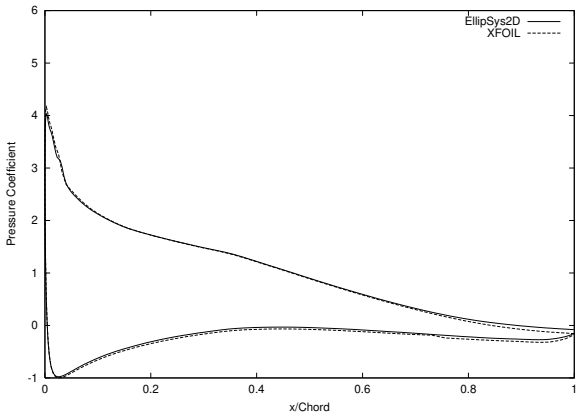

(b) $\alpha = 10^o$

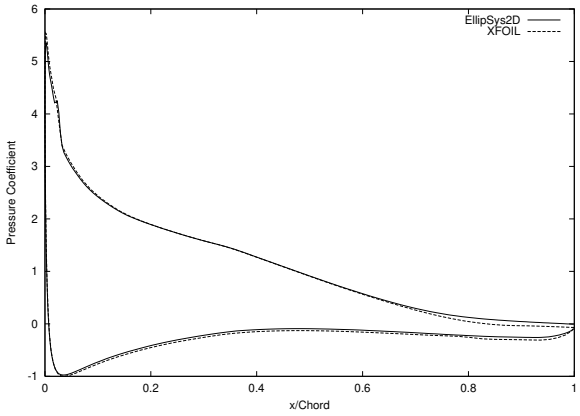

(c) $\alpha = 12^o$

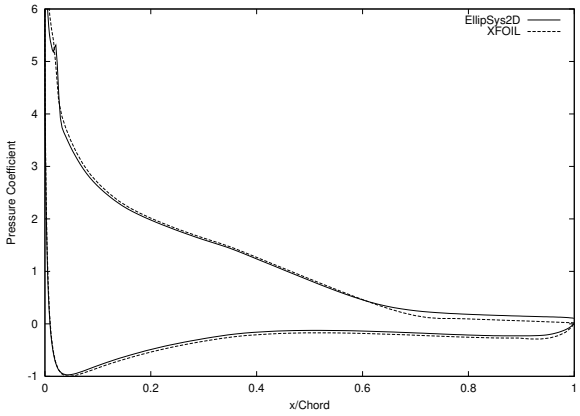

(d) $\alpha = 14^o$

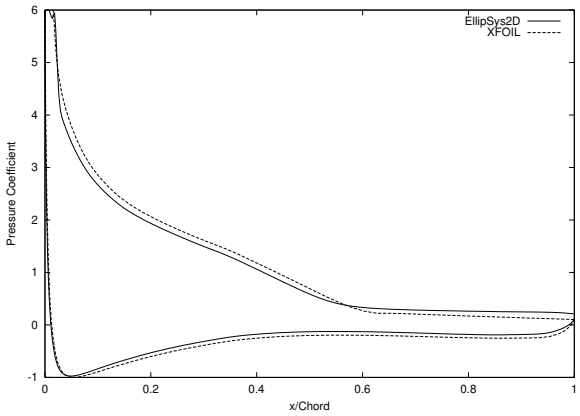

(e) $\alpha = 16^o$

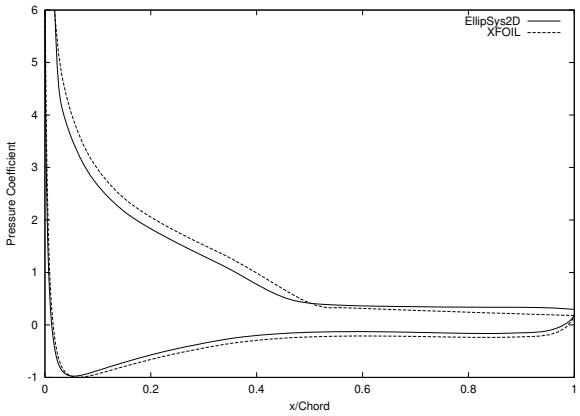

(f) $\alpha = 18^o$

Figure 15. Pressure Coefficient Distributions (NACA 63-218)

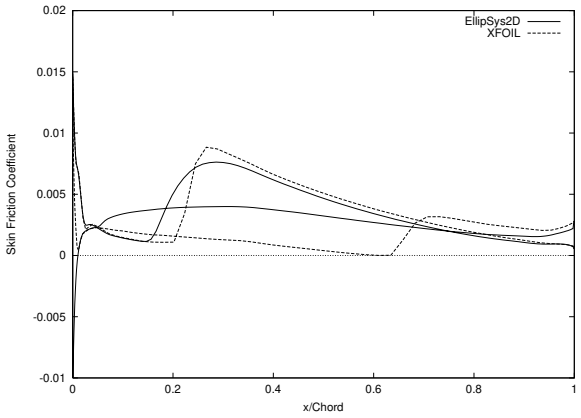

(a) $\alpha = 6^o$

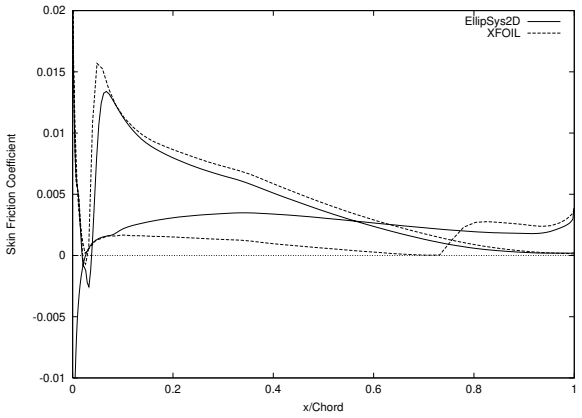

(b) $\alpha = 10^o$

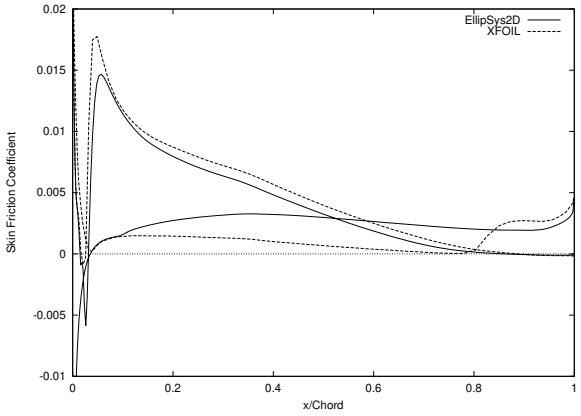

(c) $\alpha = 12^o$

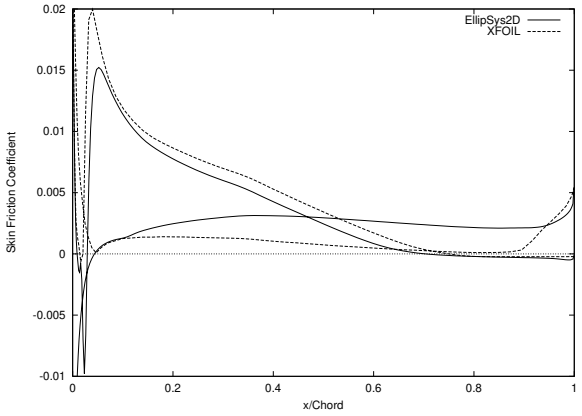

(d) $\alpha = 14^o$

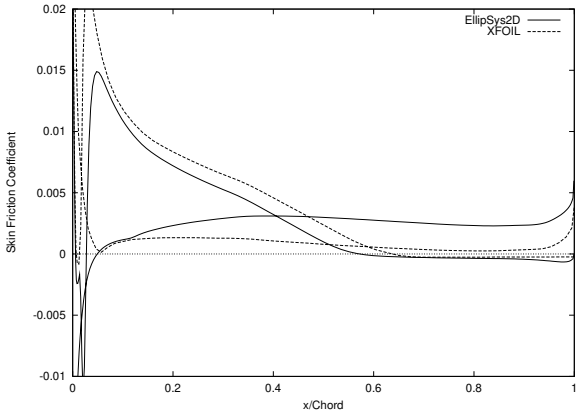

(e) $\alpha = 16^o$

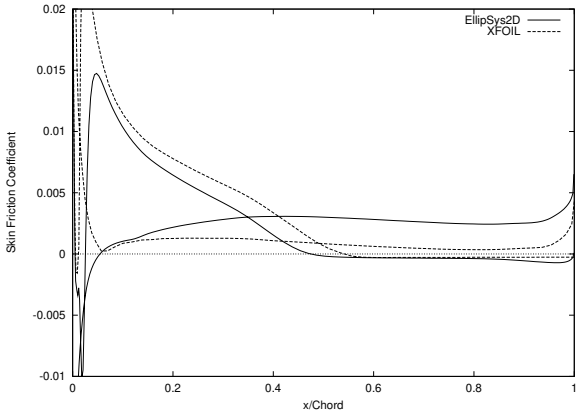

(f) $\alpha = 18^o$

Figure 16. Skin Friction Coefficient Distributions (NACA 63-218)

NACA 63-221

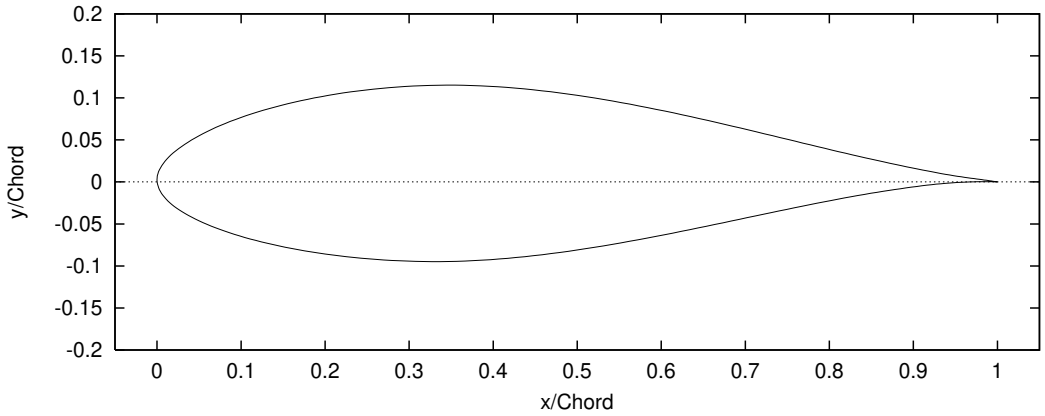

Figure 17. NACA 63-221 Airfoil

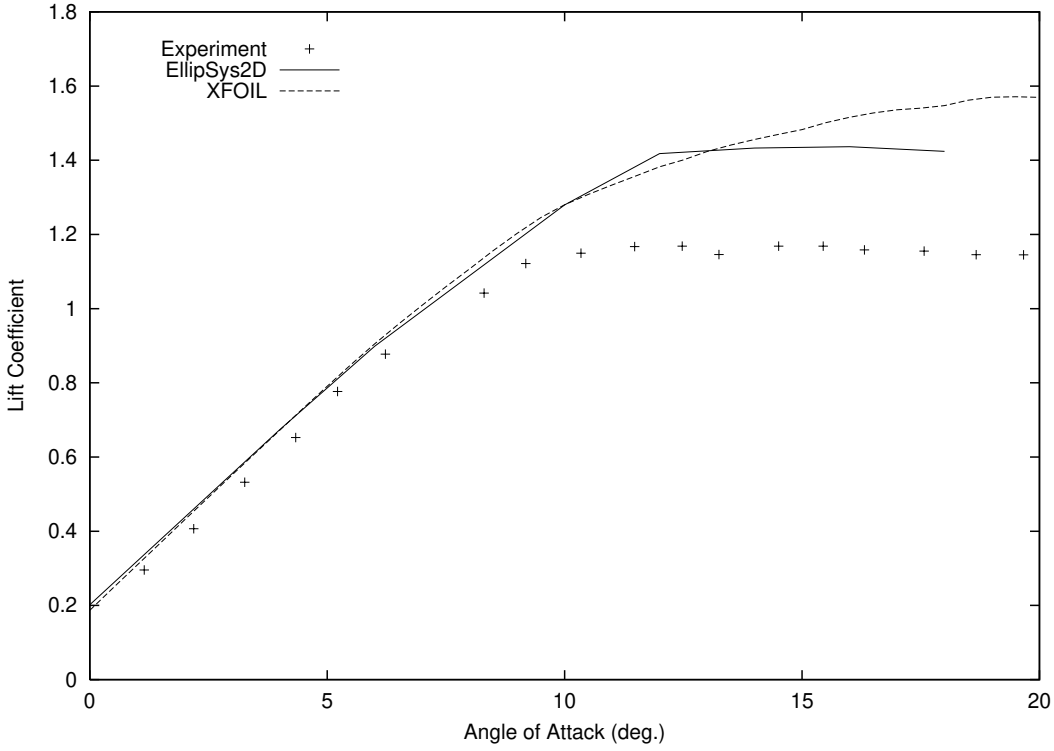

Figure 18. Lift Coefficient Curve (NACA 63-221, Experiment [1])

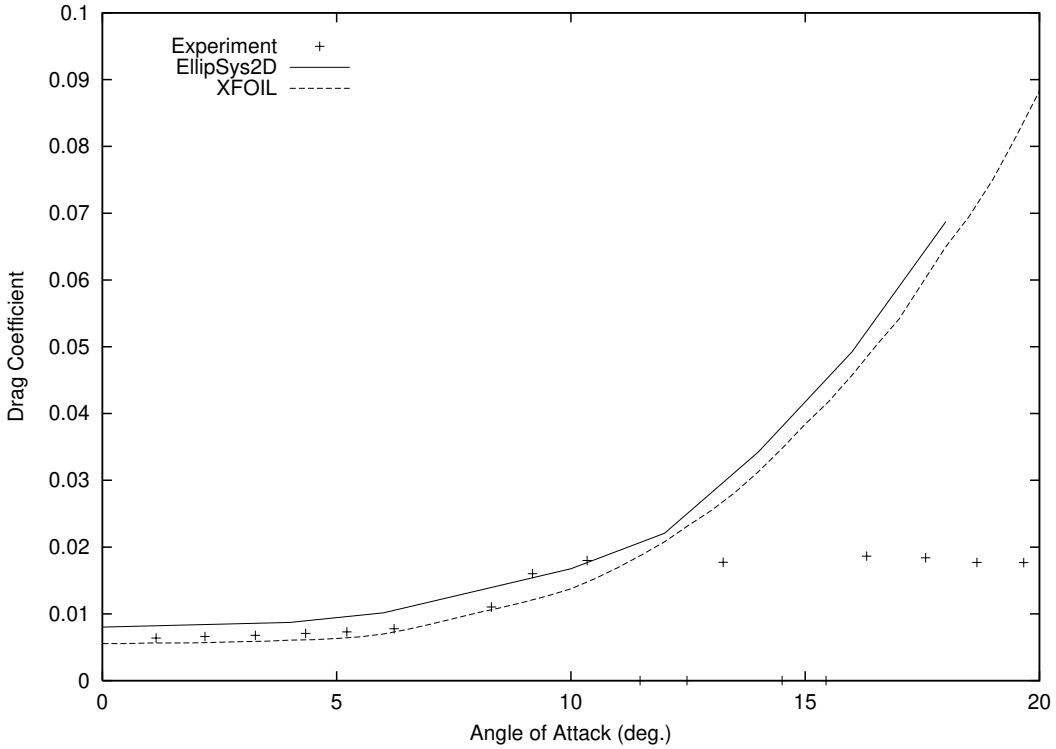

Figure 19. Drag Coefficient Curve (NACA 63-221, Experiment [1])

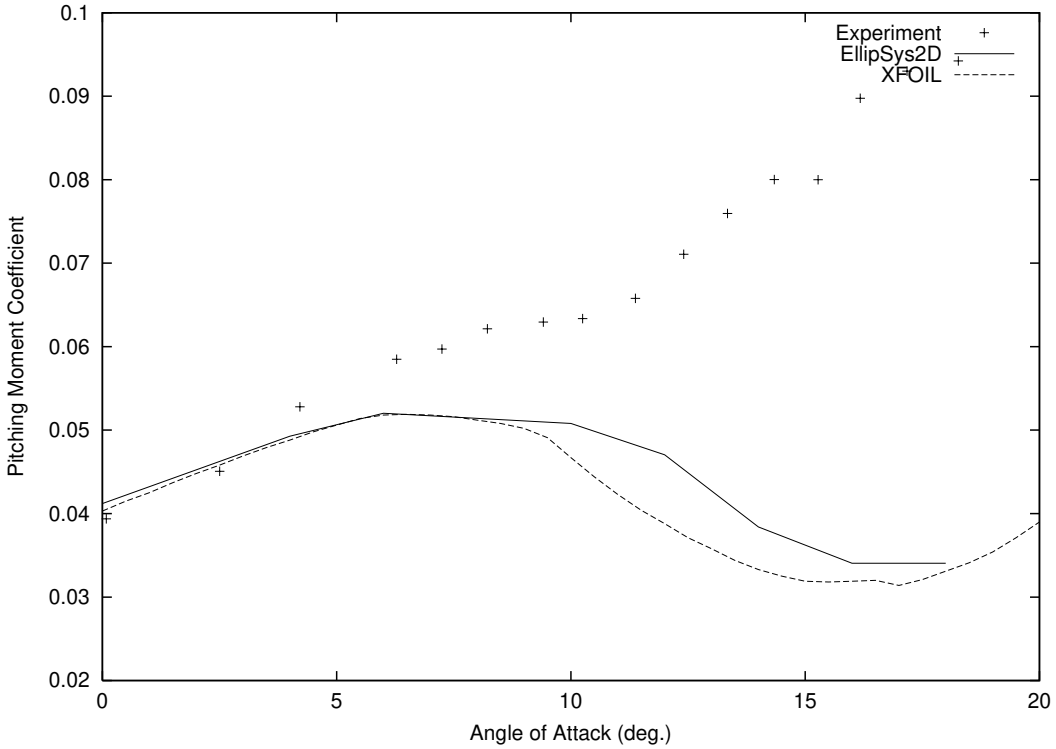

Figure 20. Pitching Moment Coefficient Curve (NACA 63-221, Experiment [1])

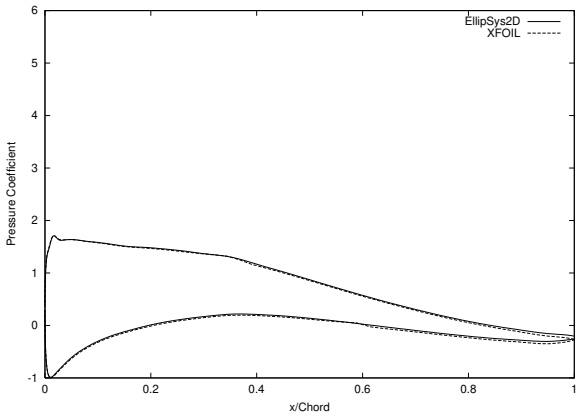

(a) $\alpha = 6^o$

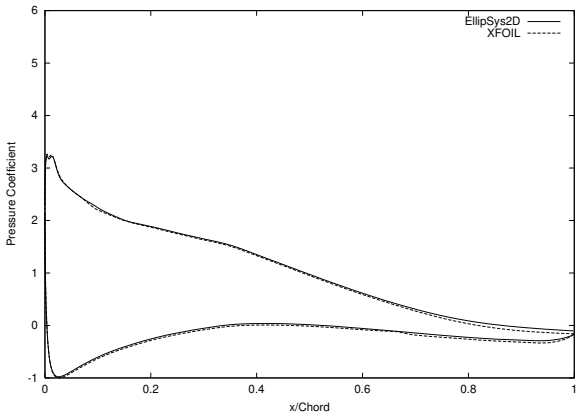

(b) $\alpha = 10^o$

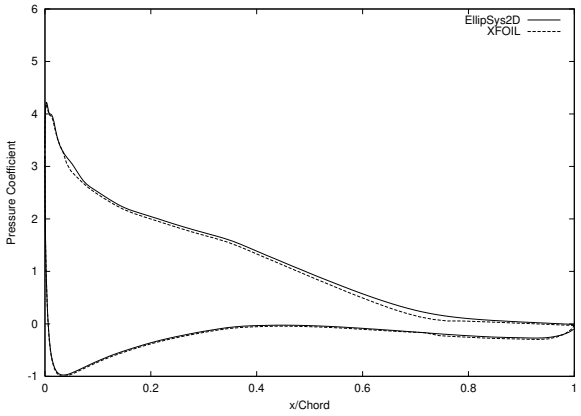

(c) $\alpha = 12^o$

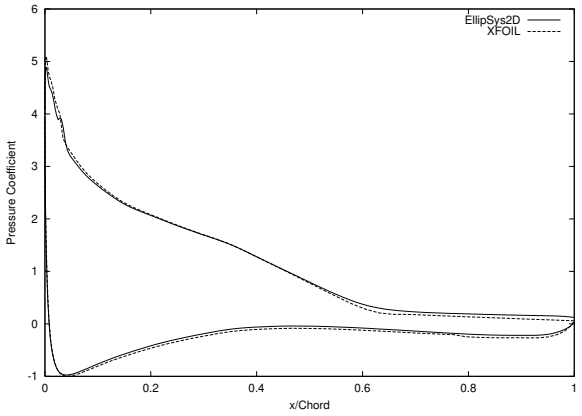

(d) $\alpha = 14^o$

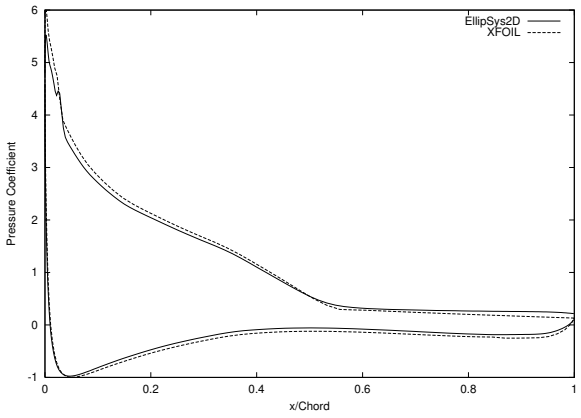

(e) $\alpha = 16^o$

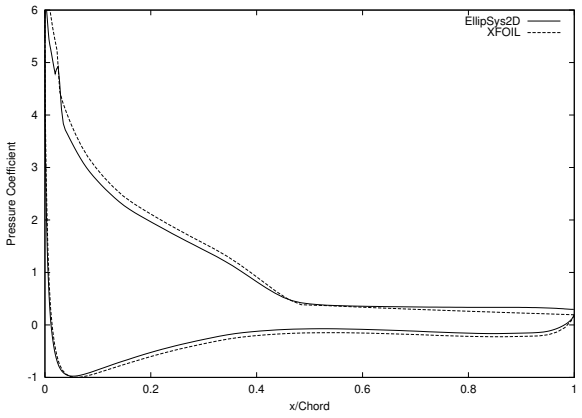

(f) $\alpha = 18^o$

Figure 21. Pressure Coefficient Distributions (NACA 63-221)

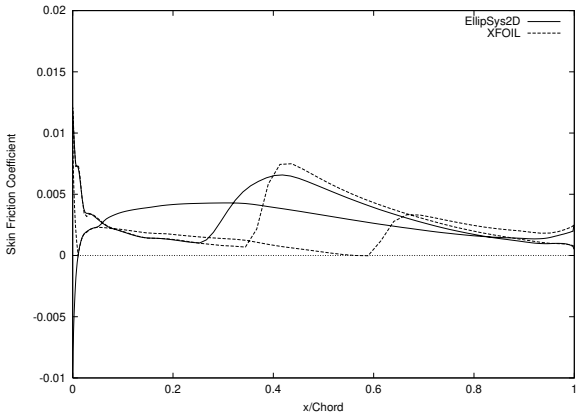

(a) $\alpha = 6^o$

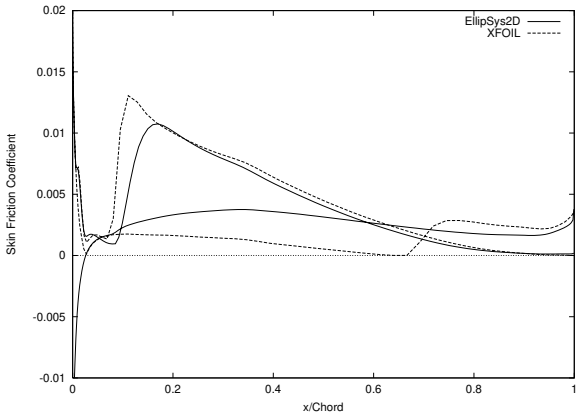

(b) $\alpha = 10^o$

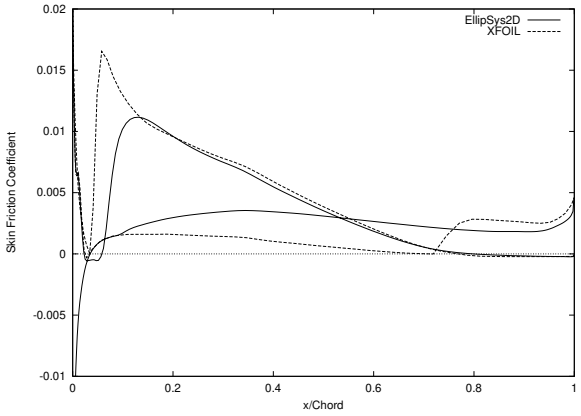

(c) $\alpha = 12^o$

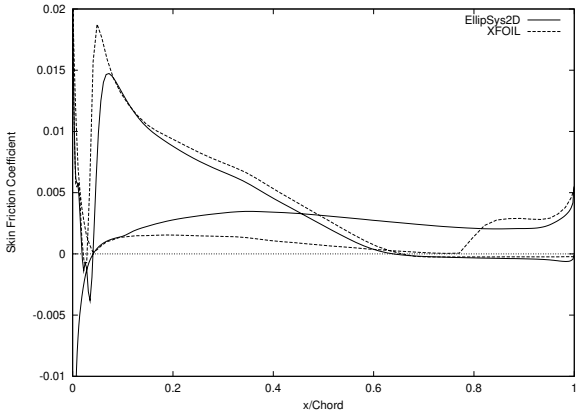

(d) $\alpha = 14^o$

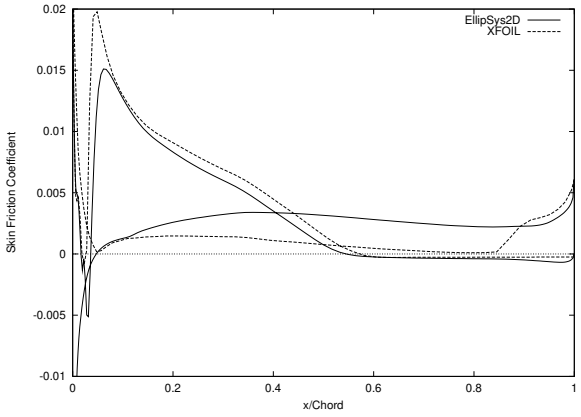

(e) $\alpha = 16^o$

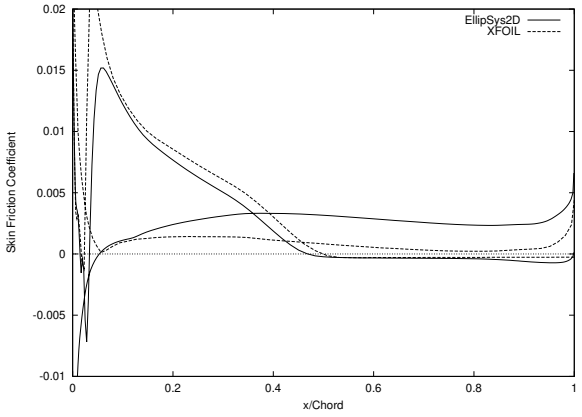

(f) $\alpha = 18^o$

Figure 22. Skin Friction Coefficient Distributions (NACA 63-221)

NACA 63-415

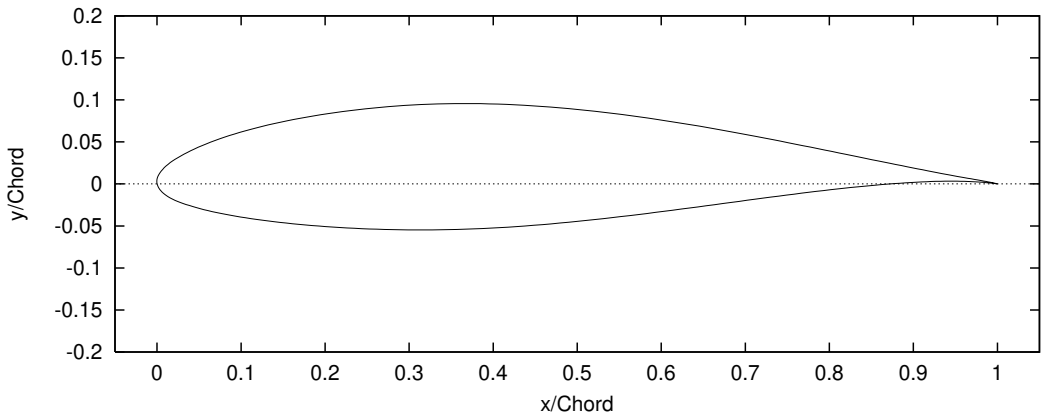

Figure 23. NACA 63-415 Airfoil

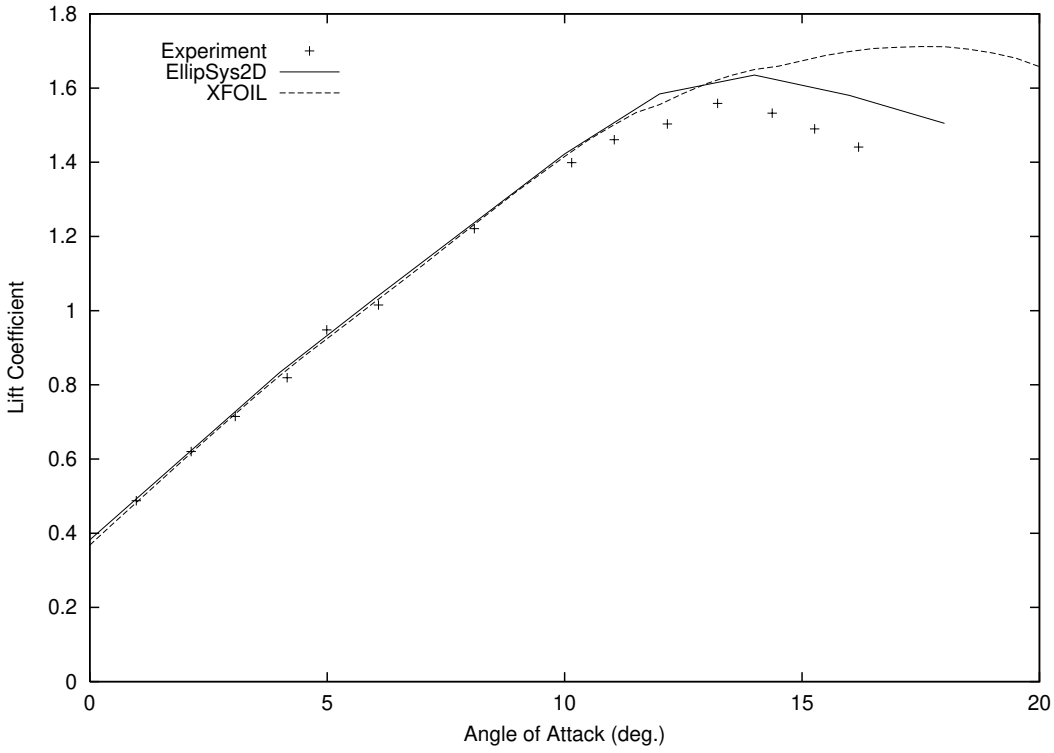

Figure 24. Lift Coefficient Curve (NACA 63-415, Experiment [1])

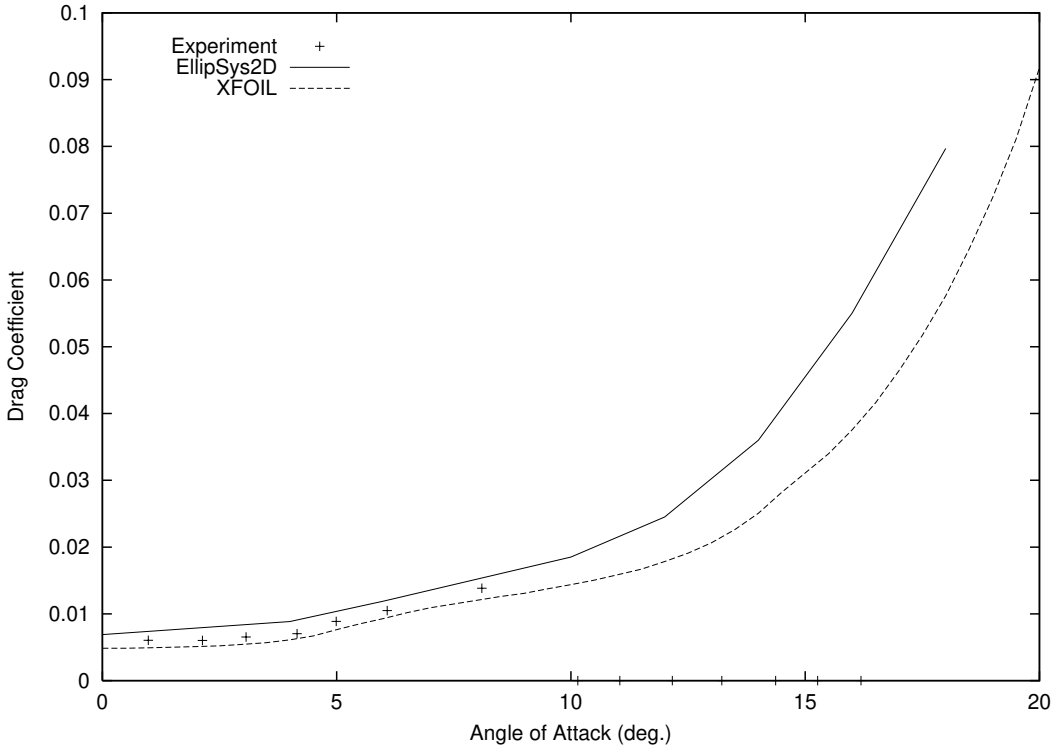

Figure 25. Drag Coefficient Curve (NACA 63-415, Experiment [1])

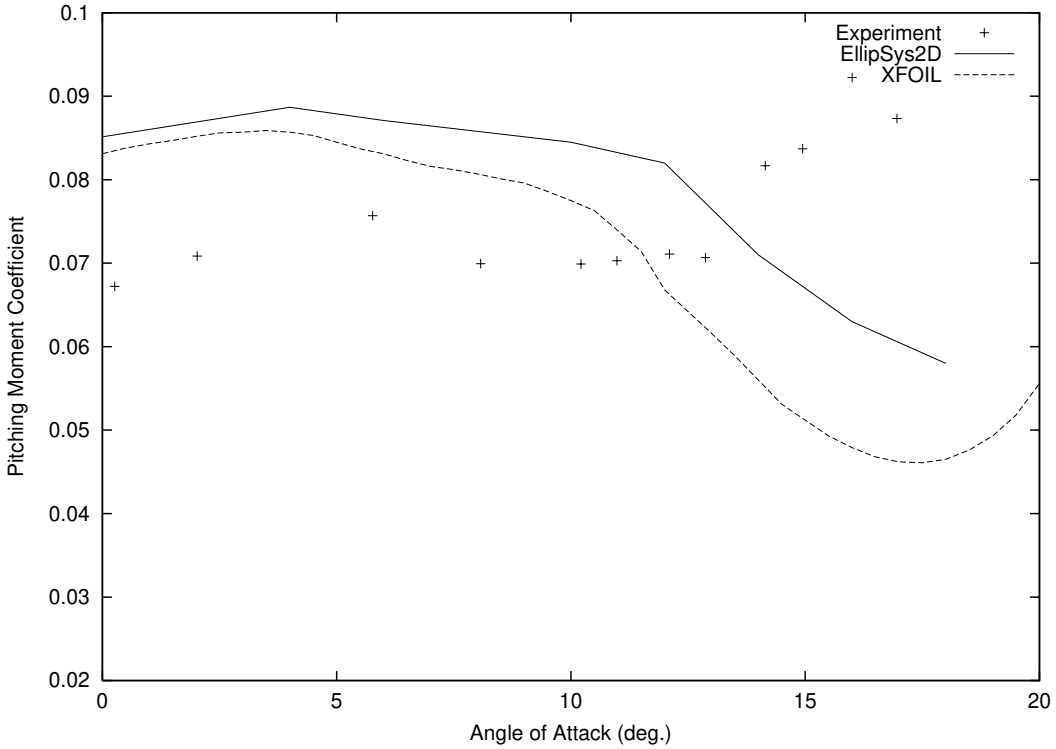

Figure 26. Pitching Moment Coefficient Curve (NACA 63-415, Experiment [1])

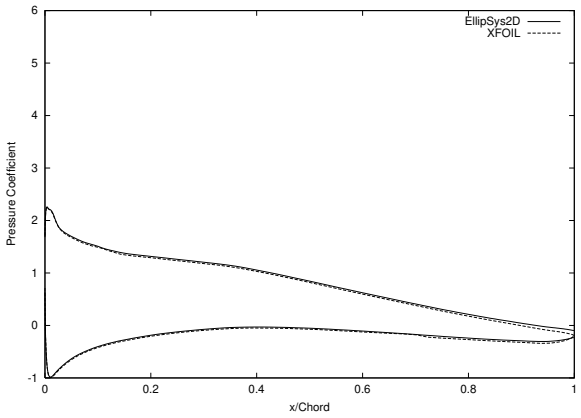

(a) $\alpha = 6^o$

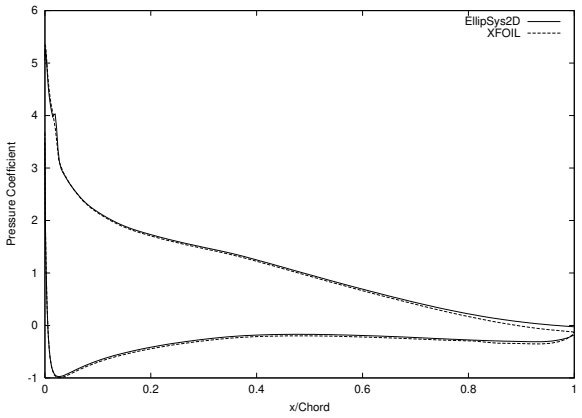

(b) $\alpha = 10^o$

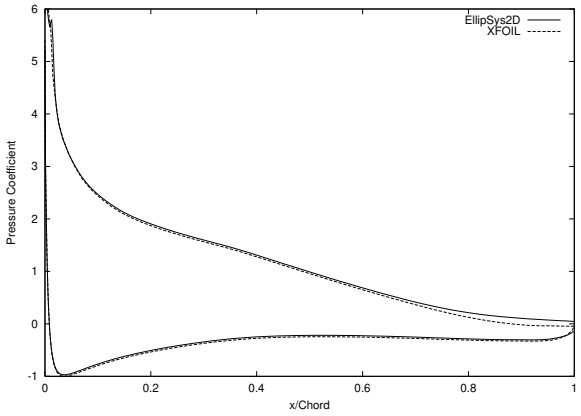

(c) $\alpha = 12^o$

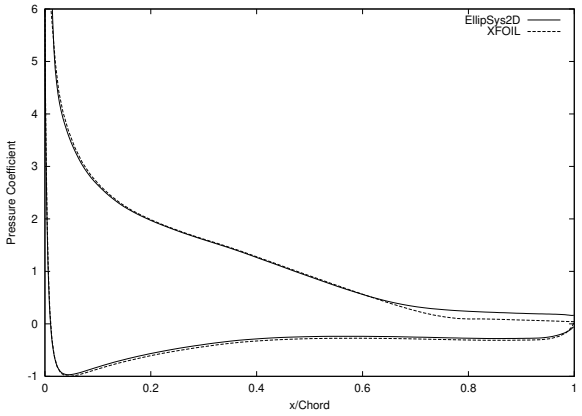

(d) $\alpha = 14^o$

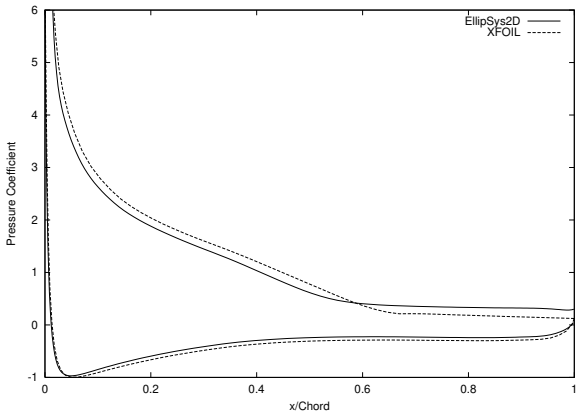

(e) $\alpha = 16^o$

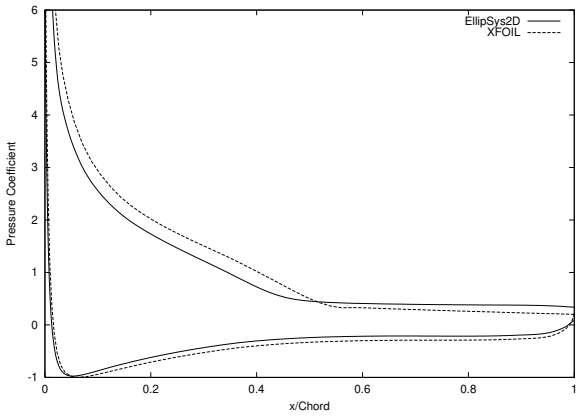

(f) $\alpha = 18^o$

Figure 27. Pressure Coefficient Distributions (NACA 63-415)

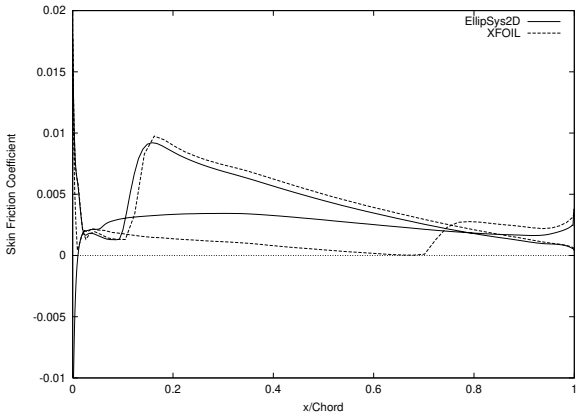

(a) $\alpha = 6^o$

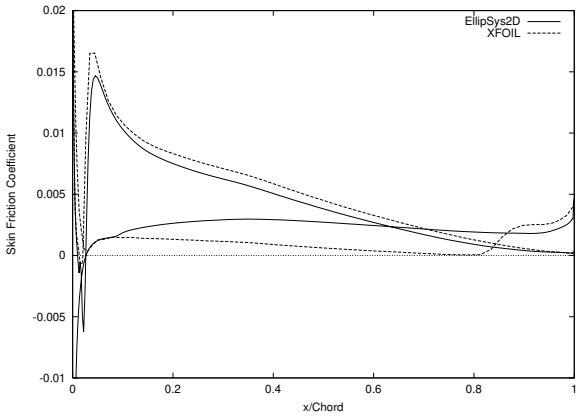

(b) $\alpha = 10^o$

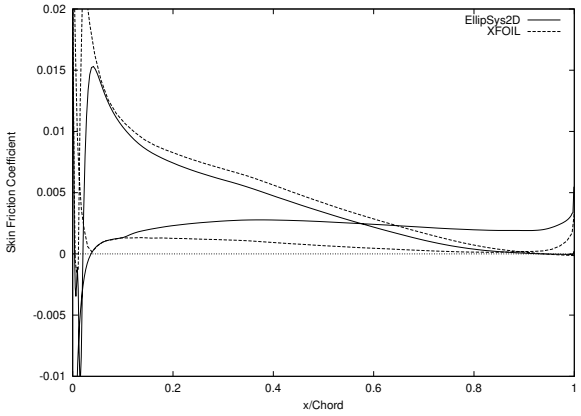

(c) $\alpha = 12^o$

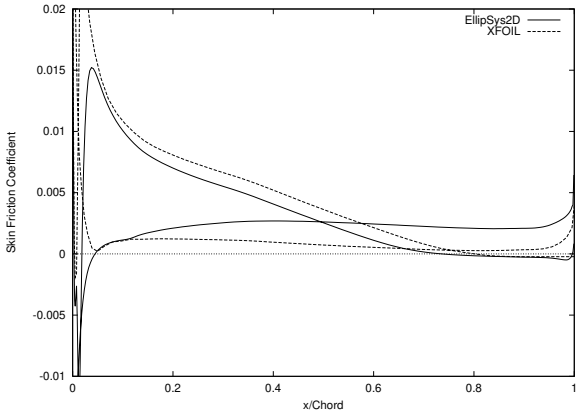

(d) $\alpha = 14^o$

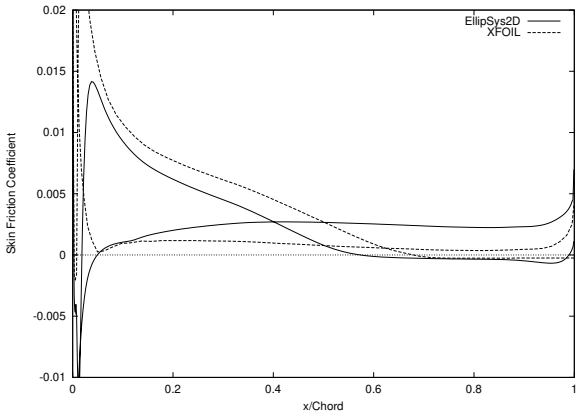

(e) $\alpha = 16^o$

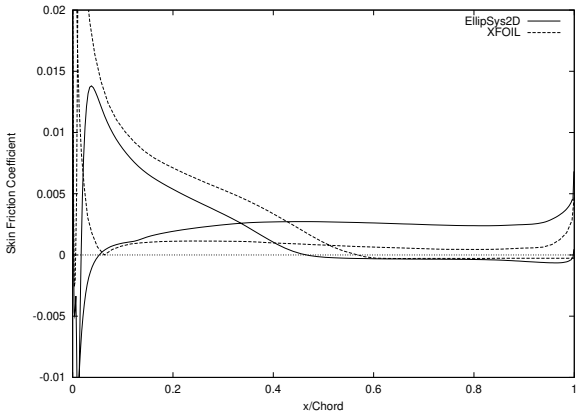

(f) $\alpha = 18^o$

Figure 28. Skin Friction Coefficient Distributions (NACA 63-415)

NACA 63-418

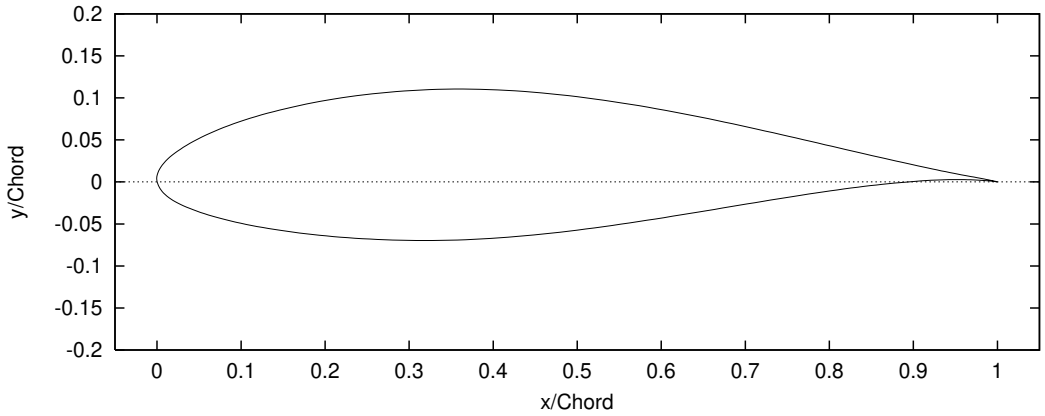

Figure 29. NACA 63-418 Airfoil

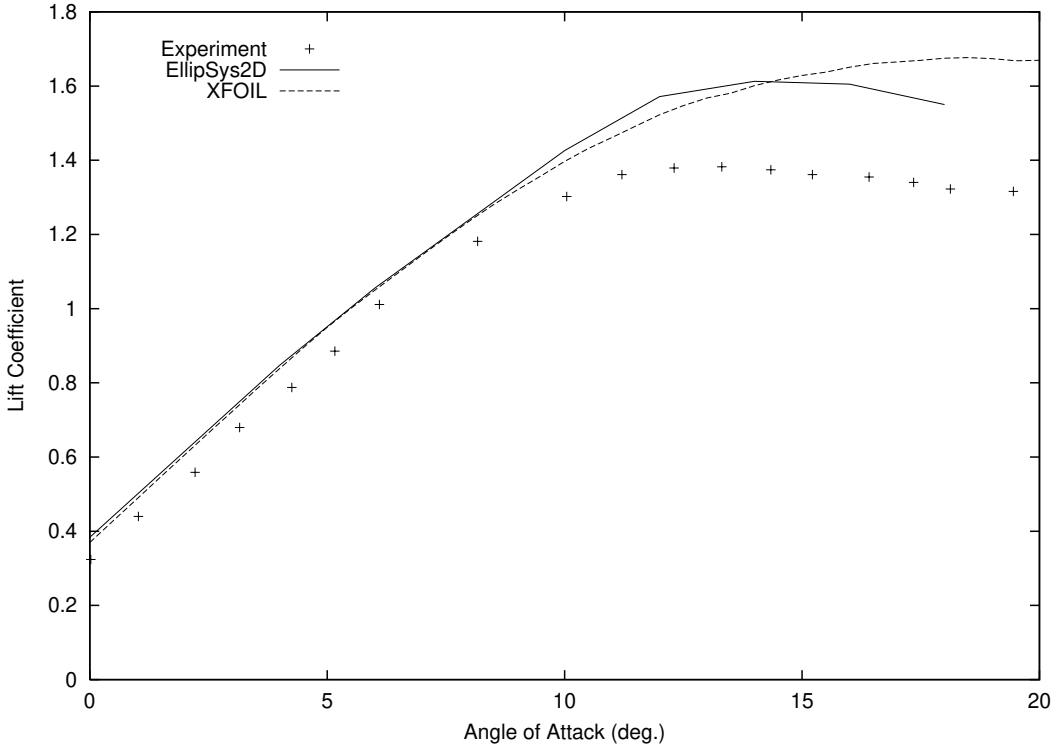

Figure 30. Lift Coefficient Curve (NACA 63-418, Experiment [1])

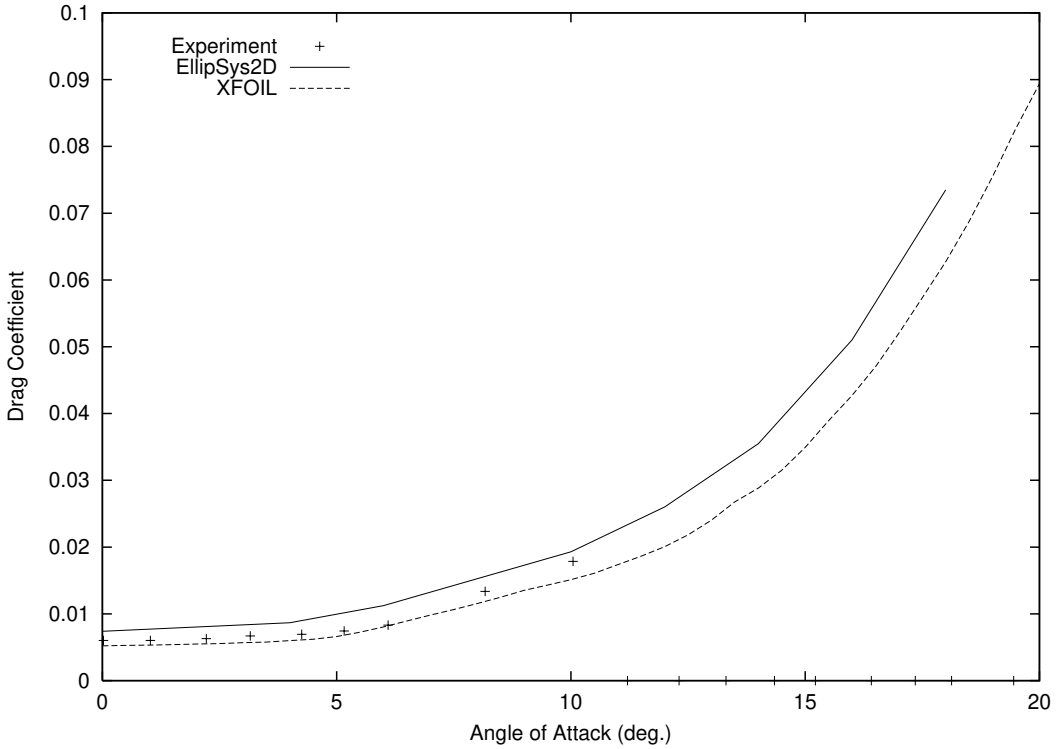

Figure 31. Drag Coefficient Curve (NACA 63-418, Experiment [1])

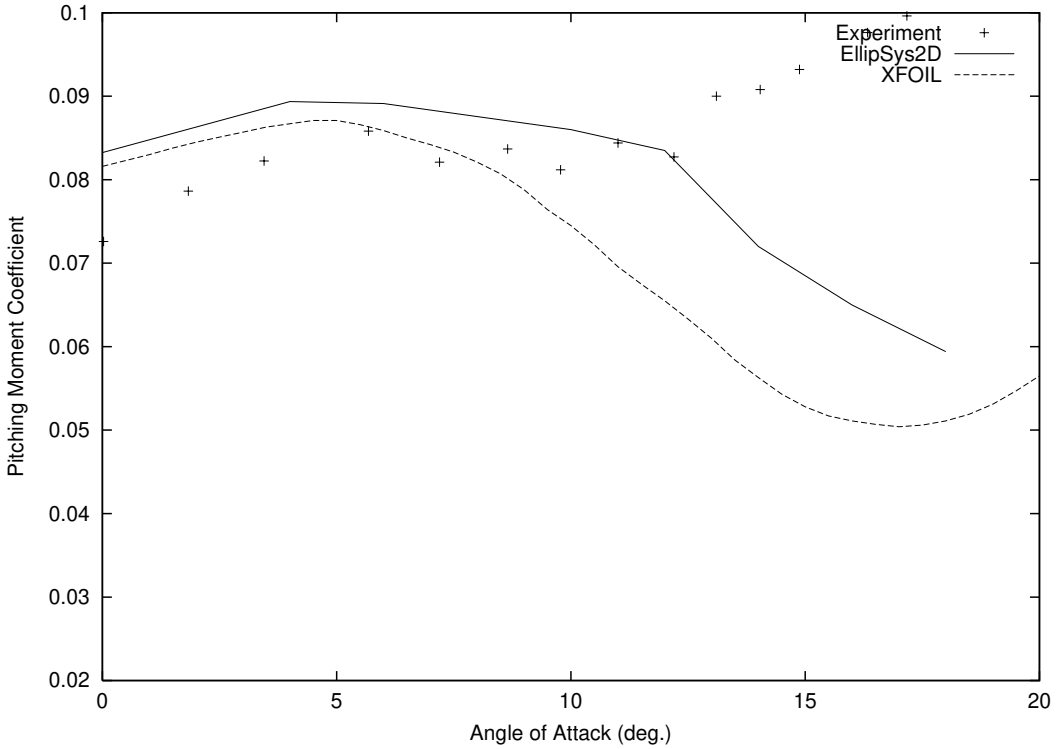

Figure 32. Pitching Moment Coefficient Curve (NACA 63-418, Experiment [1])

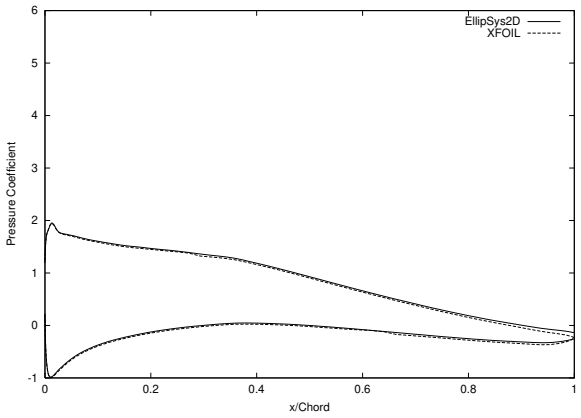

(a) $\alpha = 6^o$

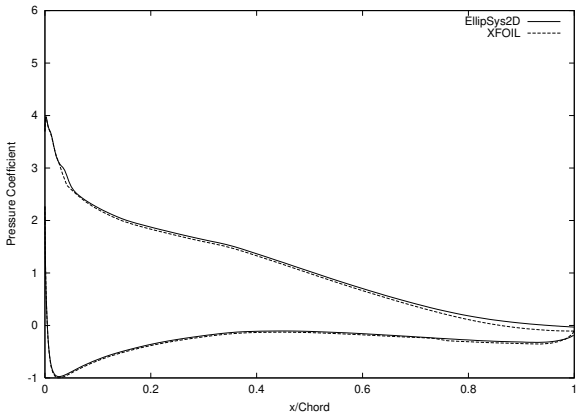

(b) $\alpha = 10^o$

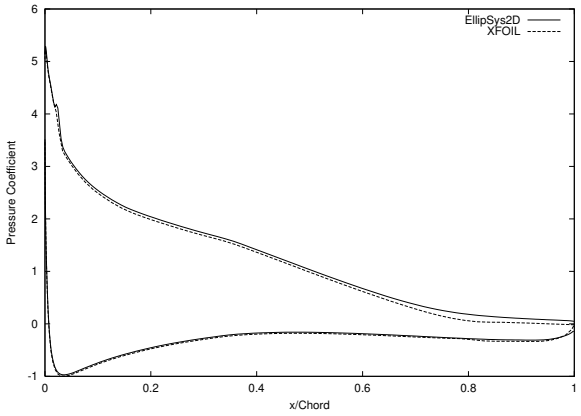

(c) $\alpha = 12^o$

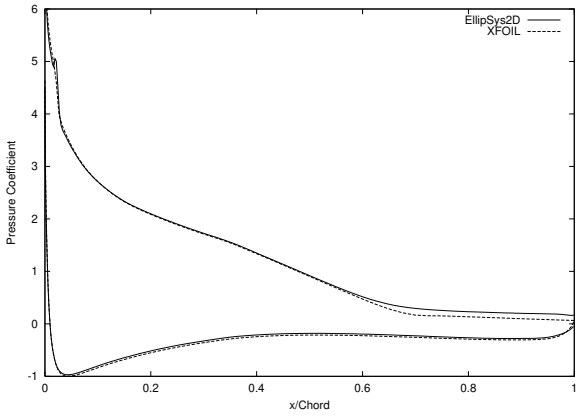

(d) $\alpha = 14^o$

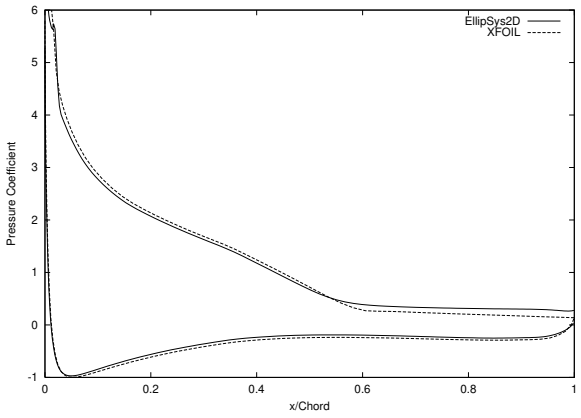

(e) $\alpha = 16^o$

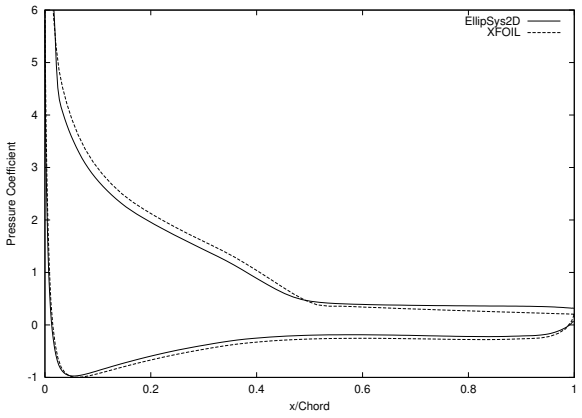

(f) $\alpha = 18^o$

Figure 33. Pressure Coefficient Distributions (NACA 63-418)

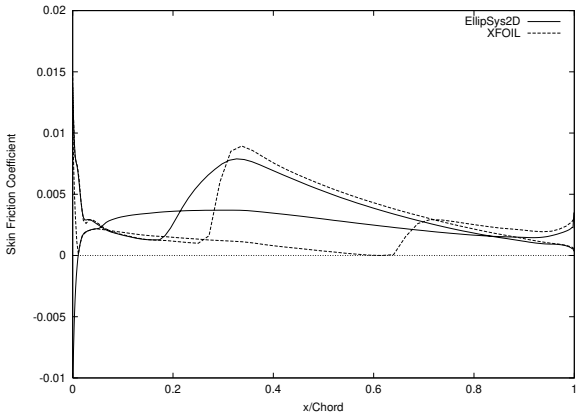

(a) $\alpha = 6^o$

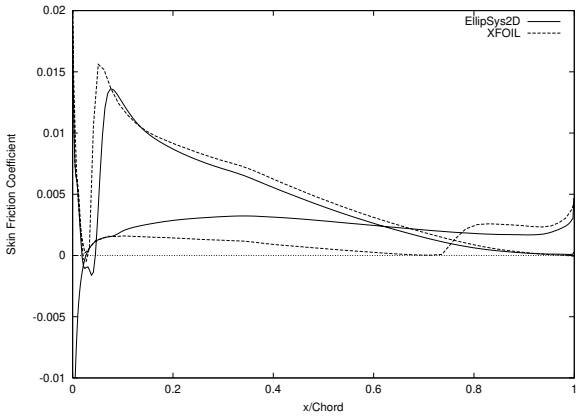

(b) $\alpha = 10^o$

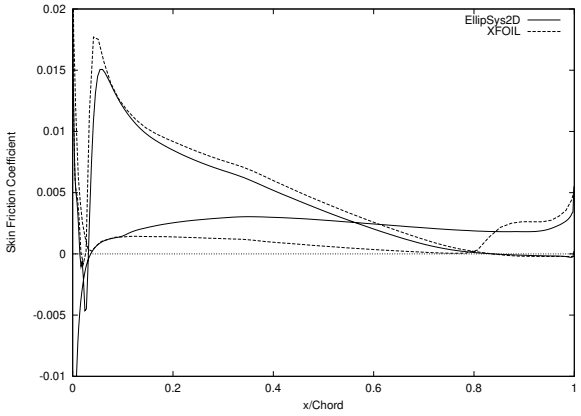

(c) $\alpha = 12^o$

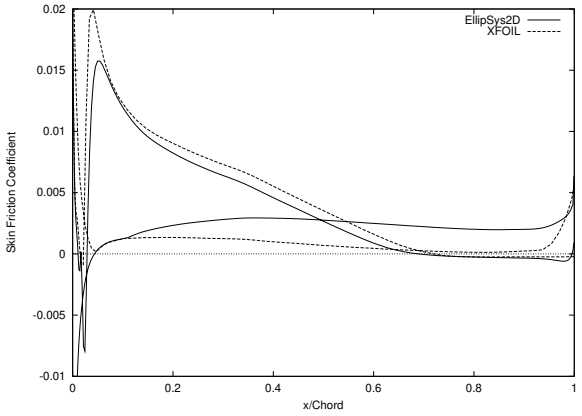

(d) $\alpha = 14^o$

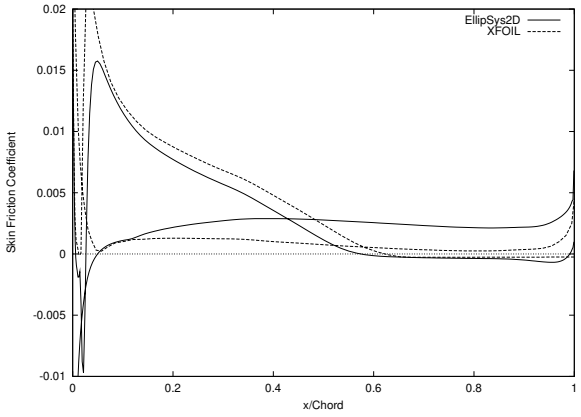

(e) $\alpha = 16^o$

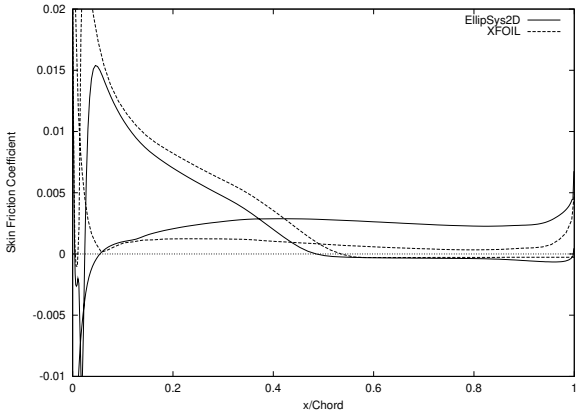

(f) $\alpha = 18^o$

Figure 34. Skin Friction Coefficient Distributions (NACA 63-418)

NACA 63-421

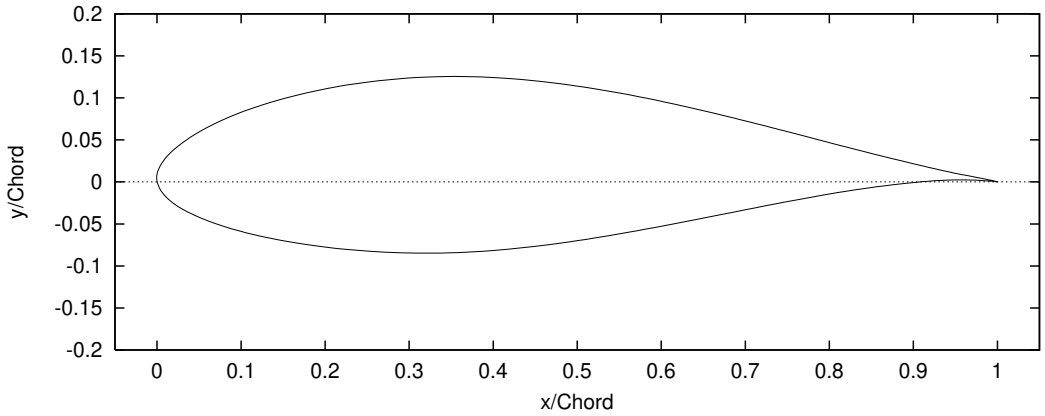

Figure 35. NACA 63-421 Airfoil

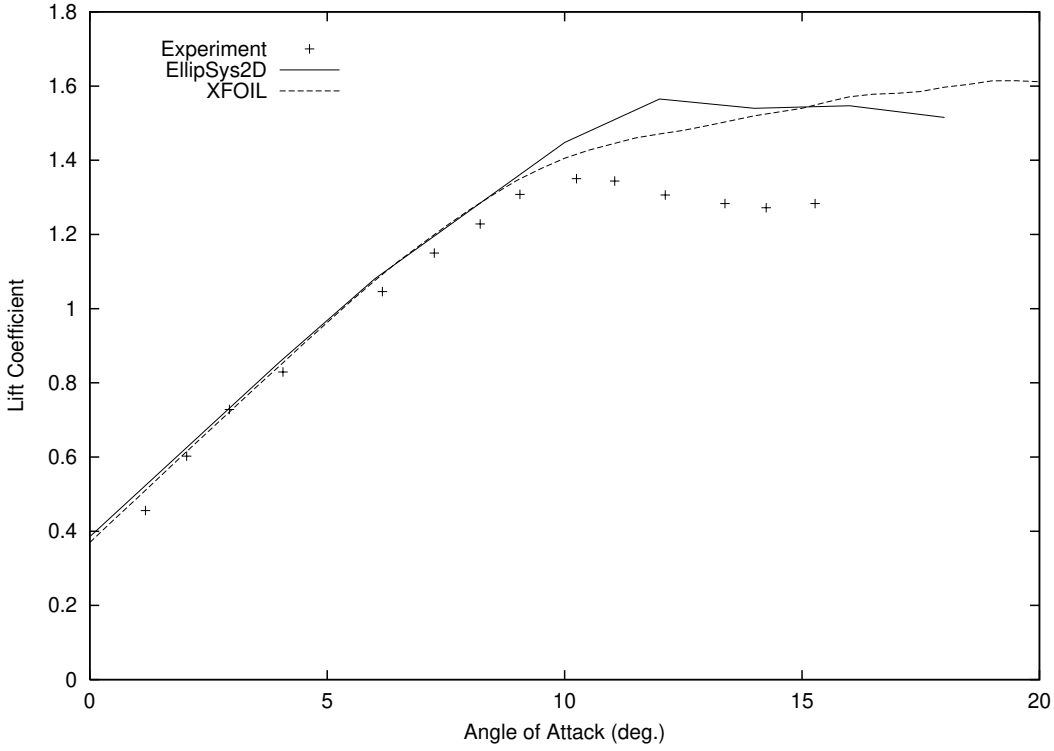

Figure 36. Lift Coefficient Curve (NACA 63-421, Experiment [1])

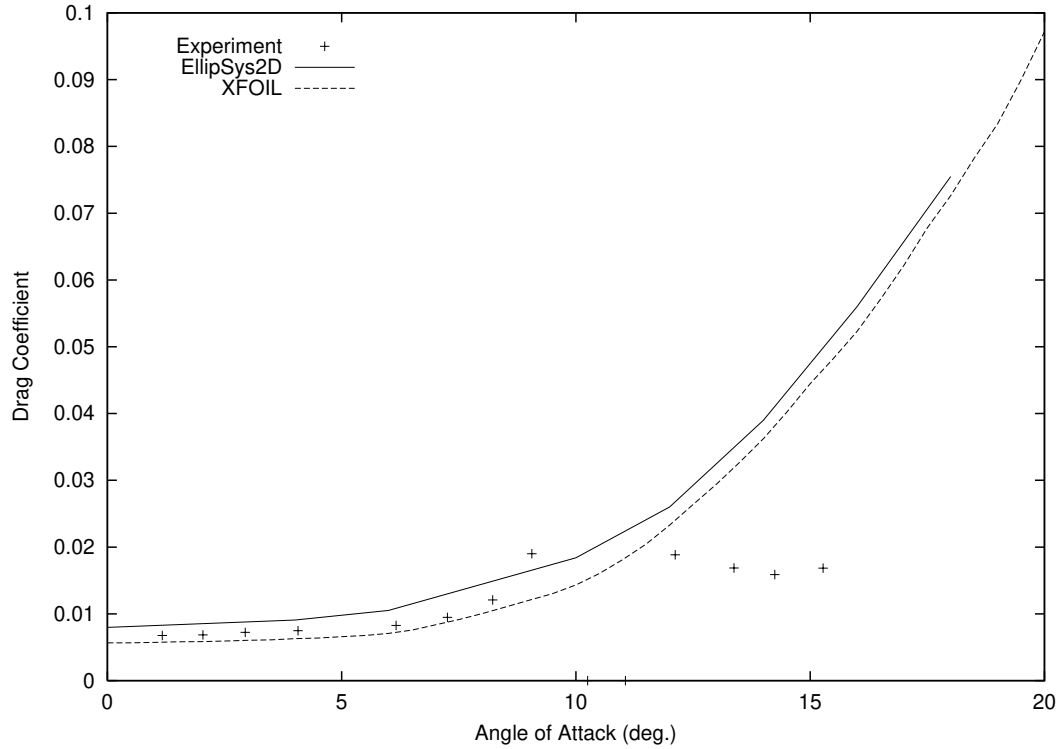

Figure 37. Drag Coefficient Curve (NACA 63-421, Experiment [1])

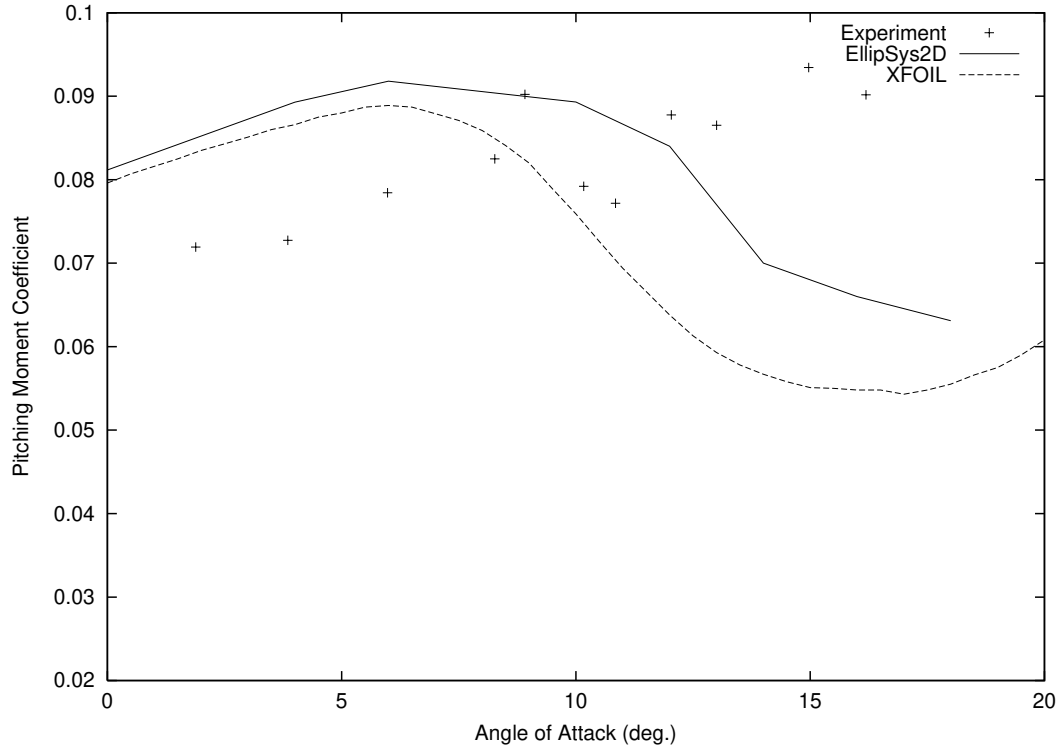

Figure 38. Pitching Moment Coefficient Curve (NACA 63-421, Experiment [1])

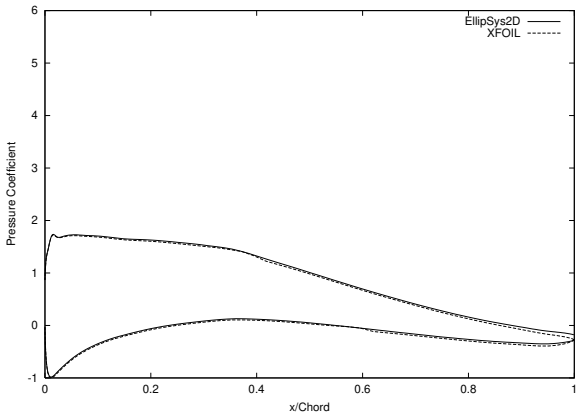

(a) $\alpha = 6^o$

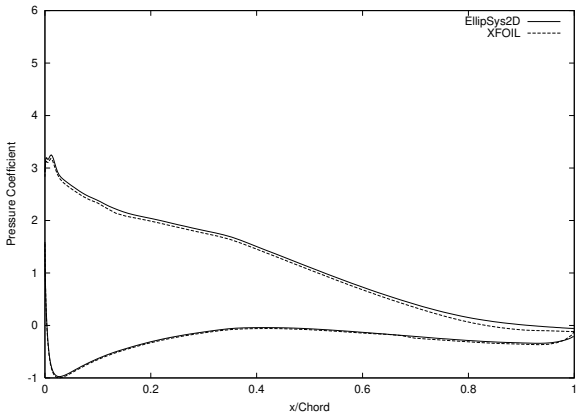

(b) $\alpha = 10^o$

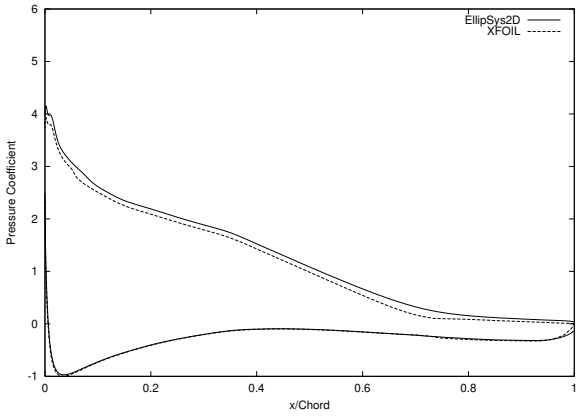

(c) $\alpha = 12^o$

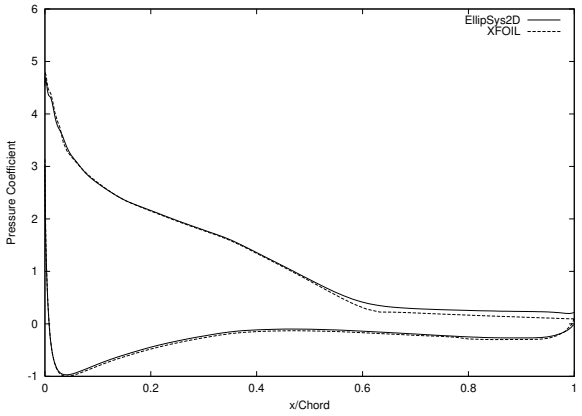

(d) $\alpha = 14^o$

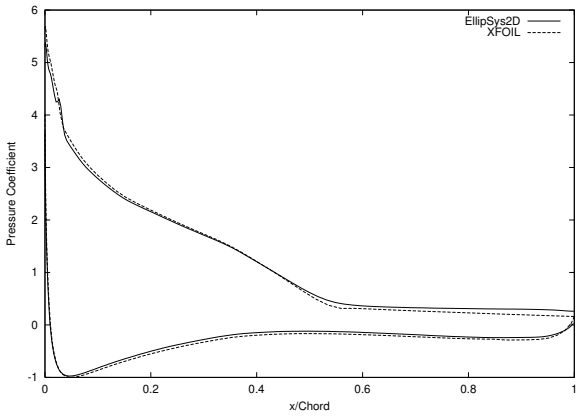

(e) $\alpha = 16^o$

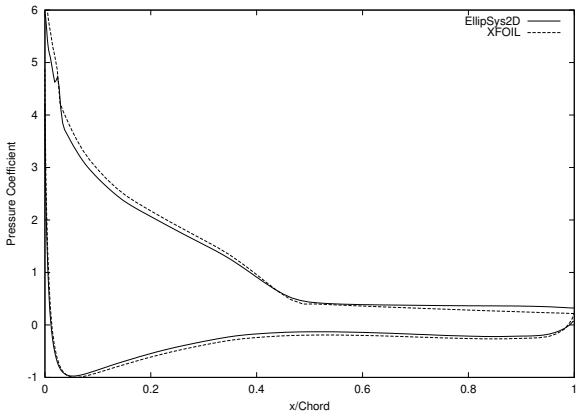

(f) $\alpha = 18^o$

Figure 39. Pressure Coefficient Distributions (NACA 63-421)

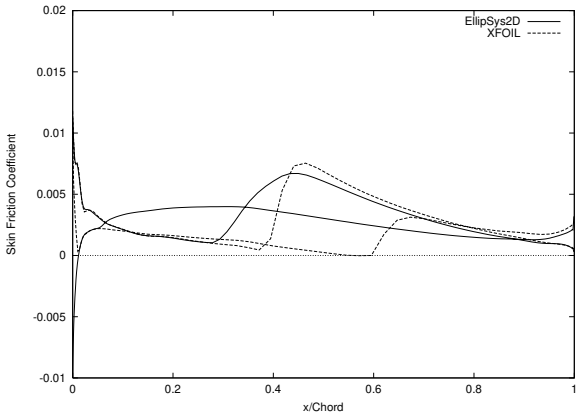

(a) $\alpha = 6^o$

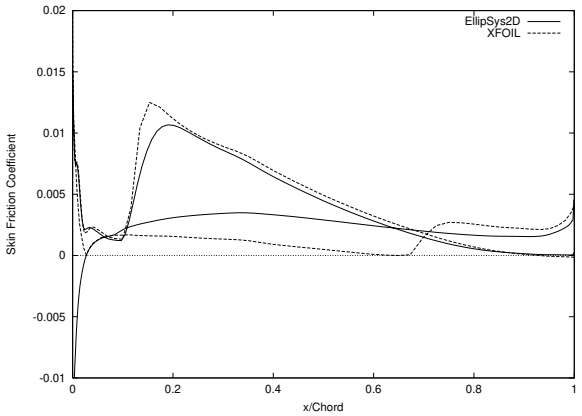

(b) $\alpha = 10^o$

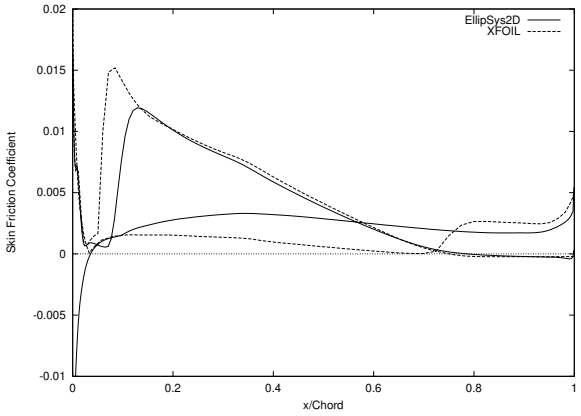

(c) $\alpha = 12^o$

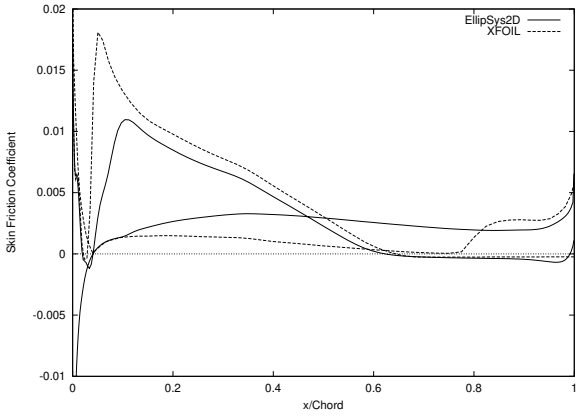

(d) $\alpha = 14^o$

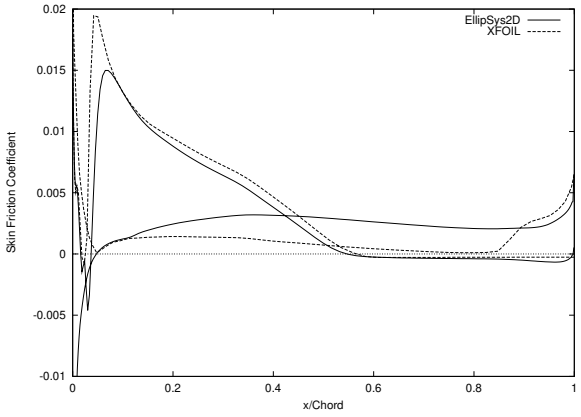

(e) $\alpha = 16^o$

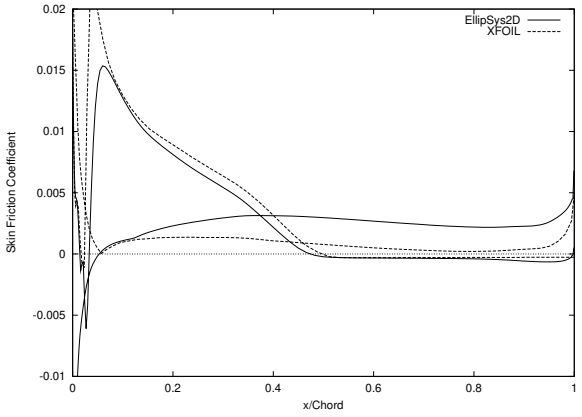

(f) $\alpha = 18^o$

Figure 40. Skin Friction Coefficient Distributions (NACA 63-421)

NACA 64-415

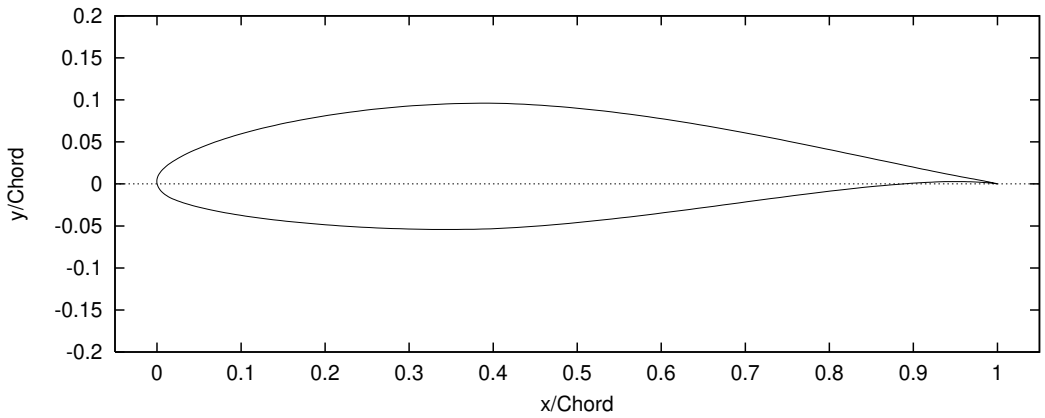

Figure 41. NACA 64-415 Airfoil

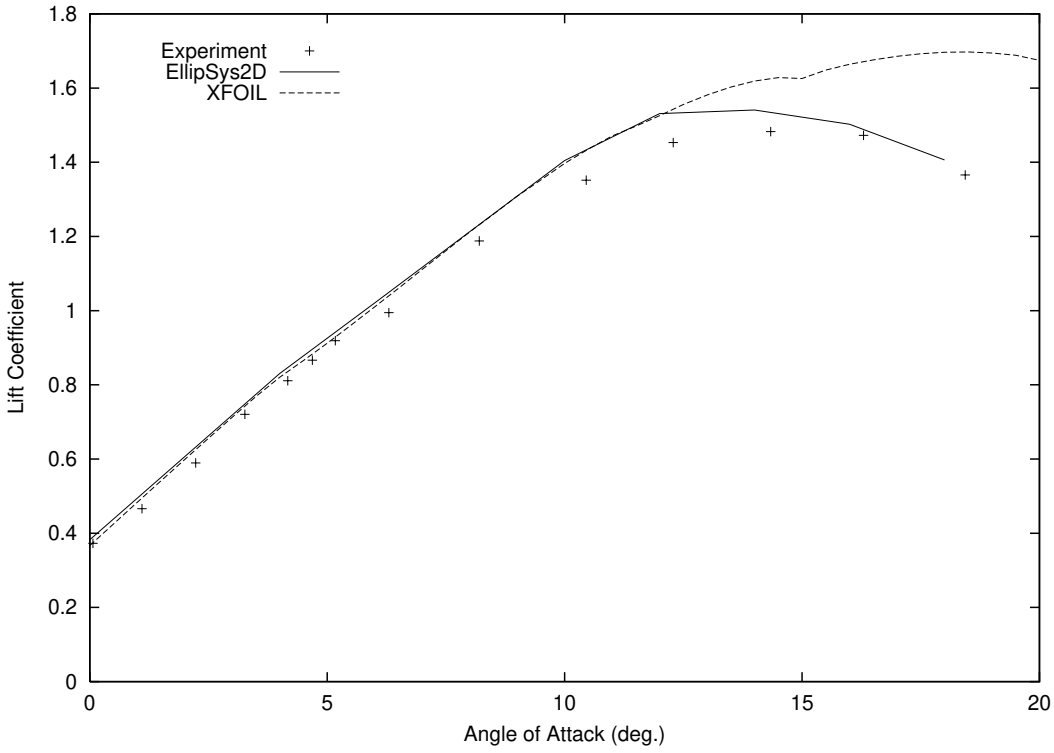

Figure 42. Lift Coefficient Curve (NACA 64-415, Experiment [1])

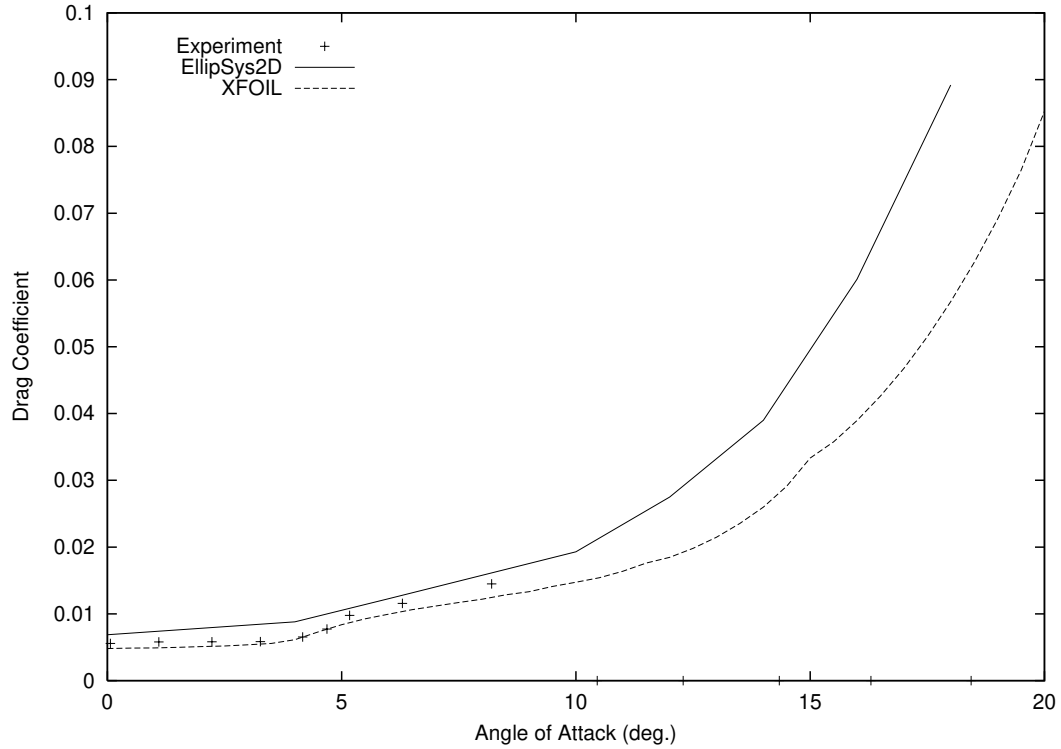

Figure 43. Drag Coefficient Curve (NACA 64-415, Experiment [1])

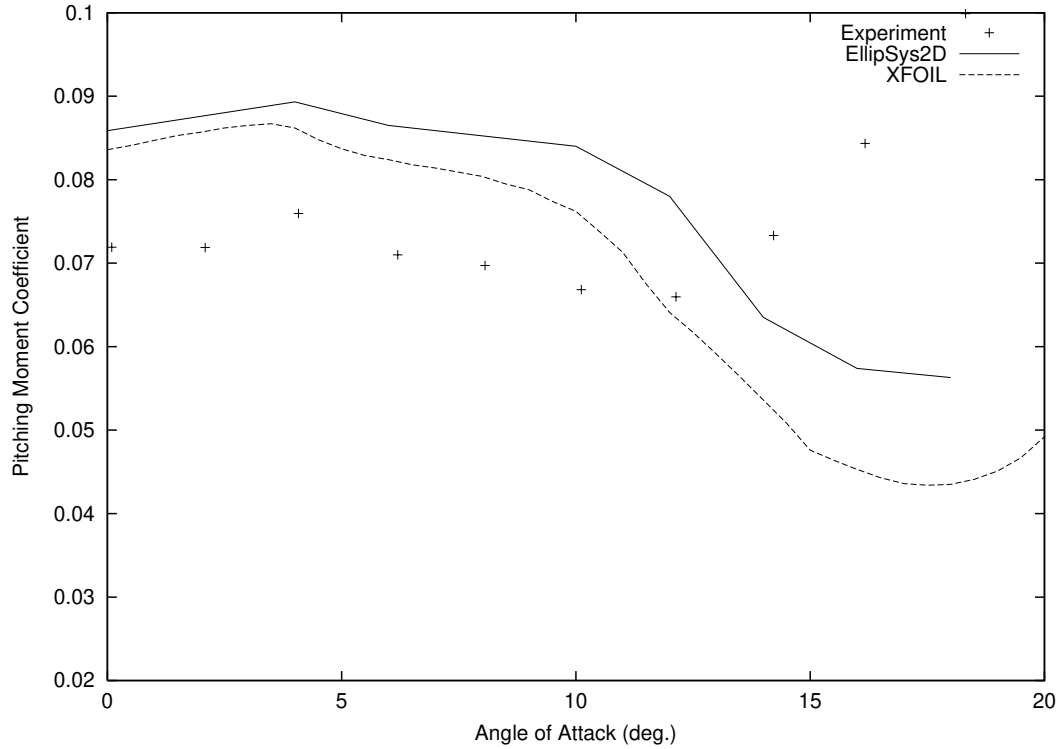

Figure 44. Pitching Moment Coefficient Curve (NACA 64-415, Experiment [1])

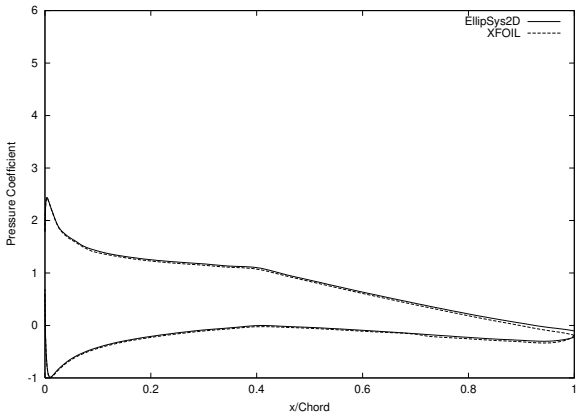

(a) $\alpha = 6^o$

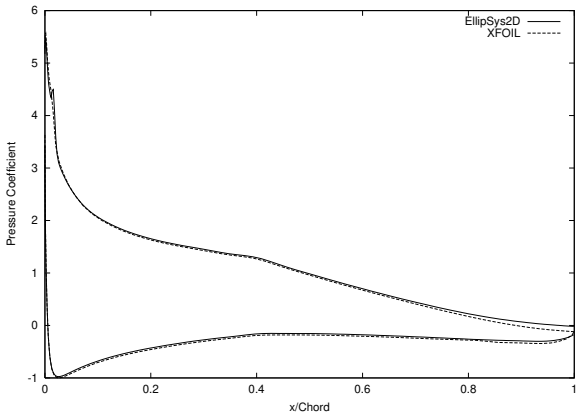

(b) $\alpha = 10^o$

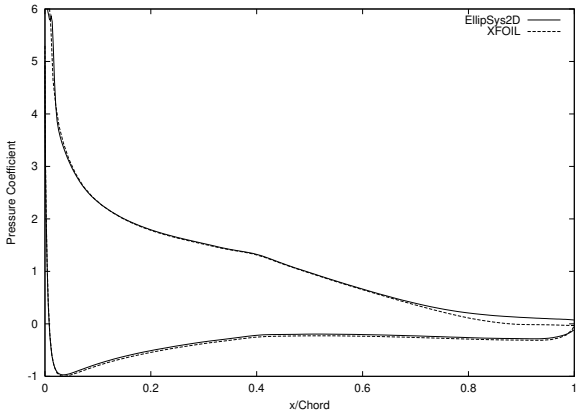

(c) $\alpha = 12^o$

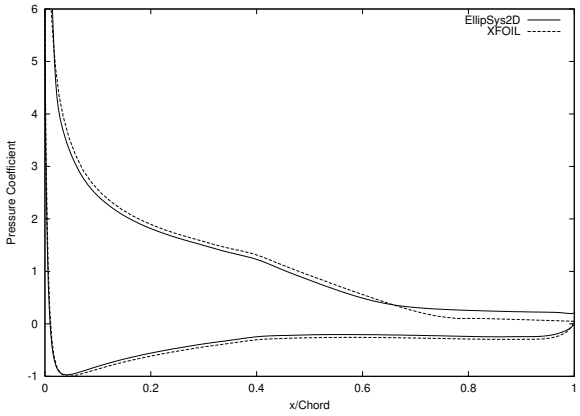

(d) $\alpha = 14^o$

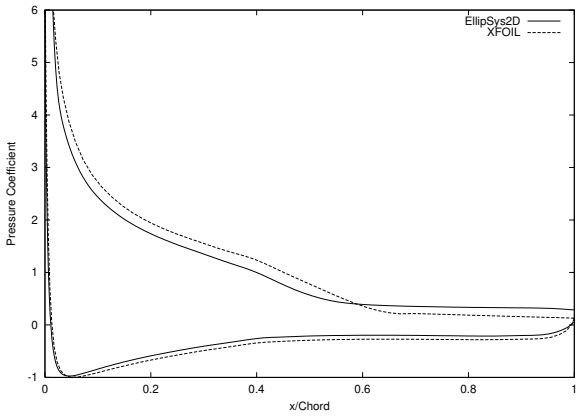

(e) $\alpha = 16^o$

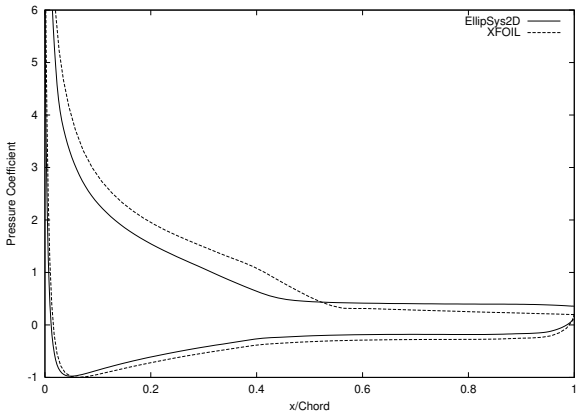

(f) $\alpha = 18^o$

Figure 45. Pressure Coefficient Distributions (NACA 64-415)

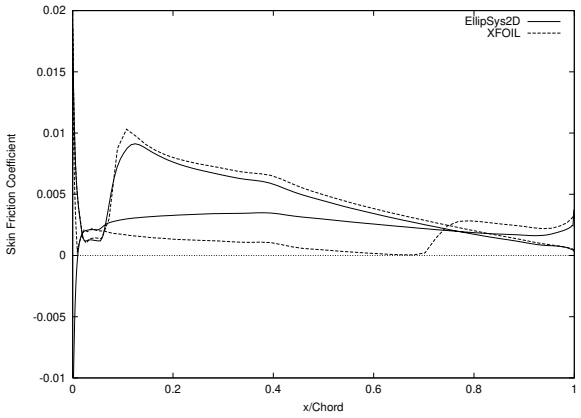

(a) $\alpha = 6^o$

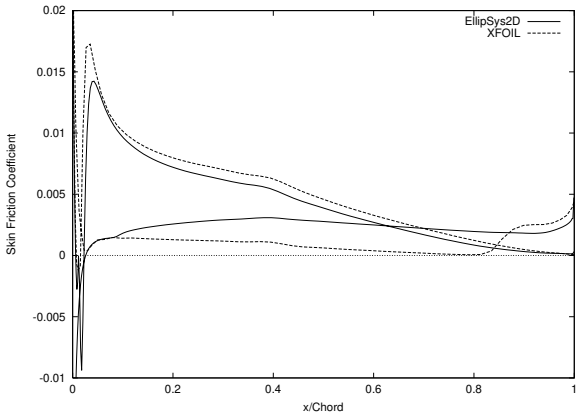

(b) $\alpha = 10^o$

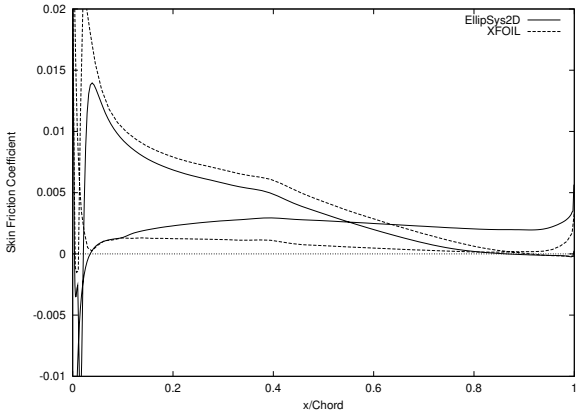

(c) $\alpha = 12^o$

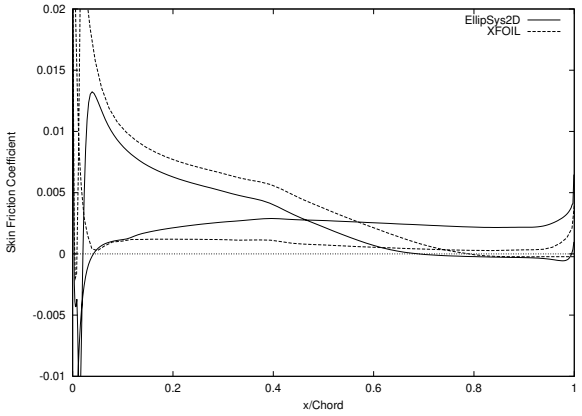

(d) $\alpha = 14^o$

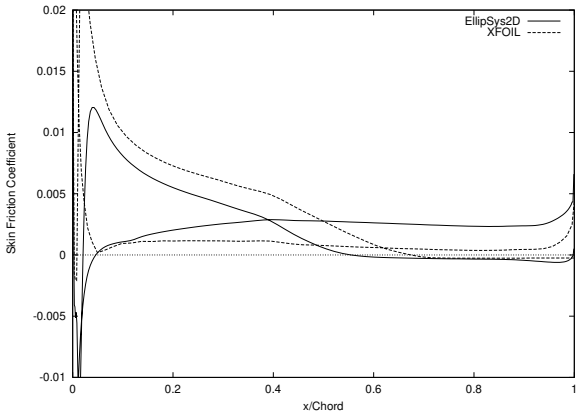

(e) $\alpha = 16^o$

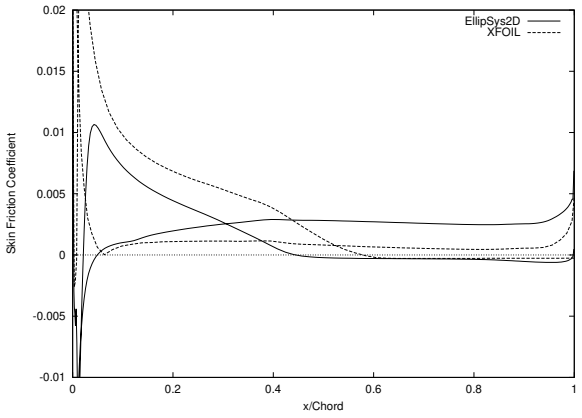

(f) $\alpha = 18^o$

Figure 46. Skin Friction Coefficient Distributions (NACA 64-415)

NACA 64-421

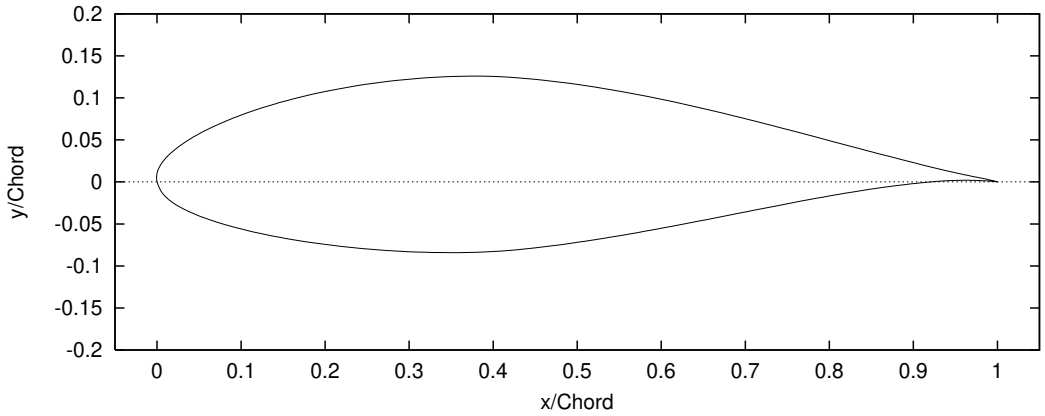

Figure 47. NACA 64-421 Airfoil

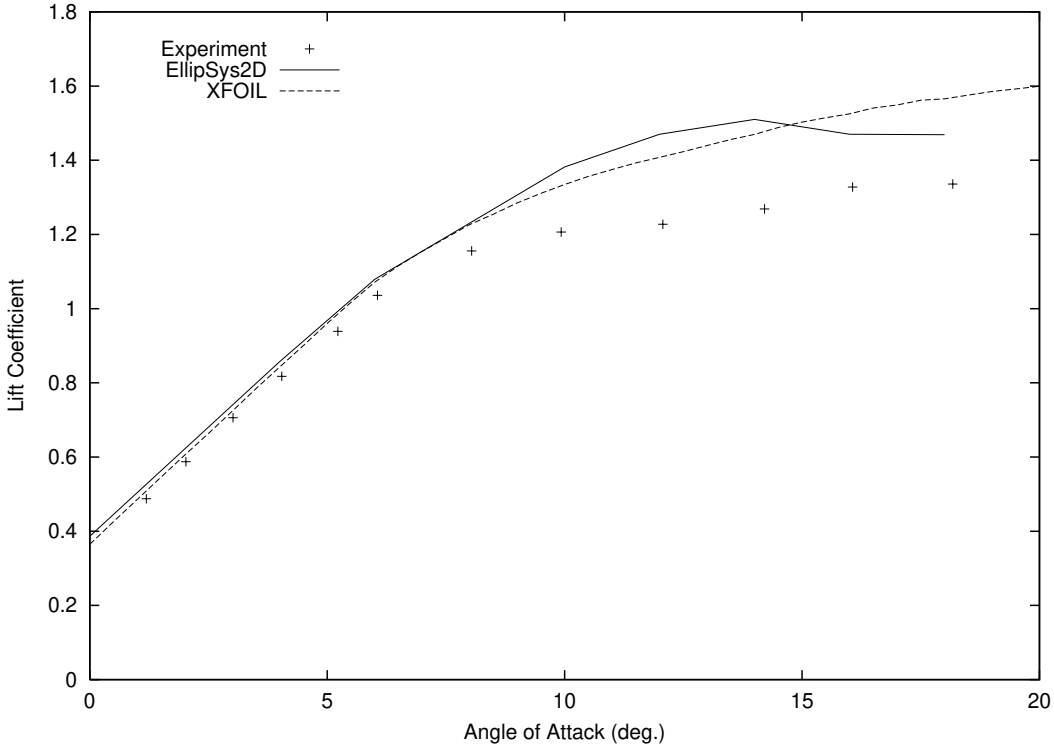

Figure 48. Lift Coefficient Curve (NACA 64-421, Experiment [1])

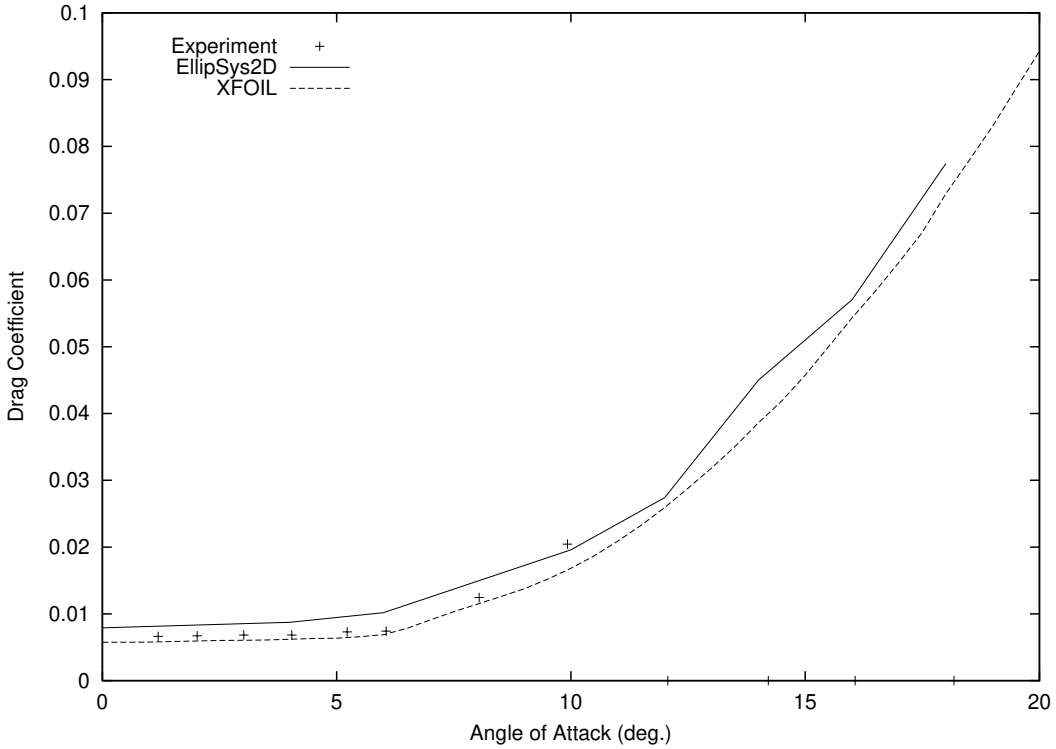

Figure 49. Drag Coefficient Curve (NACA 64-421, Experiment [1])

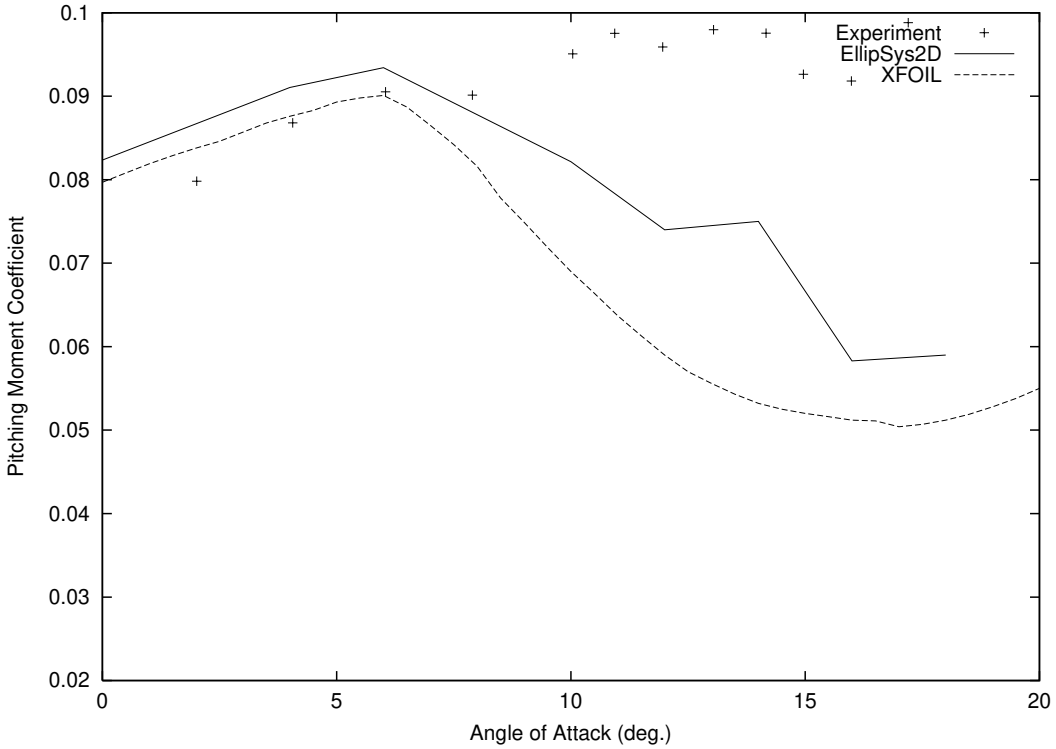

Figure 50. Pitching Moment Coefficient Curve (NACA 64-421, Experiment [1])

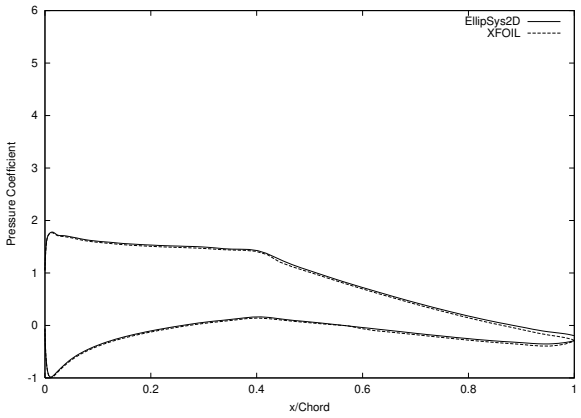

(a) $\alpha = 6^o$

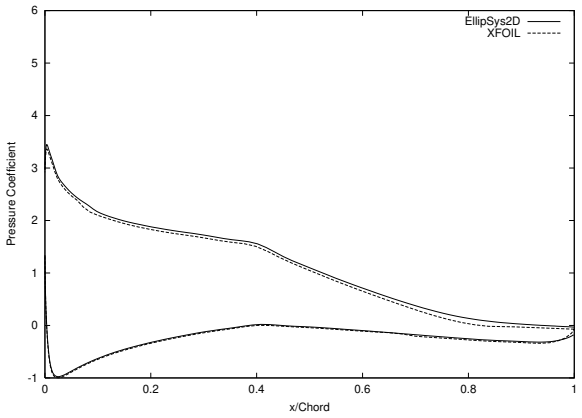

(b) $\alpha = 10^o$

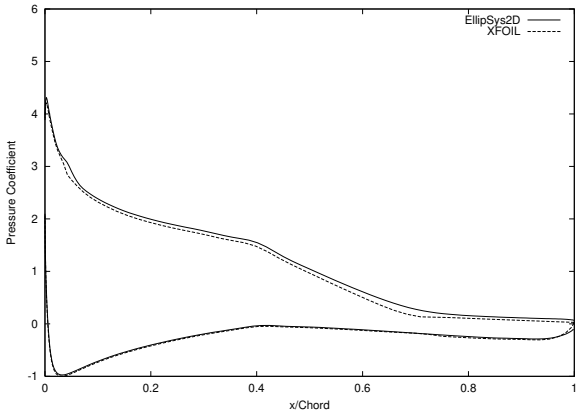

(c) $\alpha = 12^o$

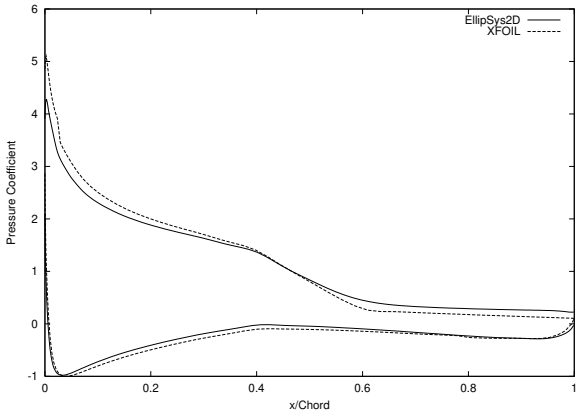

(d) $\alpha = 14^o$

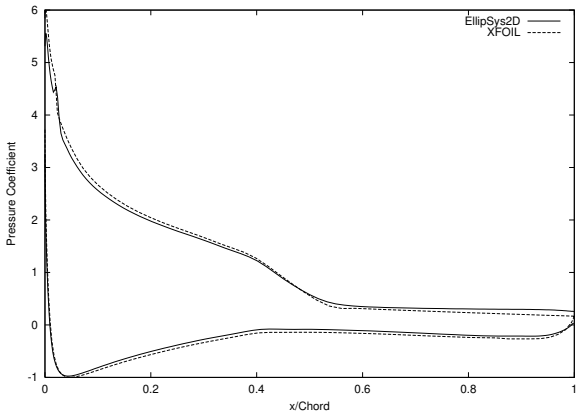

(e) $\alpha = 16^o$

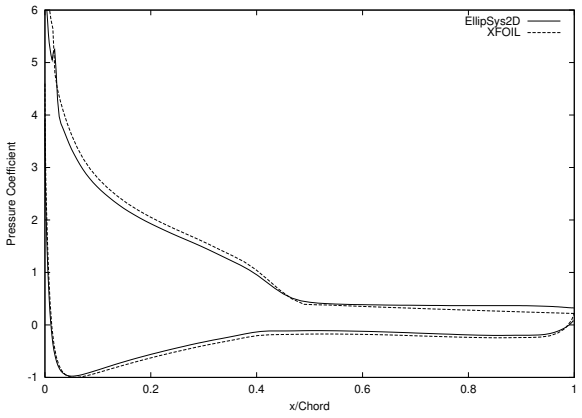

(f) $\alpha = 18^o$

Figure 51. Pressure Coefficient Distributions (NACA 64-421)

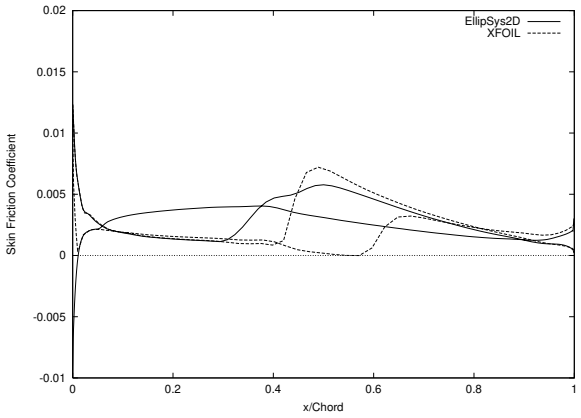

(a) $\alpha = 6^o$

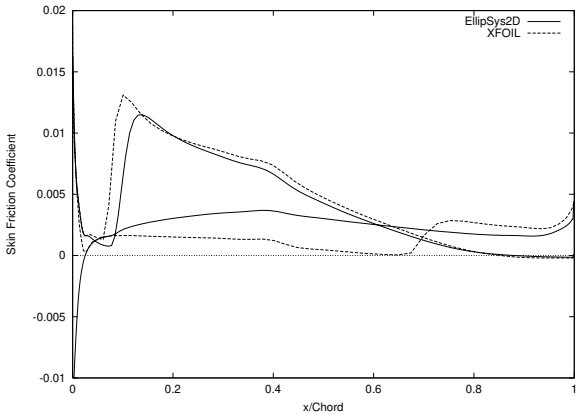

(b) $\alpha = 10^o$

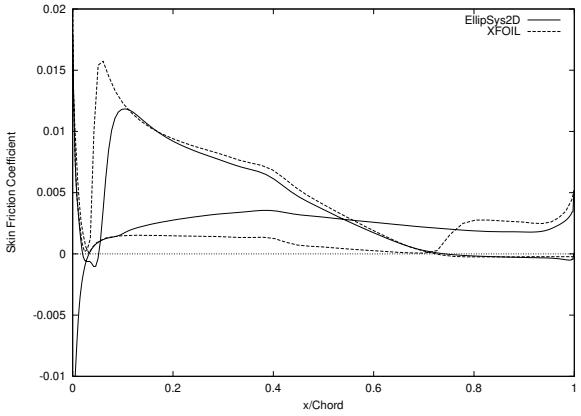

(c) $\alpha = 12^o$

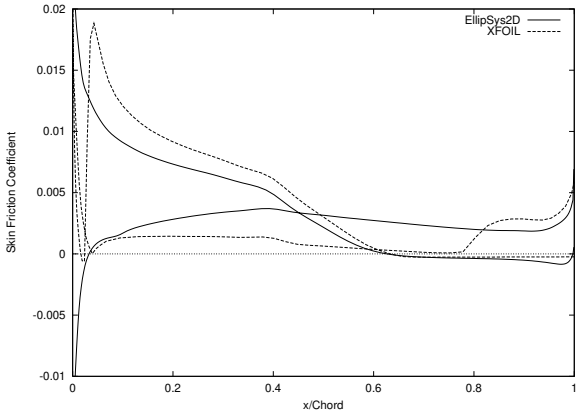

(d) $\alpha = 14^o$

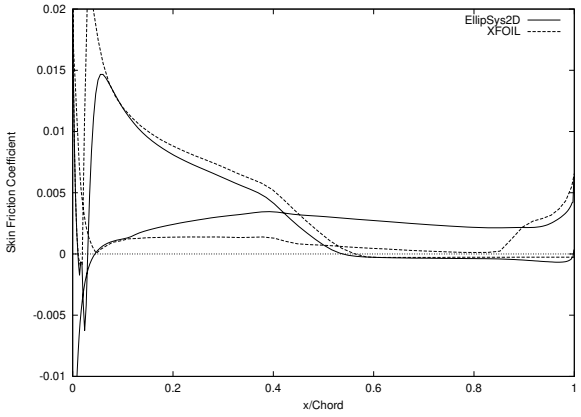

(e) $\alpha = 16^o$

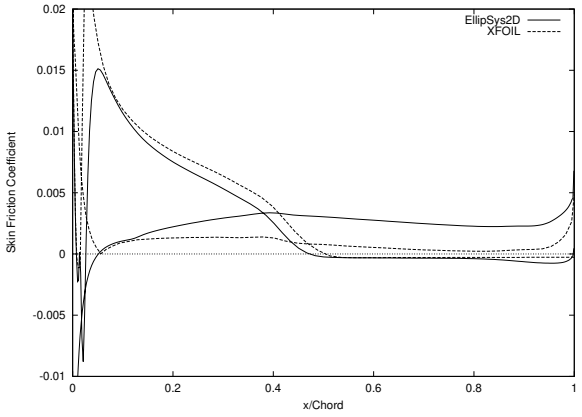

(f) $\alpha = 18^o$

Figure 52. Skin Friction Coefficient Distributions (NACA 64-421)

NACA 65-415

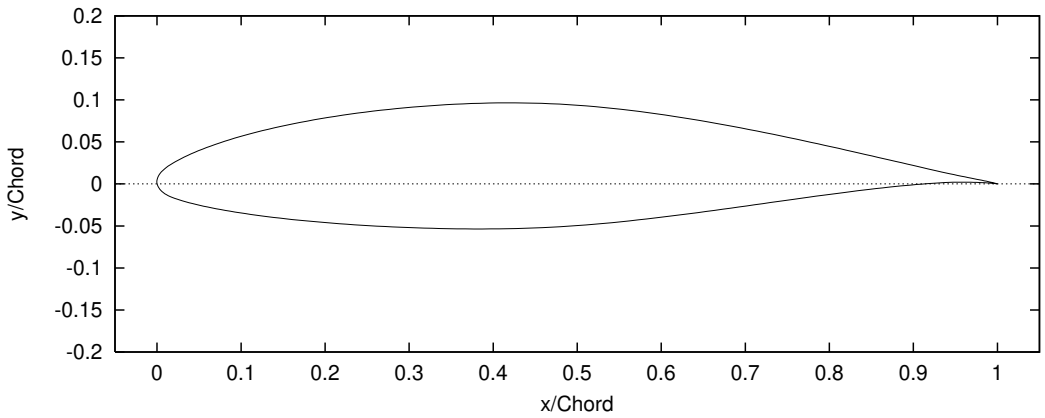

Figure 53. NACA 65-415 Airfoil

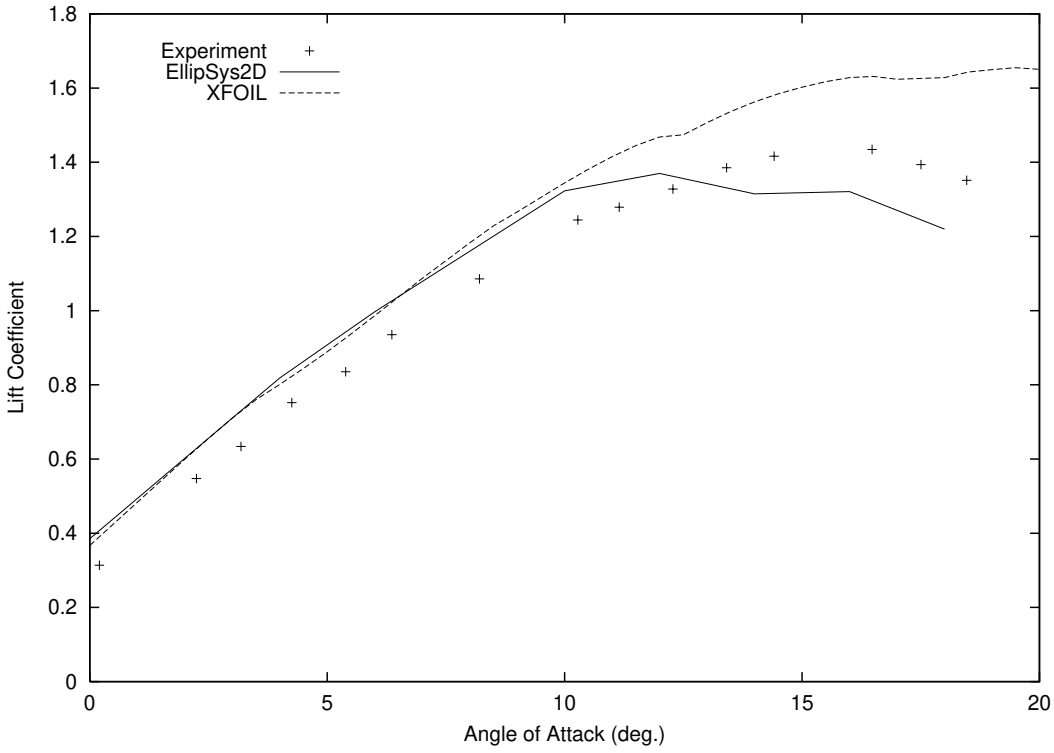

Figure 54. Lift Coefficient Curve (NACA 65-415, Experiment [1])

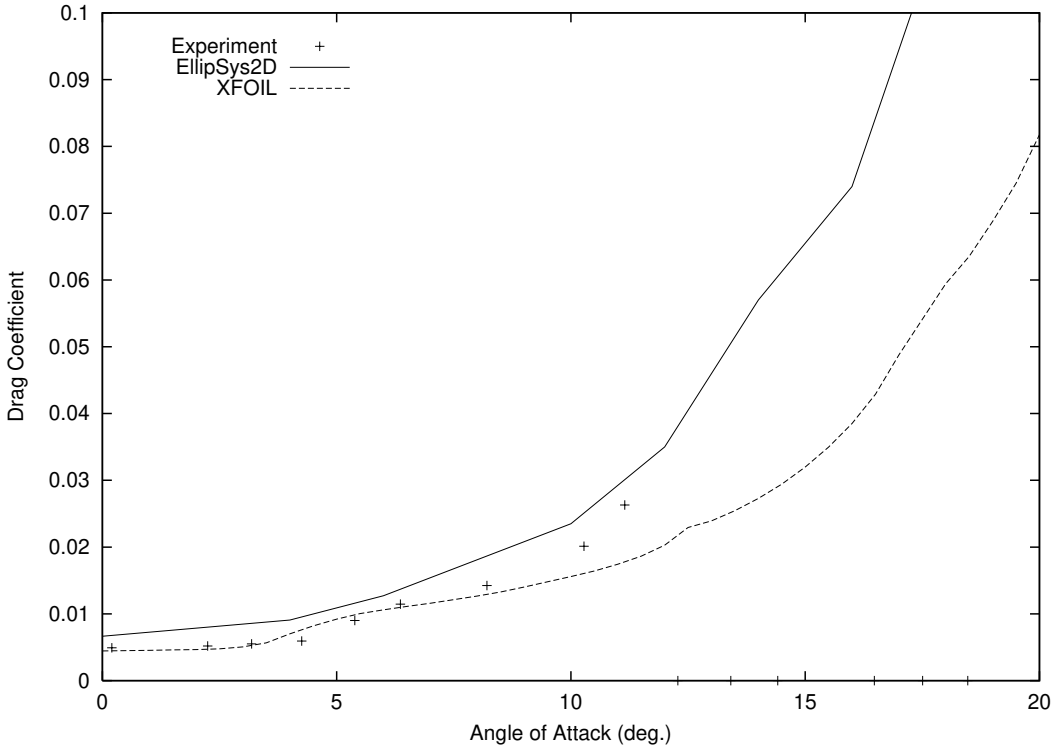

Figure 55. Drag Coefficient Curve (NACA 65-415, Experiment [1])

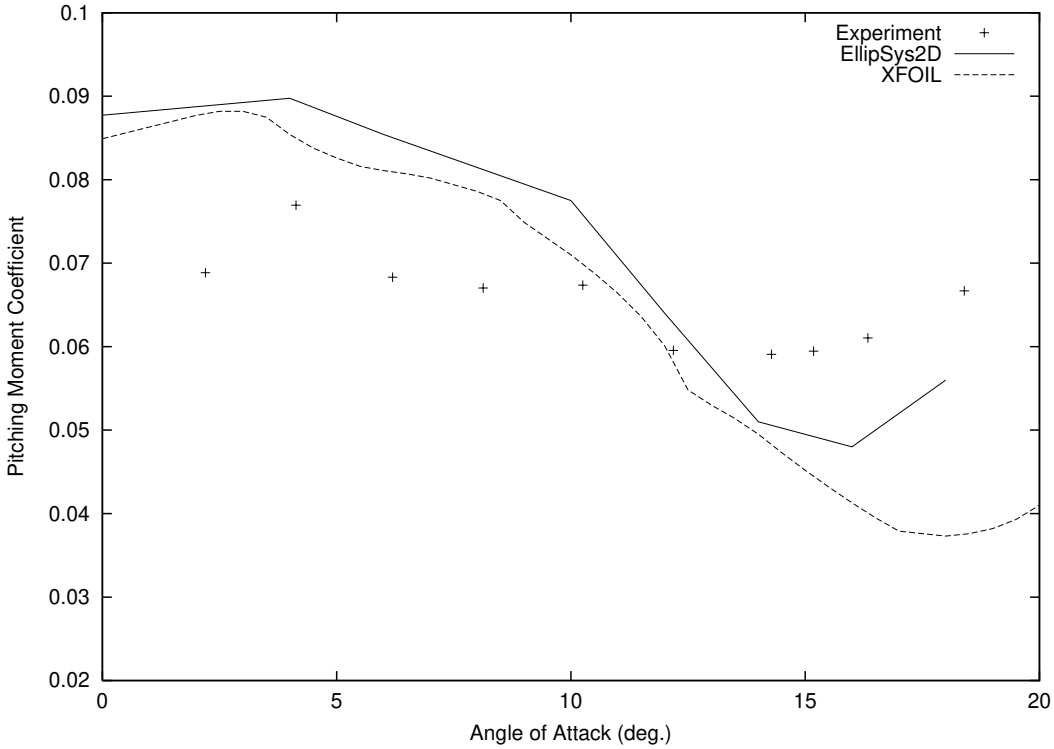

Figure 56. Pitching Moment Coefficient Curve (NACA 65-415, Experiment [1])

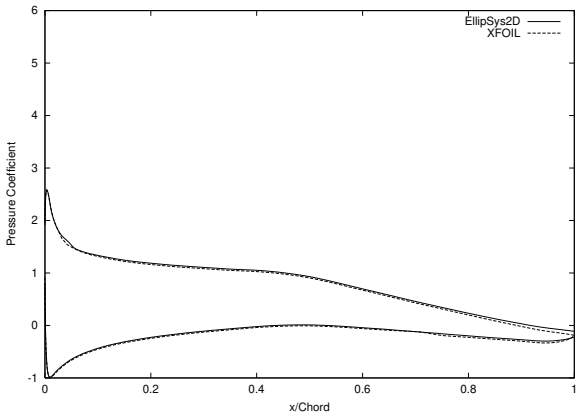

(a) $\alpha = 6^o$

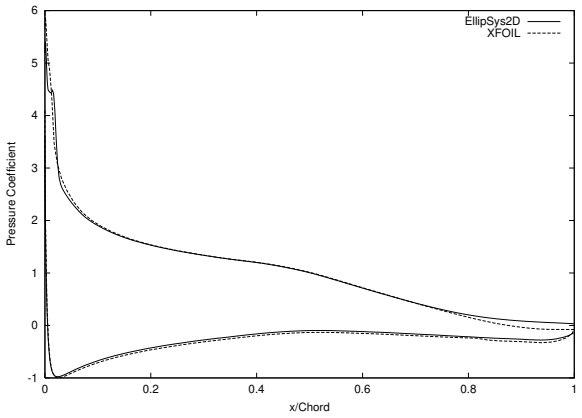

(b) $\alpha = 10^o$

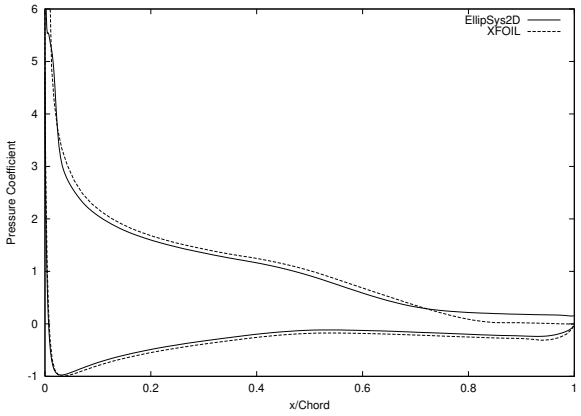

(c) $\alpha = 12^o$

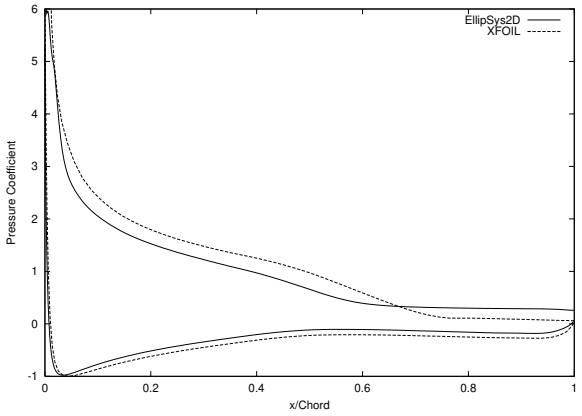

(d) $\alpha = 14^o$

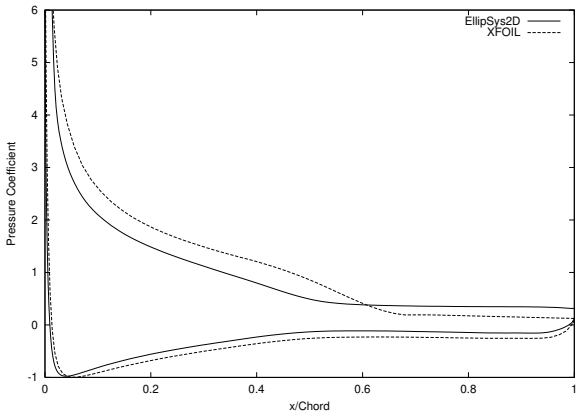

(e) $\alpha = 16^o$

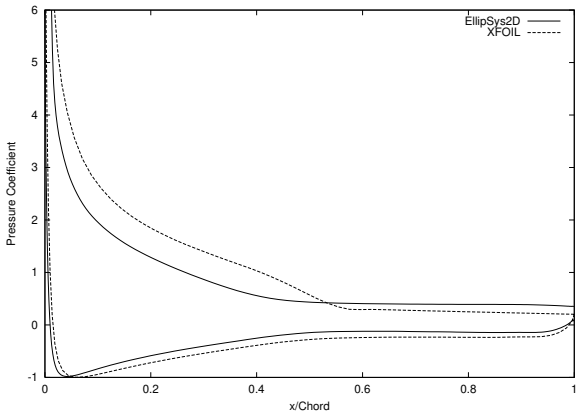

(f) $\alpha = 18^o$

Figure 57. Pressure Coefficient Distributions (NACA 65-415)

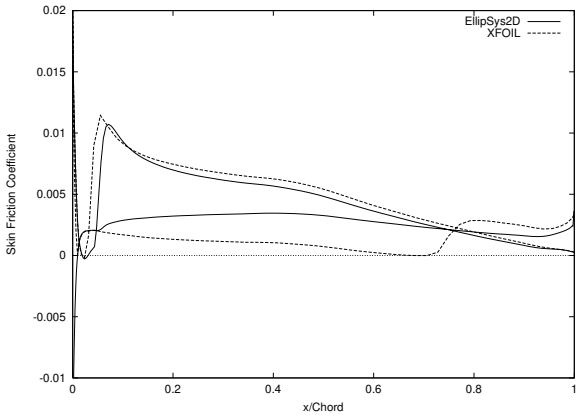

(a) $\alpha = 6^o$

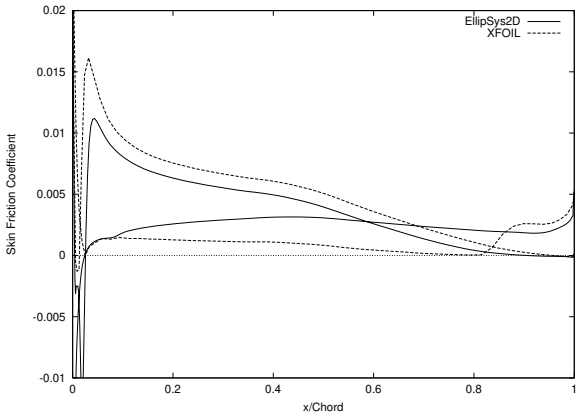

(b) $\alpha = 10^o$

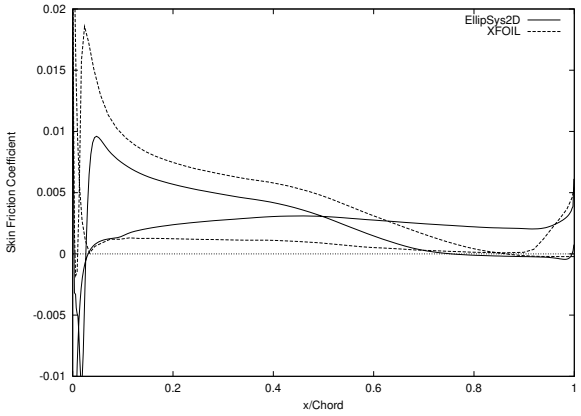

(c) $\alpha = 12^o$

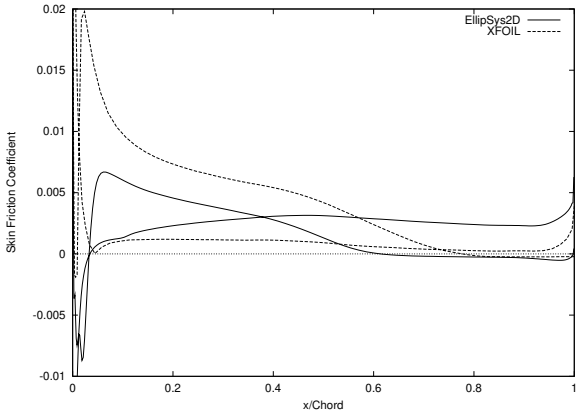

(d) $\alpha = 14^o$

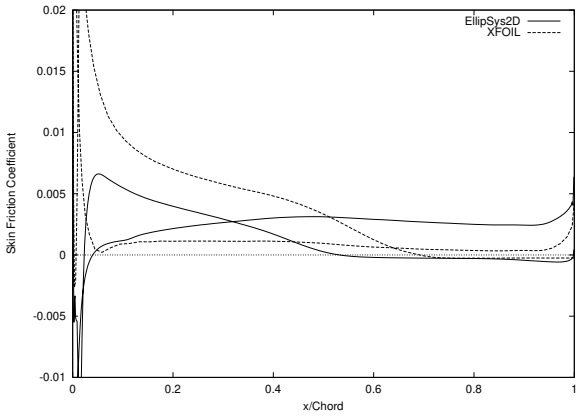

(e) $\alpha = 16^o$

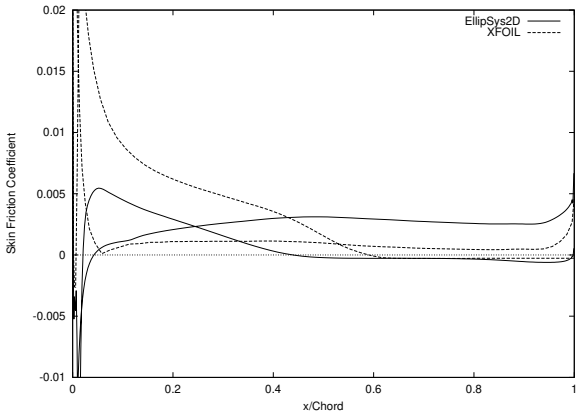

(f) $\alpha = 18^o$

Figure 58. Skin Friction Coefficient Distributions (NACA 65-415)

NACA 65-421

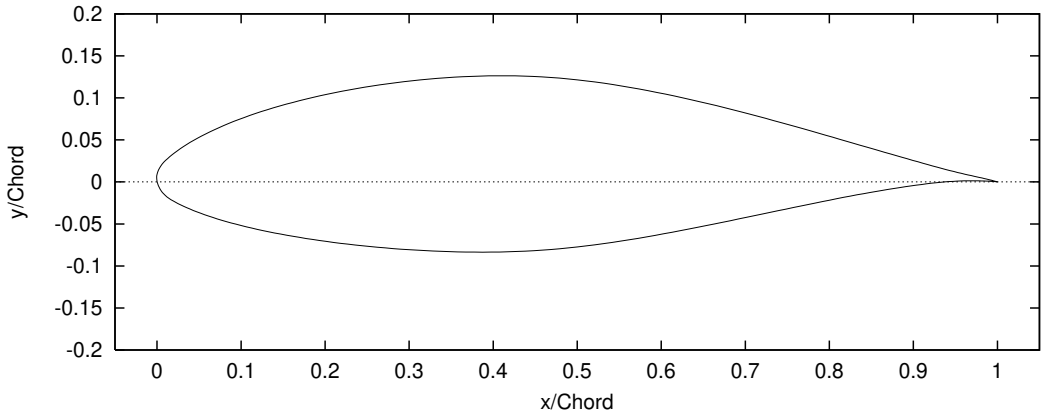

Figure 59. NACA 65-421 Airfoil

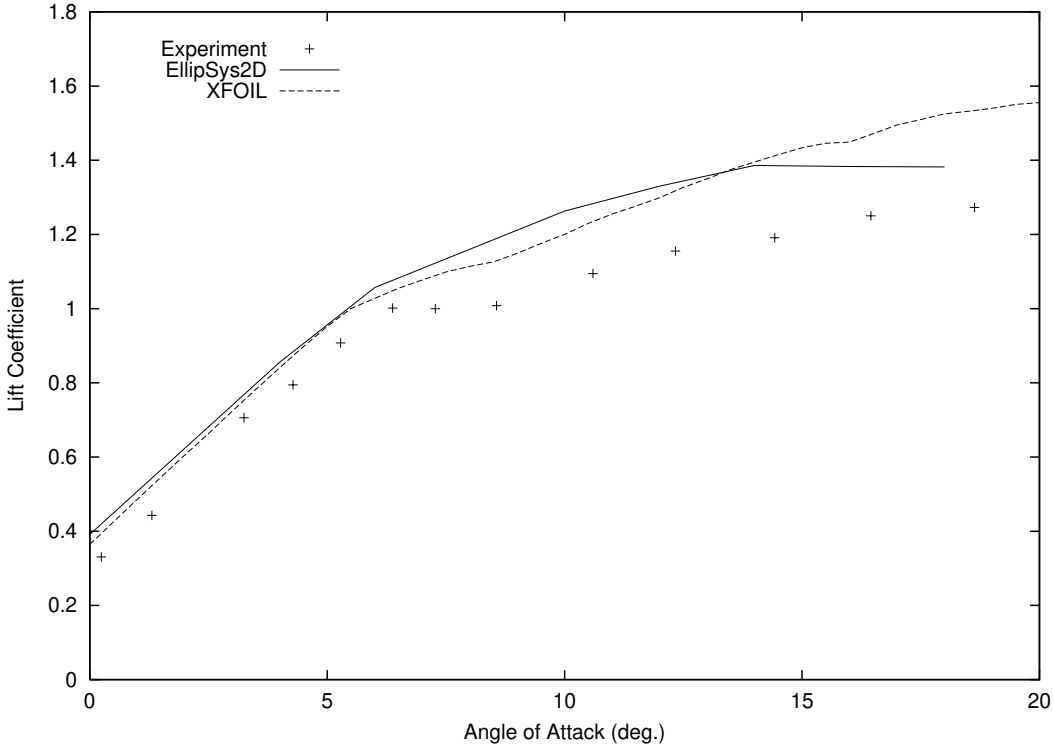

Figure 60. Lift Coefficient Curve (NACA 65-421, Experiment [1])

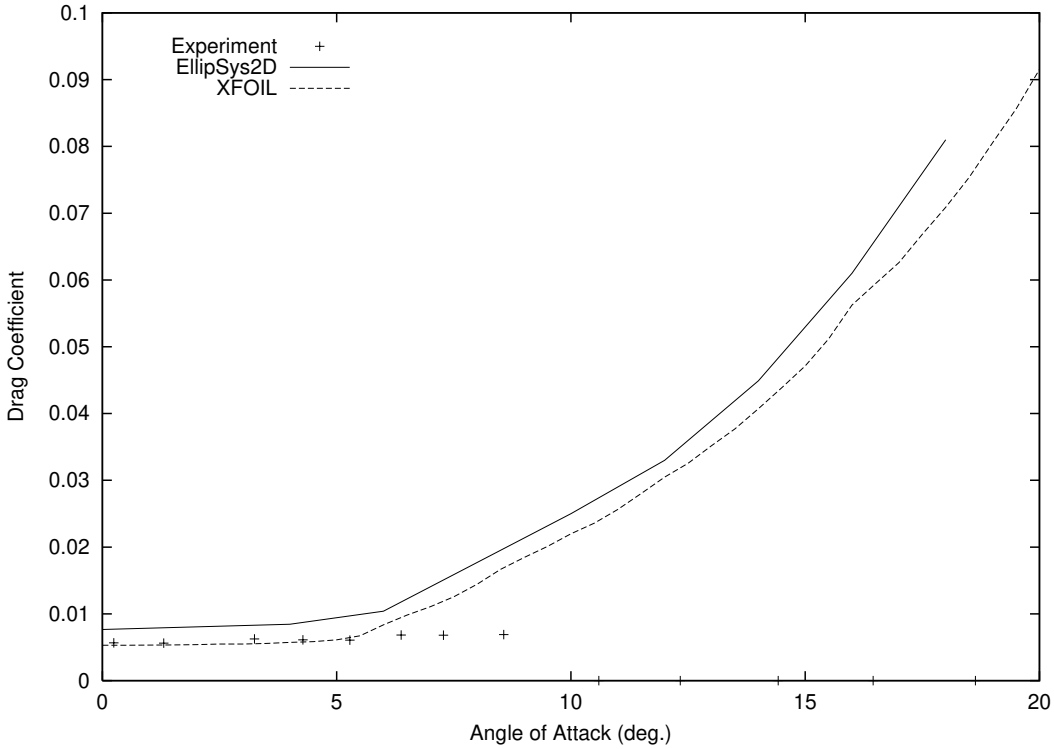

Figure 61. Drag Coefficient Curve (NACA 65-421, Experiment [1])

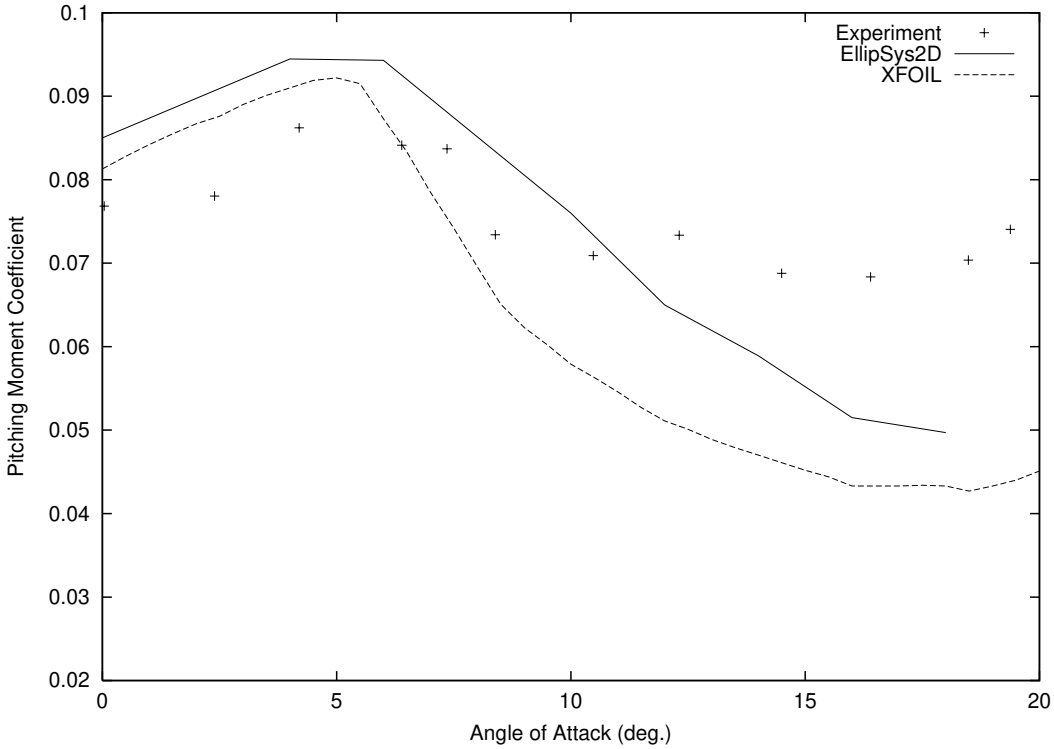

Figure 62. Pitching Moment Coefficient Curve (NACA 65-421, Experiment [1])

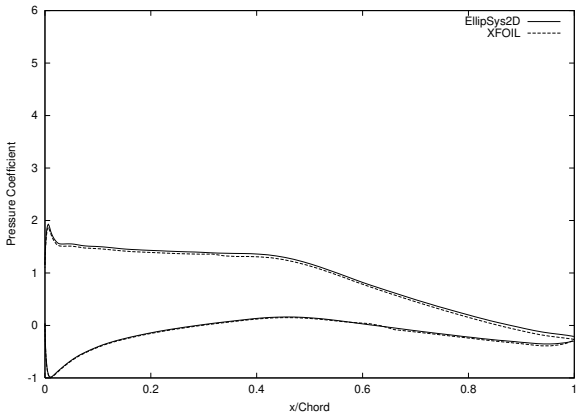

(a) $\alpha = 6^o$

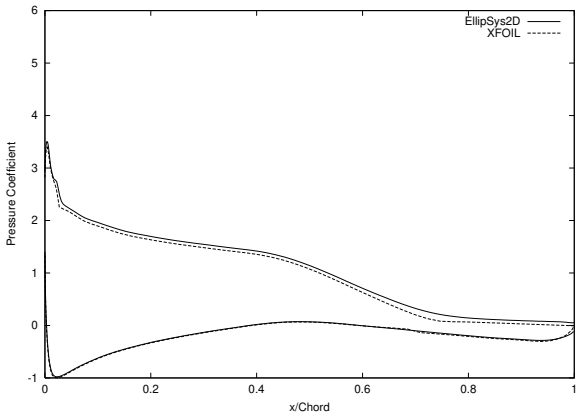

(b) $\alpha = 10^o$

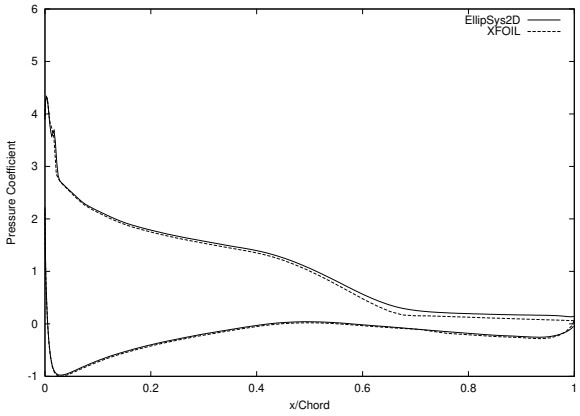

(c) $\alpha = 12^o$

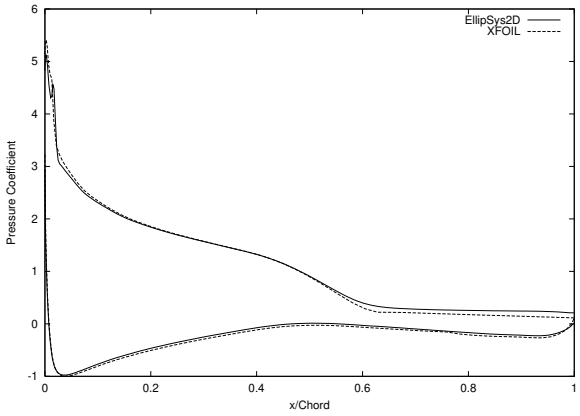

(d) $\alpha = 14^o$

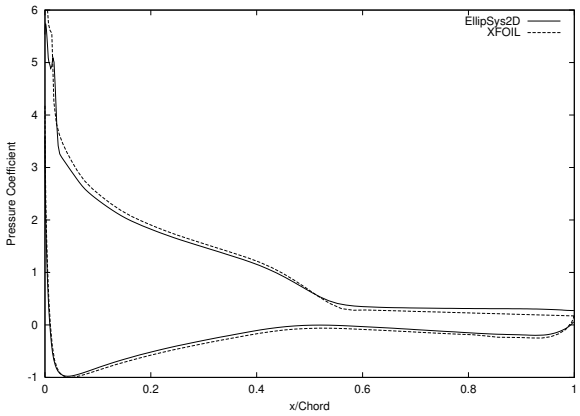

(e) $\alpha = 16^o$

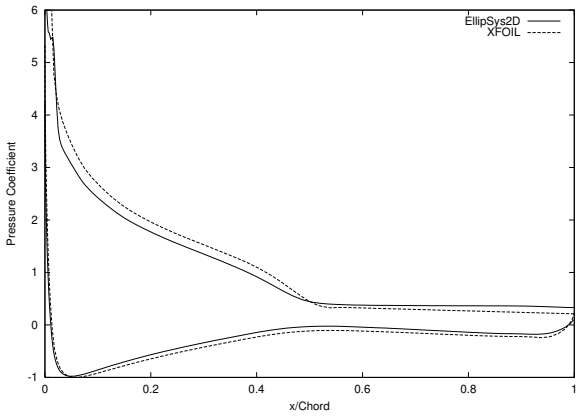

(f) $\alpha = 18^o$

Figure 63. Pressure Coefficient Distributions (NACA 65-421)

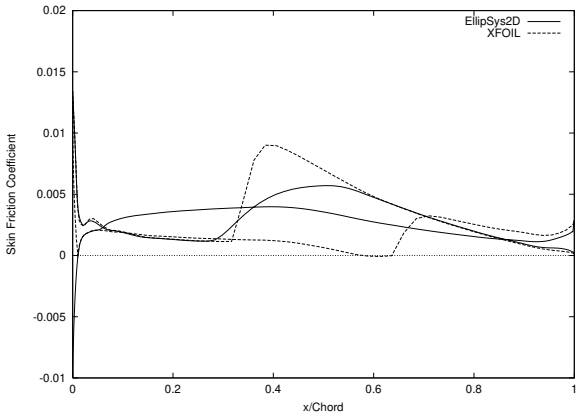

(a) $\alpha = 6^o$

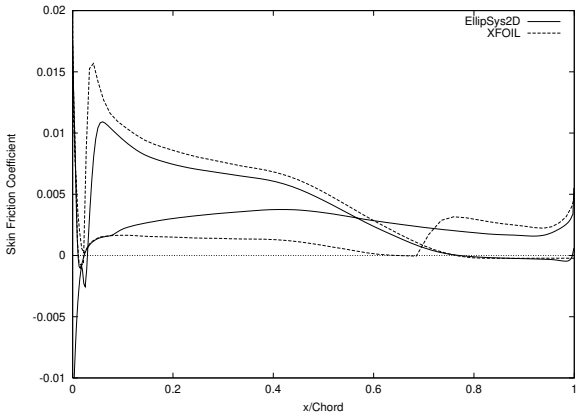

(b) $\alpha = 10^o$

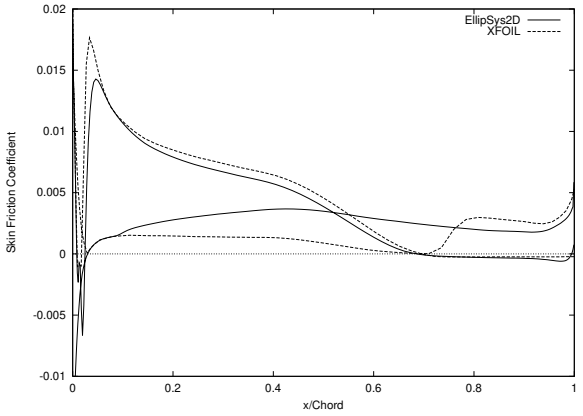

(c) $\alpha = 12^o$

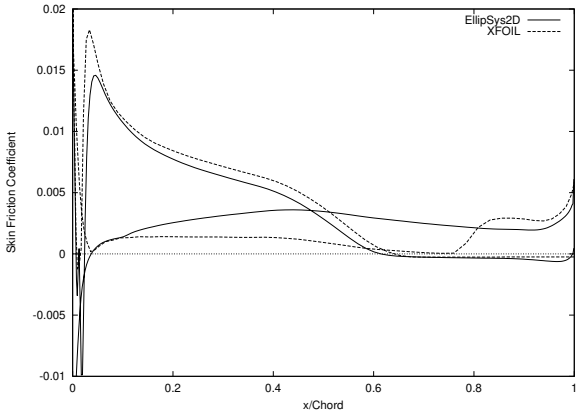

(d) $\alpha = 14^o$

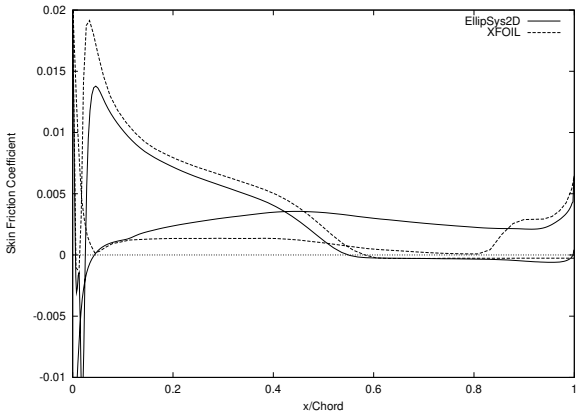

(e) $\alpha = 16^o$

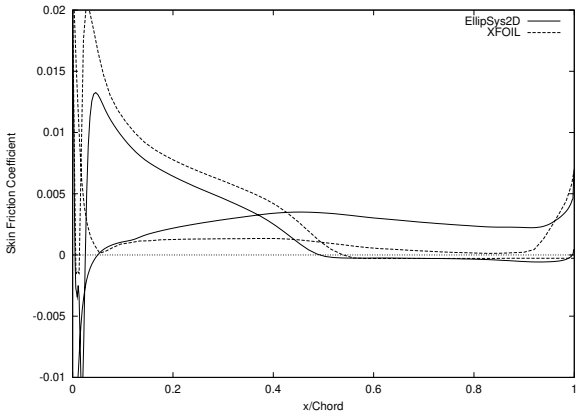

(f) $\alpha = 18^o$

Figure 64. Skin Friction Coefficient Distributions (NACA 65-421)

3 NACA 63-215 and NACA 63-415 Airfoils (VELUX Measurements)

These airfoils belong to the NACA wing section family. They were measured in the VELUX wind tunnel [11], which has an open test section. The testing facility is described in detail by Fuglsang *et al* [11]. The Reynolds number of the experiment (and for the computations) was equal to 1.1×10^6 for the NACA 63-215 airfoil, and 1.6×10^6 for the NACA 63-415. Note that these are the free-stream Reynolds numbers that have been measured in the wind tunnel.

3.1 Method

The C-meshes used for the computations had 384 cells in the direction along the airfoil, 256 of them being on the airfoil, and 64 cells in the direction away from the airfoil. The non-dimensional height of the cell at the airfoil was 1×10^{-5}.

The computations were performed with the SUDS-scheme for the convective terms. The $k - \omega$ SST turbulence model by Menter was used for the turbulent viscosity [16]. As the turbulence level was relatively high in the wind tunnel, it was expected that a fully turbulent computation might give better results. Therefore, both fully turbulent simulations and computations with the Michel transition model [17], together with the empirical function given by Chen and Thyson [8] for modelling the turbulence intermittency, were conducted. Numerical results were obtained with stationary computations.

It must be noted that for the first airfoil, due to large oscillations of the results for high angles of attack in steady state computations with transition model, the simulations for these large angles were performed in an unsteady mode in order to enhance the numerical stability of the method (with a non-dimensional time step equal to 10^{-2}). The influence can clearly be seen on the pressure coefficient on Figs.69(d-e-f) and the skin friction coefficient (Figs.70(d-e-f)). The same problem was encountered for the second airfoil only for the highest angle of attack ($\alpha = 21.3^o$) for which pressure and skin friction coefficients are not presented.

3.2 Results

As for the NACA 63-215 airfoil, the computational results and experimental data were in good agreement, except for after stall. As it can be seen on Figs.66-67-68, the simulations were quite insensitive to the transition modelling in the linear region. It must be noted that the experiment and simulations were in good agreement in this region, when it was not the case with the very same airfoil measured in another wind tunnel (see section 2).

As for the NACA 63-415 airfoil, experiment and simulations were in rather good agreement in the linear region, but computations predicted a higher maximum lift.

NACA 63-215(V)

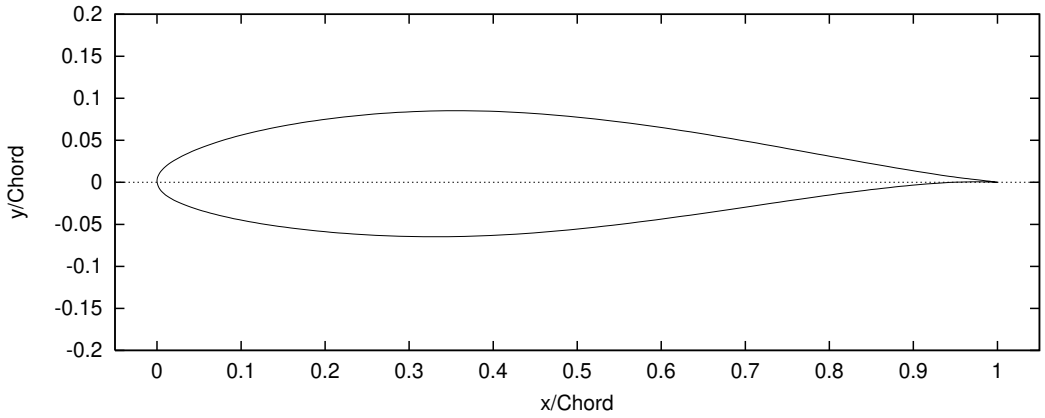

Figure 65. NACA 63-215 Airfoil

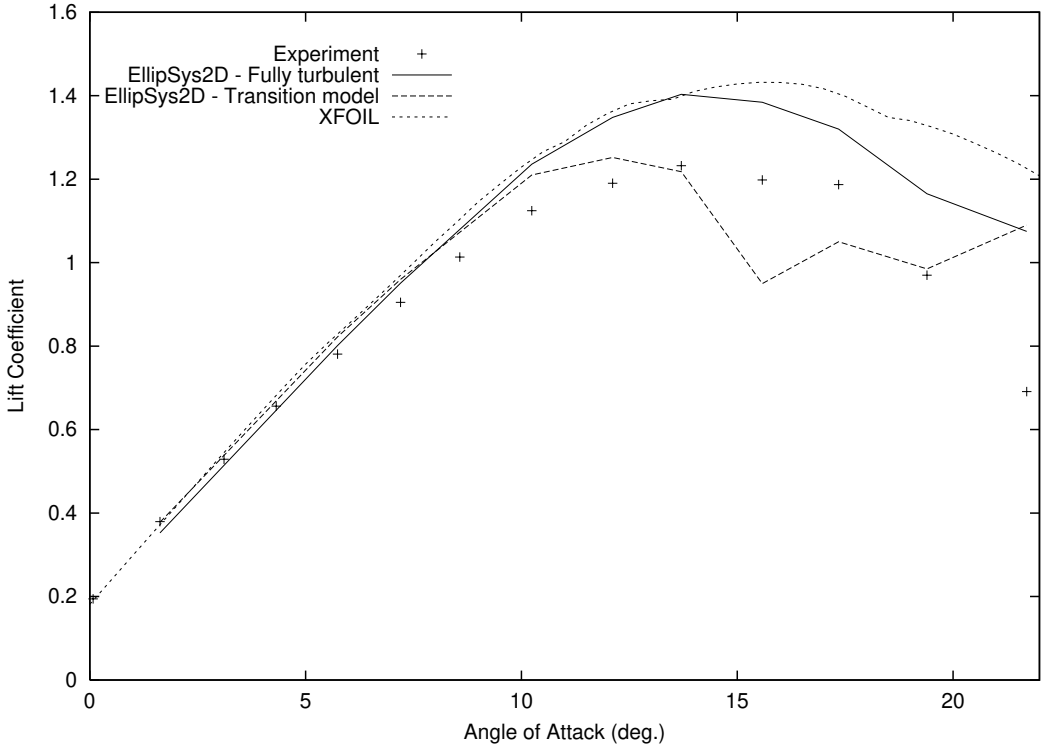

Figure 66. Lift Coefficient Curve (NACA 63-215(V), Experiment [11])

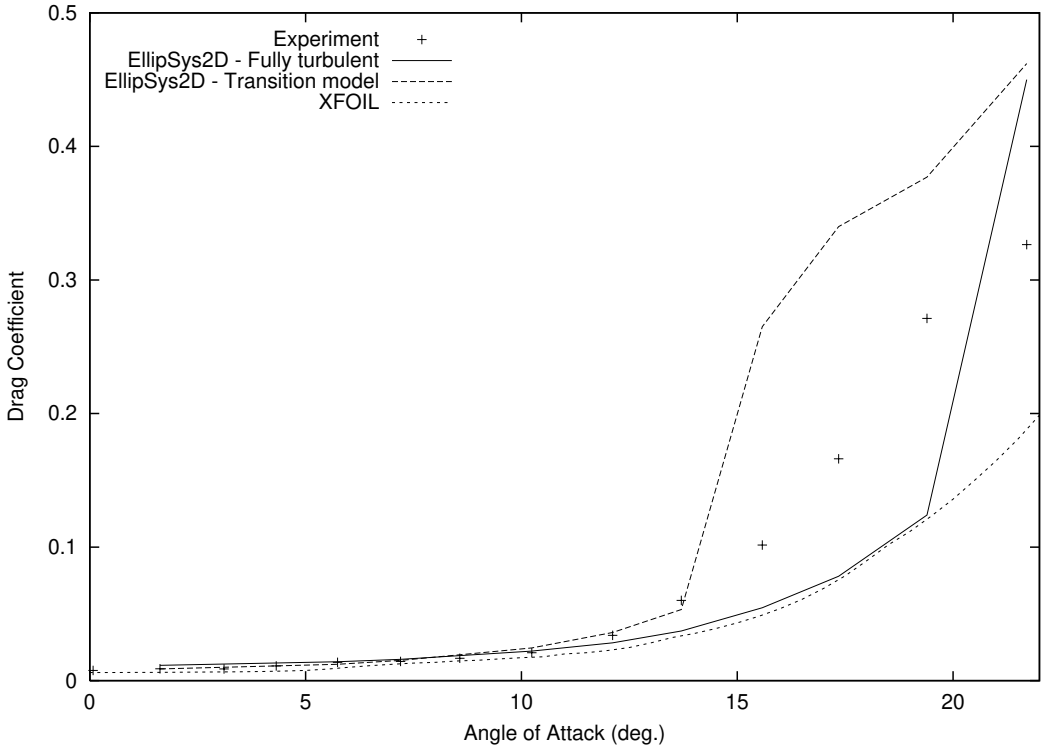

Figure 67. Drag Coefficient Curve (NACA 63-215(V), Experiment [11])

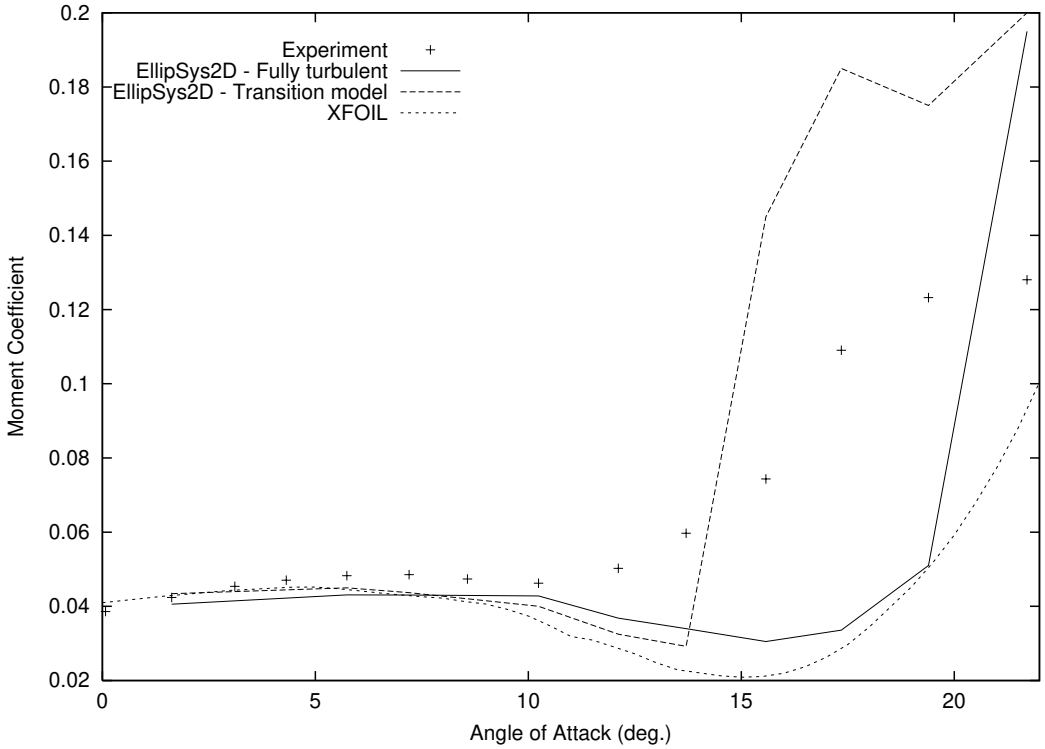

Figure 68. Pitching Moment Coefficient Curve (NACA 63-215(V), Experiment [11])

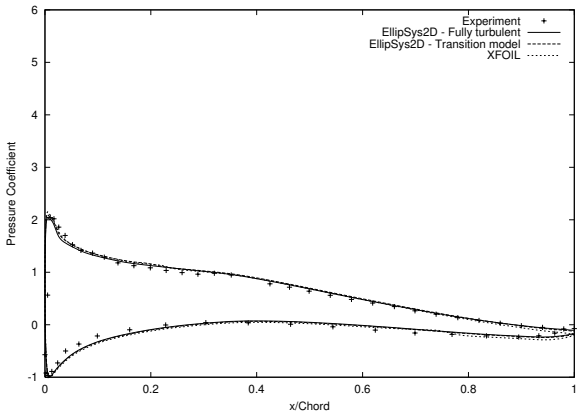

(a) $\alpha = 5.741^o$

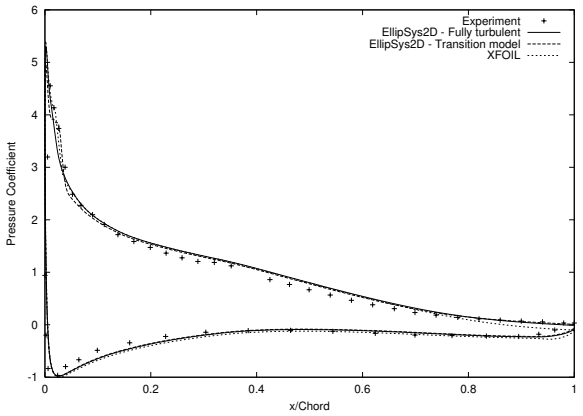

(b) $\alpha = 10.238^o$

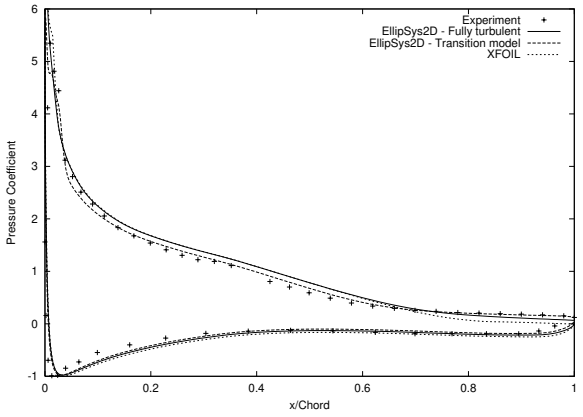

(c) $\alpha = 12.112^o$

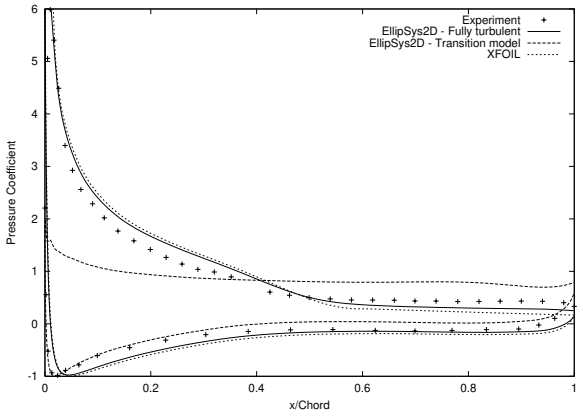

(d) $\alpha = 15.578^o$

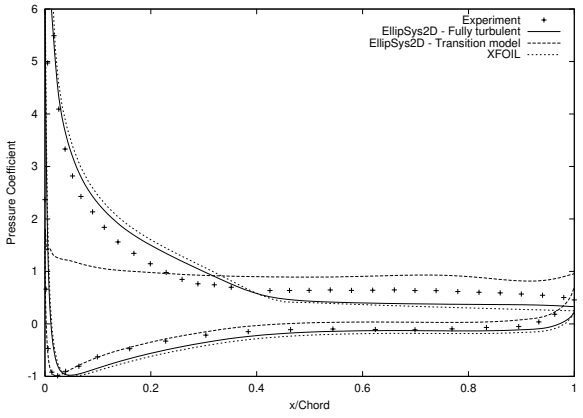

(e) $\alpha = 17.347^o$

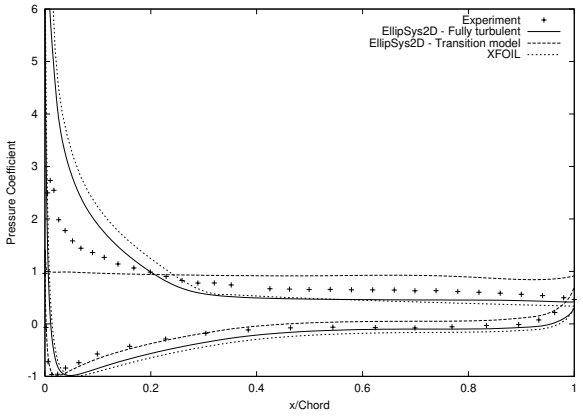

(f) $\alpha = 19.393^o$

Figure 69. Pressure Coefficient Distributions (NACA 63-215(V), Experiment [11])

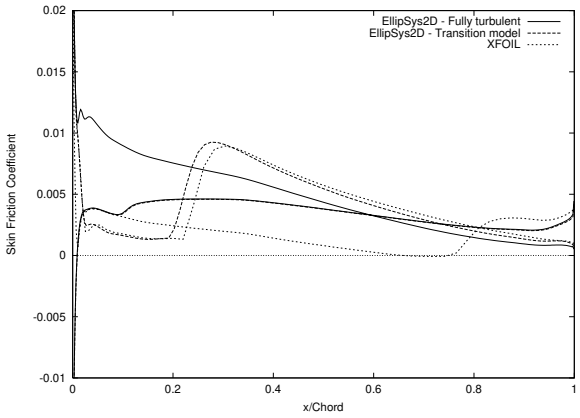

(a) $\alpha = 5.741^o$

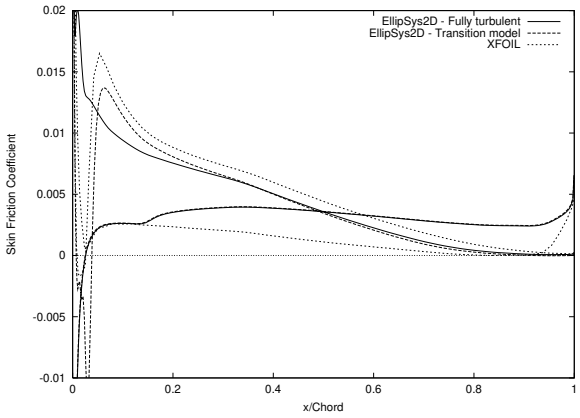

(b) $\alpha = 10.238^o$

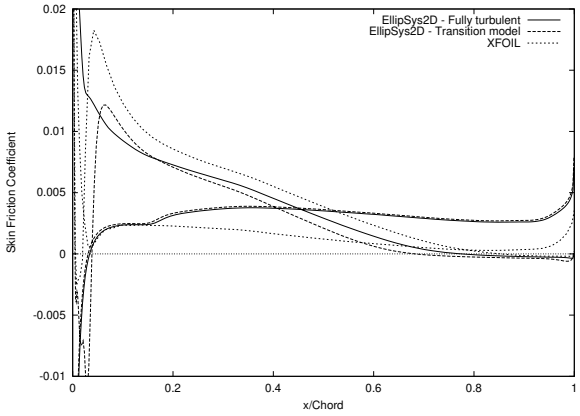

(c) $\alpha = 12.112^o$

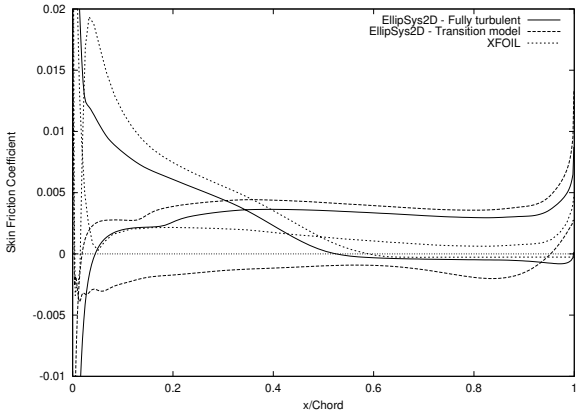

(d) $\alpha = 15.578^o$

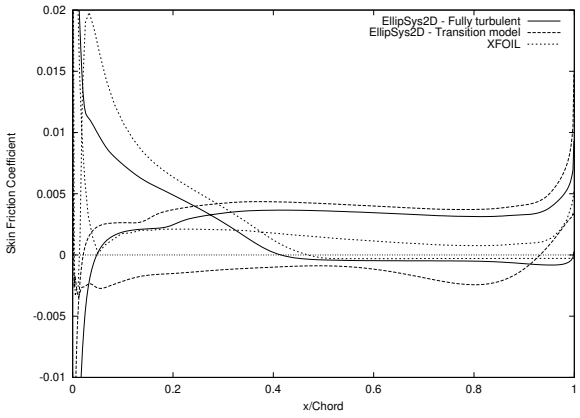

(e) $\alpha = 17.347^o$

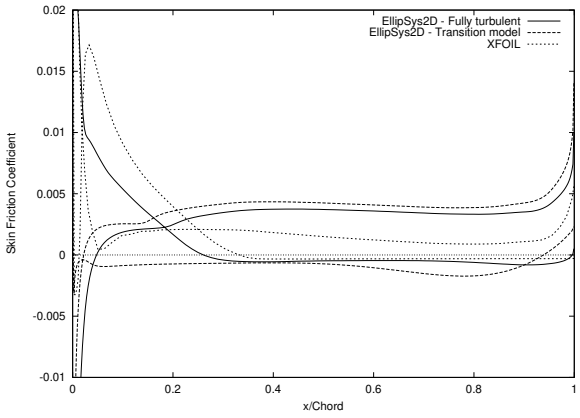

(f) $\alpha = 19.393^o$

Figure 70. Skin Friction Coefficient Distributions (NACA 63-215(V))

NACA 63-415(V)

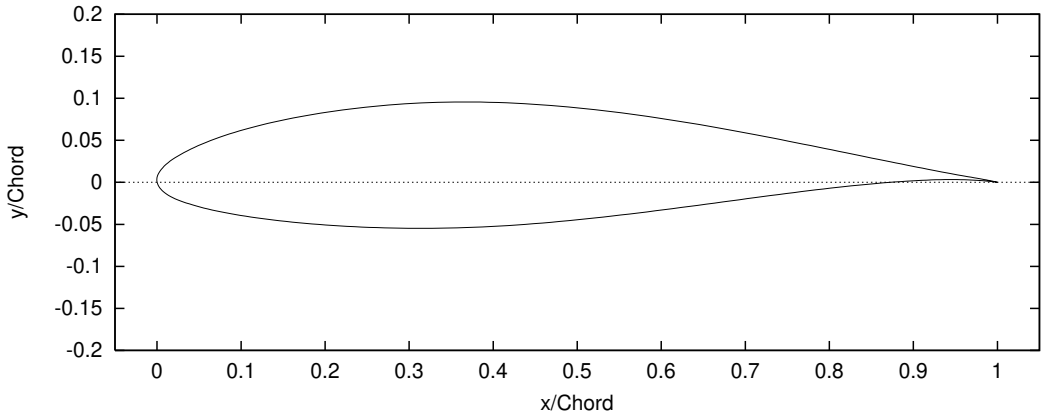

Figure 71. NACA 63-415 Airfoil

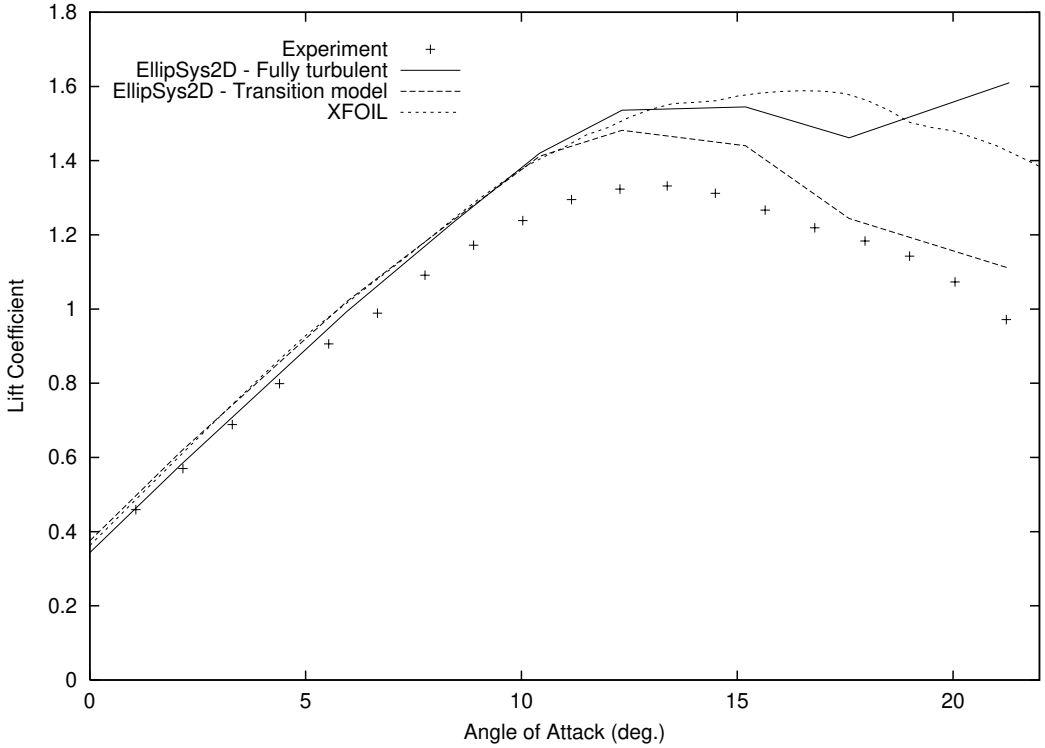

Figure 72. Lift Coefficient Curve (NACA 63-415(V), Experiment [11])

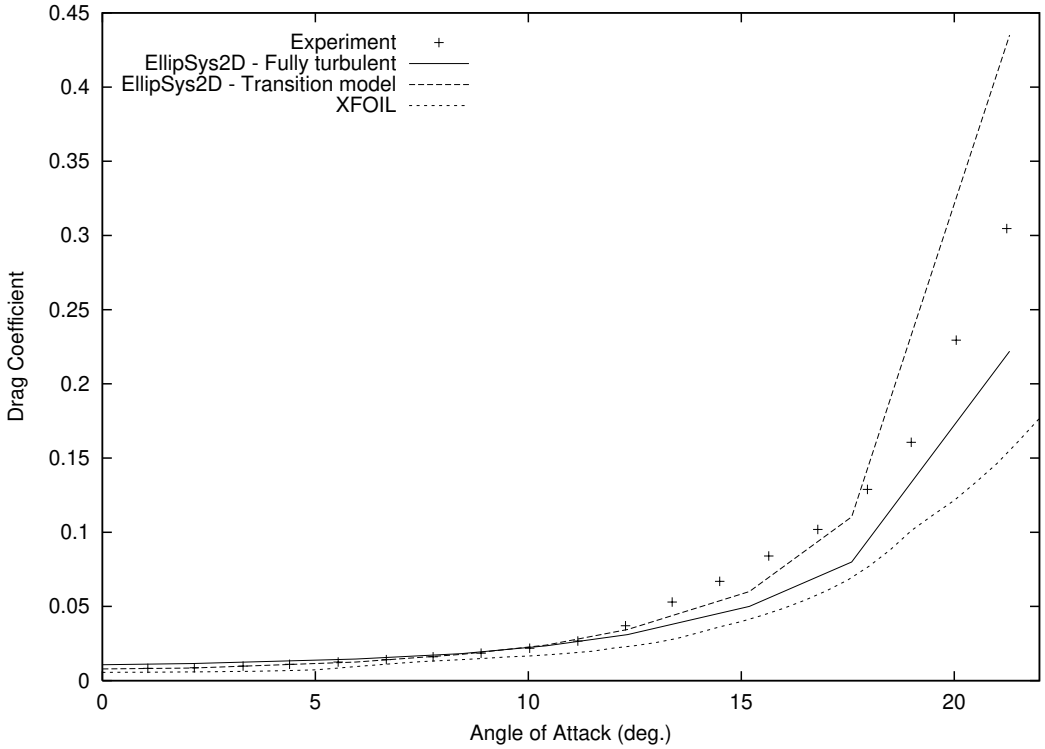

Figure 73. Drag Coefficient Curve (NACA 63-415(V), Experiment [11])

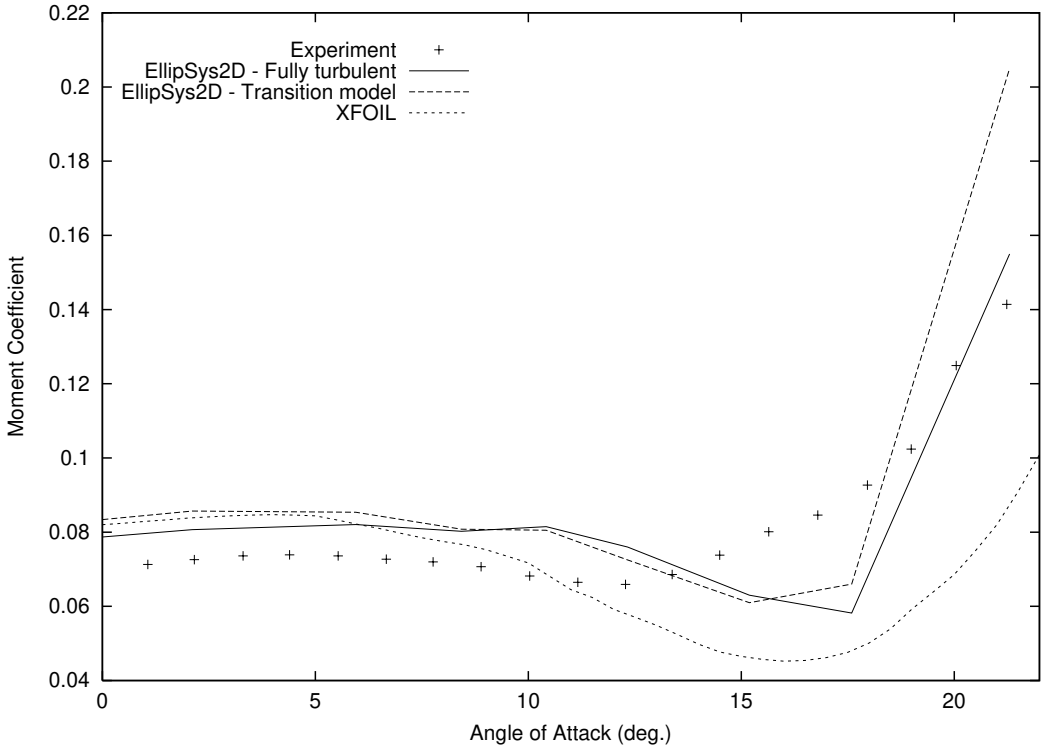

Figure 74. Pitching Moment Coefficient Curve (NACA 63-415(V), Experiment [11])

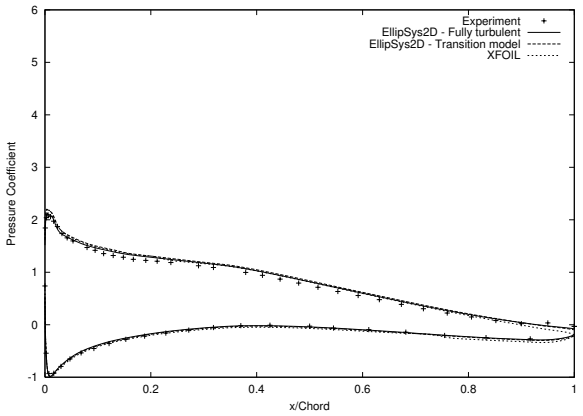

(a) $\alpha = 5.95^o$

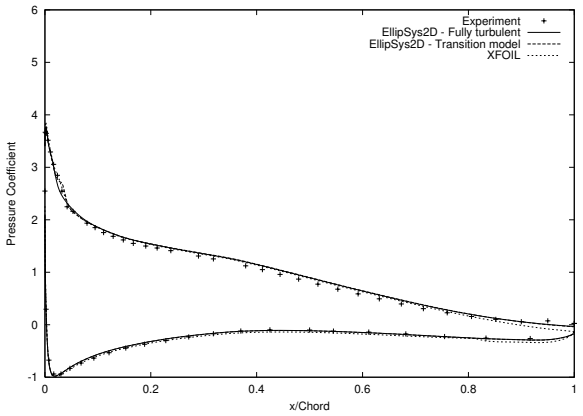

(b) $\alpha = 08.43^o$

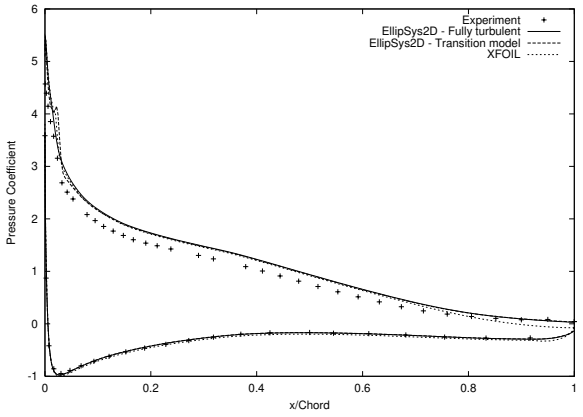

(c) $\alpha = 10.42^o$

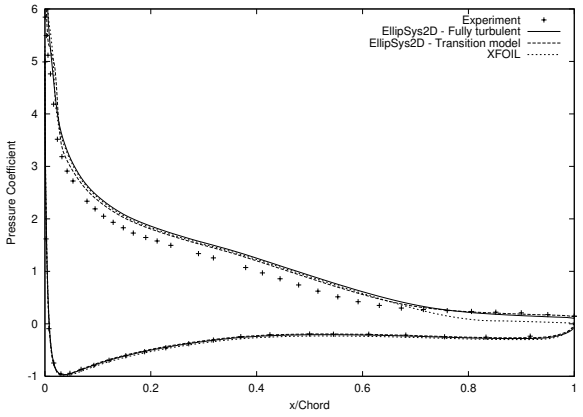

(d) $\alpha = 12.33^o$

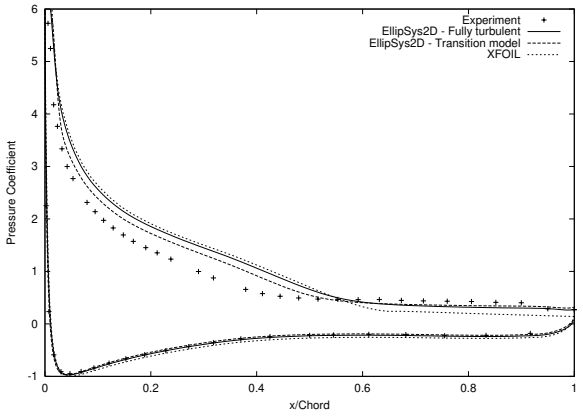

(e) $\alpha = 15.19^o$

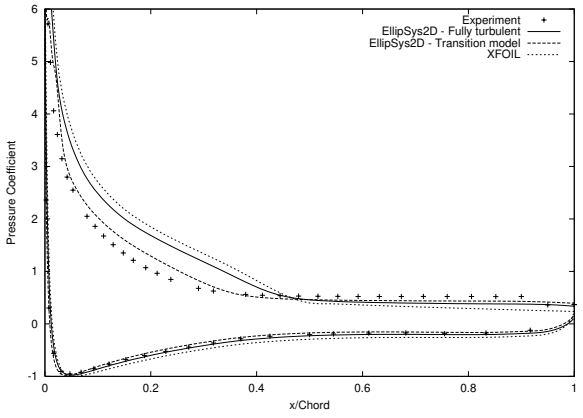

(f) $\alpha = 17.59^o$

Figure 75. Pressure Coefficient Distributions (NACA 63-415(V), Experiment [11])

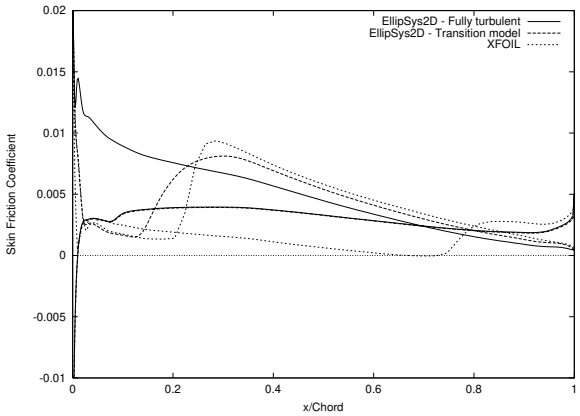

(a) $\alpha = 5.95^o$

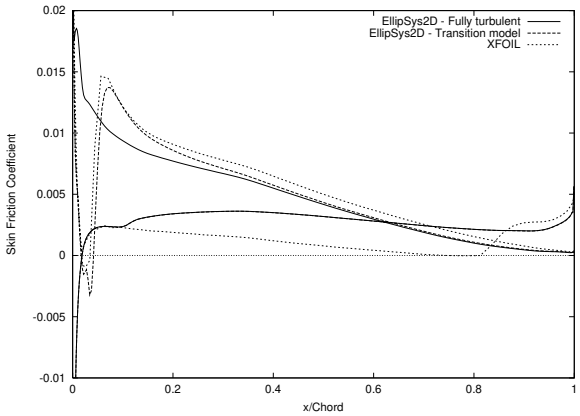

(b) $\alpha = 8.43^o$

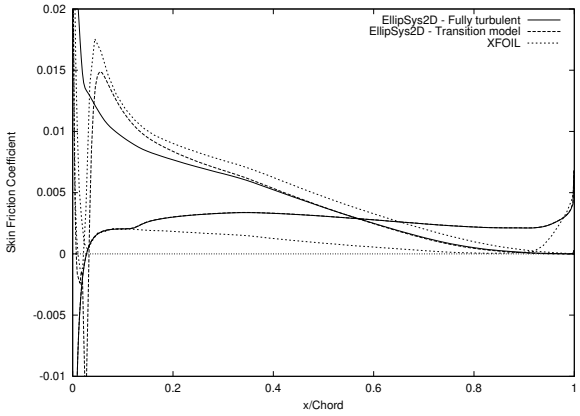

(c) $\alpha = 10.42^o$

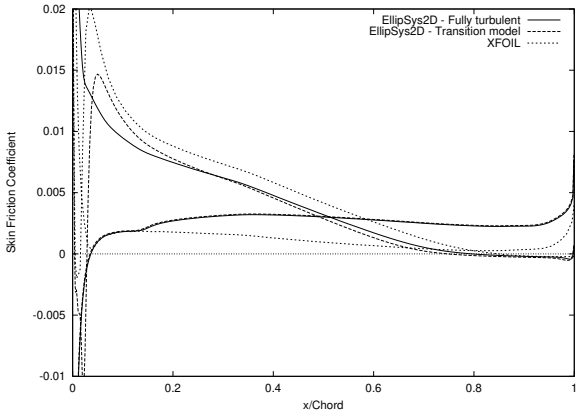

(d) $\alpha = 12.33^o$

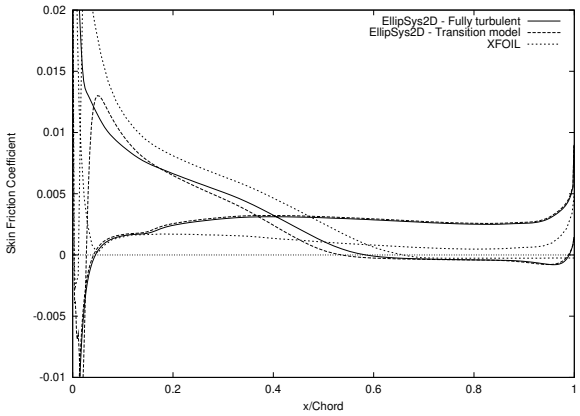

(e) $\alpha = 15.19^o$

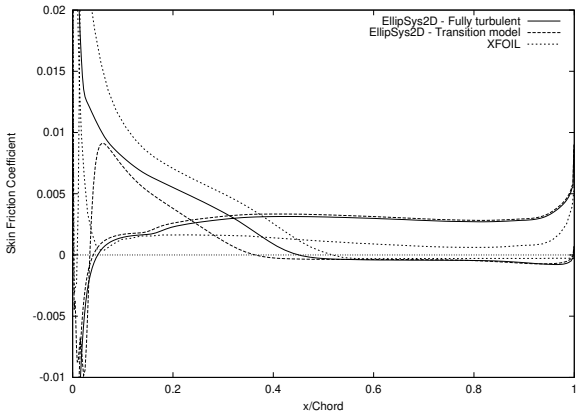

(f) $\alpha = 17.59^o$

Figure 76. Skin Friction Coefficient Distributions (NACA 63-415(V))

4 NACA 63-430 Airfoil (VELUX Measurements)

This airfoil belongs to the NACA wing section family. It has been measured in the VELUX wind tunnel [10], which has an open test section. The testing facility is described in detail by Fuglsang *et al* [11]. The Reynolds number of the experiment (and for the computations) was equal to 1.5×10^6.

4.1 Method

The C-mesh used for the computation had 384 cells in the direction along the airfoil, 256 of them being on the airfoil, and 64 cells in the direction away from the airfoil. The non-dimensional height of the cell at the airfoil was 1×10^{-5}.

The computations were performed with the SUDS-scheme for the convective terms. The $k - \omega$ SST turbulence model by Menter was used for the turbulent viscosity [16]. As the turbulence level was relatively high in the wind tunnel, it was expected that a fully turbulent computation might give better results. Therefore, both fully turbulent simulations and computations with the Michel transition model [17], together with the empirical function given by Chen and Thyson [8] for modelling the turbulence intermittency, were conducted. Numerical results were obtained with stationary computations.

4.2 Results

Neither the fully turbulent computations, nor the simulations with transition model, were able to correctly estimate the experimental data. Moreover, the discrepancies are quite large.

NACA 63-430(V)

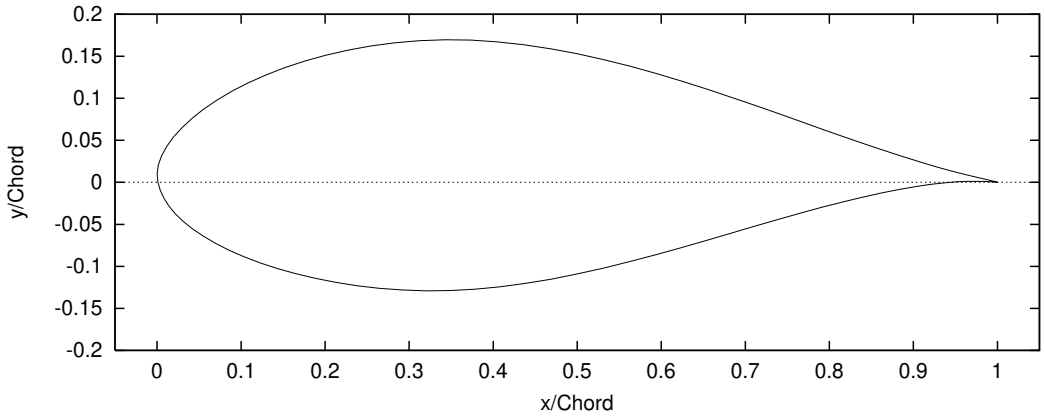

Figure 77. NACA 63-430 Airfoil

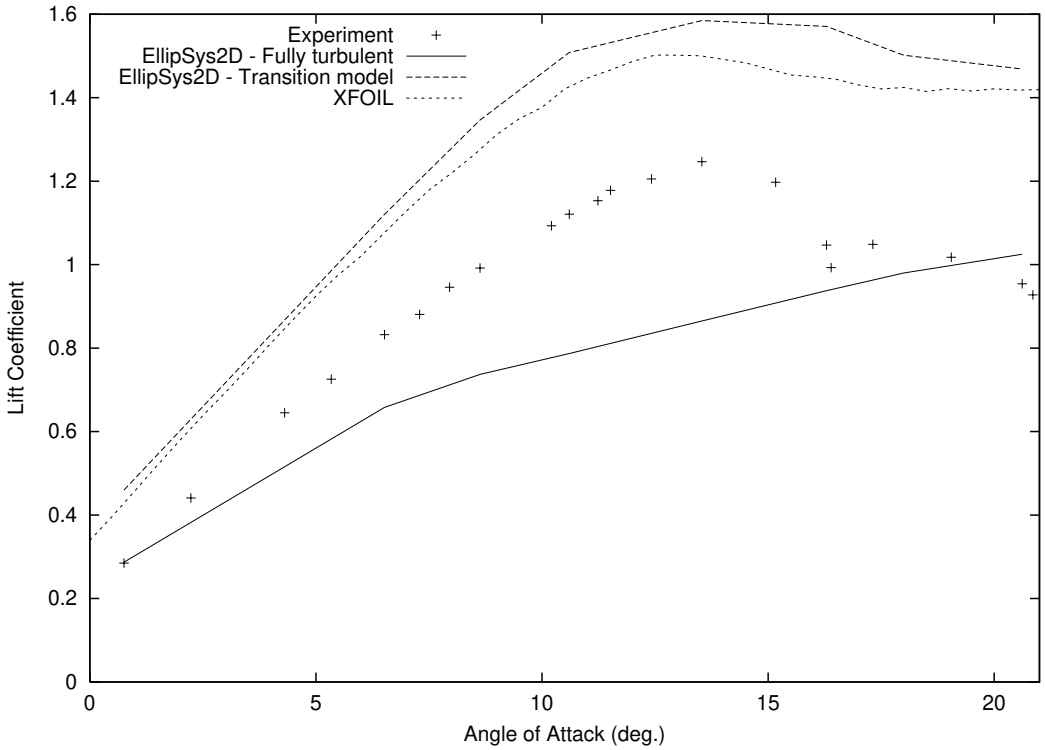

Figure 78. Lift Coefficient Curve (NACA 63-430(V), Experiment [10])

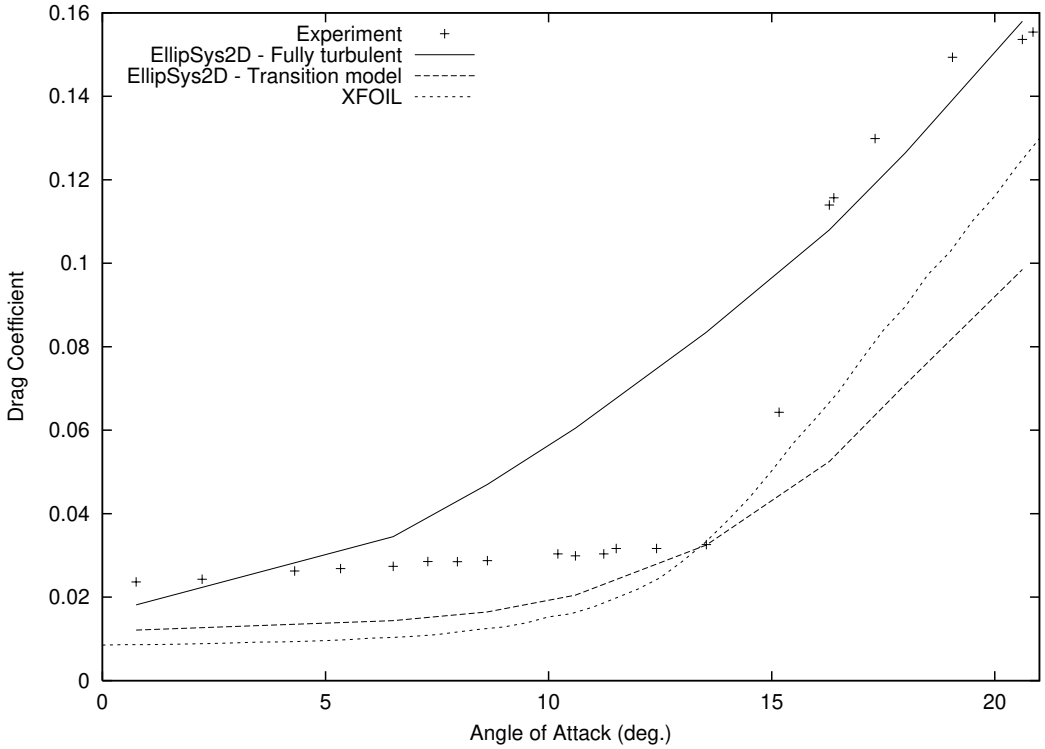

Figure 79. Drag Coefficient Curve (NACA 63-430(V), Experiment [10])

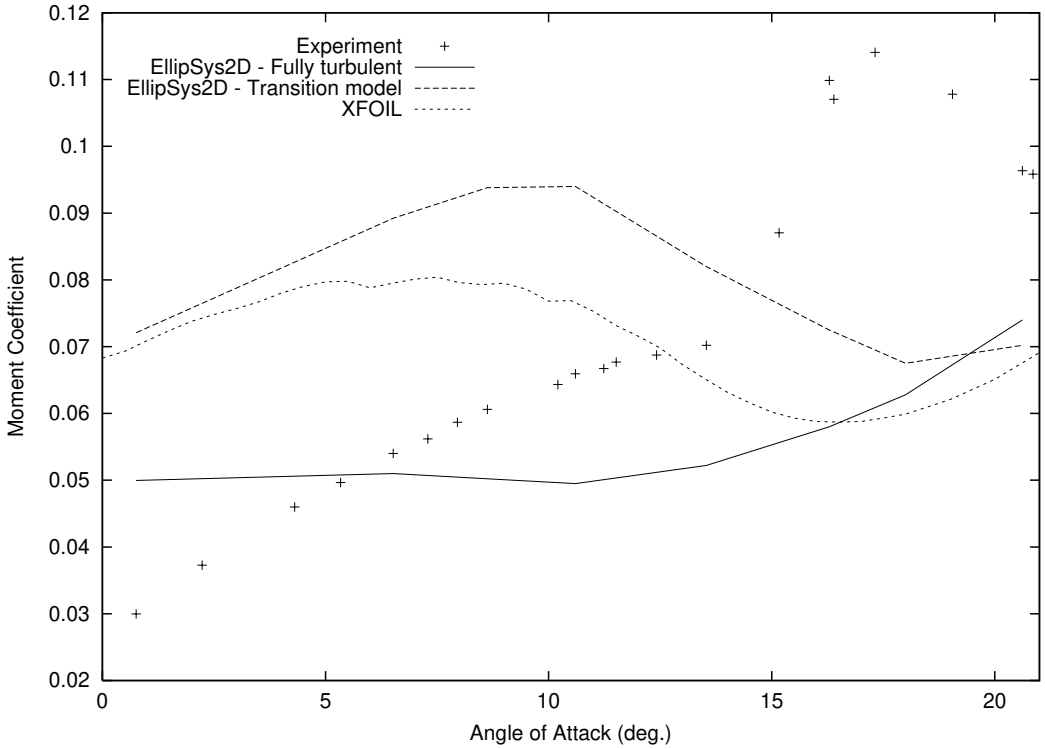

Figure 80. Pitching Moment Coefficient Curve (NACA 63-430(V), Experiment [10])

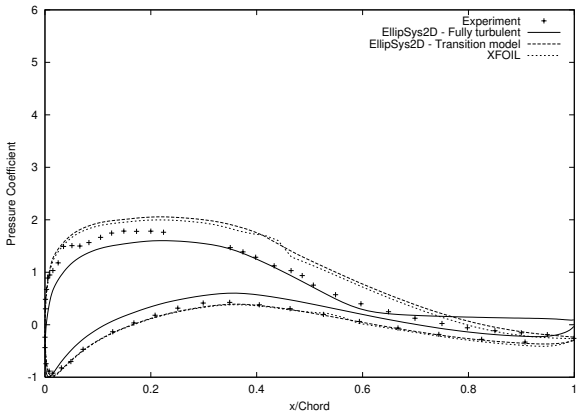

(a) $\alpha = 6.518^o$

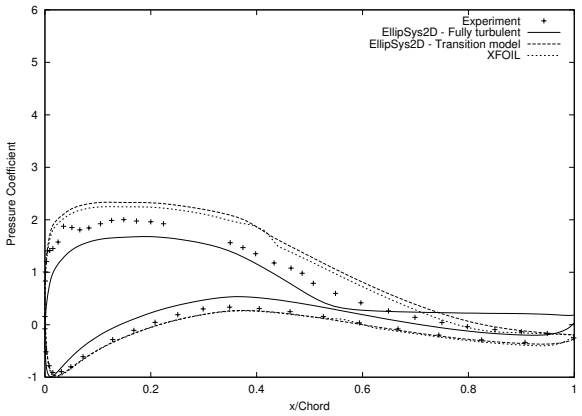

(b) $\alpha = 8.628^o$

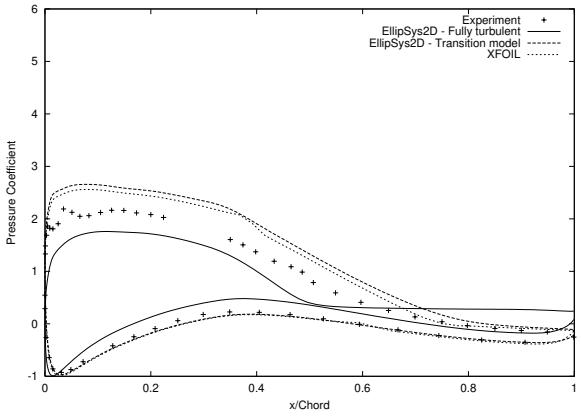

(c) $\alpha = 10.602^o$

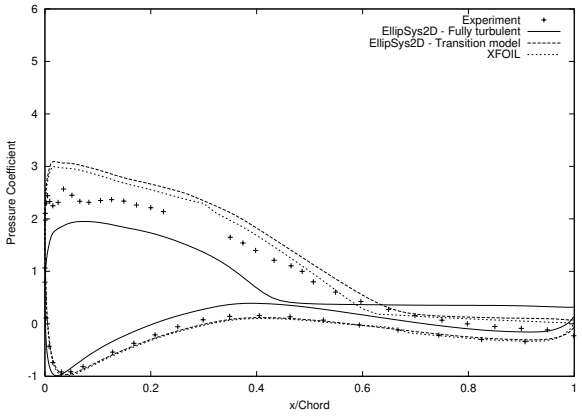

(d) $\alpha = 13.535^o$

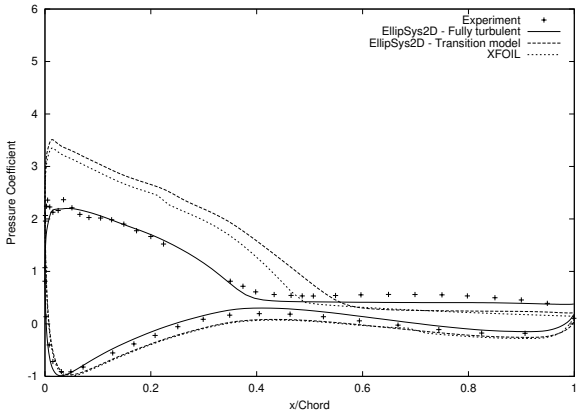

(e) $\alpha = 16.29^o$

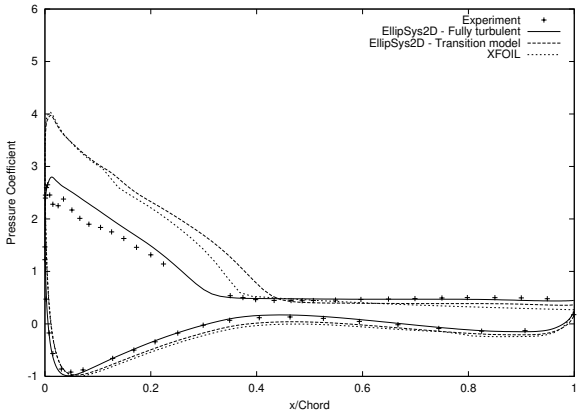

(f) $\alpha = 20.617^o$

Figure 81. Pressure Coefficient Distributions (NACA 63-430(V), Experiment [10])

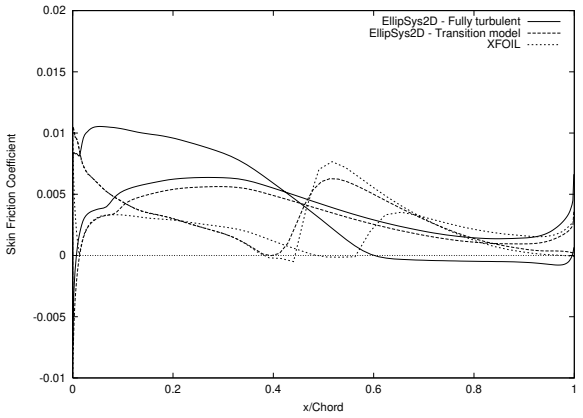

(a) $\alpha = 6.518^o$

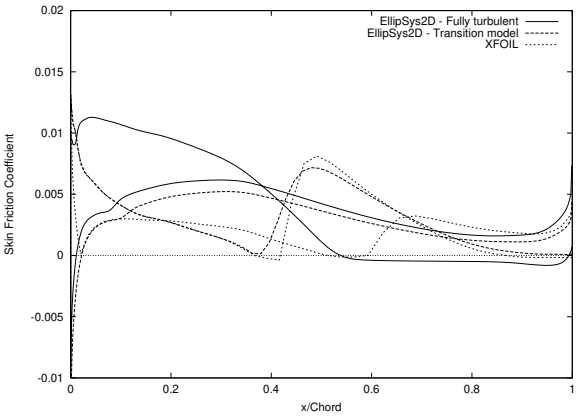

(b) $\alpha = 8.628^o$

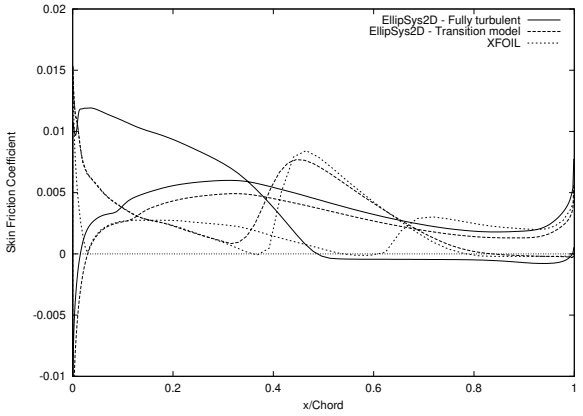

(c) $\alpha = 10.602^o$

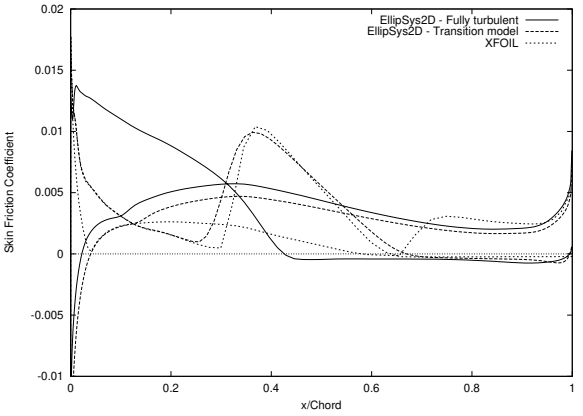

(d) $\alpha = 13.535^o$

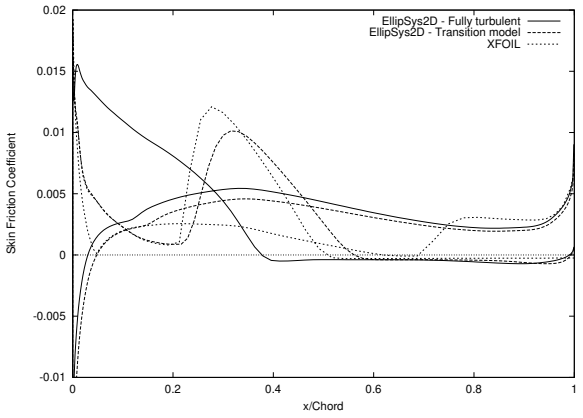

(e) $\alpha = 16.29^o$

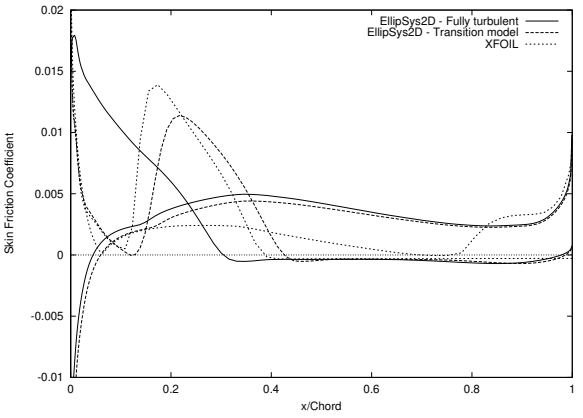

(f) $\alpha = 20.617^o$

Figure 82. Skin Friction Coefficient Distributions (NACA 63-430(V))

5 RISØ-A1 Family Airfoils

In this section, three airfoils of the RISØ-A1 family were tested. These airfoils were developed and optimized at Risø National Laboratory for use on wind turbines [12]. The airfoils were tested in the VELUX wind tunnel, which has an open test section with a background turbulence level of 1%. It is described in detail by Fuglsang *et al* [11]. All tests were carried out at the highest possible Reynolds number $Re = 1.6 \times 10^6$ (see [13] for more details about the measurements).

The following three airfoils were studied:

- RISØ-A1-18
- RISØ-A1-21
- RISØ-A1-24

5.1 Method

Although these airfoils have a blunt trailing edge, C-meshes were used for all the computations. Therefore, the airfoils were slightly sharpened at the trailing edge. The meshes had 384 cells in the direction along the airfoil, 256 of them being on the airfoil, and 64 cells in the direction away from the airfoil. The non-dimensional height of the cell at the airfoil was 1×10^{-5}.

The SUDS-scheme was used for the convective terms in all computations. Turbulence was simulated by the $k - \omega$ SST model by Menter [16]. Both fully turbulent computations and computations with the transition model by Michel [17], together with the empirical function given by Chen and Thyson [8] for modelling the turbulence intermittency, were performed. The reason for this was that the fully turbulent computations were expected to give rather good results as the background turbulence level in the wind tunnel was relatively high. This might trigger an early transition to turbulence in the airfoil boundary layer. Numerical results were obtained with stationary computations.

5.2 Results

The computational results showed relative good agreement with the experiments for the three airfoils. In the linear region, the simulations with transition model were closer to the experimental data, whereas the fully turbulent computations were closer in the stalled region. Simulations with transition model predicted stall at a higher angle of attack than the experiment and overestimated the maximum lift.

RISØ-A1-18

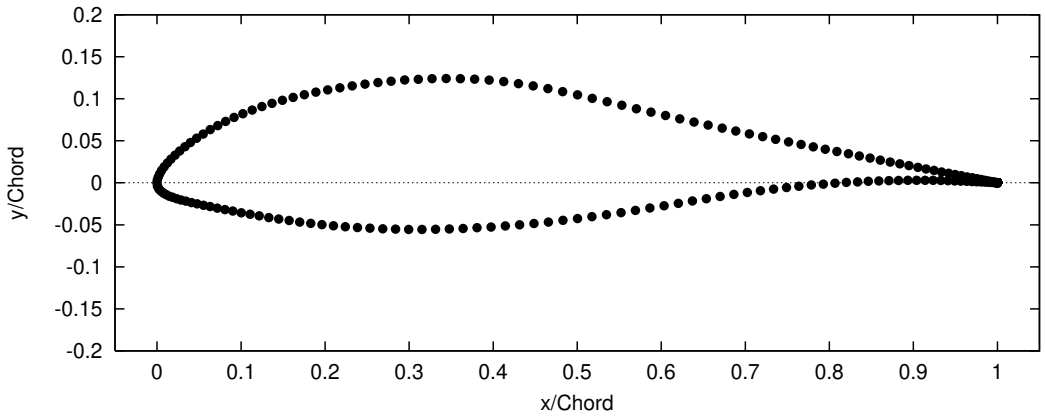

Figure 83. RISØ-A1-18 Airfoil

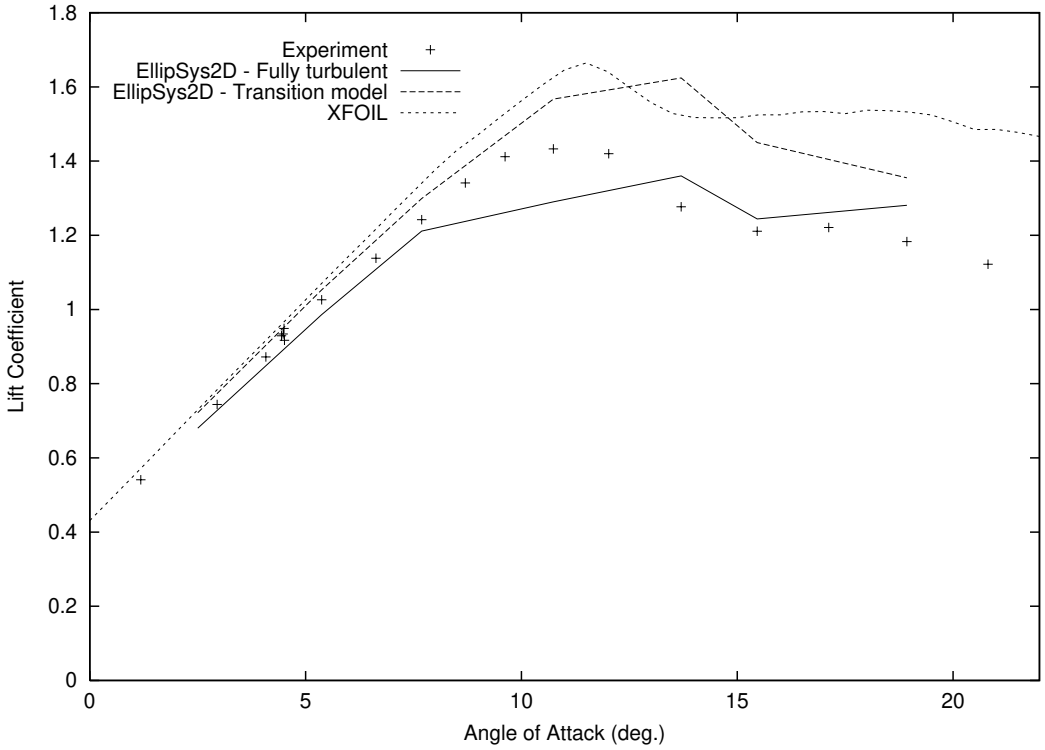

Figure 84. Lift Coefficient Curve (RISØ-A1-18, Experiment [13])

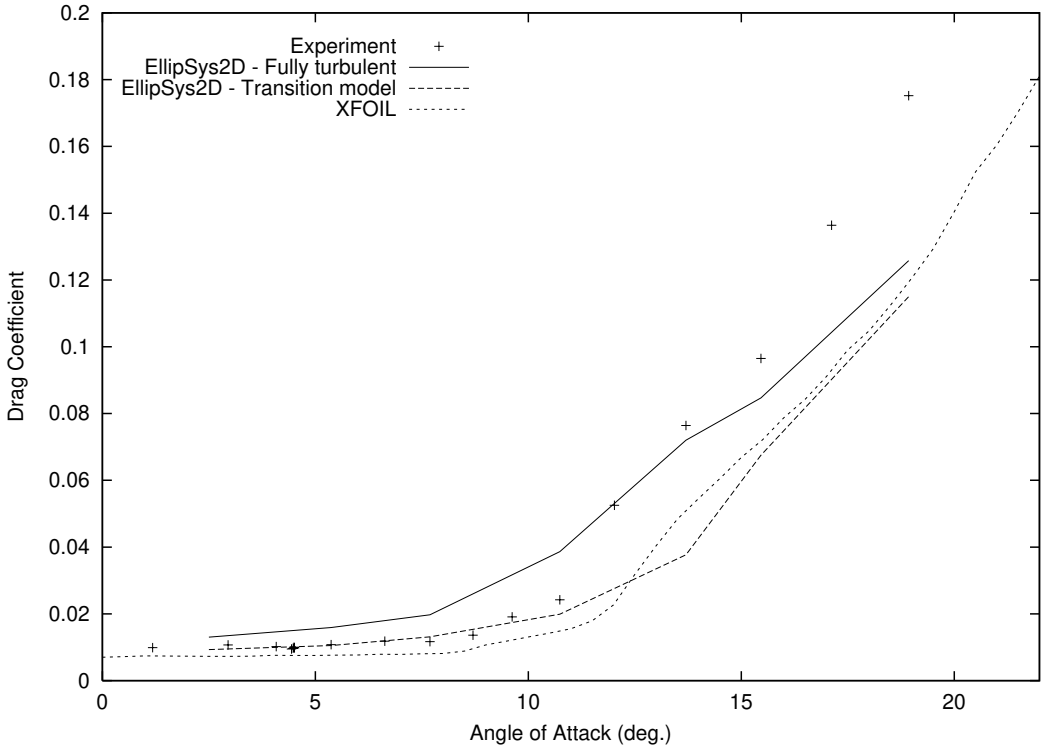

Figure 85. Drag Coefficient Curve (RISØ-A1-18, Experiment [13])

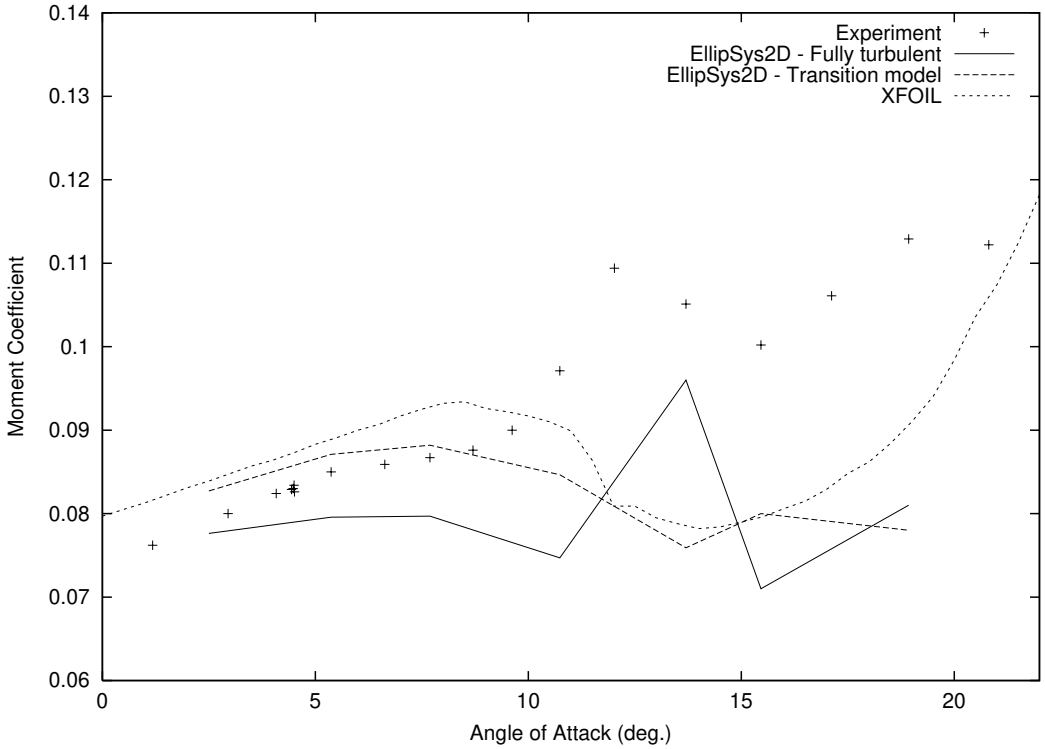

Figure 86. Pitching Moment Coefficient Curve (RISØ-A1-18, Experiment [13])

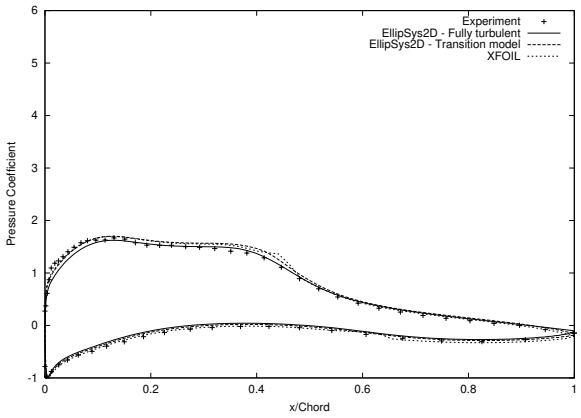

(a) $\alpha = 5.37^o$

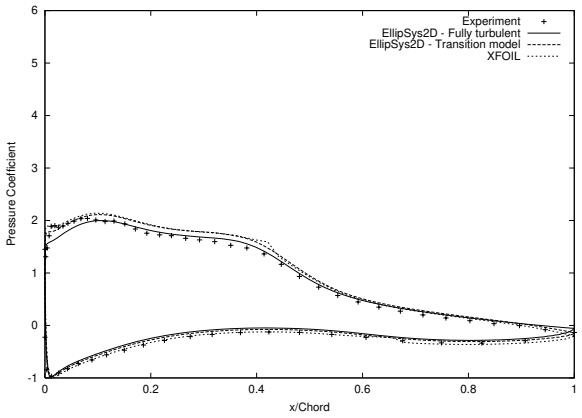

(b) $\alpha = 7.69^o$

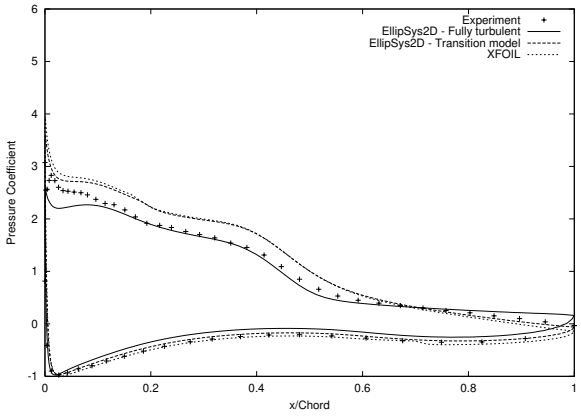

(c) $\alpha = 10.74^o$

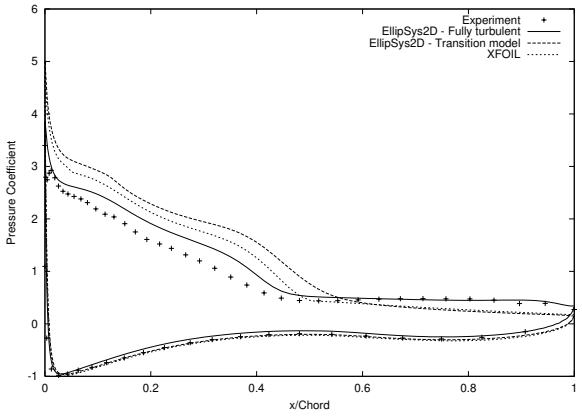

(d) $\alpha = 13.70^o$

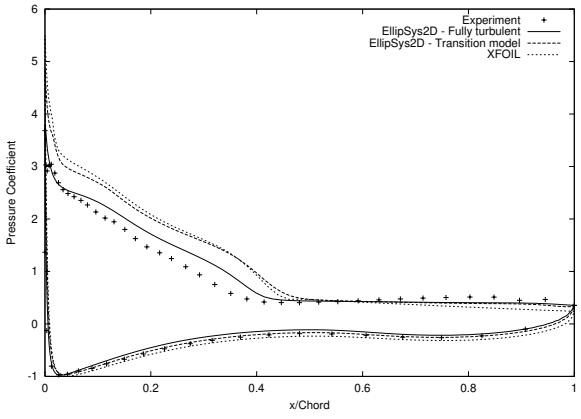

(e) $\alpha = 15.46^o$

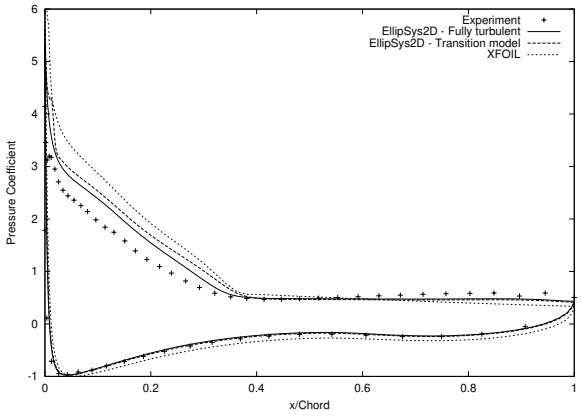

(f) $\alpha = 18.93^o$

Figure 87. Pressure Coefficient Distributions (RISØ-A1-18, Experiment [13])

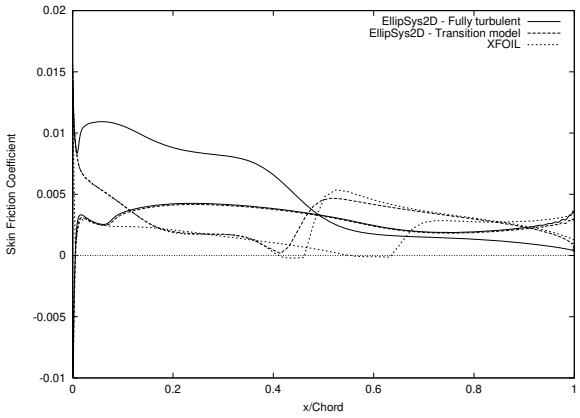

(a) $\alpha = 5.37^o$

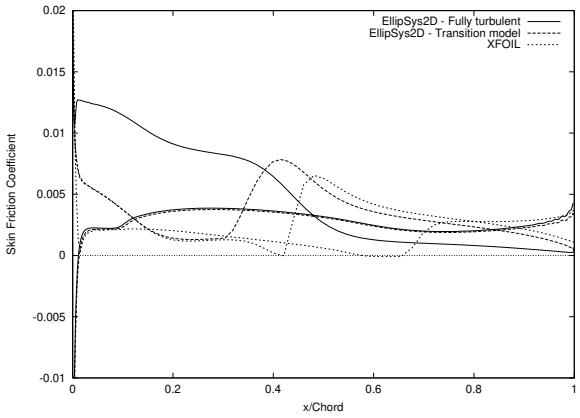

(b) $\alpha = 7.69^o$

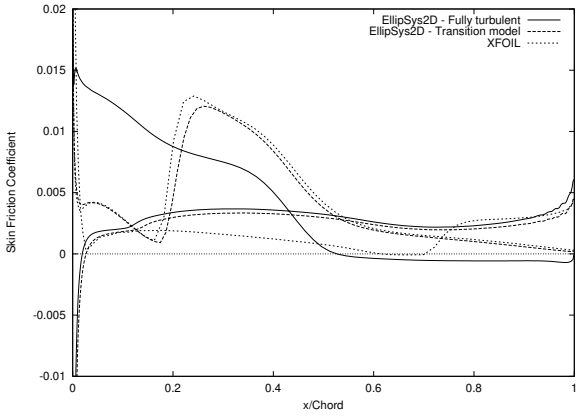

(c) $\alpha = 10.74^o$

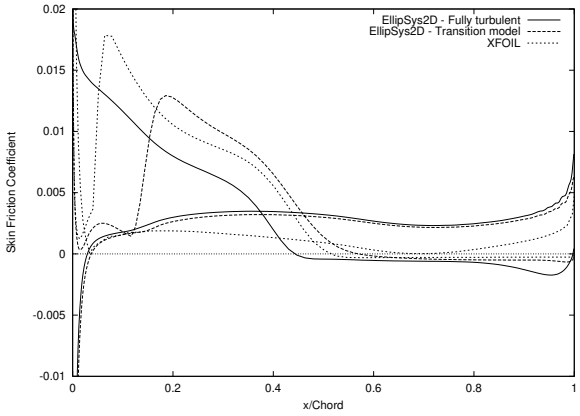

(d) $\alpha = 13.70^o$

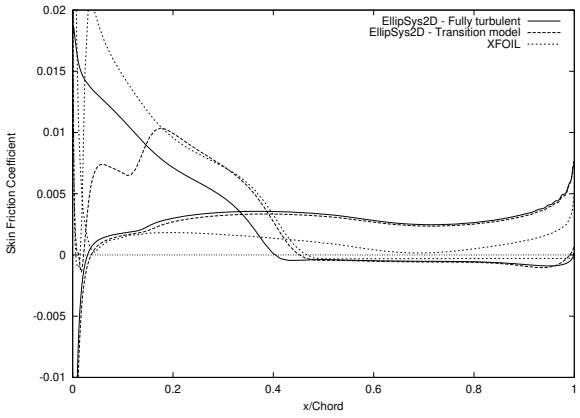

(e) $\alpha = 15.46^o$

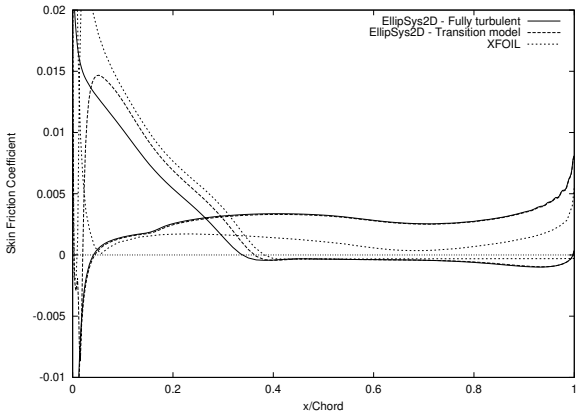

(f) $\alpha = 18.93^o$

Figure 88. Skin Friction Coefficient Distributions (RISØ-A1-18)

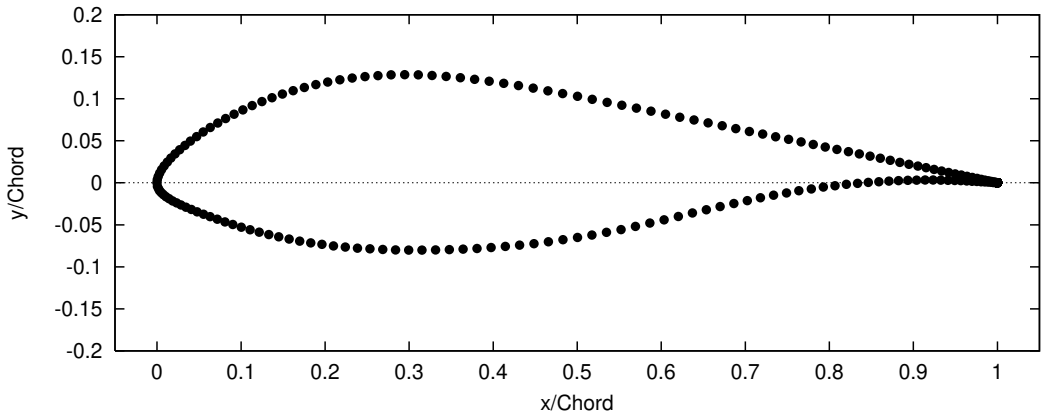

Figure 89. RISØ-A1-21 Airfoil

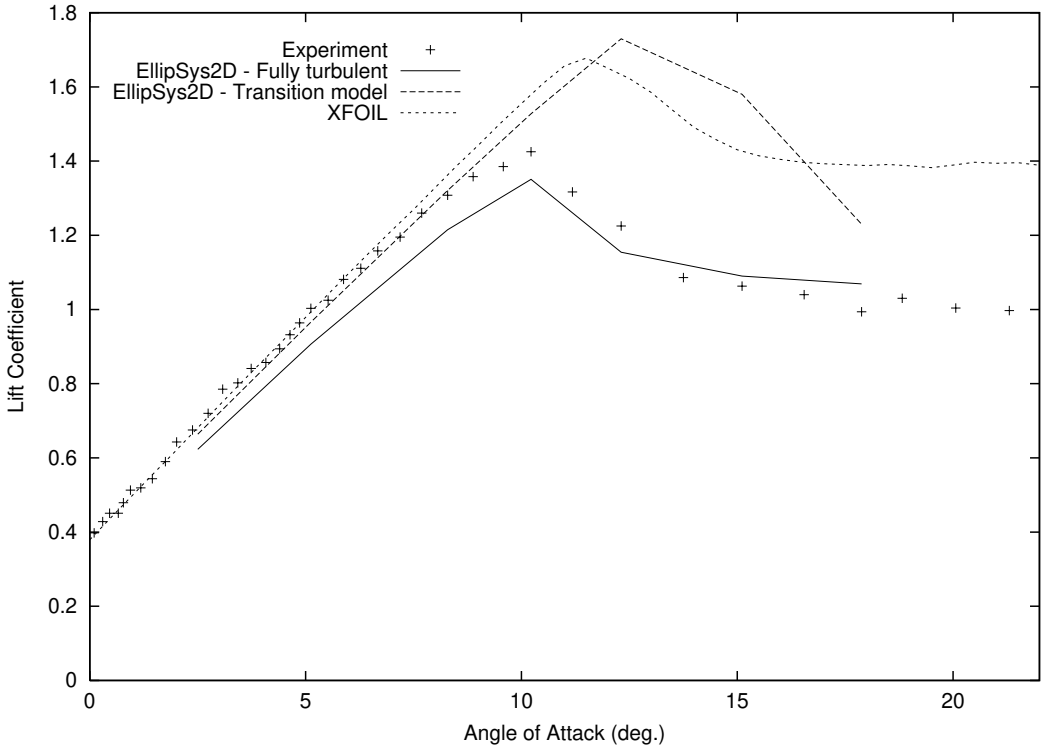

Figure 90. Lift Coefficient Curve (RISØ-A1-21, Experiment [13])

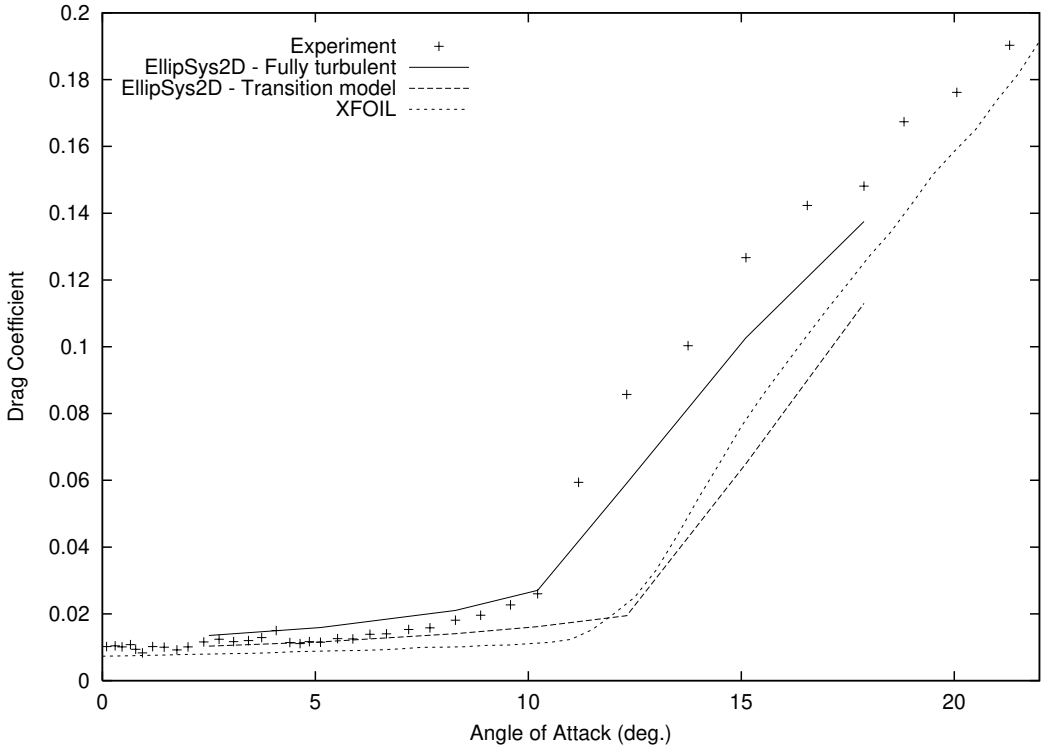

Figure 91. Drag Coefficient Curve (RISØ-A1-21, Experiment [13])

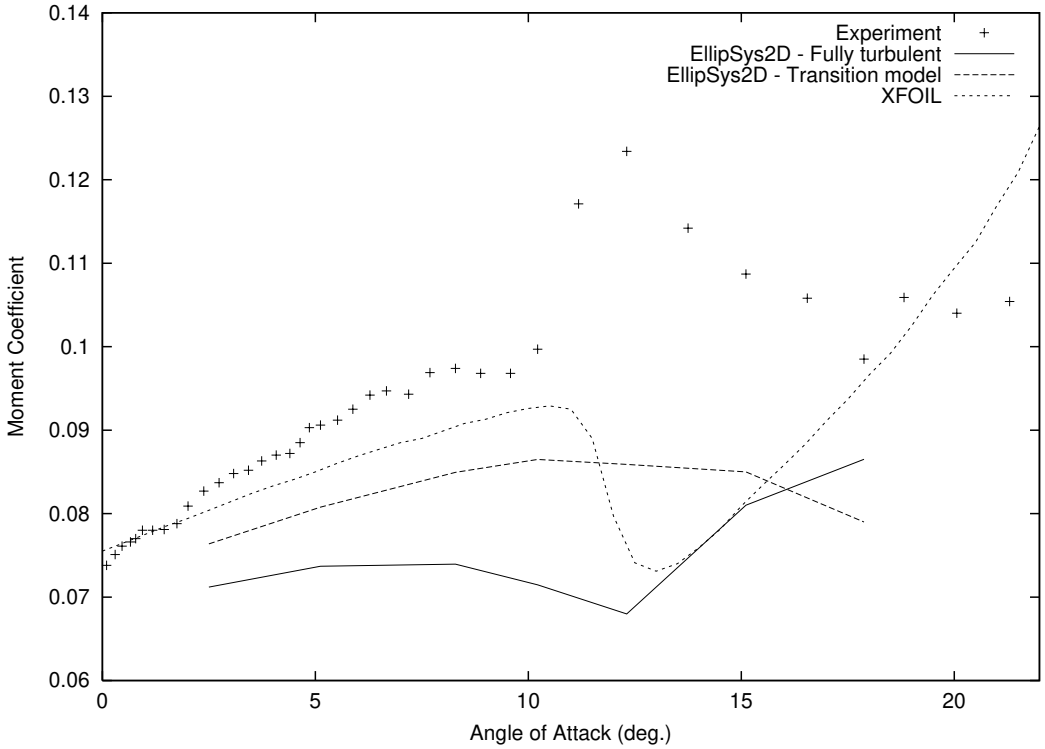

Figure 92. Pitching Moment Coefficient Curve (RISØ-A1-21, Experiment [13])

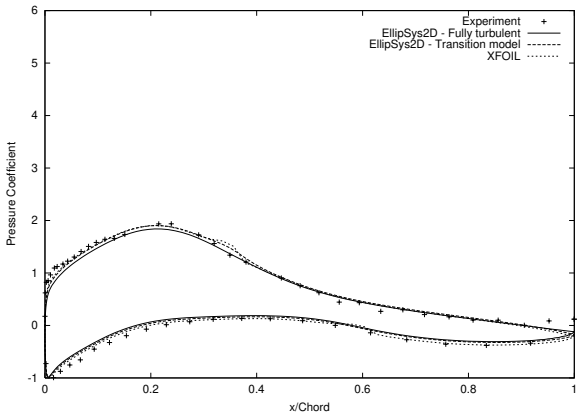

(a) $\alpha = 5.12^o$

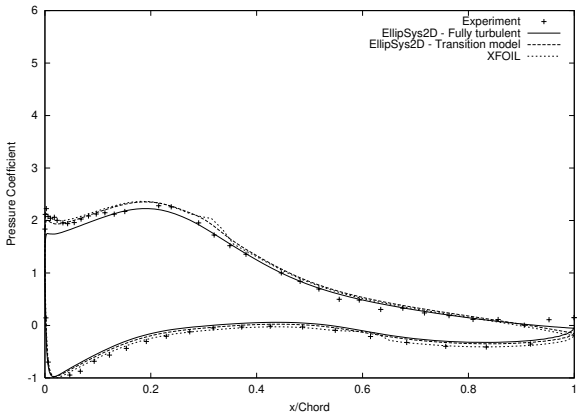

(b) $\alpha = 8.29^o$

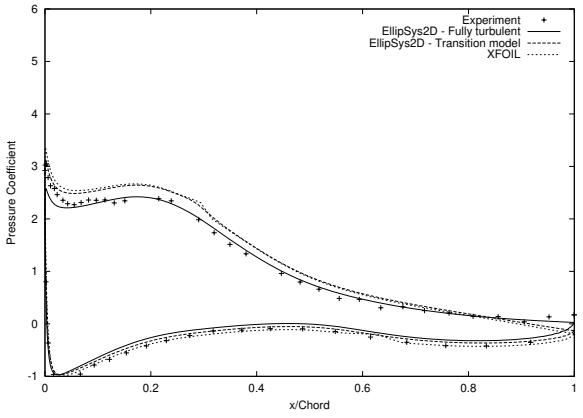

(c) $\alpha = 10.22^o$

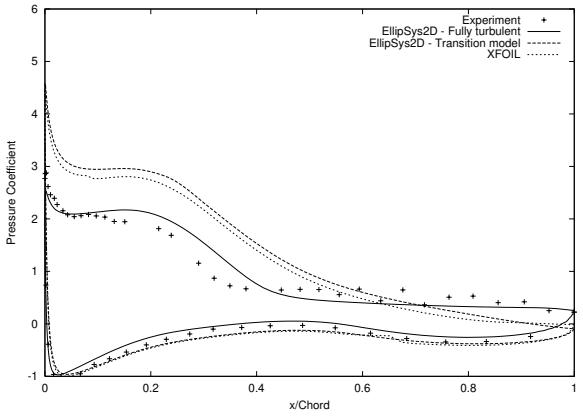

(d) $\alpha = 12.31^o$

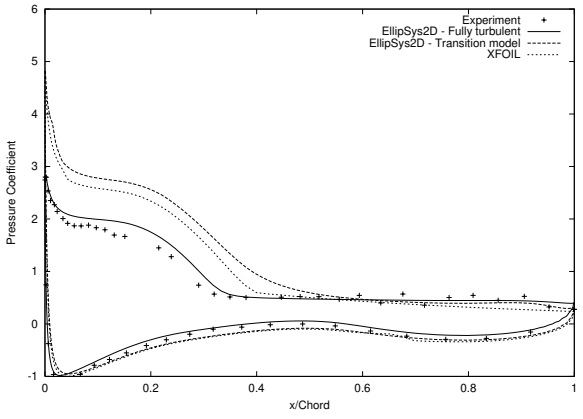

(e) $\alpha = 15.11^o$

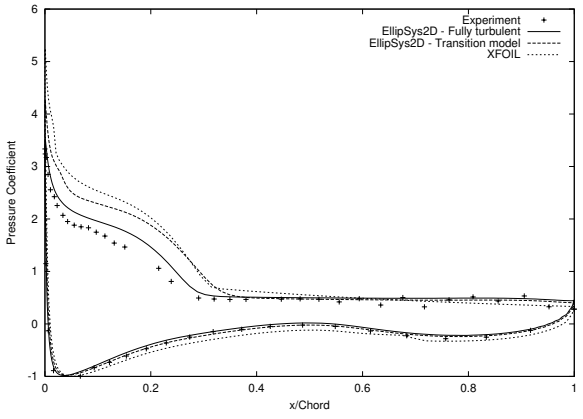

(f) $\alpha = 17.88^o$

Figure 93. Pressure Coefficient Distributions (RISØ-A1-21, Experiment [13])

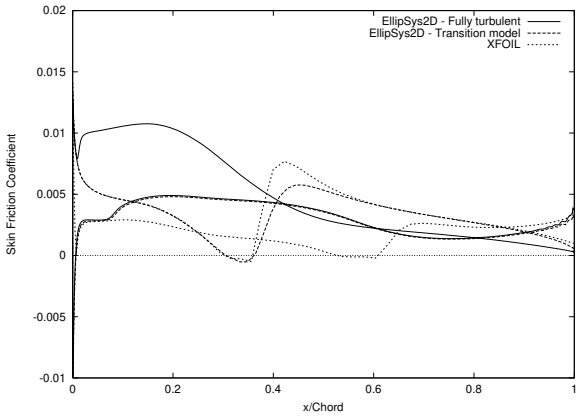

(a) $\alpha = 5.12^o$

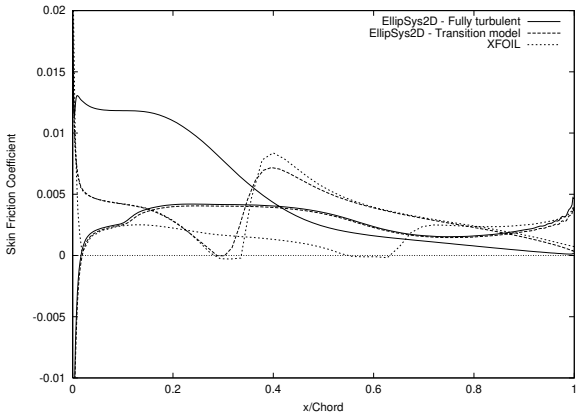

(b) $\alpha = 8.29^o$

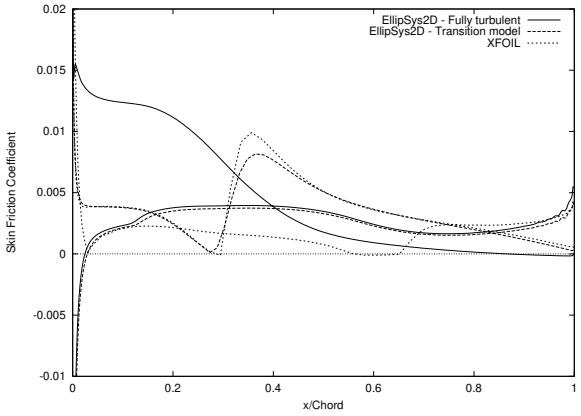

(c) $\alpha = 10.22^o$

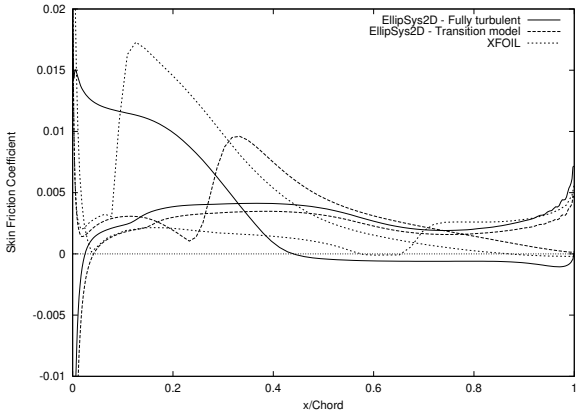

(d) $\alpha = 12.31^o$

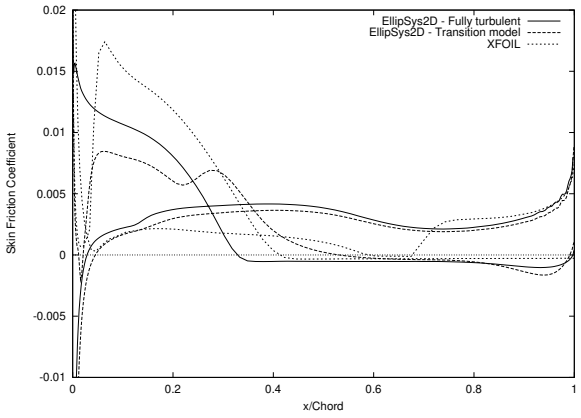

(e) $\alpha = 15.11^o$

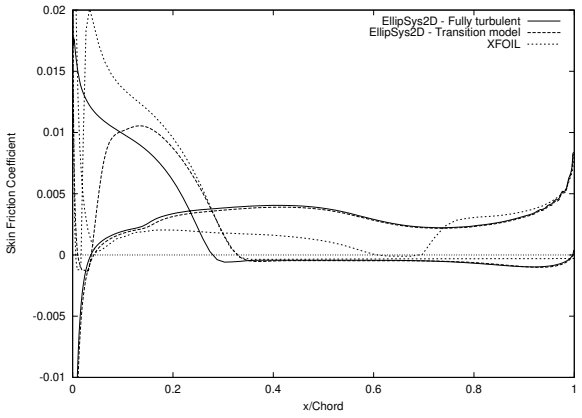

(f) $\alpha = 17.88^o$

Figure 94. Skin Friction Coefficient Distributions (RISØ-A1-21)

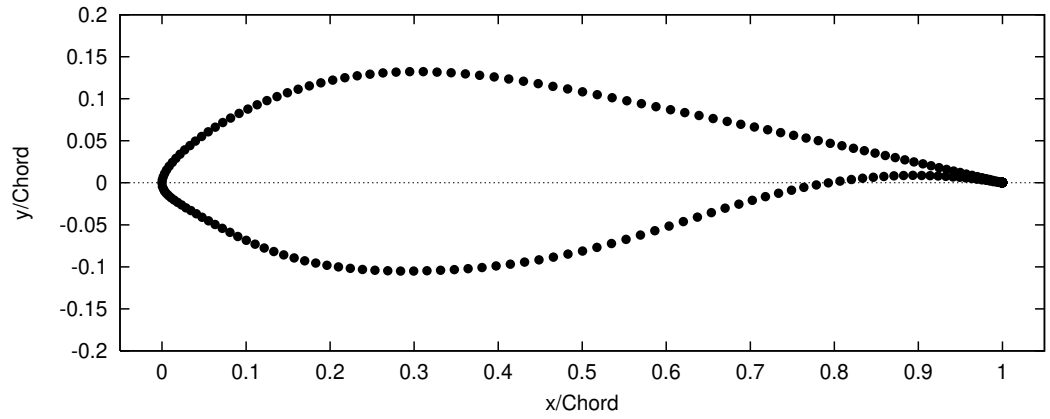

Figure 95. RISØ-A1-24 Airfoil

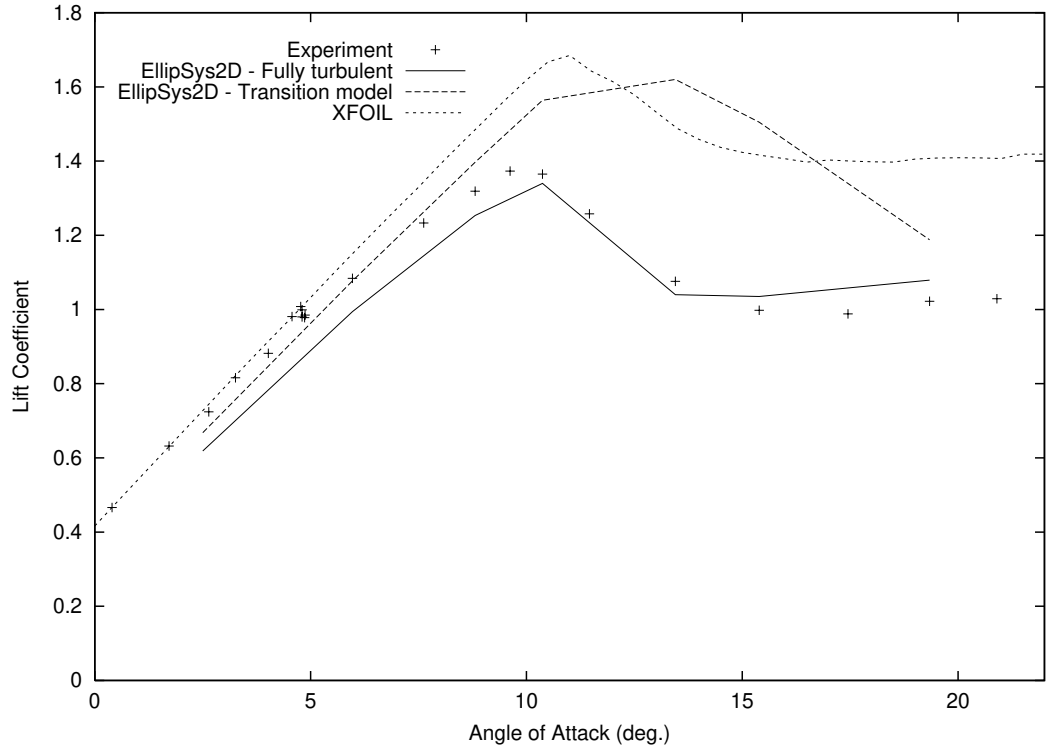

Figure 96. Lift Coefficient Curve (RISØ-A1-24, Experiment [13])

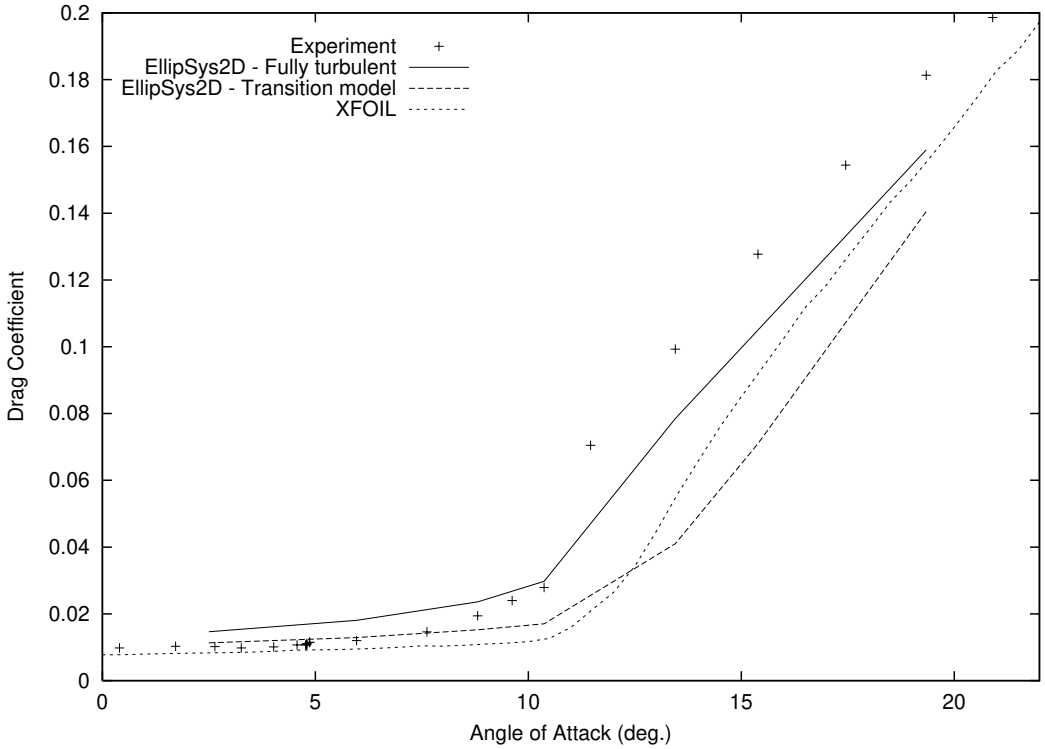

Figure 97. Drag Coefficient Curve (RISØ-A1-24, Experiment [13])

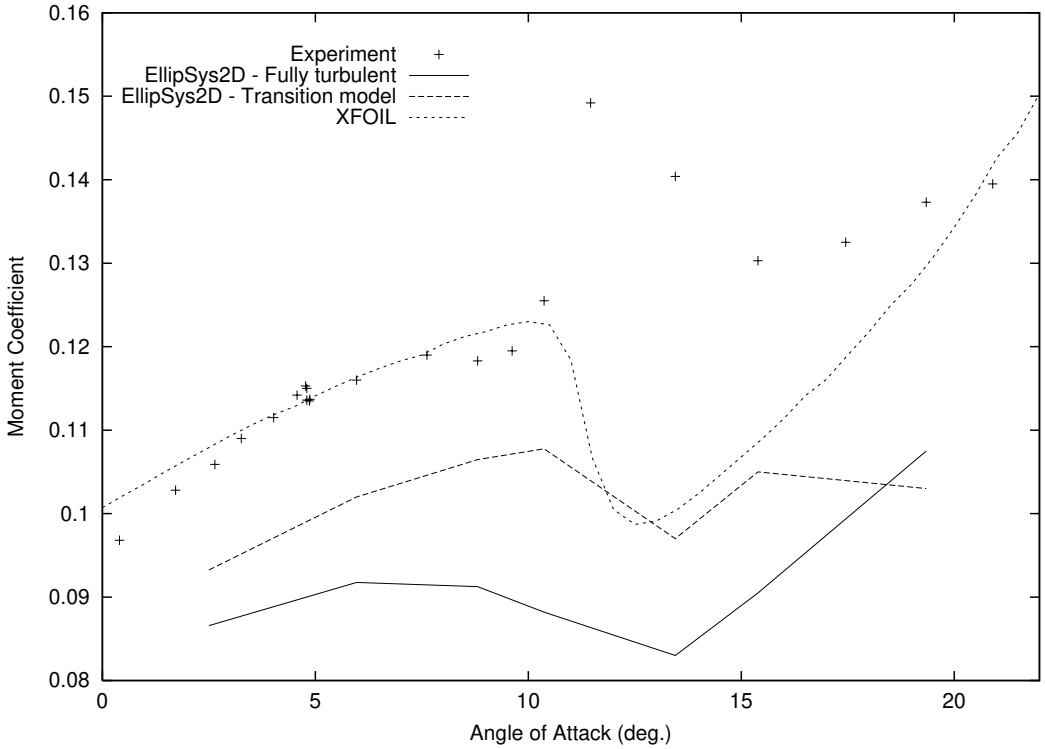

Figure 98. Pitching Moment Coefficient Curve (RISØ-A1-24, Experiment [13])

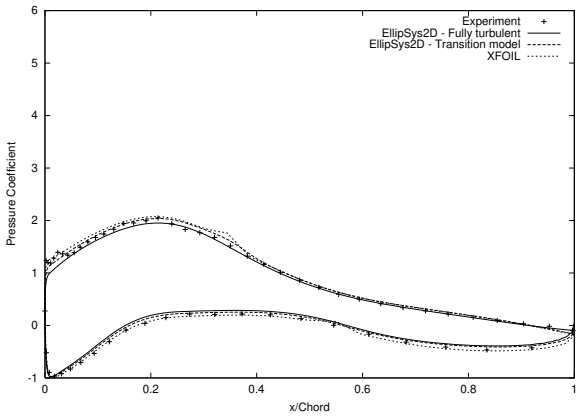

(a) $\alpha = 5.97^o$

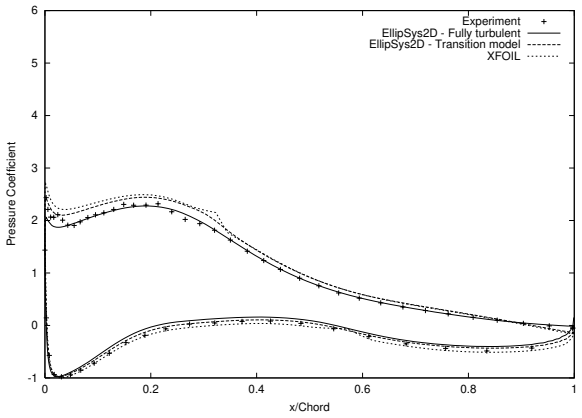

(b) $\alpha = 8.81^o$

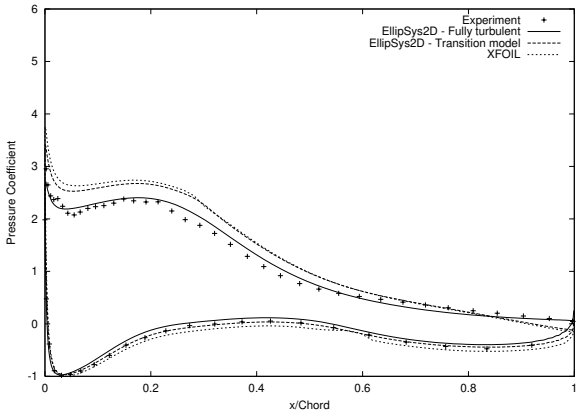

(c) $\alpha = 10.37^o$

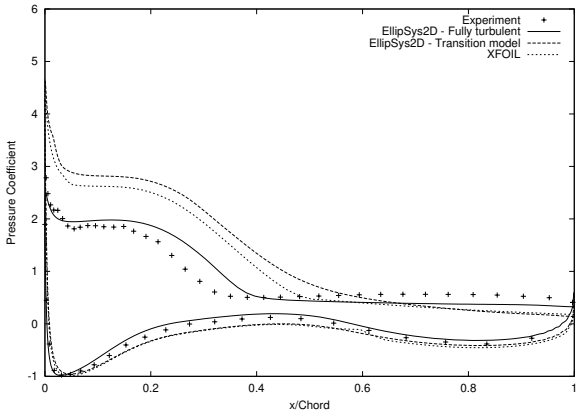

(d) $\alpha = 13.45^o$

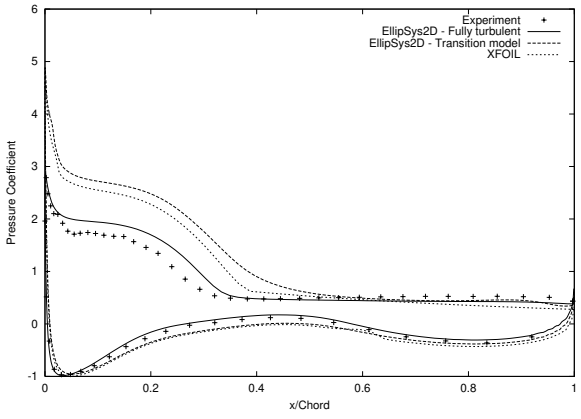

(e) $\alpha = 15.39^o$

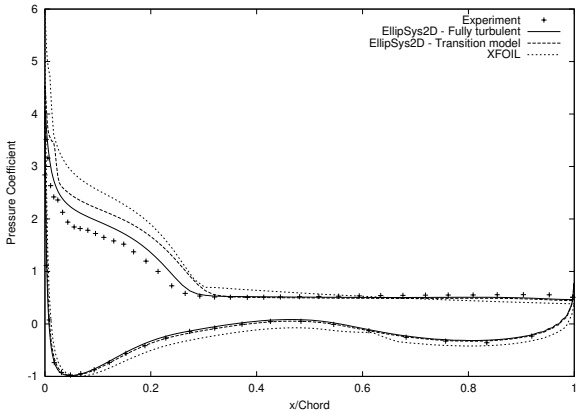

(f) $\alpha = 19.34^o$

Figure 99. Pressure Coefficient Distributions (RISØ-A1-24, Experiment [13])

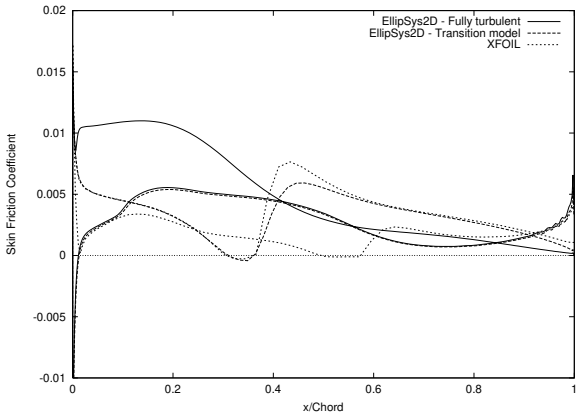

(a) $\alpha = 5.97^o$

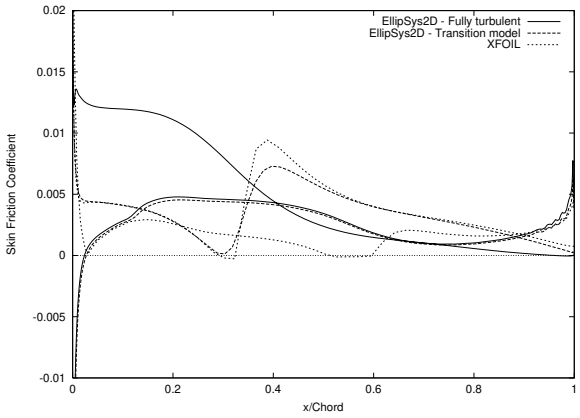

(b) $\alpha = 8.81^o$

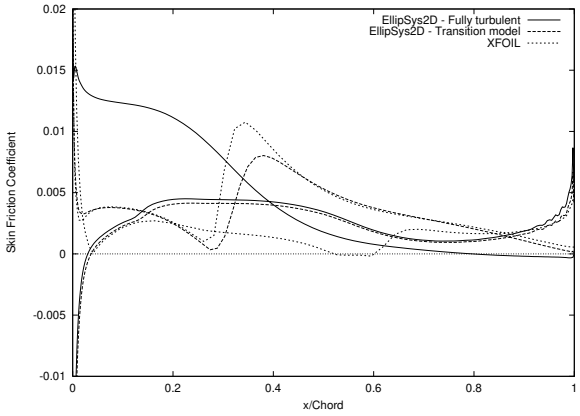

(c) $\alpha = 10.37^o$

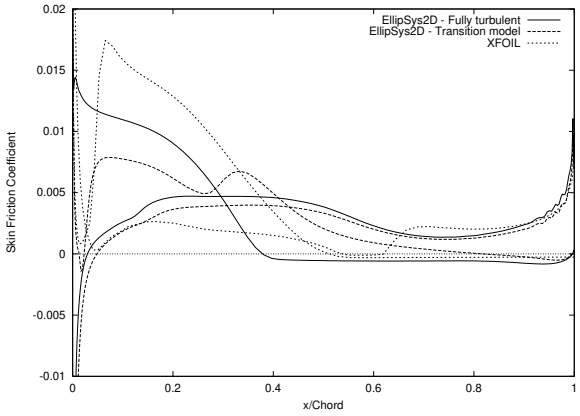

(d) $\alpha = 13.45^o$

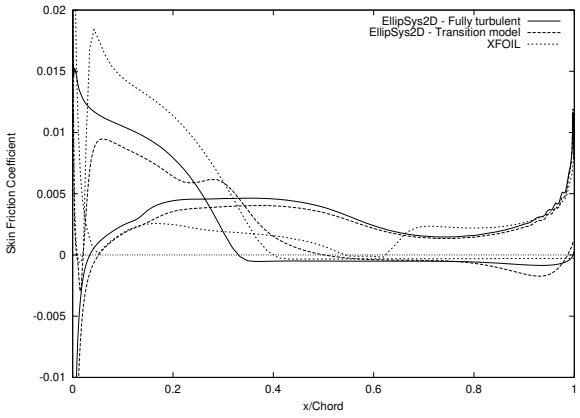

(e) $\alpha = 15.39^o$

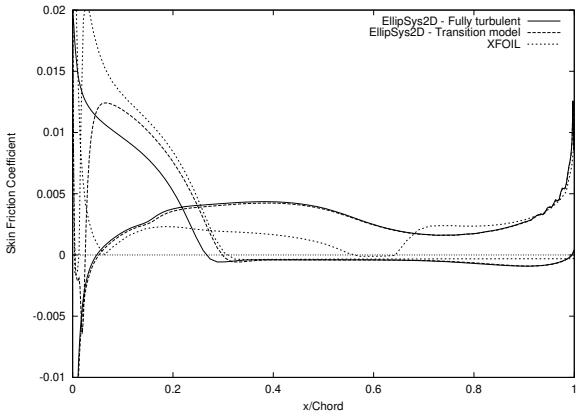

(f) $\alpha = 19.34^o$

Figure 100. Skin Friction Coefficient Distributions (RISØ-A1-24)

6 FFA-W3-211 Airfoil

The FFA-W3-211 airfoil manufactured and equipped at FFA (The Aeronautical Research Institute of Sweden) was investigated. It is a 21% thickness airfoil. It was tested in the low speed wind tunnel L2000 (located at KTH, Royal Institute of Technology, Stockholm) with a turbulence intensity of 0.15% [6, 7]. The Reynolds number of the experiment was $Re = 1.8 \times 10^6$. Two sets of measurements were used herein. The first was obtained with an adhesive tape at the airfoil upper and lower side at $x/Chord = 5\%$, in order to trigger boundary layer transition at these locations. Transition was let free for the second one.

6.1 Method

A C-mesh was used to compute the flow around this airfoil with 384 cells in the direction along the airfoil, 256 of them being on the airfoil, and 64 cells in the direction away from the airfoil. The non-dimensional height of the cell at the airfoil was 1×10^{-5}.

The computations were performed with the SUDS-scheme for the convective terms, together with the $k - \omega$ SST turbulence model by Menter [16] for the turbulent viscosity. The transition was fixed at $x/Chord = 5\%$ on both sides of the airfoil when comparing with the first set of measurements. The transition model by Michel [17], together with the empirical function given by Chen and Thyson [8] for modelling the turbulence intermittency, was used when comparing with free-transition measurements. Numerical results were obtained with stationary computations.

6.2 Results

For both cases (fixed and free transition), the computational results matched the experimental data in the linear region, but stall was predicted at a too high angle of attack, and a greater maximum lift was computed. However, results were in slightly better agreement for the case with free transition.

FFA-W3-211, Fixed Transition

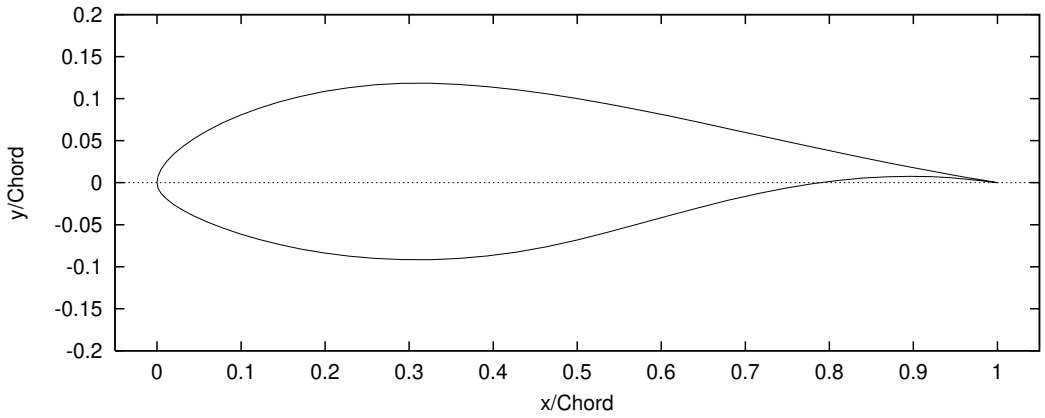

Figure 101. FFA-W3-211 Airfoil

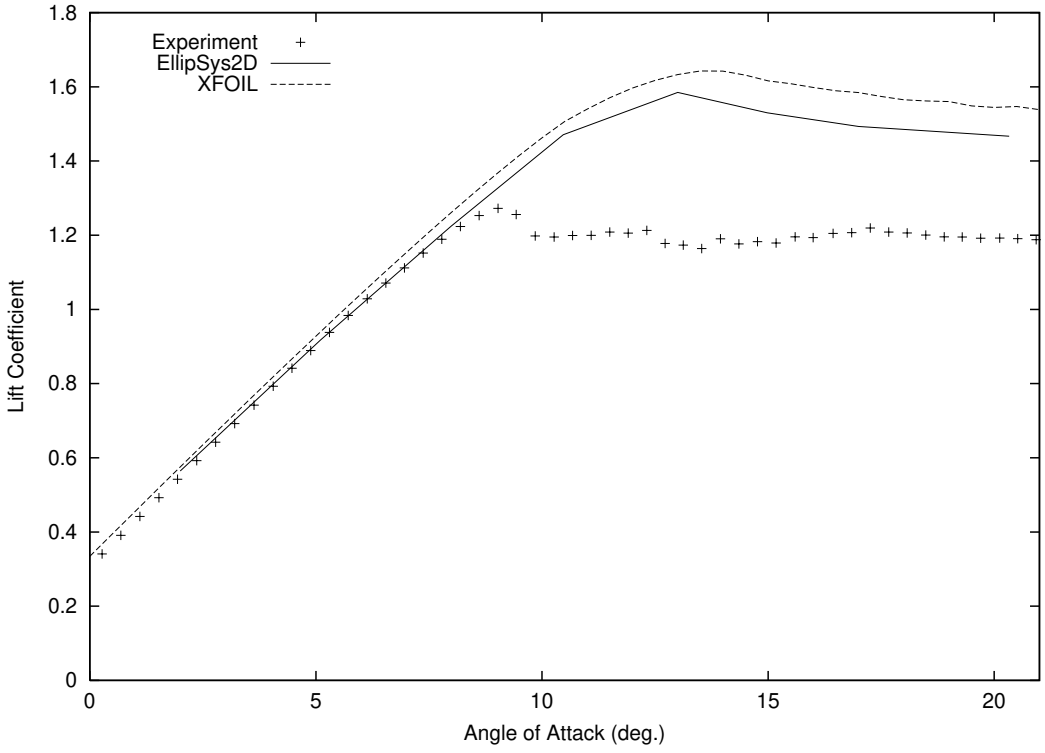

Figure 102. Lift Coefficient Curve (FFA-W3-211, Fixed Transition, Experiment [7])

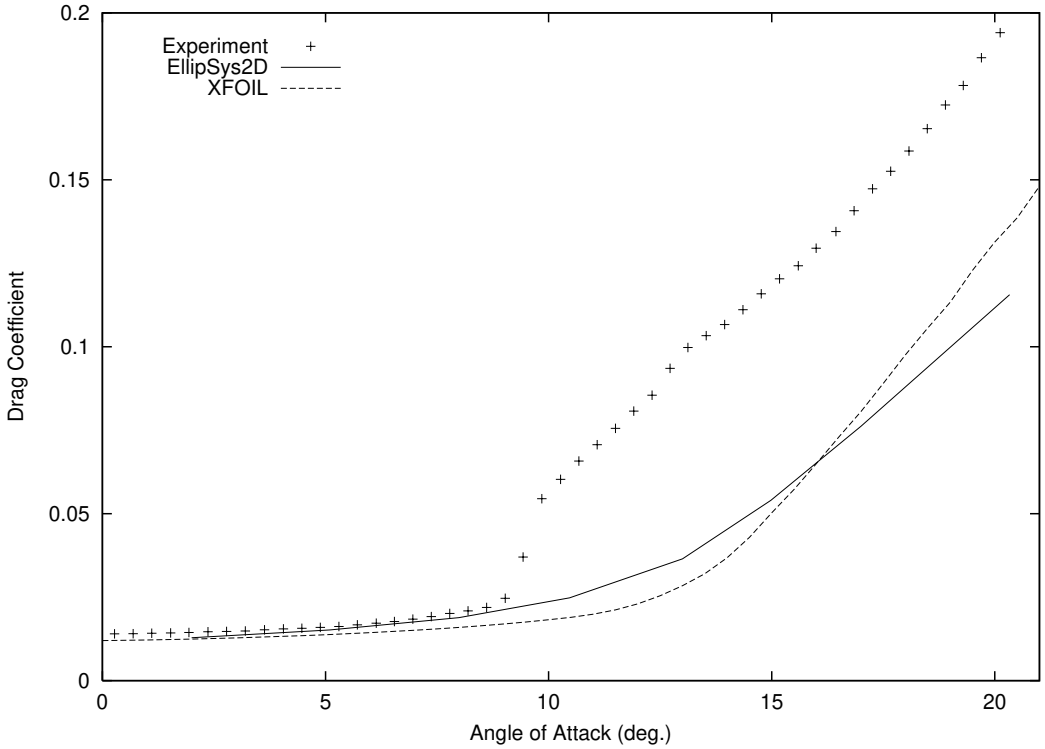

Figure 103. Drag Coefficient Curve (FFA-W3-211, Fixed Transition, Experiment [7])

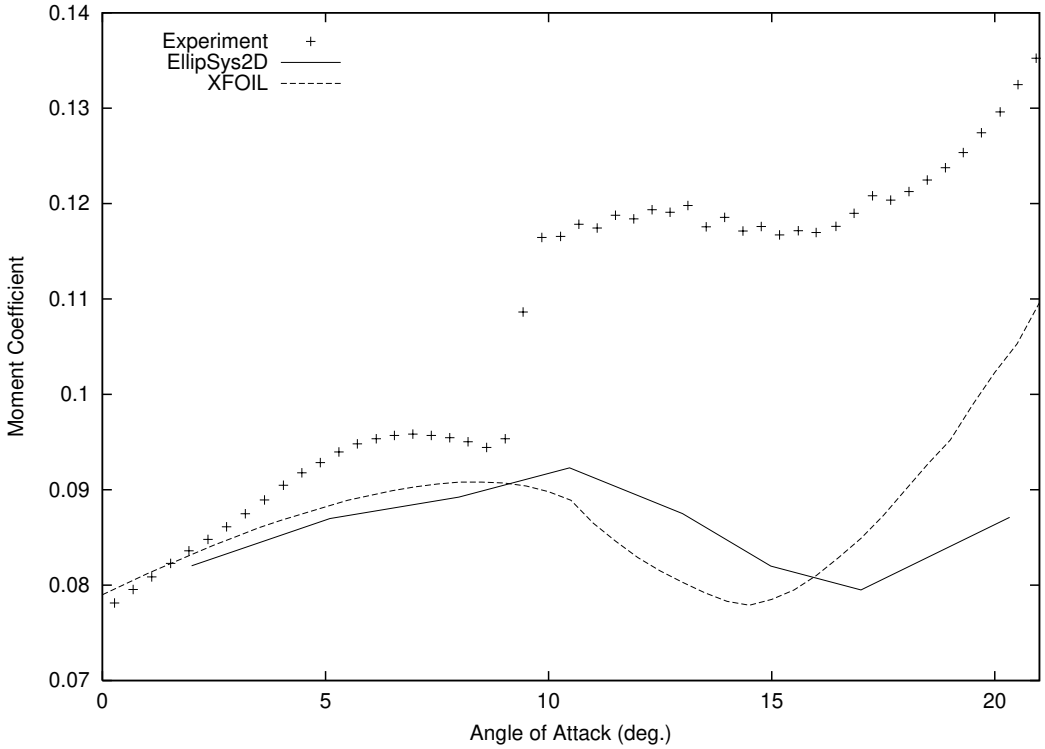

Figure 104. Pitching Moment Coefficient Curve (FFA-W3-211, Fixed Transition, Experiment [7])

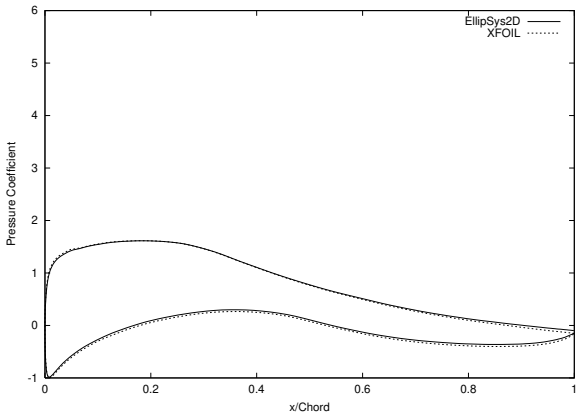

(a) $\alpha = 5.1^o$

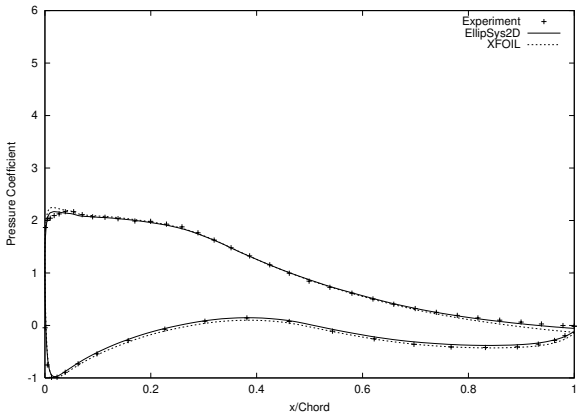

(b) $\alpha = 7.99^o$

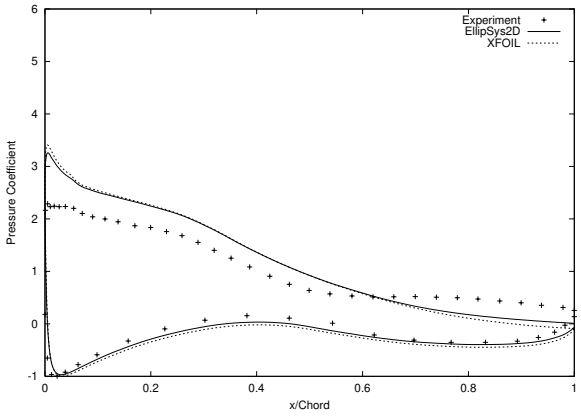

(c) $\alpha = 10.47^o$

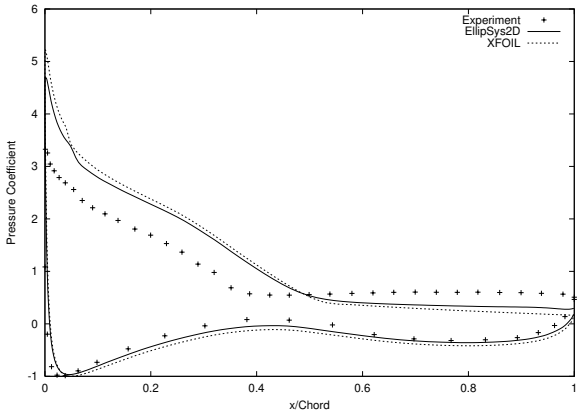

(d) $\alpha = 14.98^o$

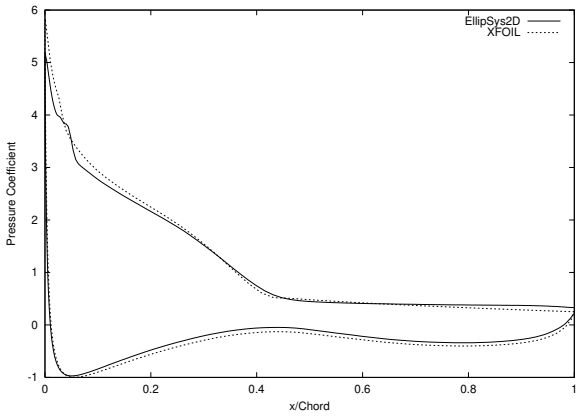

(e) $\alpha = 17.0^o$

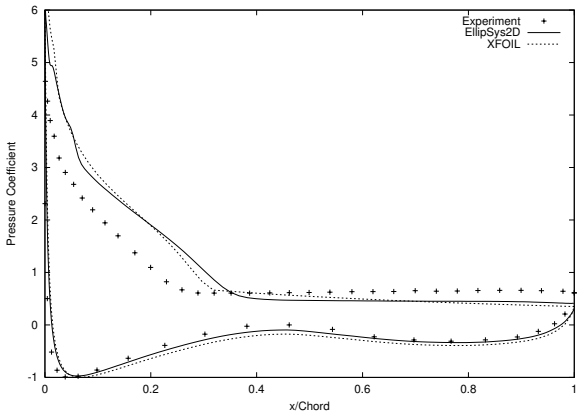

(f) $\alpha = 20.33^o$

Figure 105. Pressure Coefficient Distributions (FFA-W3-211, Fixed Transition, Experiment [7])

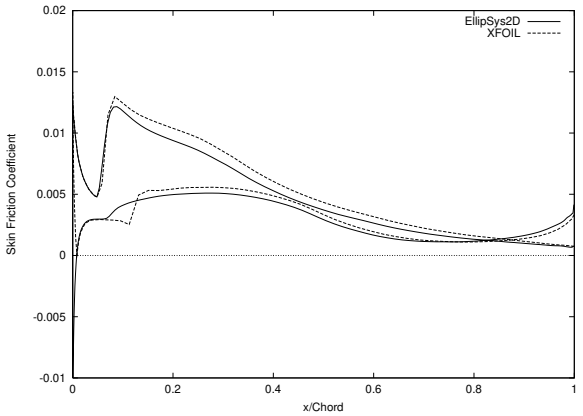

(a) $\alpha = 5.1^o$

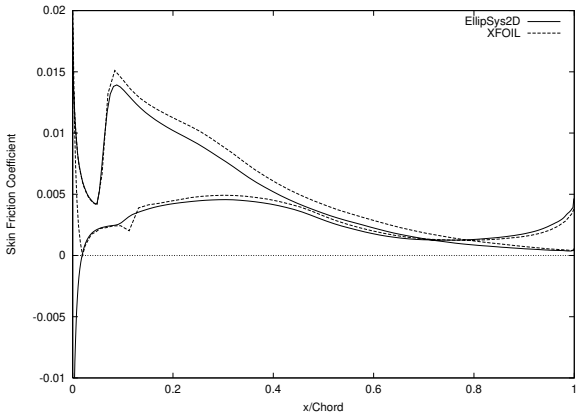

(b) $\alpha = 7.99^o$

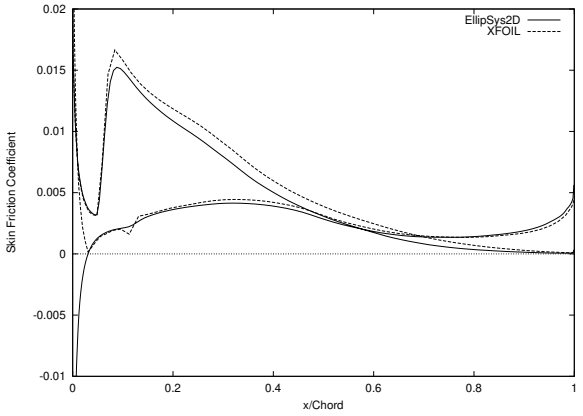

(c) $\alpha = 10.47^o$

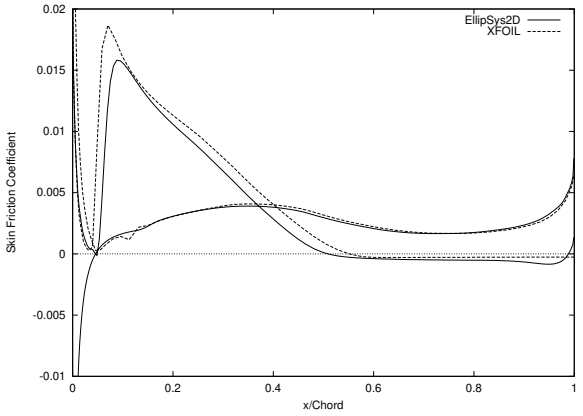

(d) $\alpha = 14.98^o$

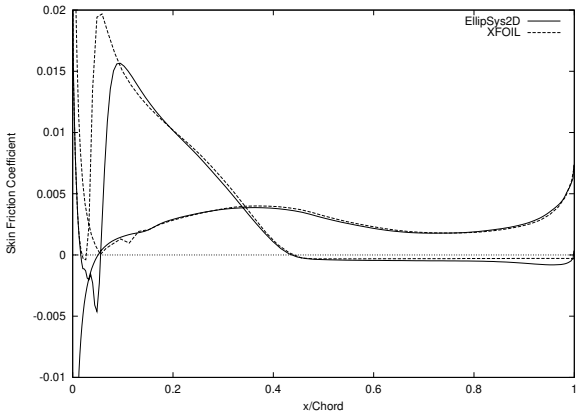

(e) $\alpha = 17.0^o$

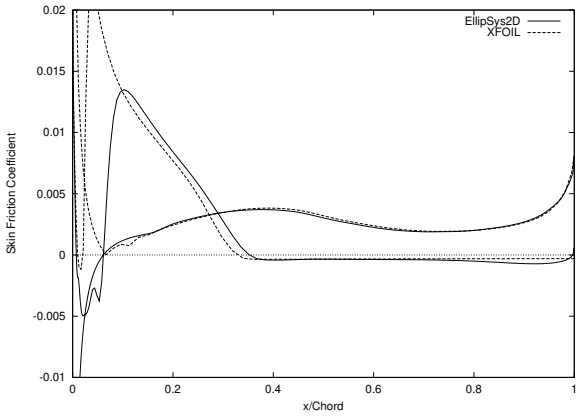

(f) $\alpha = 20.33^o$

Figure 106. Skin Friction Coefficient Distributions (FFA-W3-211, Fixed Transition)

FFA-W3-211, Free Transition

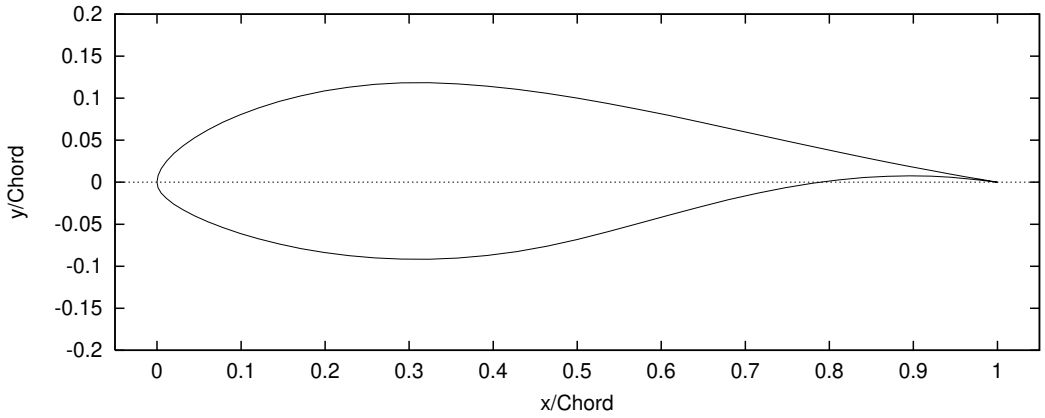

Figure 107. FFA-W3-211 Airfoil

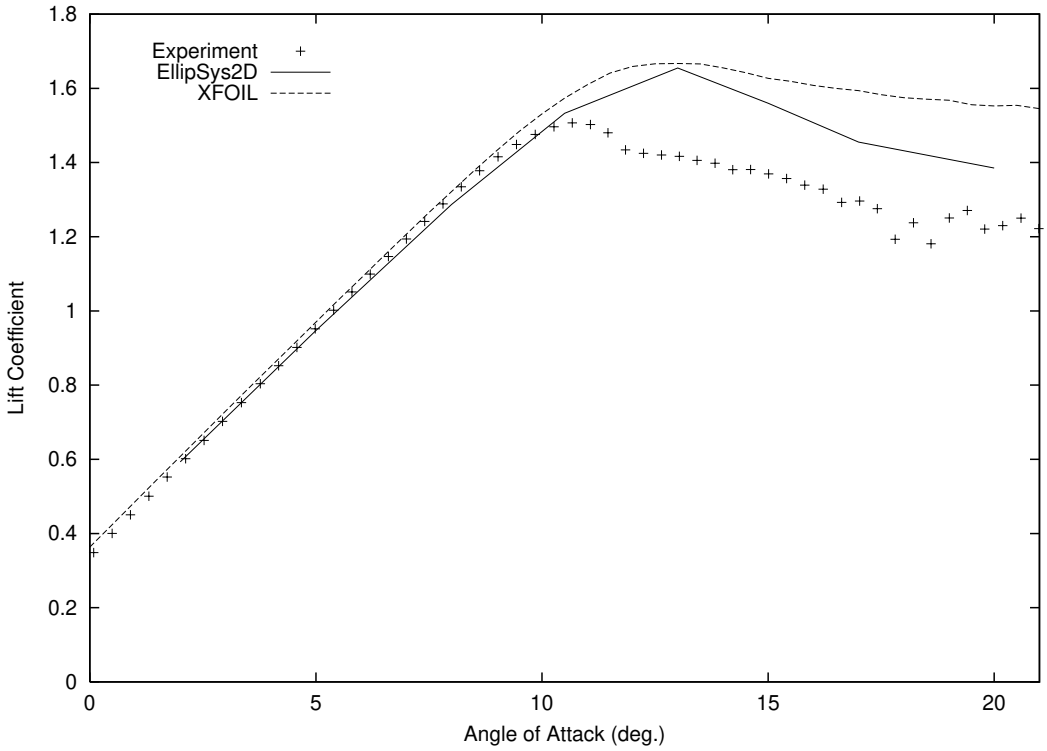

Figure 108. Lift Coefficient Curve (FFA-W3-211, Free Transition, Experiment [7])

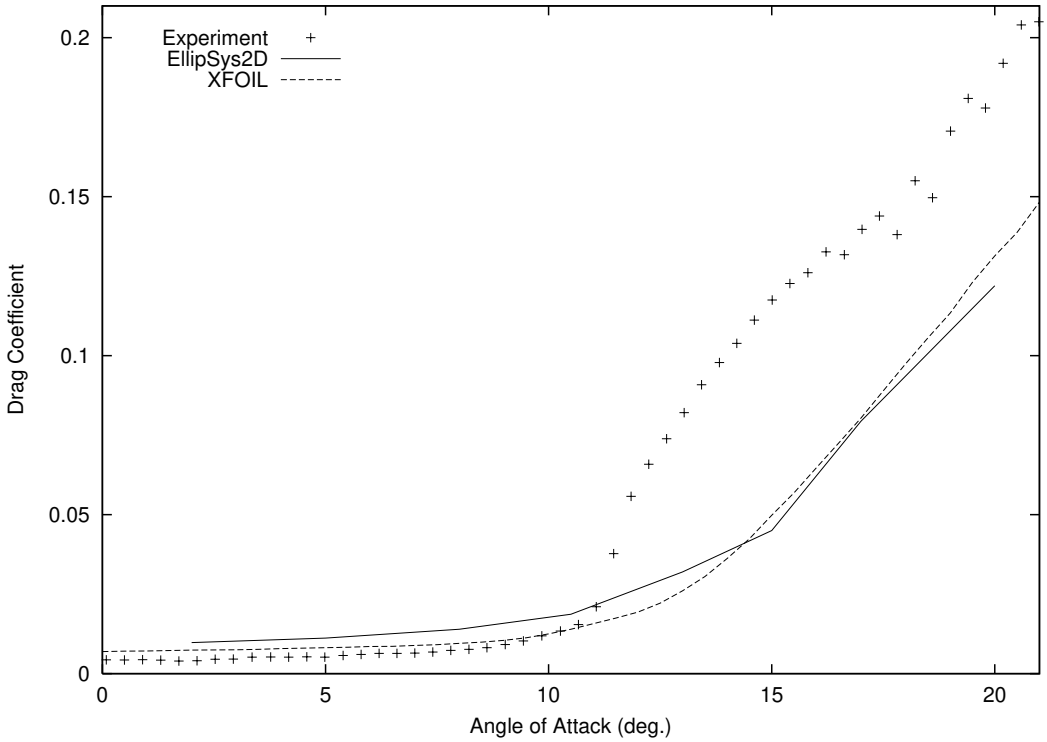

Figure 109. Drag Coefficient Curve (FFA-W3-211, Free Transition, Experiment [7])

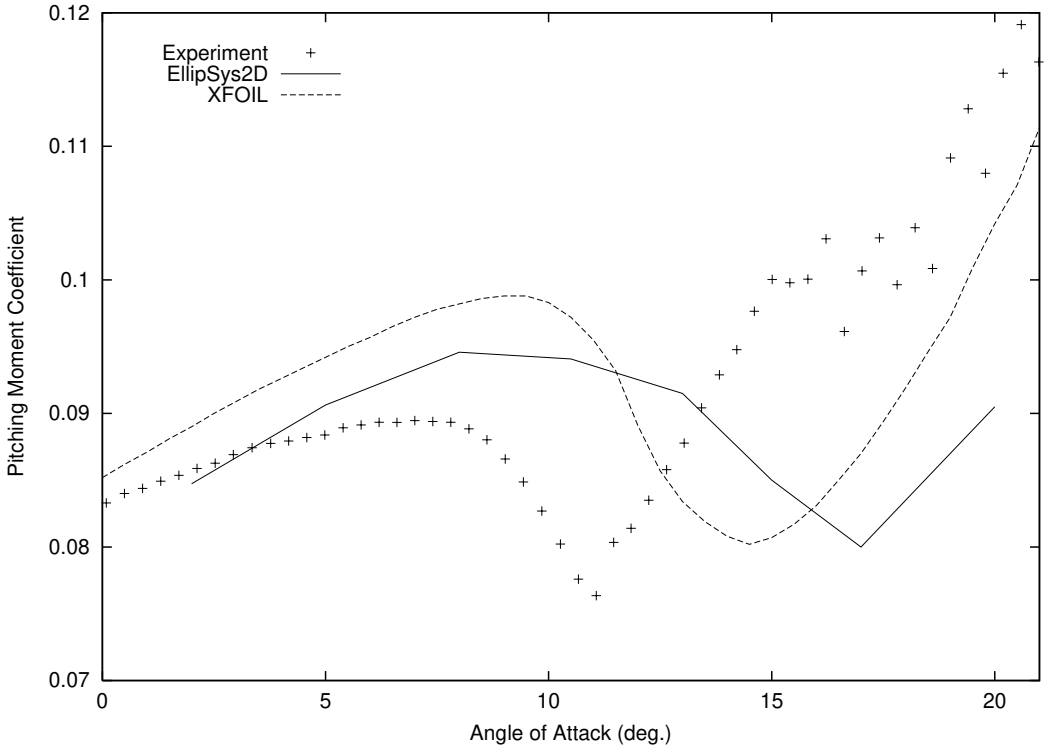

Figure 110. Pitching Moment Coefficient Curve (FFA-W3-211, Free Transition, Experiment [7])

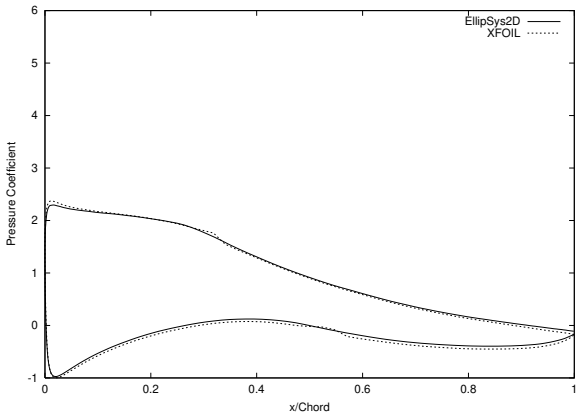

(a) $\alpha = 8.0^o$

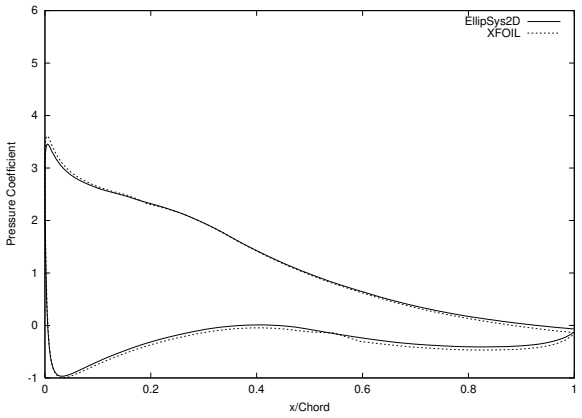

(b) $\alpha = 10.5^o$

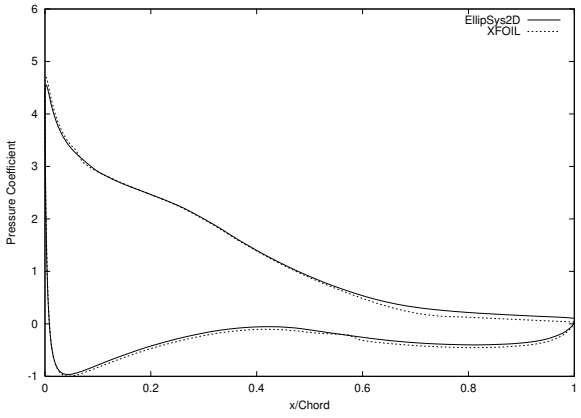

(c) $\alpha = 13.0^o$

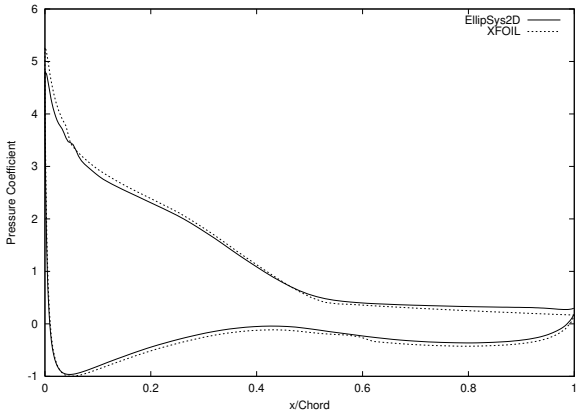

(d) $\alpha = 15.0^o$

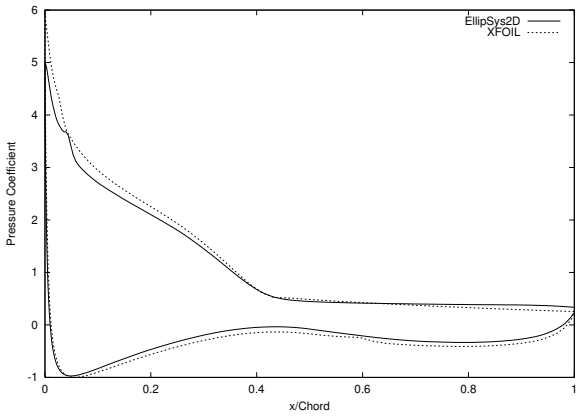

(e) $\alpha = 17.0^o$

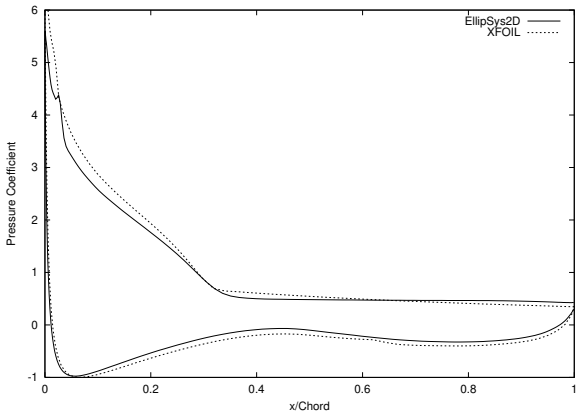

(f) $\alpha = 20.0^o$

Figure 111. Pressure Coefficient Distributions (FFA-W3-211, Free Transition)

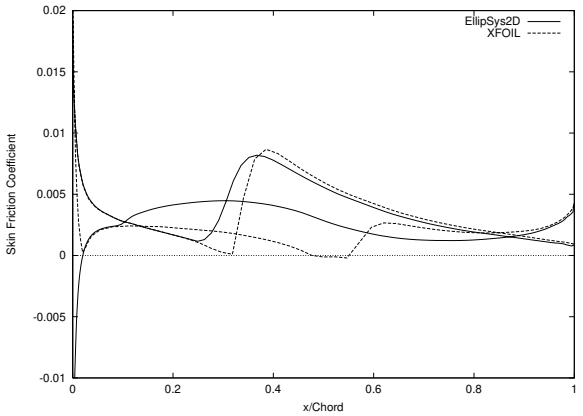

(a) $\alpha = 8.0^o$

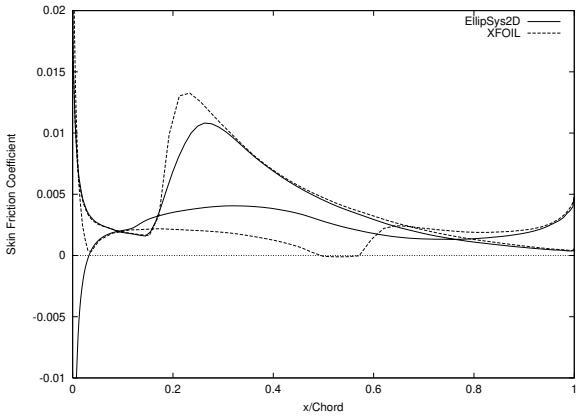

(b) $\alpha = 10.5^o$

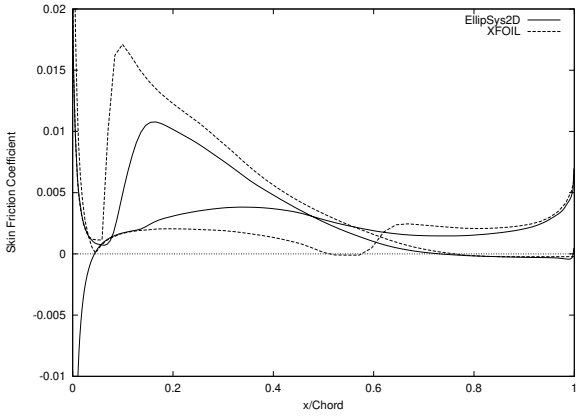

(c) $\alpha = 13.0^o$

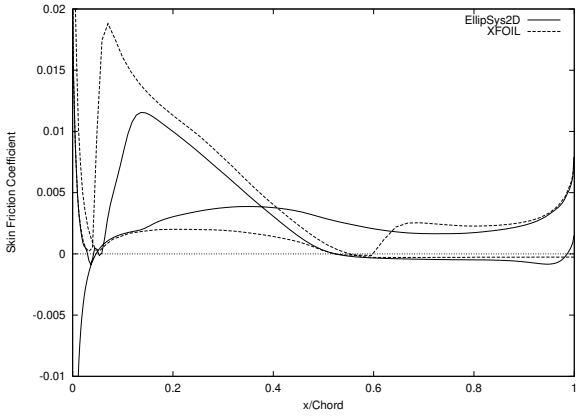

(d) $\alpha = 15.0^o$

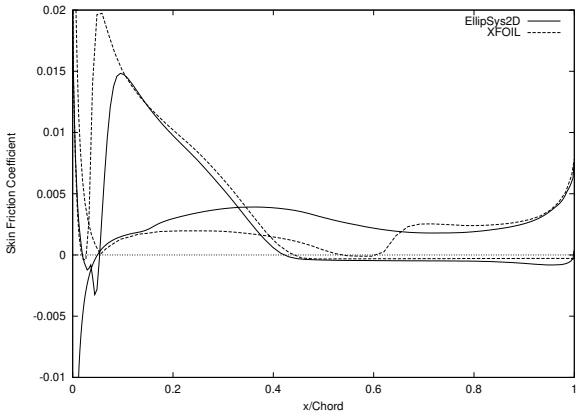

(e) $\alpha = 17.0^o$

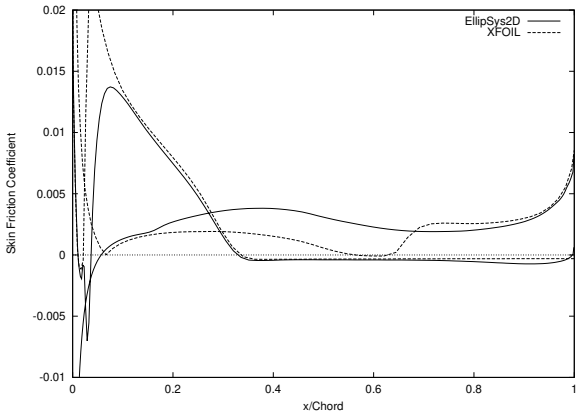

(f) $\alpha = 20.0^o$

Figure 112. Skin Friction Coefficient Distributions (FFA-W3-211, Free Transition)

7 FFA-W3-241 and FFA-W3-301 Airfoils

These two airfoils have been designed at FFA (The Aeronautical Research Institute of Sweden) by Björk [5]. They are relatively thick and have been used on the inboard part of different Danish wind turbine blades.

Measurements were carried out in the VELUX wind tunnel [10], which has an open test section. The testing facility is described in detail by Fuglsang *et al* [11]. The Reynolds number was equal to 1.5×10^6 for both airfoils measurement campaigns.

7.1 Method

The C-meshes used for the computation had 384 cells in the direction along the airfoil, 256 of them being on the airfoil, and 64 cells in the direction away from the airfoil. The non-dimensional height of the cell at the airfoil was 1×10^{-5}.

The computations were performed with the SUDS-scheme for the convective terms. As the turbulence level was relatively high in the wind tunnel, it was expected that a fully turbulent computation might give better results. Therefore, both fully turbulent simulations and computations with the Michel transition model [17], together with the empirical function given by Chen and Thyson [8] for modelling the turbulence intermittency, were conducted. The $k-\omega$ SST turbulence model by Menter [16] was used for the turbulent viscosity. Numerical results were obtained with stationary computations.

7.2 Results

For both airfoils, the computational results and experimental data were in rather good agreement in the linear region. However, the fully turbulent computations predicted stall at a correct angle of attack, contrary to the simulations with free transition that predicted stall at a much higher angle of attack.

FFA-W3-241

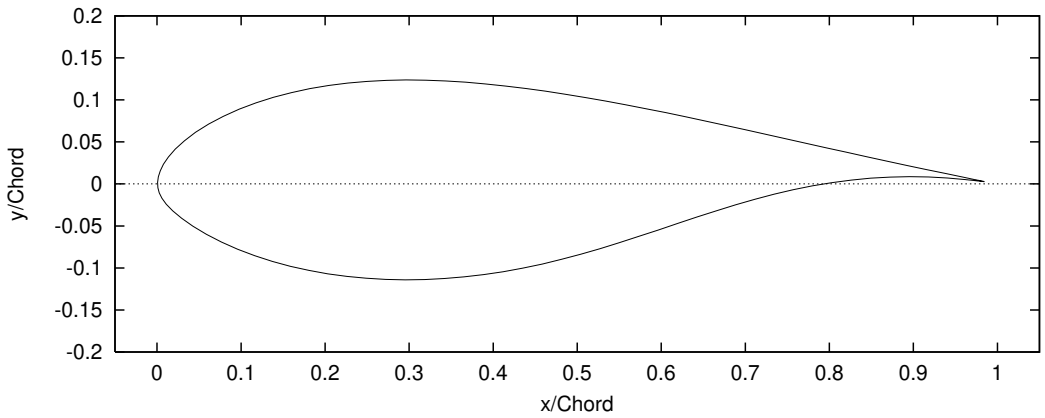

Figure 113. FFA-W3-241 Airfoil

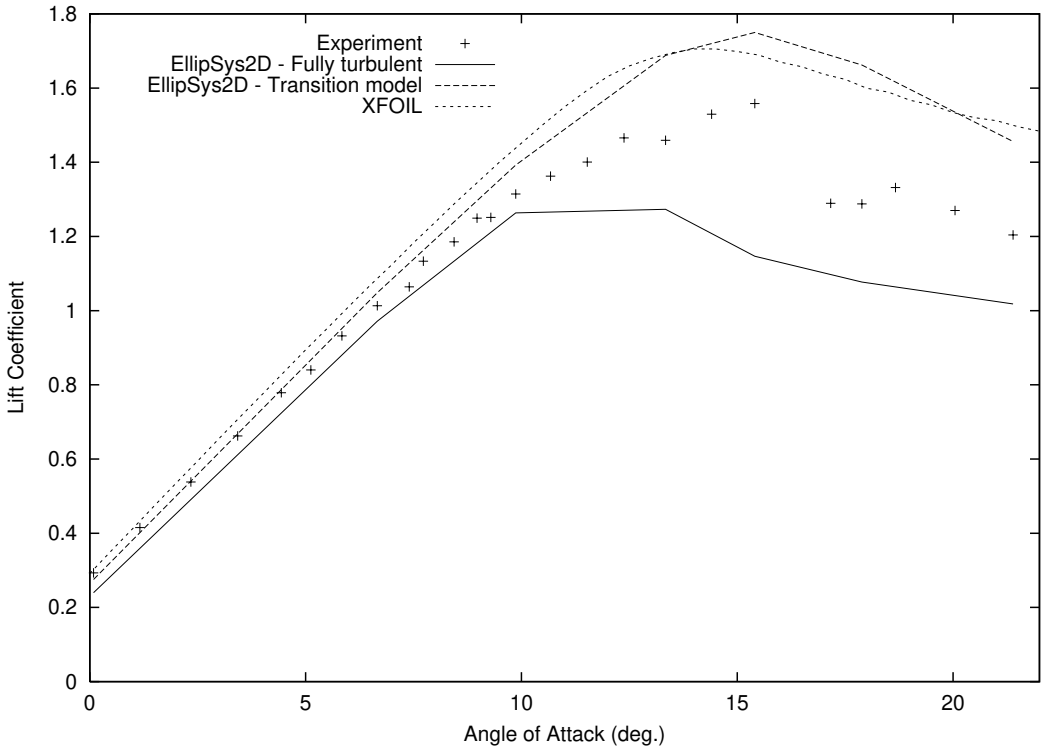

Figure 114. Lift Coefficient Curve (FFA-W3-241, Experiment [10])

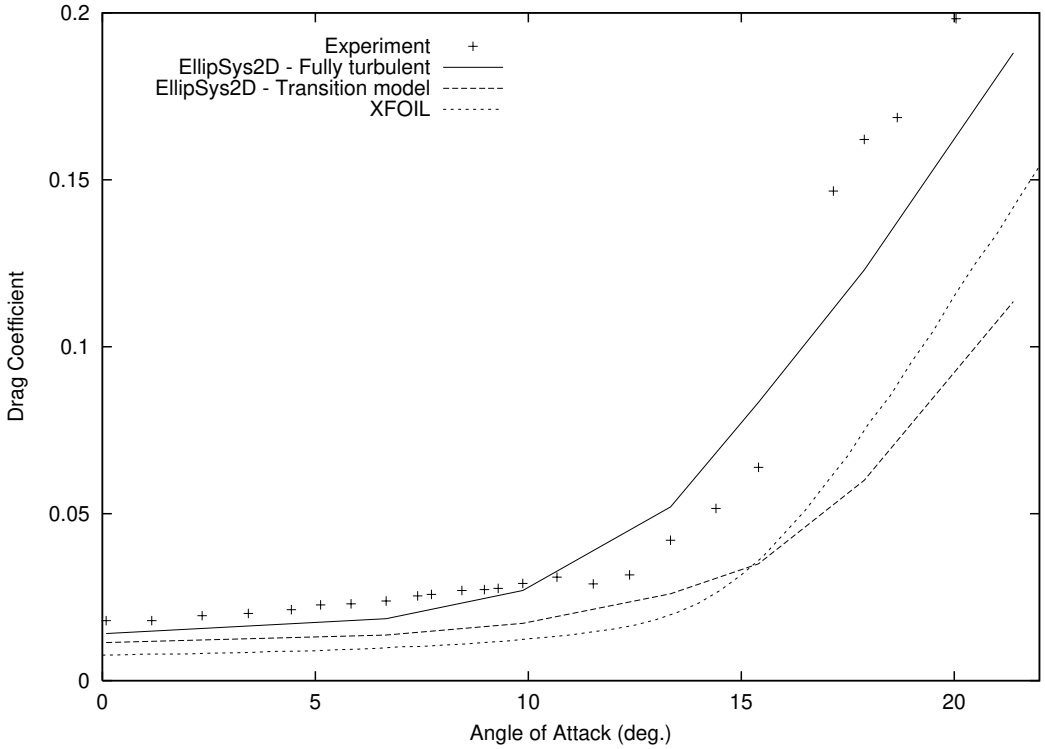

Figure 115. Drag Coefficient Curve (FFA-W3-241, Experiment [10])

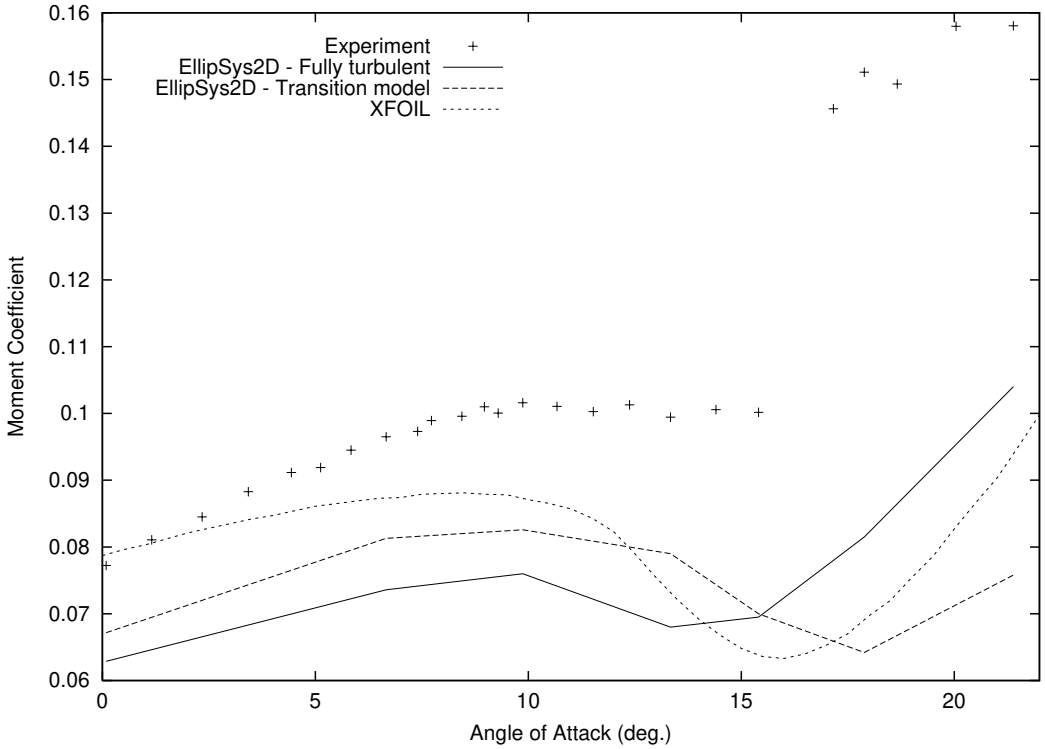

Figure 116. Pitching Moment Coefficient Curve (FFA-W3-241, Experiment [10])

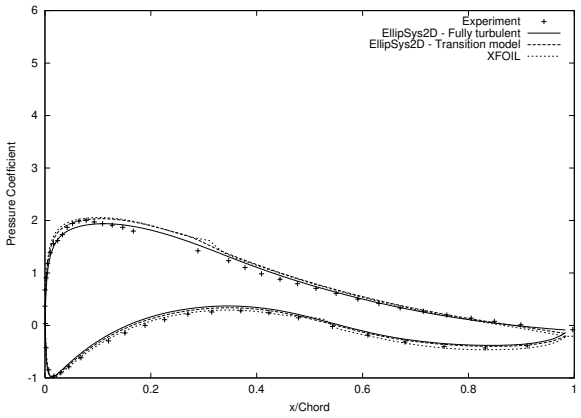

(a) $\alpha = 6.661^o$

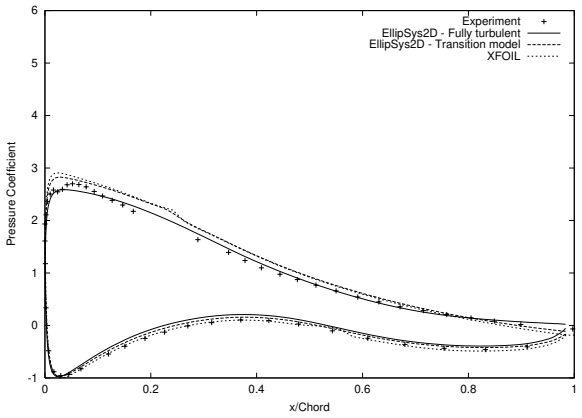

(b) $\alpha = 9.869^o$

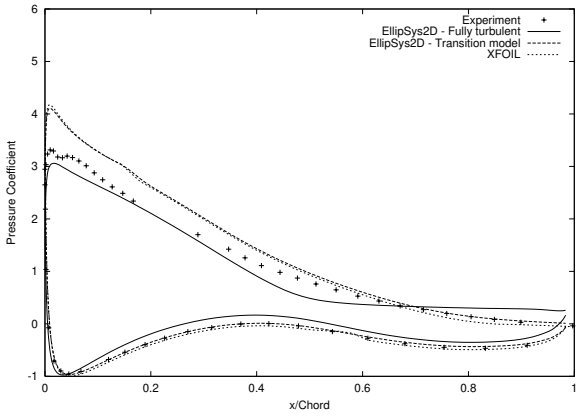

(c) $\alpha = 13.339^o$

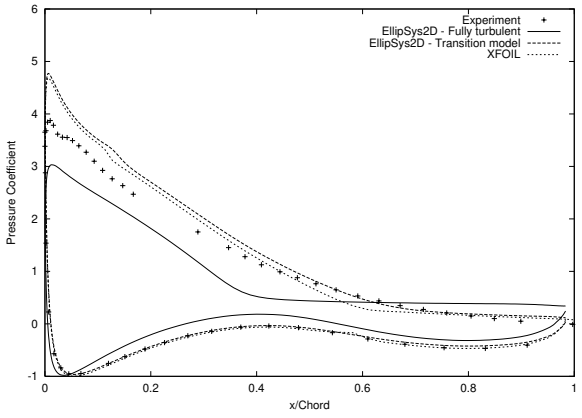

(d) $\alpha = 15.405^o$

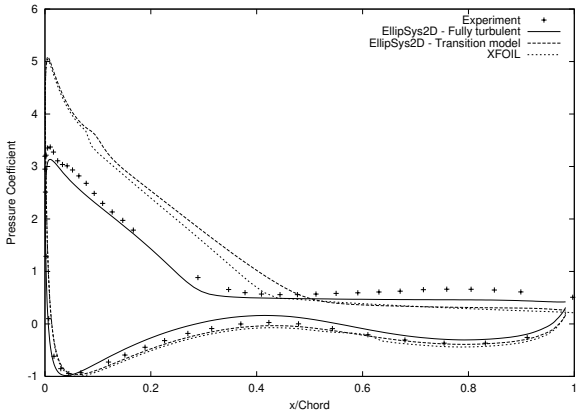

(e) $\alpha = 17.888^o$

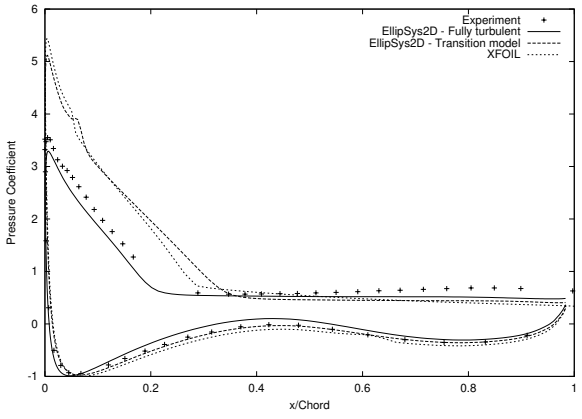

(f) $\alpha = 21.388^o$

Figure 117. Pressure Coefficient Distributions (FFA-W3-241, Experiment [10])

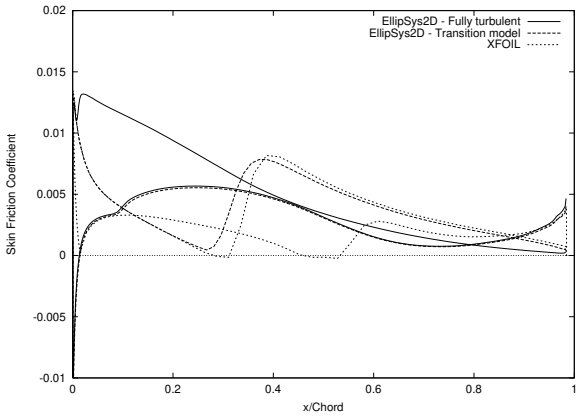

(a) $\alpha = 6.661^o$

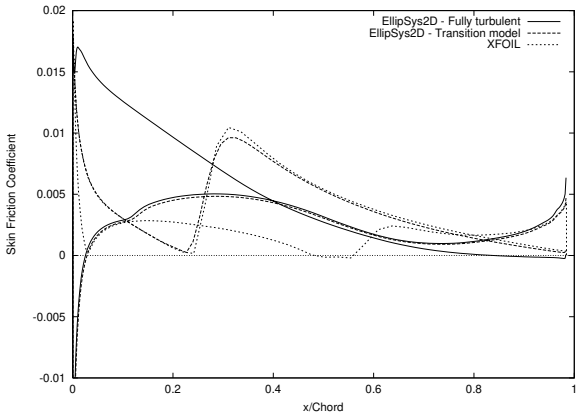

(b) $\alpha = 9.869^o$

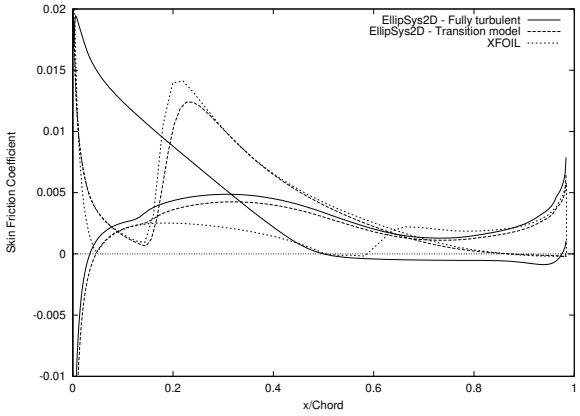

(c) $\alpha = 13.339^o$

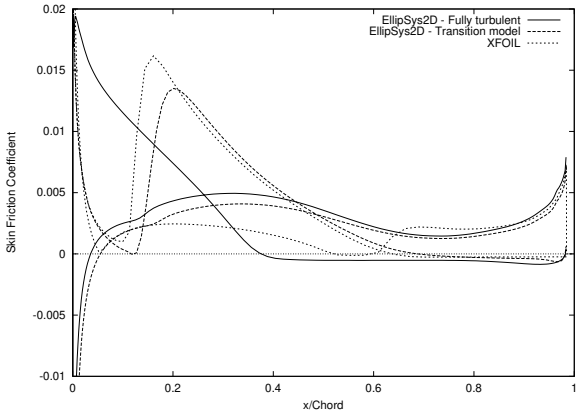

(d) $\alpha = 15.405^o$

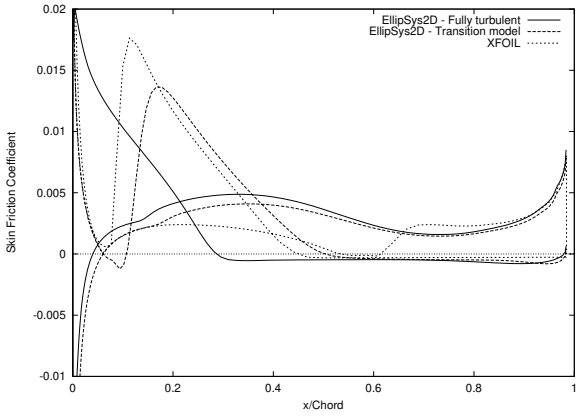

(e) $\alpha = 17.888^o$

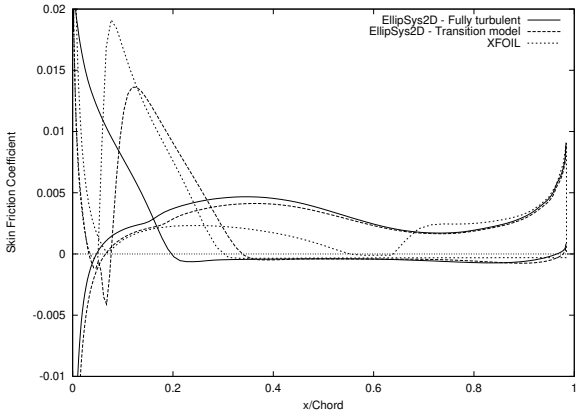

(f) $\alpha = 21.388^o$

Figure 118. Skin Friction Coefficient Distributions (FFA-W3-241)

FFA-W3-301

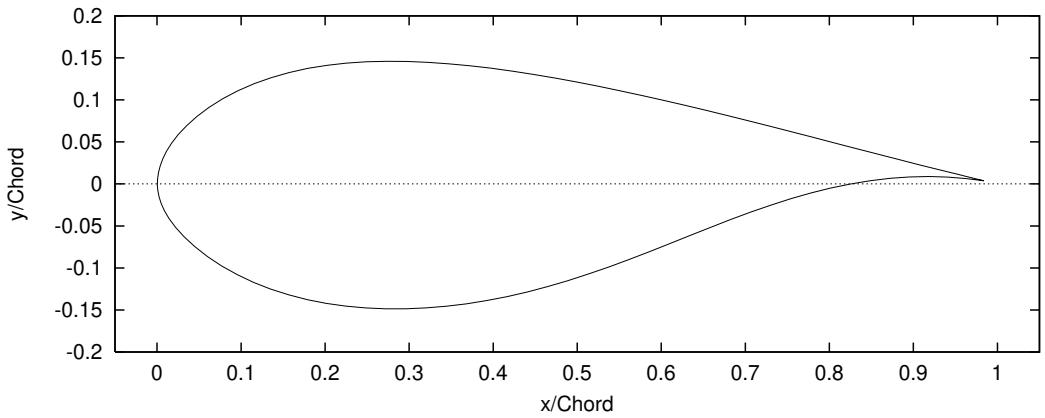

Figure 119. FFA-W3-301 Airfoil

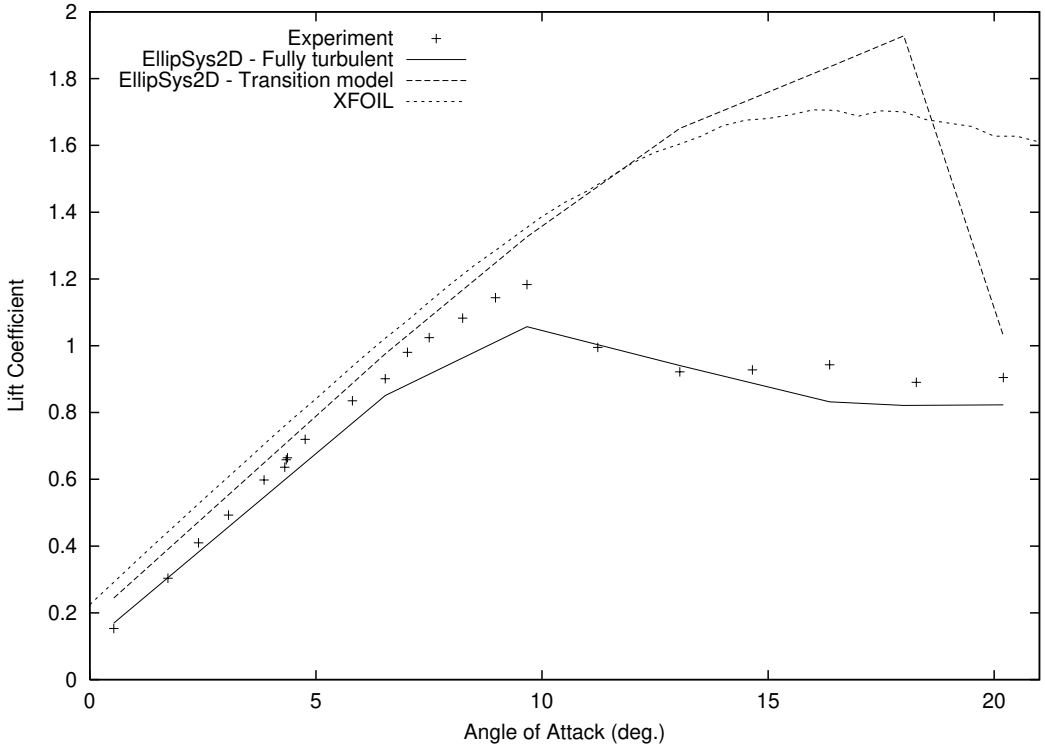

Figure 120. Lift Coefficient Curve (FFA-W3-301, Experiment [10])

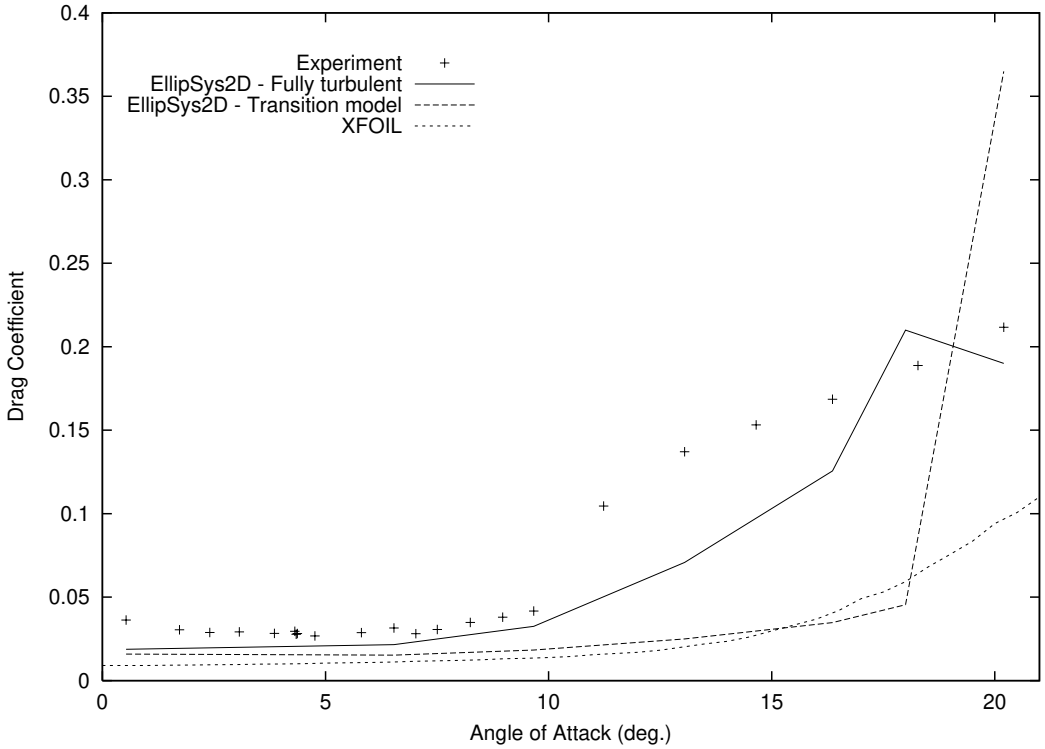

Figure 121. Drag Coefficient Curve (FFA-W3-301, Experiment [10])

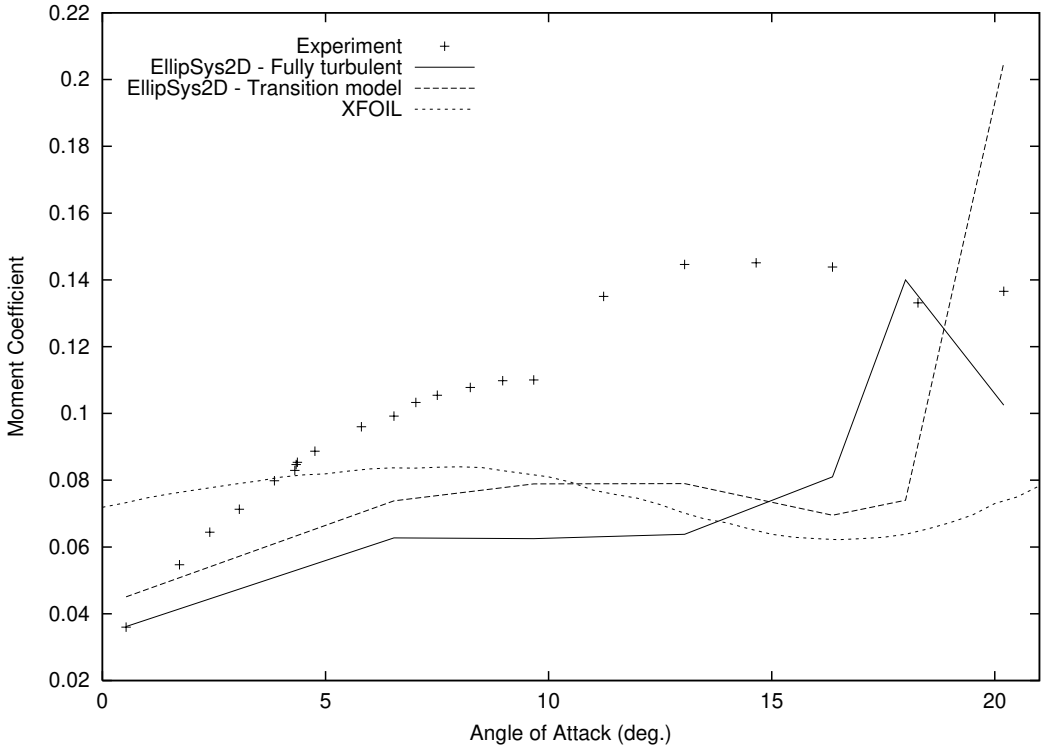

Figure 122. Pitching Moment Coefficient Curve (FFA-W3-301, Experiment [10])

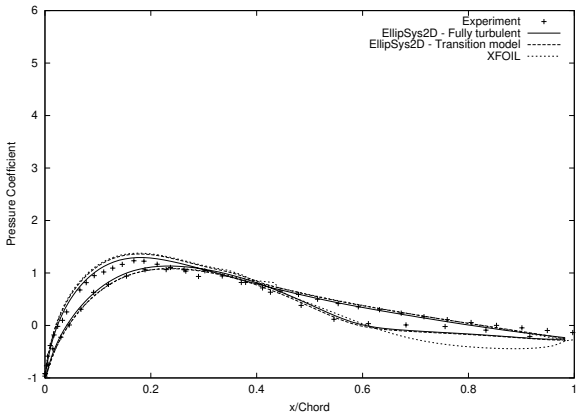

(a) $\alpha = 0.532^o$

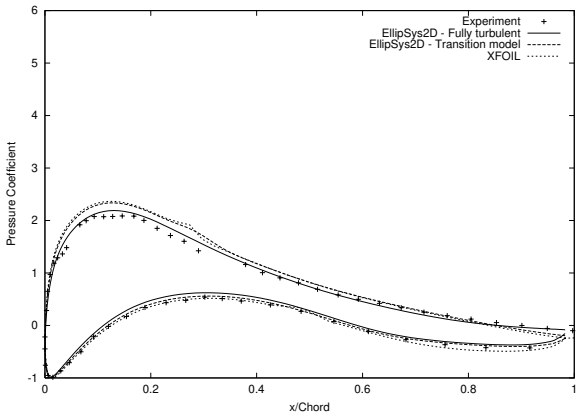

(b) $\alpha = 6.533^o$

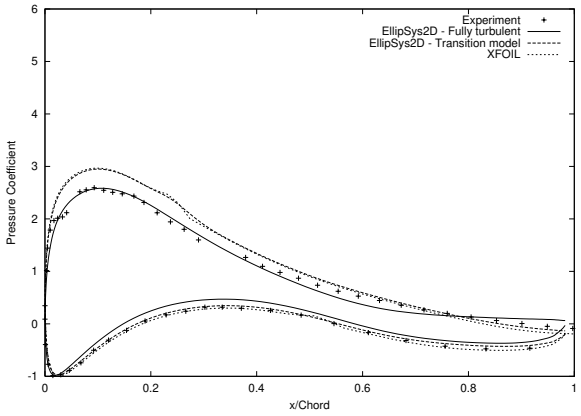

(c) $\alpha = 9.666^o$

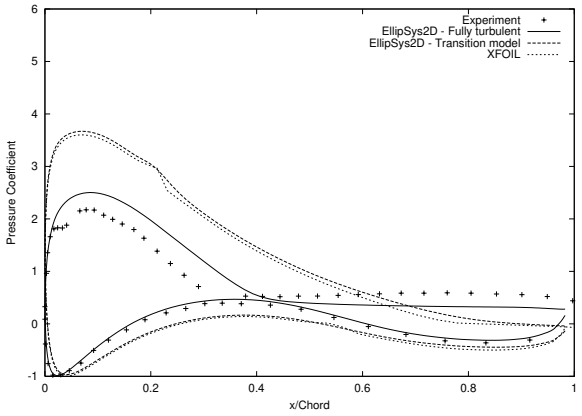

(d) $\alpha = 13.048^o$

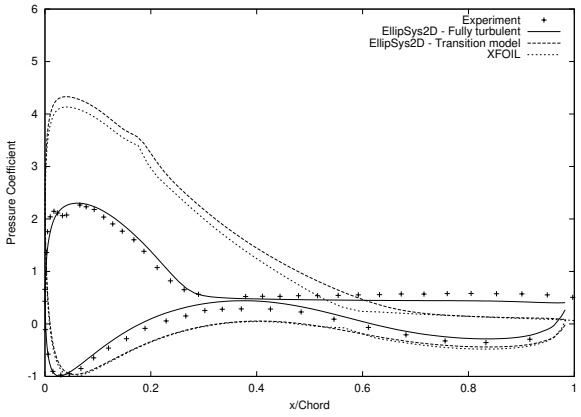

(e) $\alpha = 16.361^o$

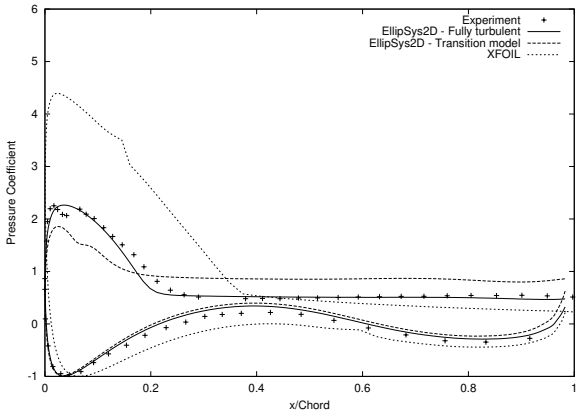

(f) $\alpha = 20.2^o$

Figure 123. Pressure Coefficient Distributions (FFA-W3-301, Experiment [10])

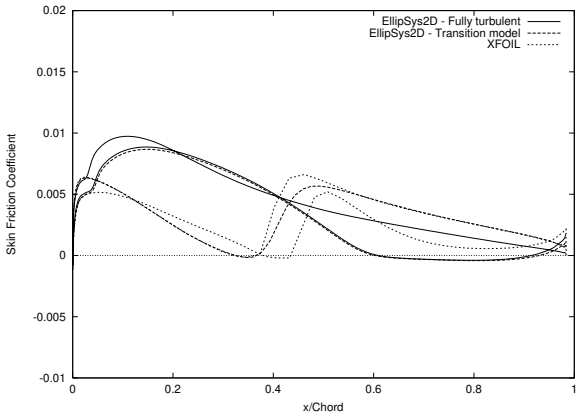

(a) $\alpha = 0.532^o$

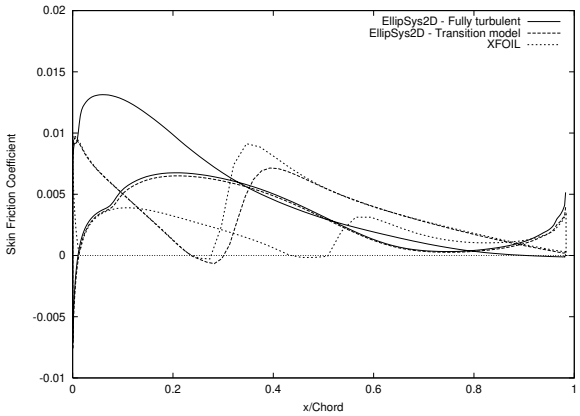

(b) $\alpha = 6.533^o$

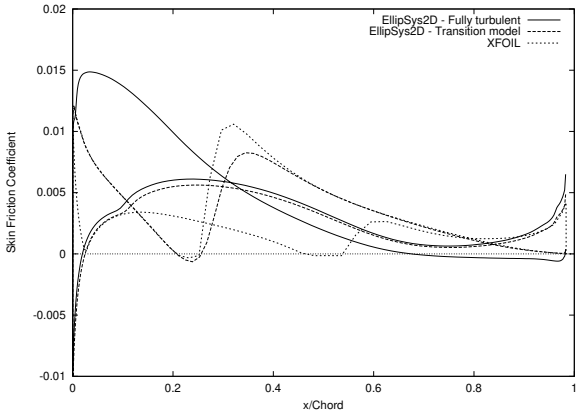

(c) $\alpha = 0.666^o$

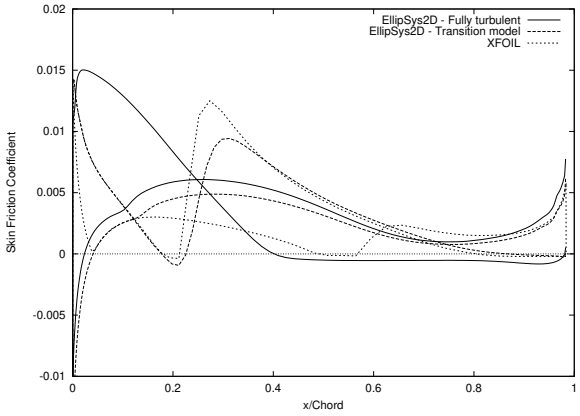

(d) $\alpha = 13.048^o$

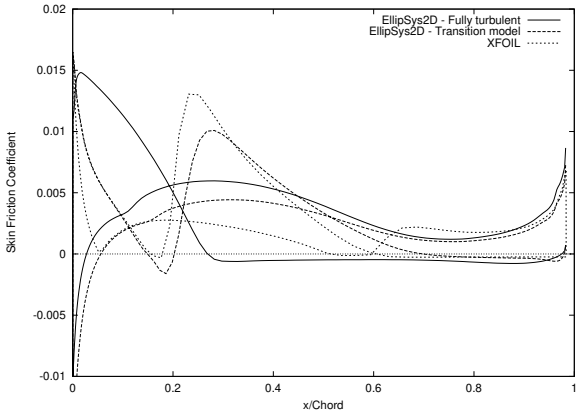

(e) $\alpha = 16.361^o$

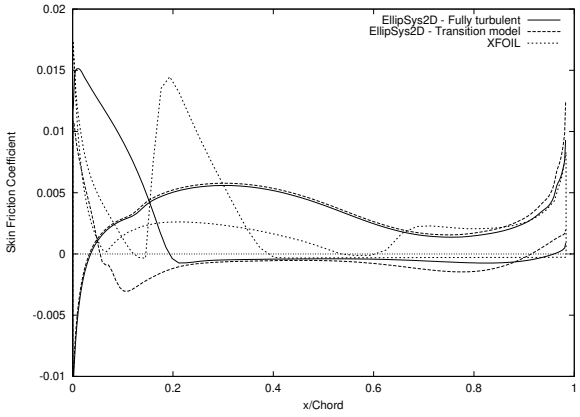

(f) $\alpha = 20.2^o$

Figure 124. Skin Friction Coefficient Distributions (FFA-W3-301)

8 S809 and S814 Airfoils

The S809 airfoil is a 21% thick wind turbine airfoil that has been designed at National Renewable Energy Laboratory (NREL), Colorado, USA, by Somers [20]. The two primary design criteria were restrained maximum lift, insensitive to surface roughness, and low profile drag.

The S814 airfoil is a 24% thick wind turbine airfoil that has been designed at National Renewable Energy Laboratory (NREL), Colorado, USA, by Somers [21]. The first objective was to achieve a maximum lift coefficient of at least 1.30 for a Reynolds number of 1.5×10^6. The second objective was to obtain low profile drag coefficients over the range of lift coefficients from 0.6 to 1.2 for the same Reynolds number.

The experiments were carried out at the low-turbulence wind tunnel at Delft University of Technology, The Netherlands. The Reynolds number of the experiments was $Re = 1.0 \times 10^6$, and the experimental results exposed herein were obtained with free transition. Numerical results were obtained with stationary computations.

8.1 Method

The C-mesh used for the computations had 384 cells in the direction along the airfoil, 256 of them being on the airfoil, and 64 cells in the direction away from the airfoil. The non-dimensional height of the cell at the airfoil was 1×10^{-5}.

The computations were performed with the SUDS-scheme for the convective terms, the $k-\omega$ SST turbulence model by Menter [16] for the turbulent viscosity, and the transition model by Michel [17], together with the empirical function given by Chen and Thyson [8] for modelling the turbulence intermittency.

8.2 Results

There was a good agreement between experimental data and computational results in the linear region. A higher maximum lift was computed in the stalled region.

S809

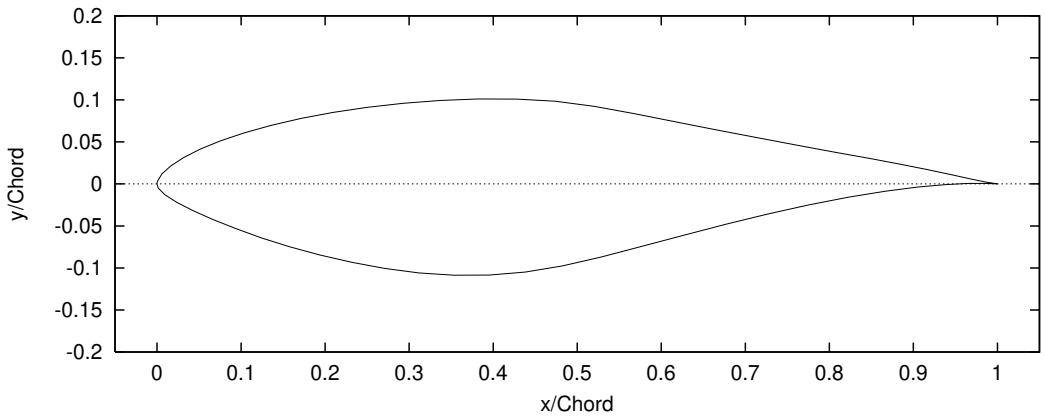

Figure 125. S809 Airfoil

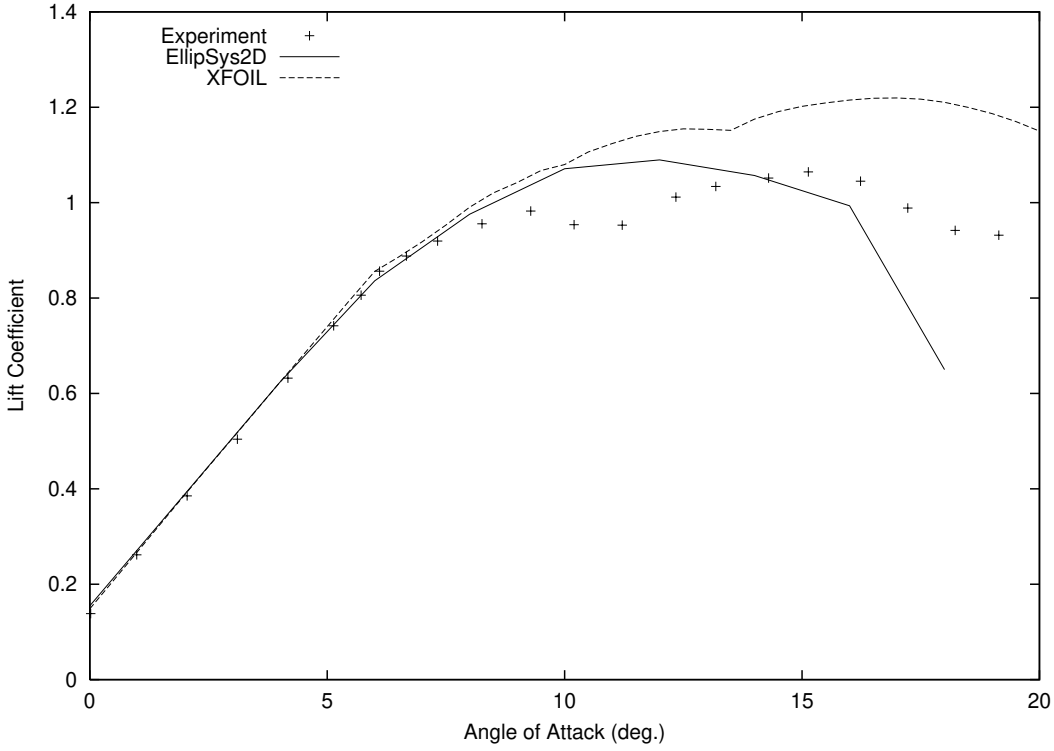

Figure 126. Lift Coefficient Curve (S809, Experiment Delft University of Technology)

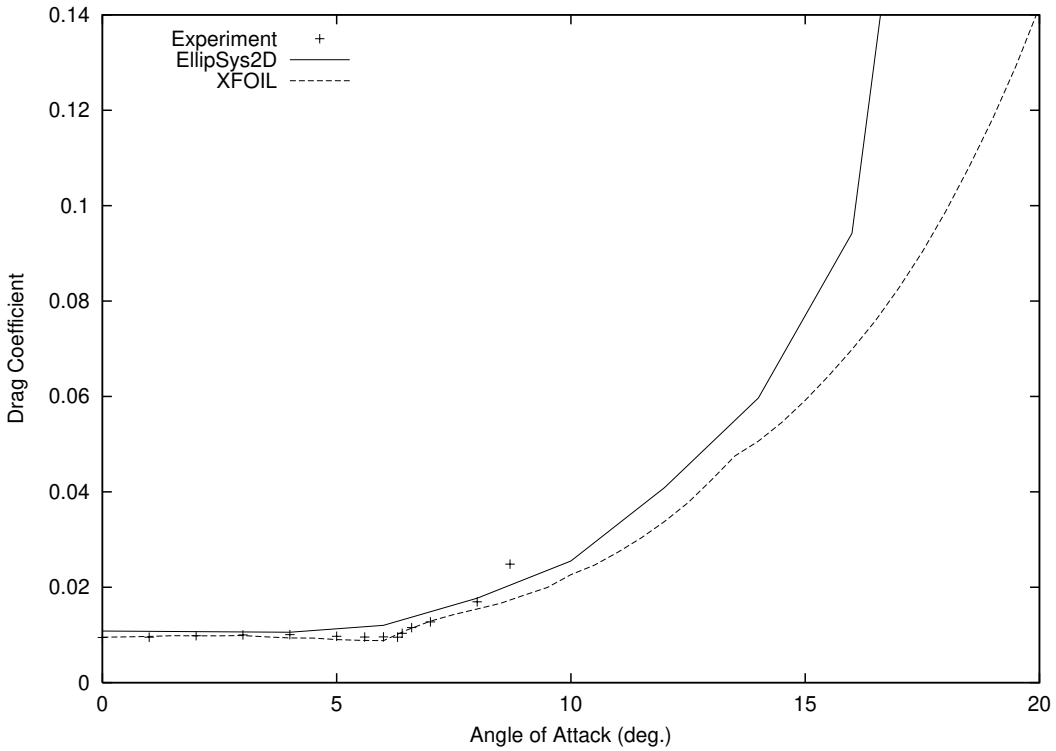

Figure 127. Drag Coefficient Curve (S809, Experiment Delft University of Technology)

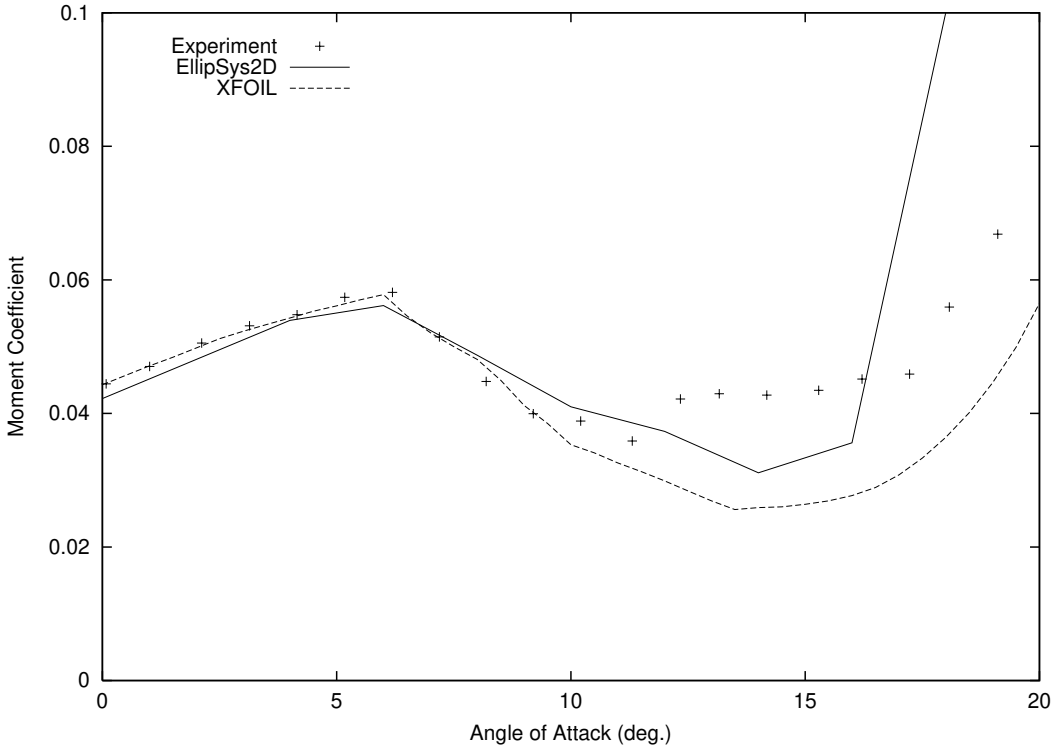

Figure 128. Pitching Moment Coefficient Curve (S809, Experiment Delft University of Technology)

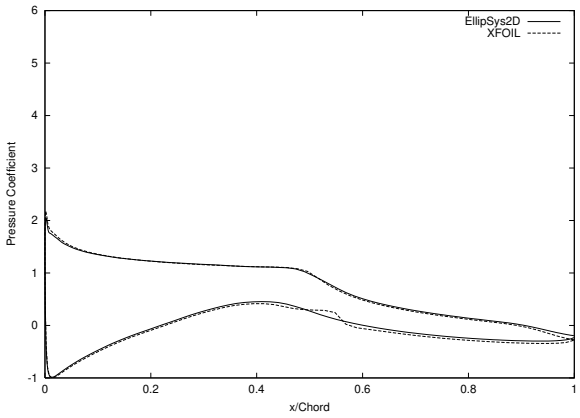

(a) $\alpha = 6.0^o$

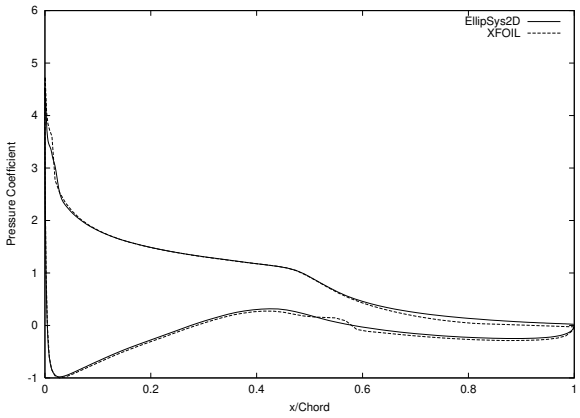

(b) $\alpha = 10.0^o$

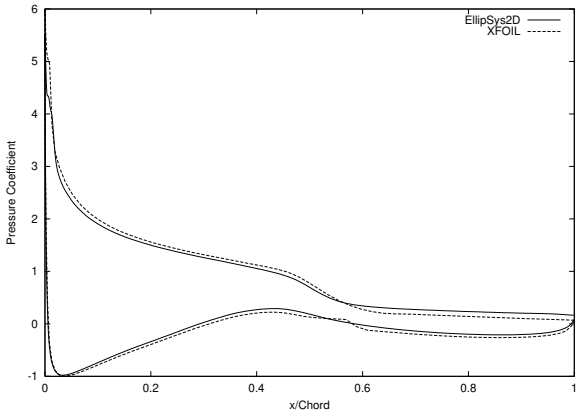

(c) $\alpha = 12.0^o$

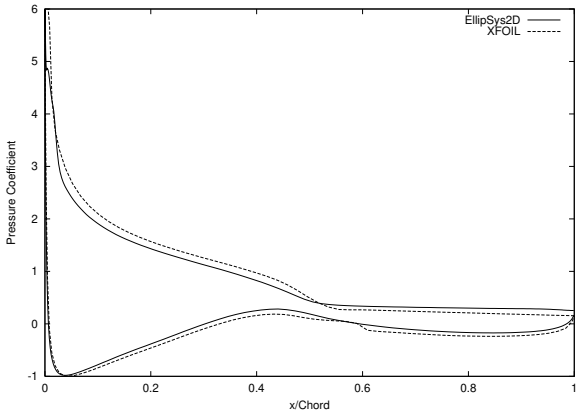

(d) $\alpha = 14.0^o$

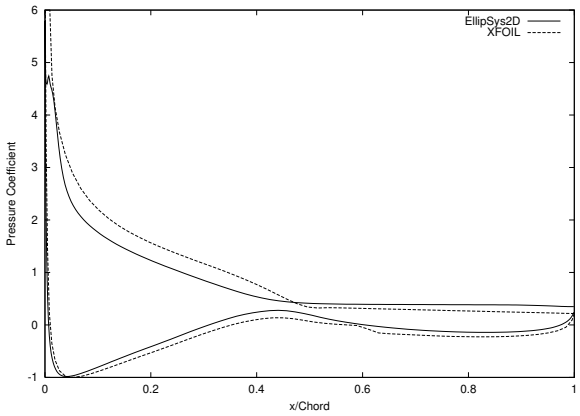

(e) $\alpha = 16.0^o$

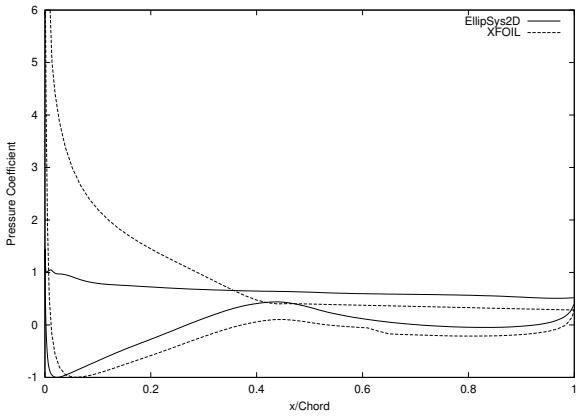

(f) $\alpha = 18.0^o$

Figure 129. Pressure Coefficient Distributions (S809)

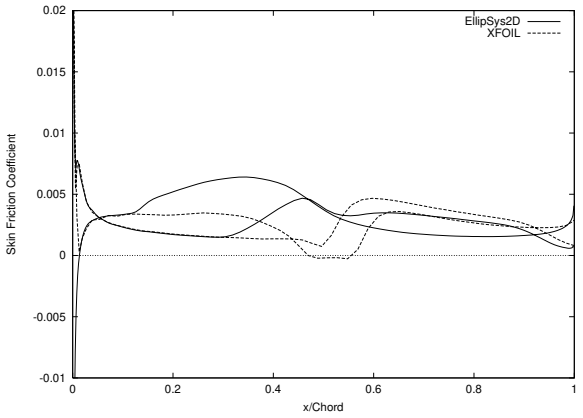

(a) $\alpha = 6.0^o$

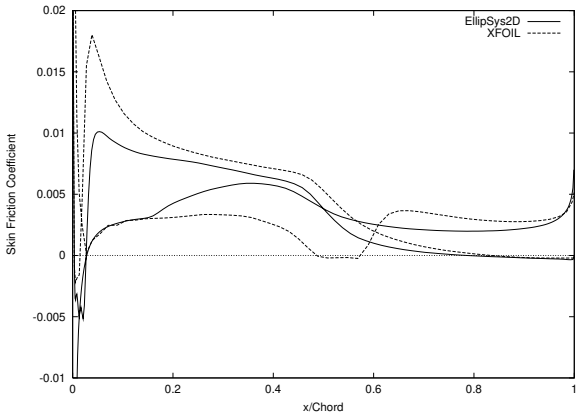

(b) $\alpha = 10.0^o$

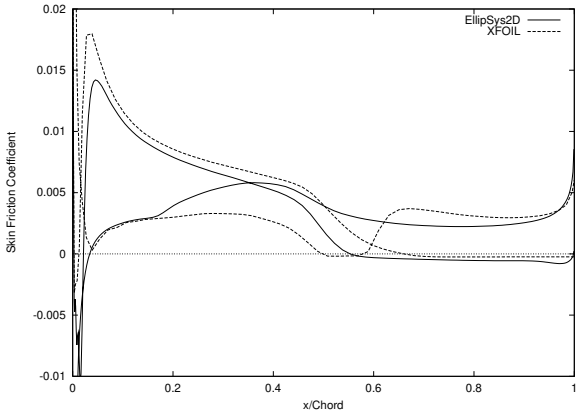

(c) $\alpha = 12.0^o$

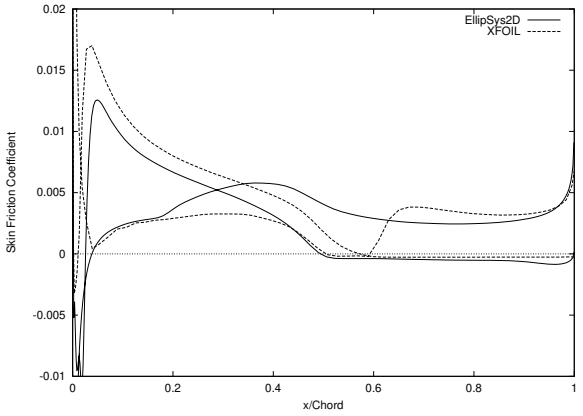

(d) $\alpha = 14.0^o$

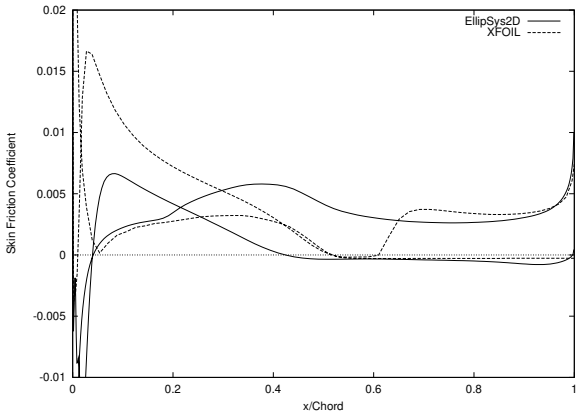

(e) $\alpha = 16.0^o$

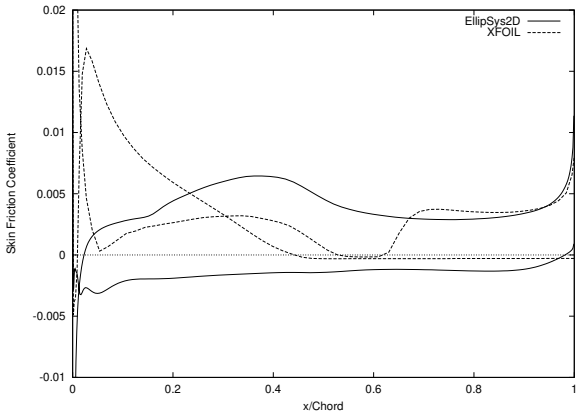

(f) $\alpha = 18.0^o$

Figure 130. Skin Friction Coefficient Distributions (S809)

S814

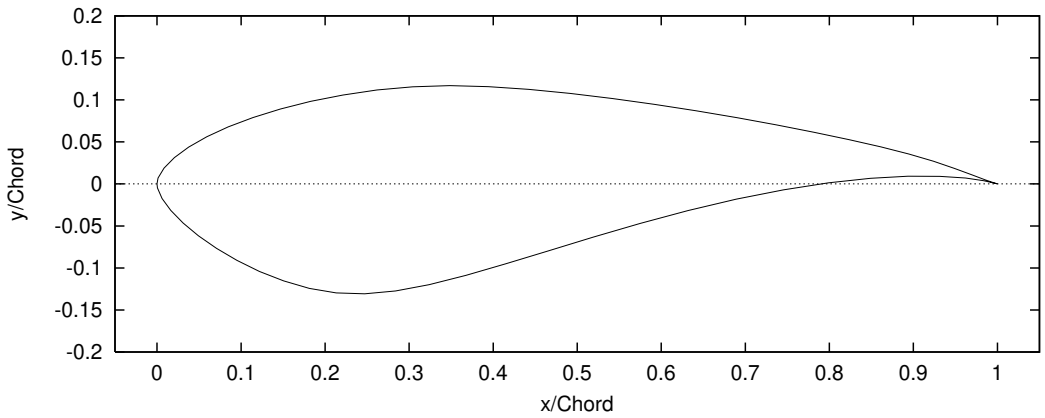

Figure 131. S814 Airfoil

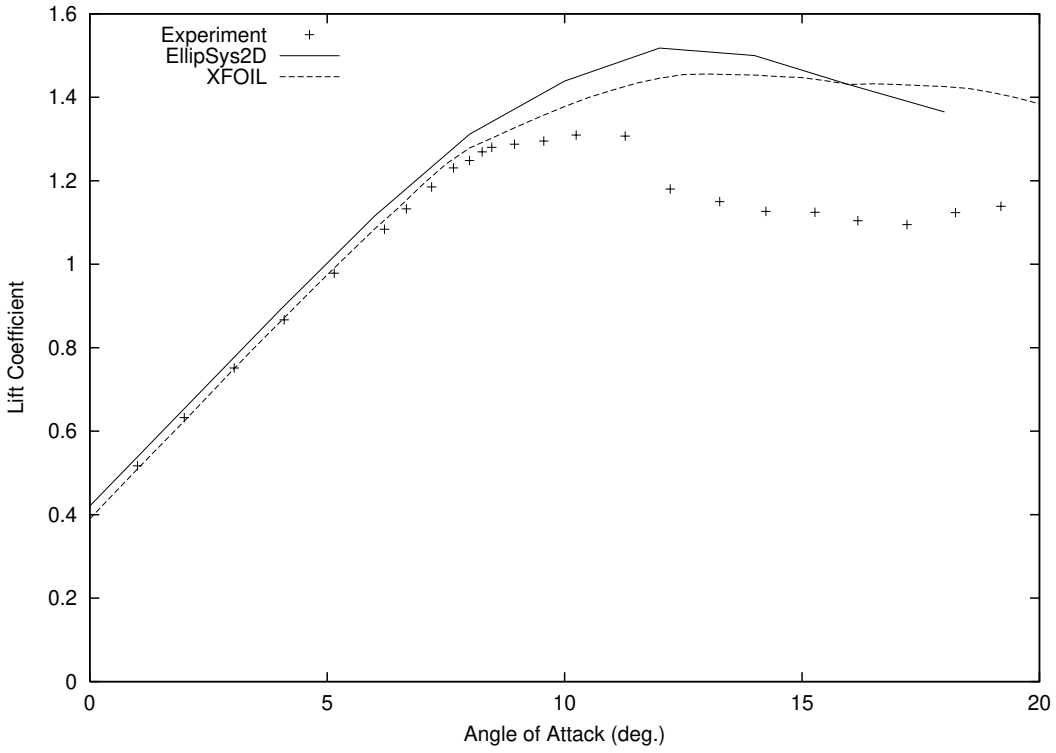

Figure 132. Lift Coefficient Curve (S814, Experiment Delft University of Technology)

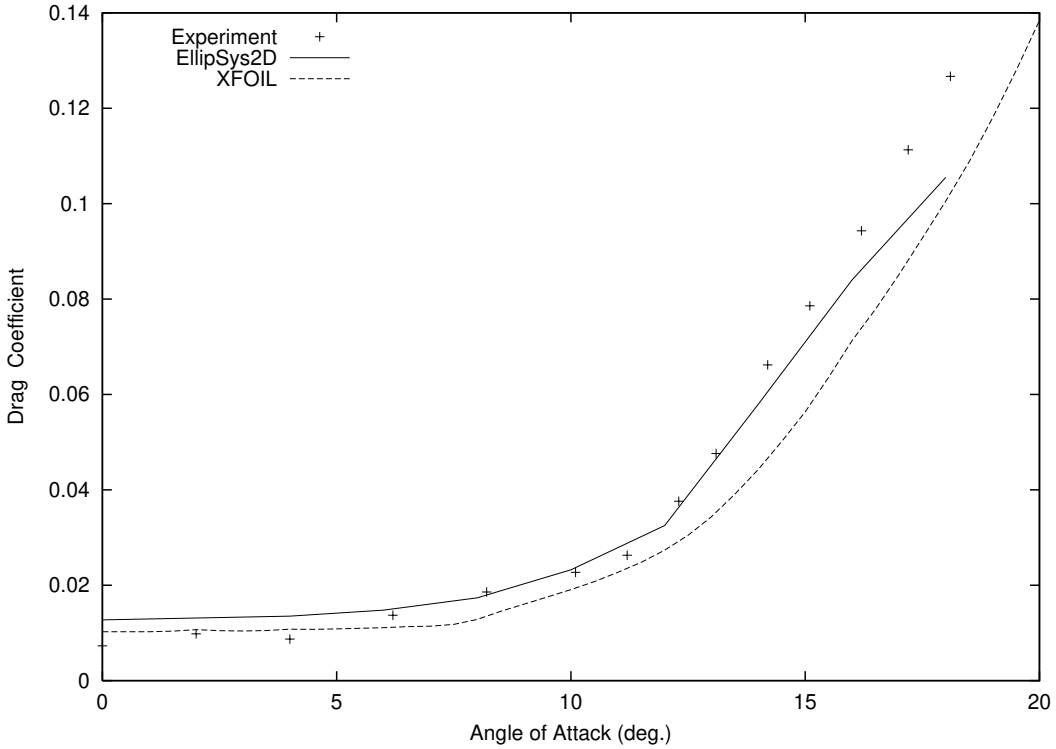

Figure 133. Drag Coefficient Curve (S814, Experiment Delft University of Technology)

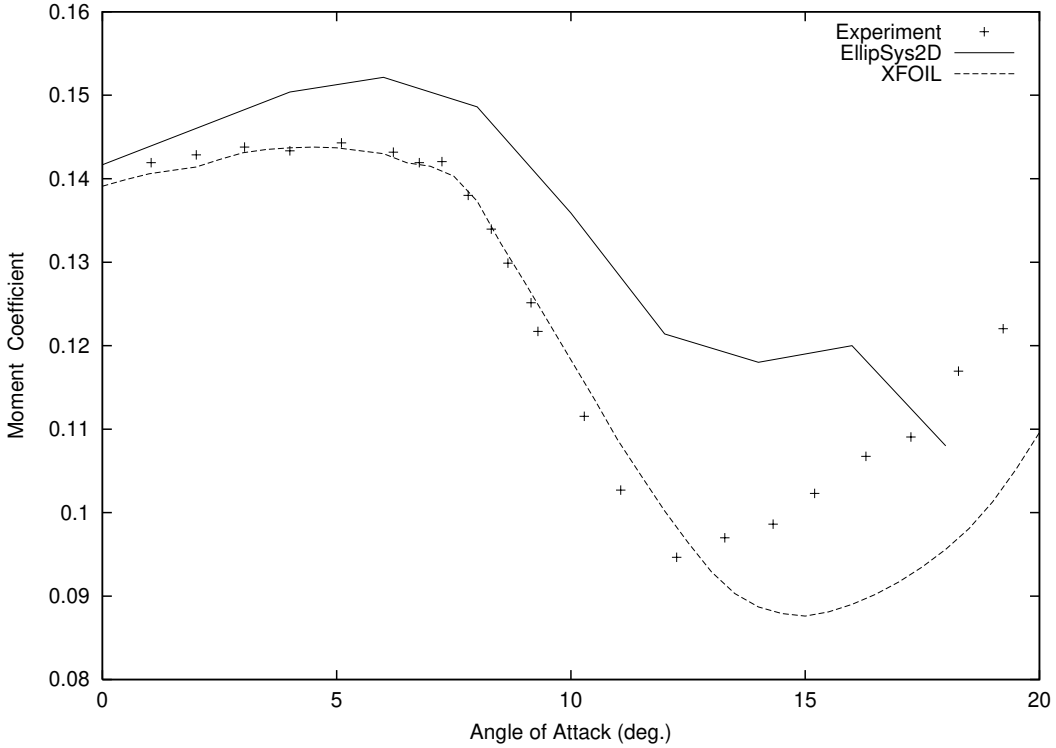

Figure 134. Pitching Moment Coefficient Curve (S814, Experiment Delft University of Technology)

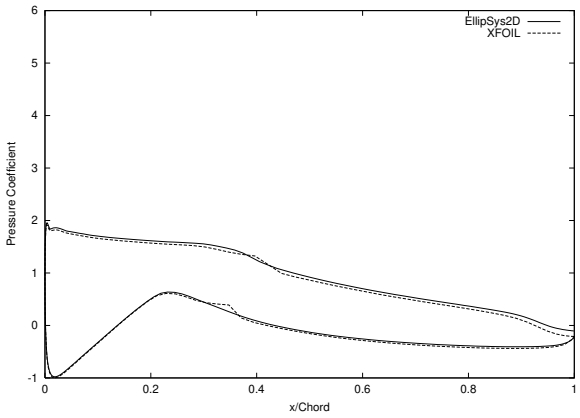

(a) $\alpha = 6.0^o$

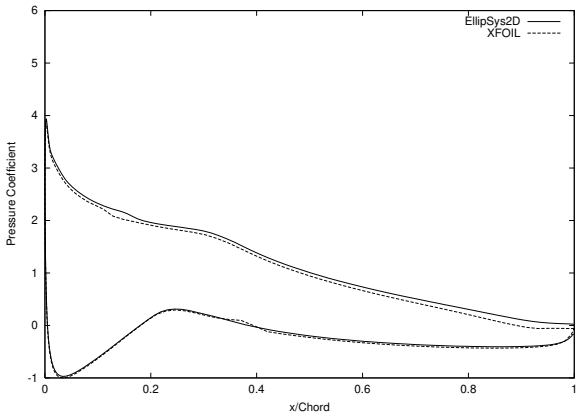

(b) $\alpha = 10.0^o$

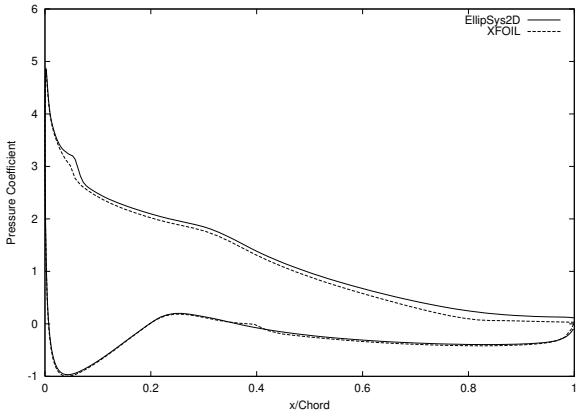

(c) $\alpha = 12.0^o$

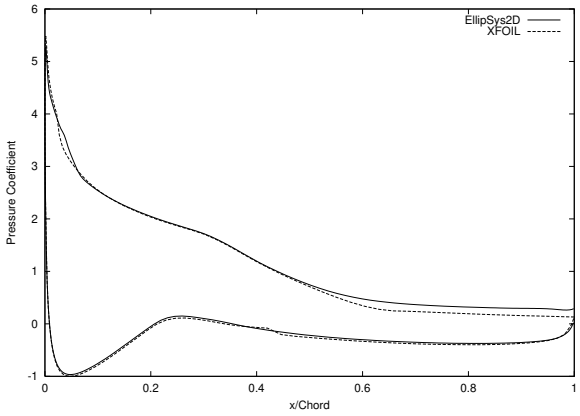

(d) $\alpha = 14.0^o$

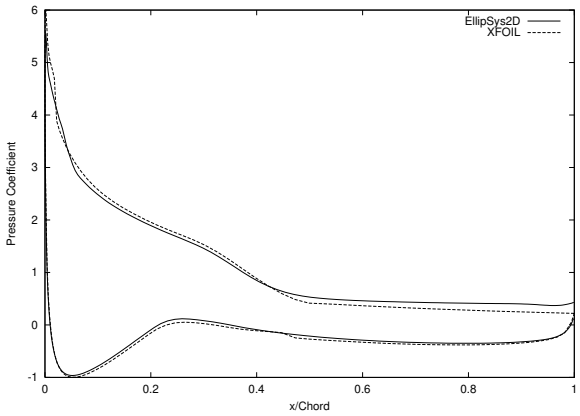

(e) $\alpha = 16.0^o$

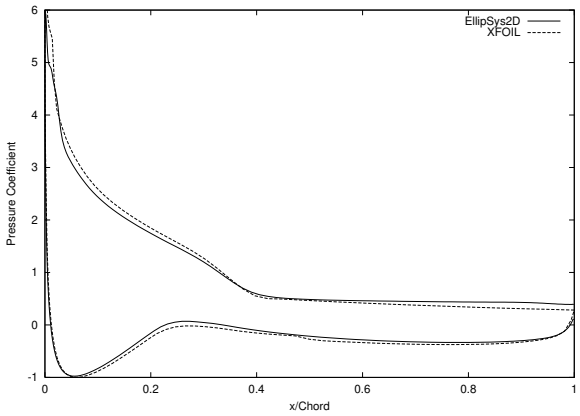

(f) $\alpha = 18.0^o$

Figure 135. Pressure Coefficient Distributions (S814)

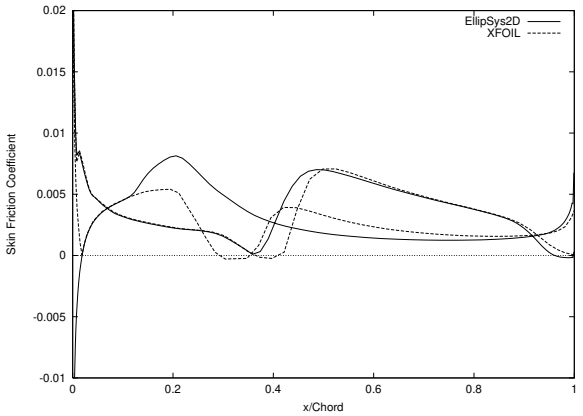

(a) $\alpha = 6.0^o$

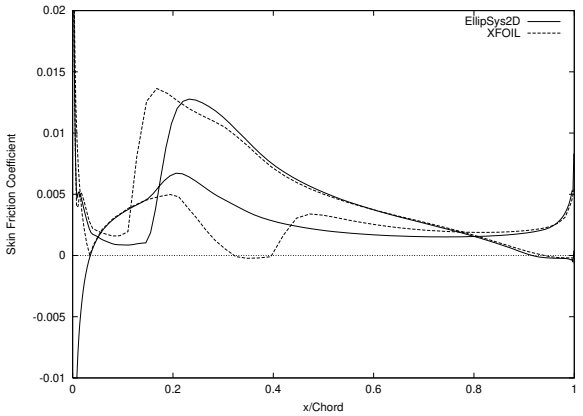

(b) $\alpha = 10.0^o$

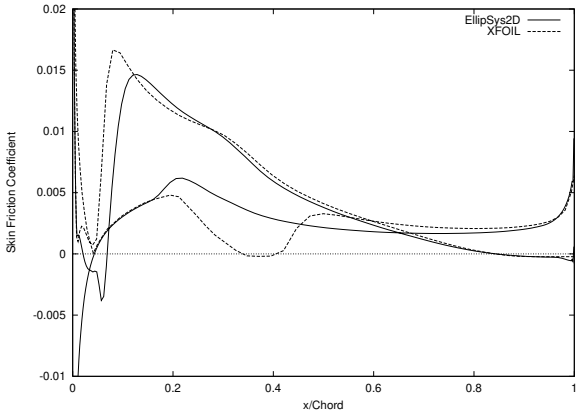

(c) $\alpha = 12.0^o$

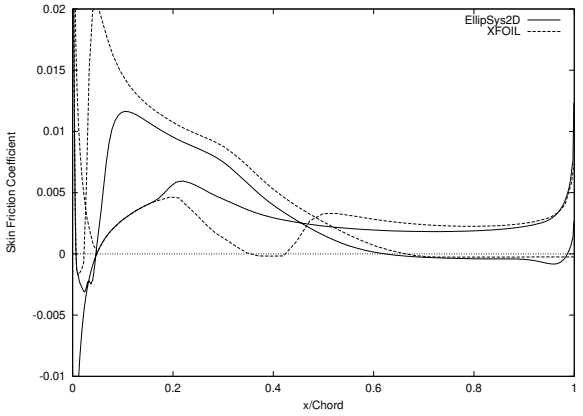

(d) $\alpha = 14.0^o$

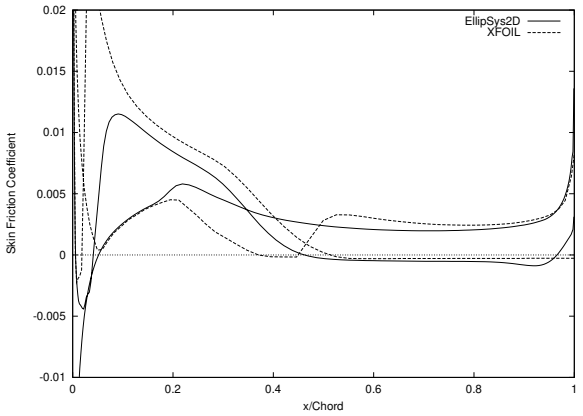

(e) $\alpha = 16.0^o$

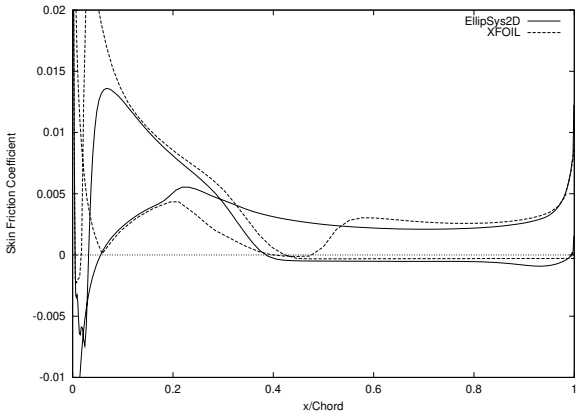

(f) $\alpha = 18.0^o$

Figure 136. Skin Friction Coefficient Distributions (S814)

9 FX66-S196-V1 Airfoil

The FX66-S196-V1 airfoil is a 19% thick airfoil designed by Althaus and Wortmann [2]. It is a typical laminar airfoil where transitional effects are large since laminar flow is present over the majority of the airfoil surface. The Reynolds number of the experiment was 1.5×10^6.

The experiment was carried out in the Laminar Wind Tunnel at the Institut for Aerodynamics and Gasdynamics in Stuttgart [2].

9.1 Method

The C-mesh used for the computation had 384 cells in the direction along the airfoil, 256 of them being on the airfoil, and 64 cells in the direction away from the airfoil. The non-dimensional height of the cell at the airfoil was 1×10^{-5}.

The computations were performed with the SUDS-scheme for the convective terms, the $k-\omega$ SST turbulence model by Menter [16] for the turbulent viscosity, and the transition model by Michel [17], together with the empirical function given by Chen and Thyson [8] for modelling the turbulence intermittency. Numerical results were obtained with stationary computations.

9.2 Results

There was a very good agreement between the experiment and the computations concerning the lift. The drag was slightly overestimated by the computations.

FX66-S196-V1

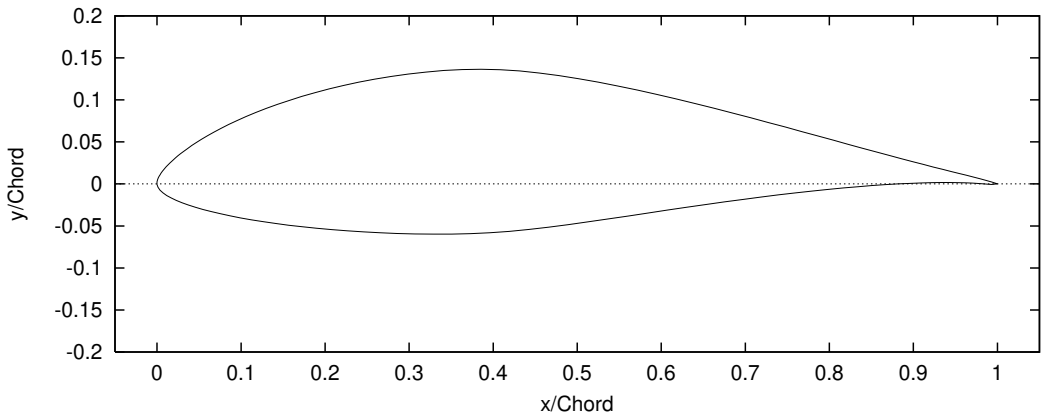

Figure 137. FX66-S196-V1 Airfoil

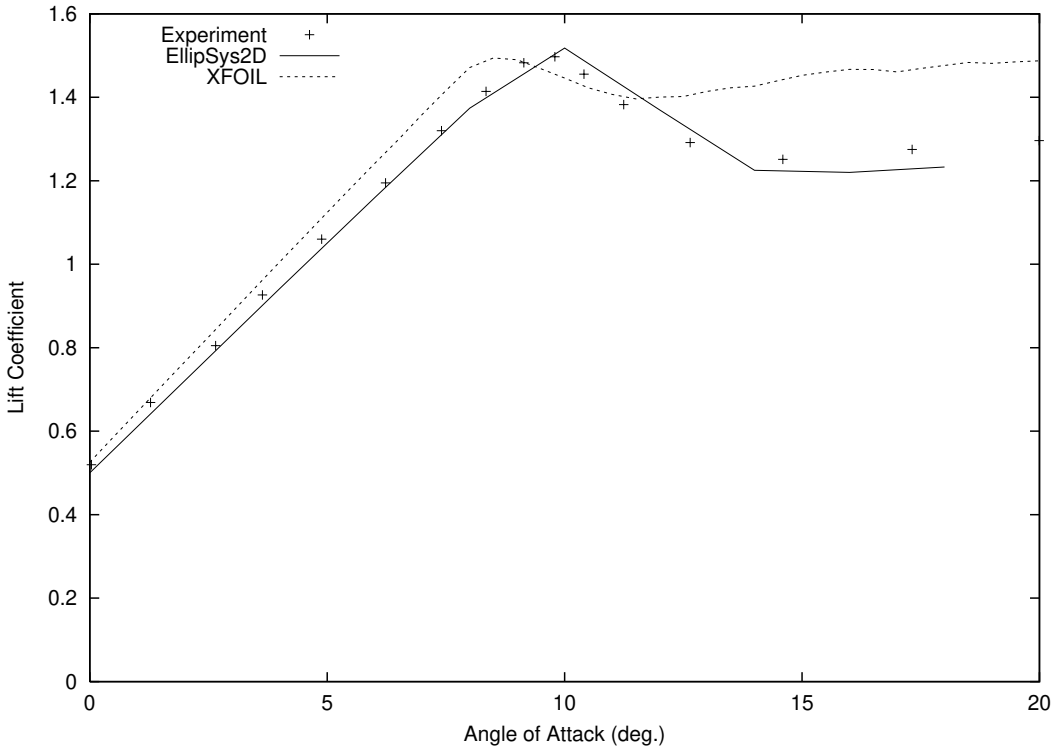

Figure 138. Lift Coefficient Curve (FX66-S196-V1, Experiment [2])

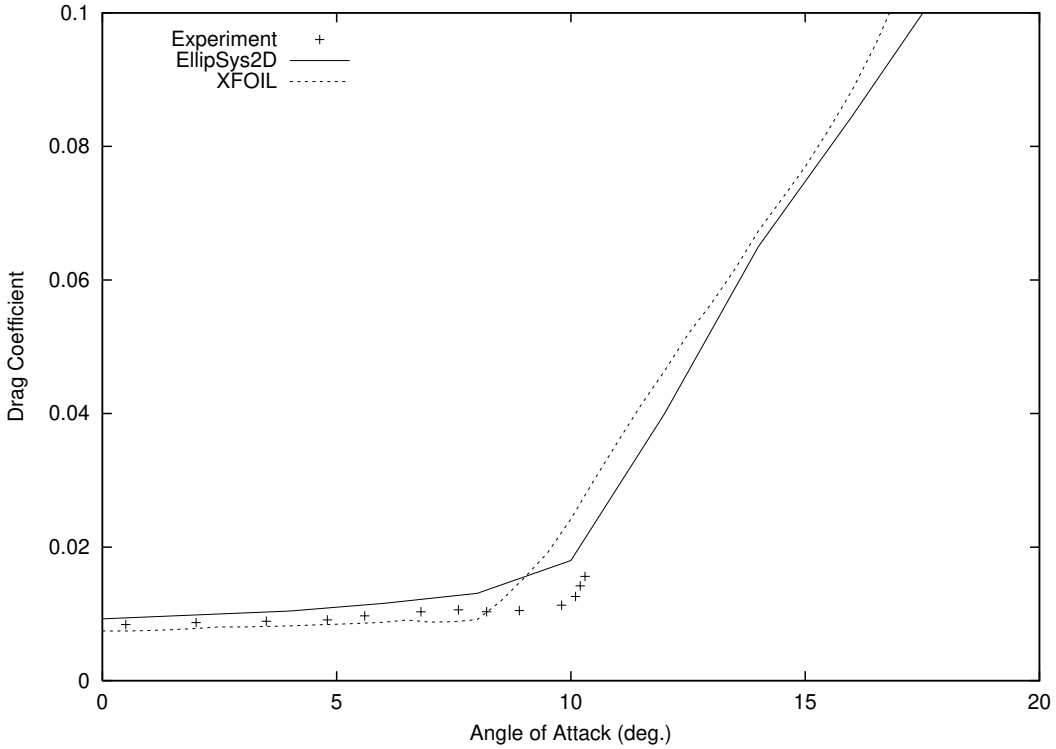

Figure 139. Drag Coefficient Curve (FX66-S196-V1, Experiment [2])

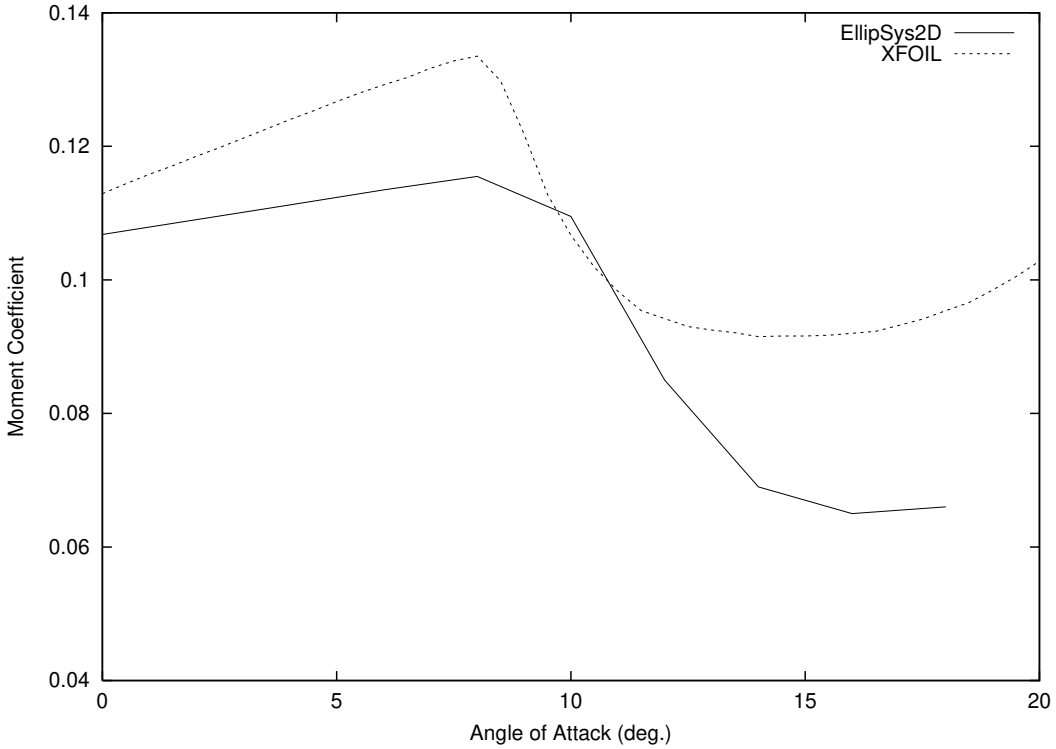

Figure 140. Pitching Moment Coefficient Curve (FX66-S196-V1)

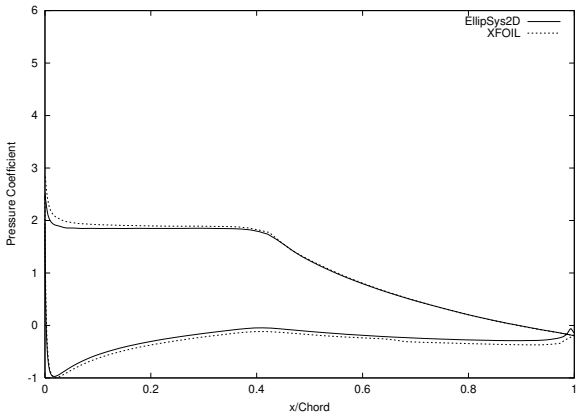

(a) $\alpha = 8.0^o$

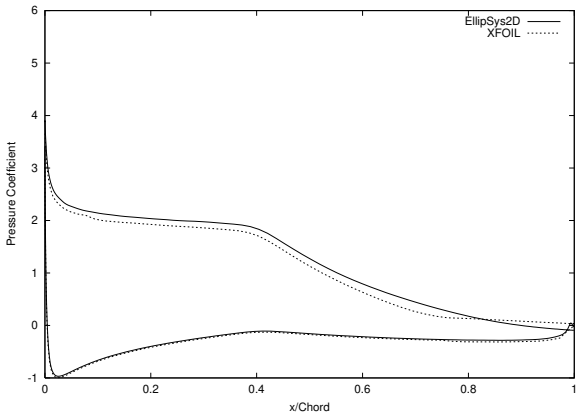

(b) $\alpha = 10.0^o$

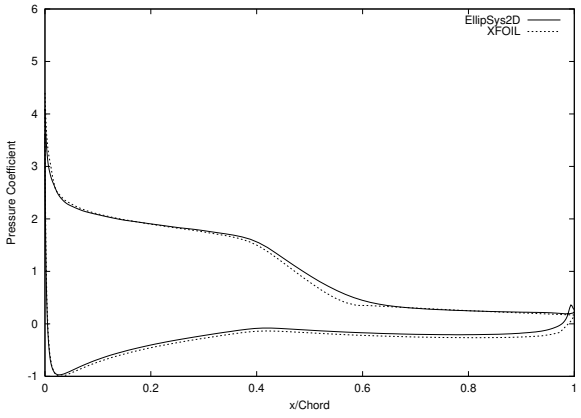

(c) $\alpha = 12.0^o$

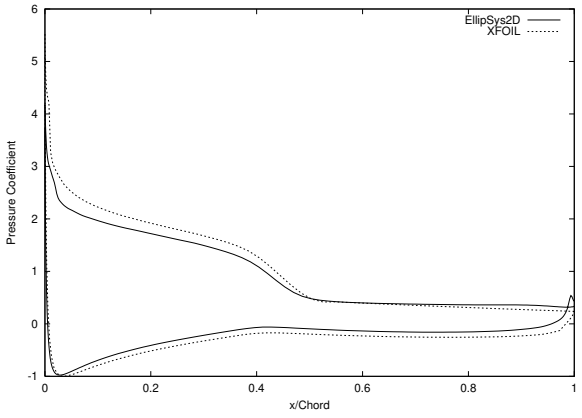

(d) $\alpha = 14.0^o$

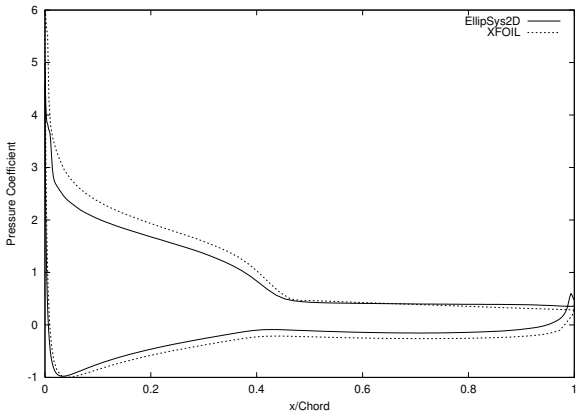

(e) $\alpha = 16.0^o$

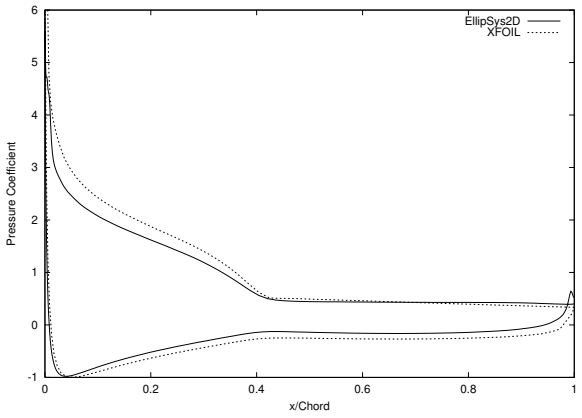

(f) $\alpha = 18.0^o$

Figure 141. Pressure Coefficient Distributions (FX66-S196-V1)

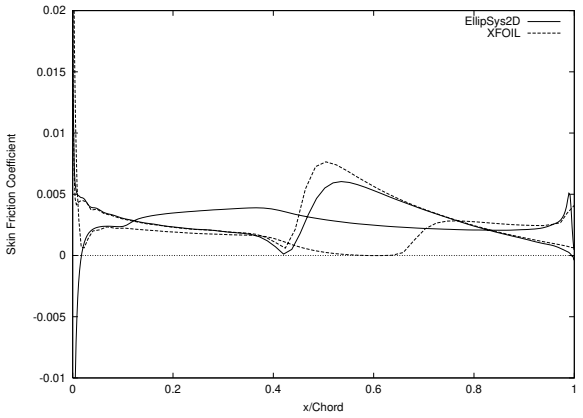

(a) $\alpha = 8.0^o$

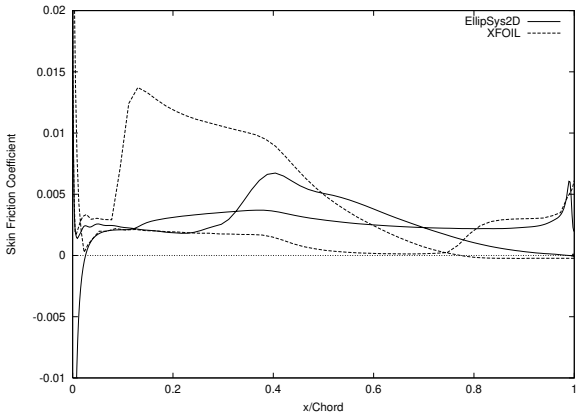

(b) $\alpha = 10.0^o$

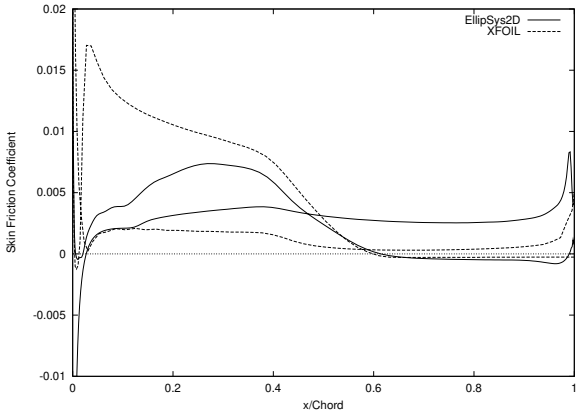

(c) $\alpha = 12.0^o$

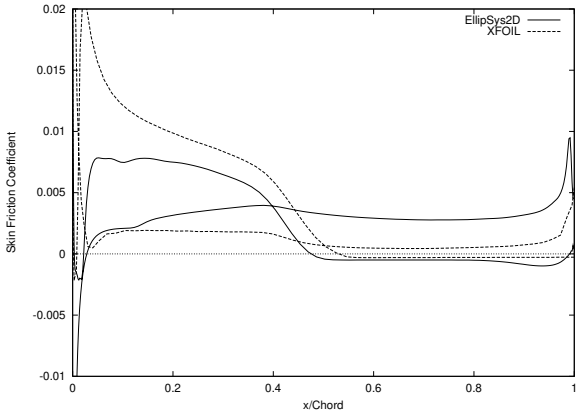

(d) $\alpha = 14.0^o$

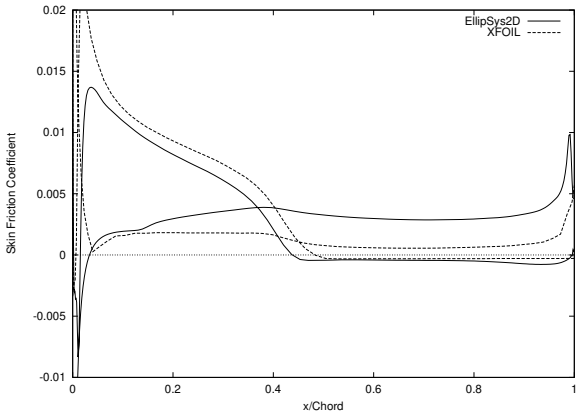

(e) $\alpha = 16.0^o$

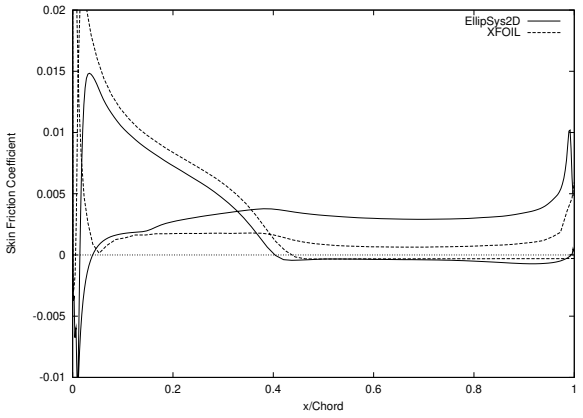

(f) $\alpha = 18.0^o$

Figure 142. Skin Friction Coefficient Distributions (FX66-S196-V1)

10 DU 91-W2-250 and DU 93-W-210 Airfoils

The 25% thick wind turbine airfoil DU 91-W2-250 was designed by Timmer [24]. Its design goals for the laminar case were a peak lift coefficient of about 1.5, relatively smooth stall and insensivity to roughness.

The measurements were performed in the low-speed low-turbulence wind tunnel of the Faculty of Aerospace Engineering of Delft University [25]. The results presented herein were obtained at a Reynolds number of 1.0×10^6 with a smooth airfoil surface.

The 21% thick wind turbine airfoil DU 93-W-210 was designed by Timmer and wind tunnel tested in the same low speed wind tunnel at Delft University of Technology.

10.1 Method

The C-mesh used for the computation had 384 cells in the direction along the airfoil, 256 of them being on the airfoil, and 64 cells in the direction away from the airfoil. The non-dimensional height of the cell at the airfoil was 1×10^{-5}.

The computations were performed with the SUDS-scheme for the convective terms, the $k-\omega$ SST turbulence model by Menter [16] for the turbulent viscosity, and the transition model by Michel [17], together with the empirical function given by Chen and Thyson [8] for modelling the turbulence intermittency. Numerical results were obtained with stationary computations.

10.2 Results

There was a rather good agreement between experiments and computations in the linear region, but the lift was overpredicted by the computations in deep stall.

DU 91-W2-250

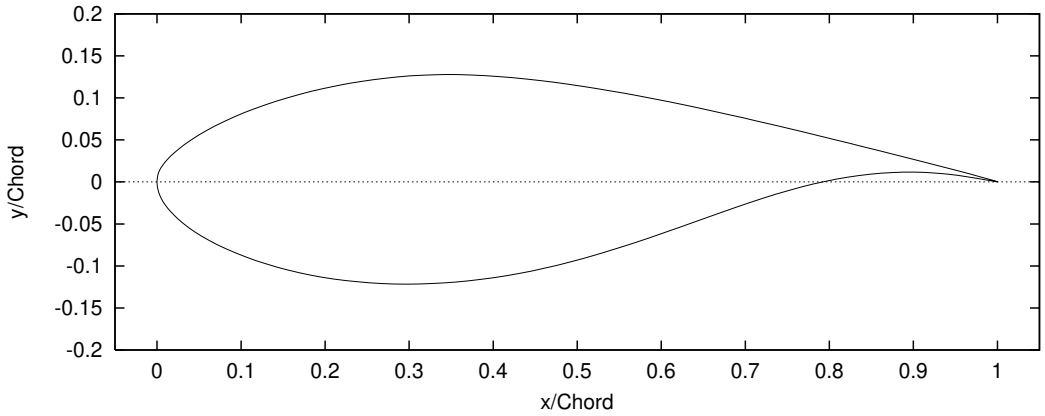

Figure 143. DU 91-W2-250 Airfoil

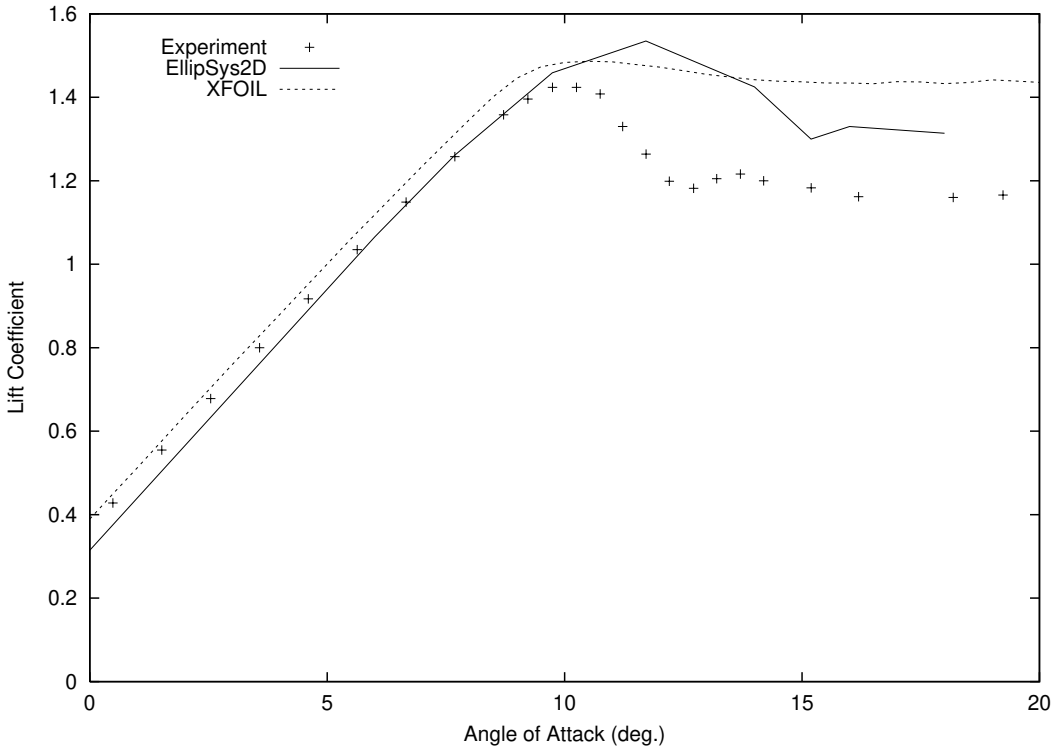

Figure 144. Lift Coefficient Curve (DU 91-W2-250, Experiment [25])

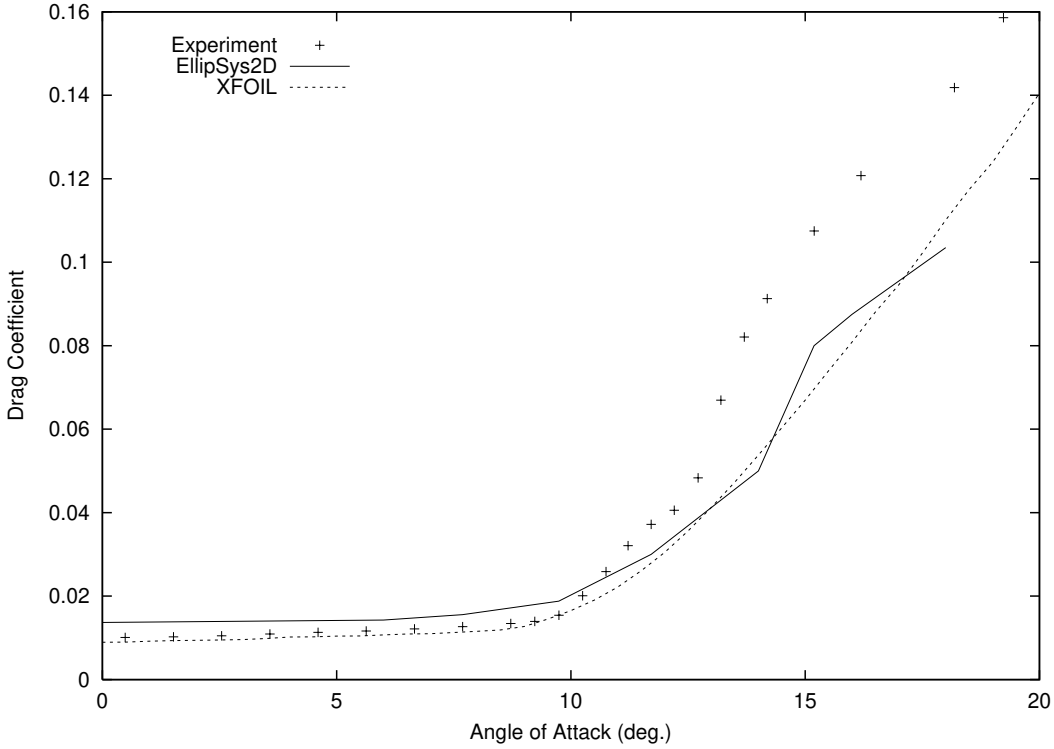

Figure 145. Drag Coefficient Curve (DU 91-W2-250, Experiment [25])

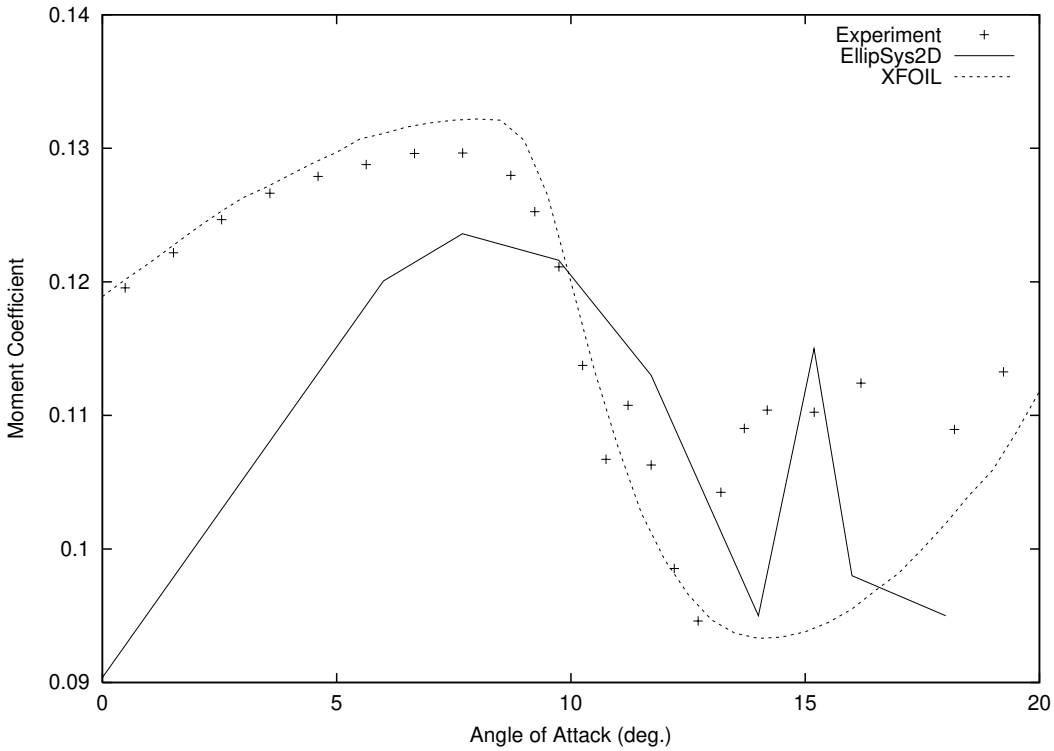

Figure 146. Pitching Moment Coefficient Curve (DU 91-W2-250, Experiment [25])

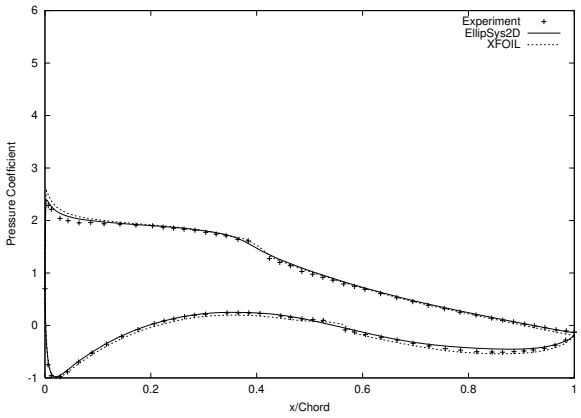

(a) $\alpha = 7.686.0^o$

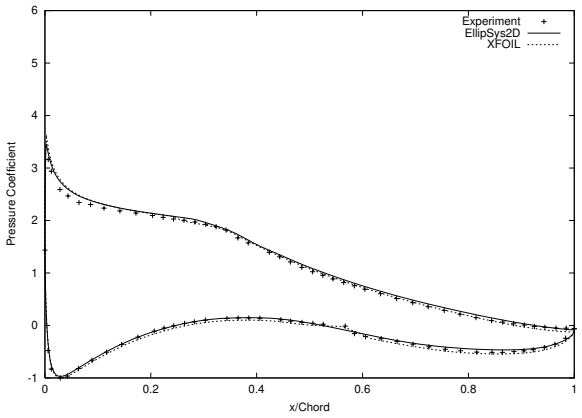

(b) $\alpha = 9.742^o$

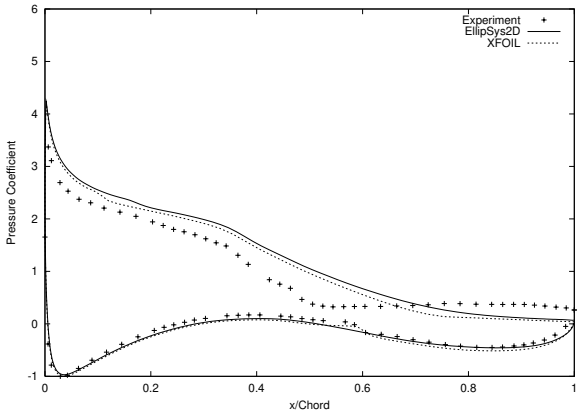

(c) $\alpha = 11.712^o$

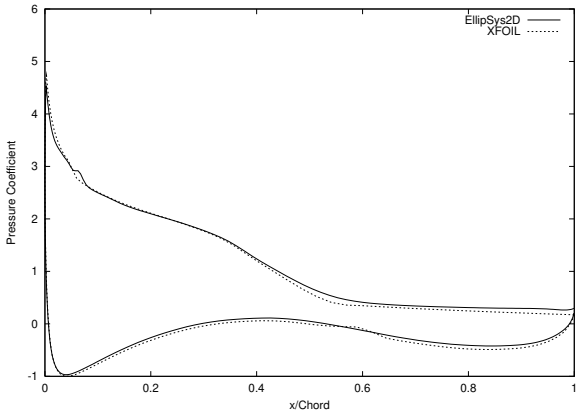

(d) $\alpha = 14.0^o$

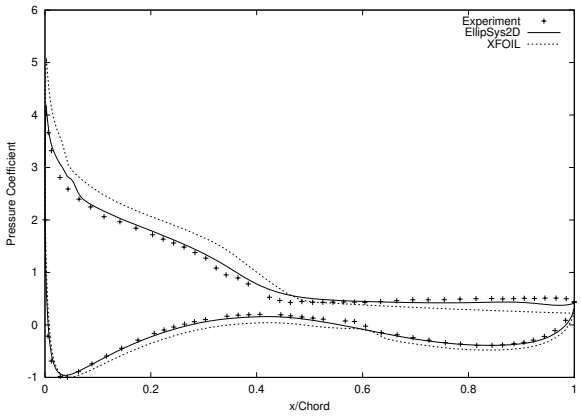

(e) $\alpha = 15.19^o$

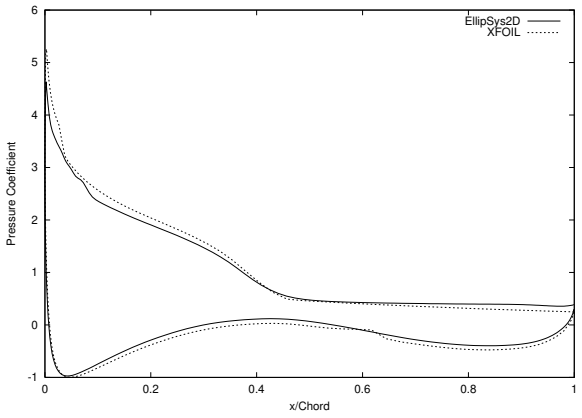

(f) $\alpha = 16.0^o$

Figure 147. Pressure Coefficient Distributions (DU 91-W-250, Experiment [25])

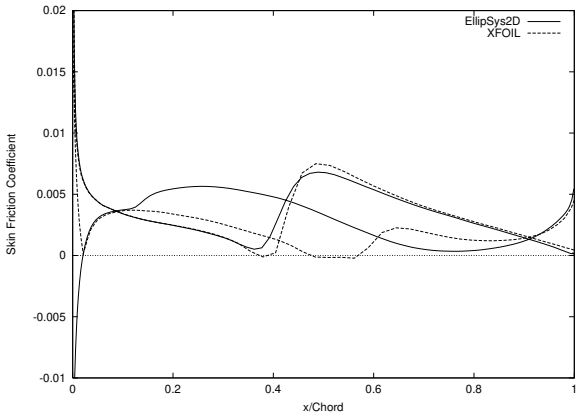

(a) $\alpha = 7.686^o$

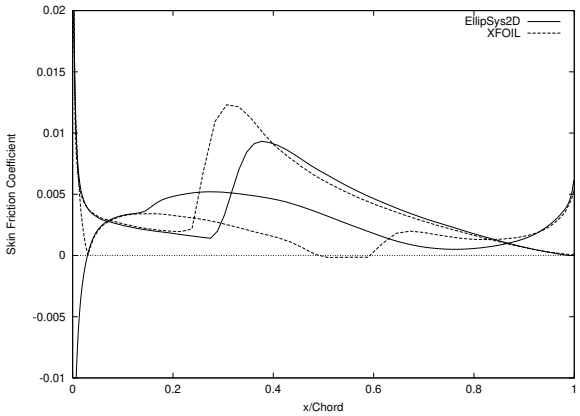

(b) $\alpha = 9.742^o$

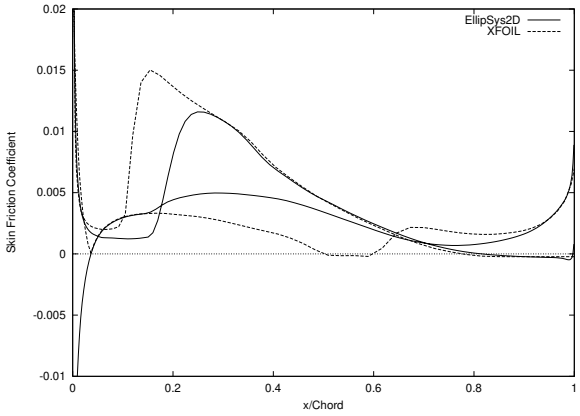

(c) $\alpha = 11.712.0^o$

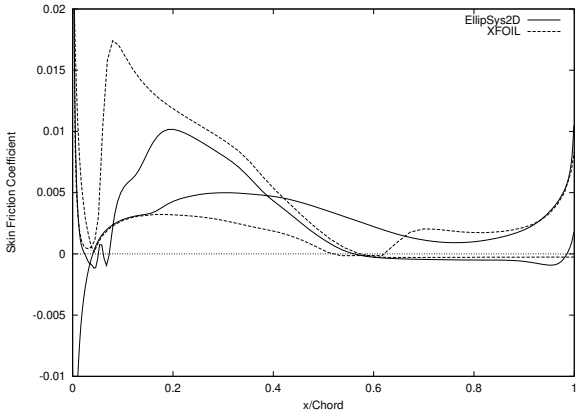

(d) $\alpha = 14.0^o$

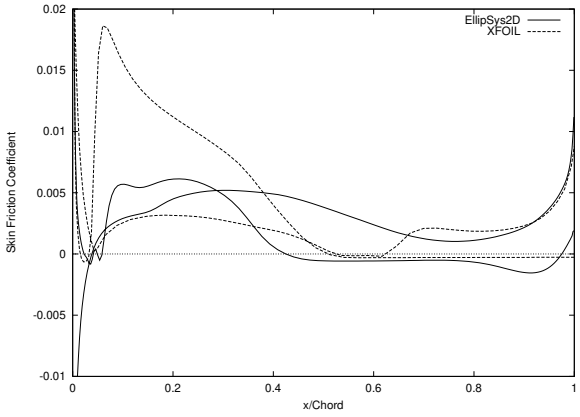

(e) $\alpha = 15.19^o$

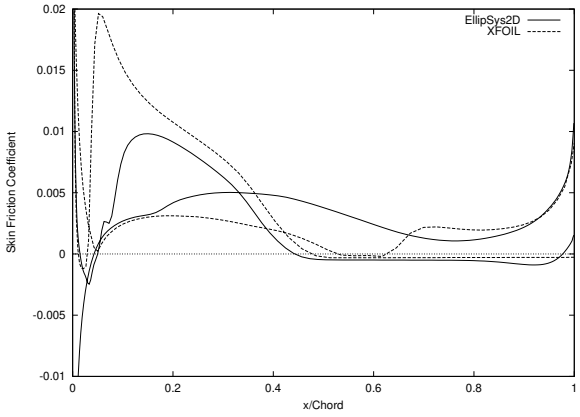

(f) $\alpha = 16.0^o$

Figure 148. Skin Friction Coefficient Distributions (DU 91-W-250)

DU 93-W-210

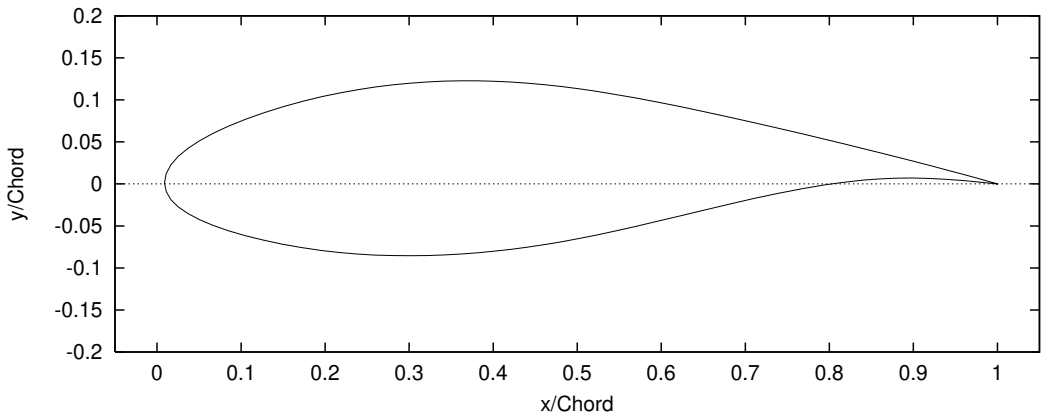

Figure 149. DU 93-W-210 Airfoil

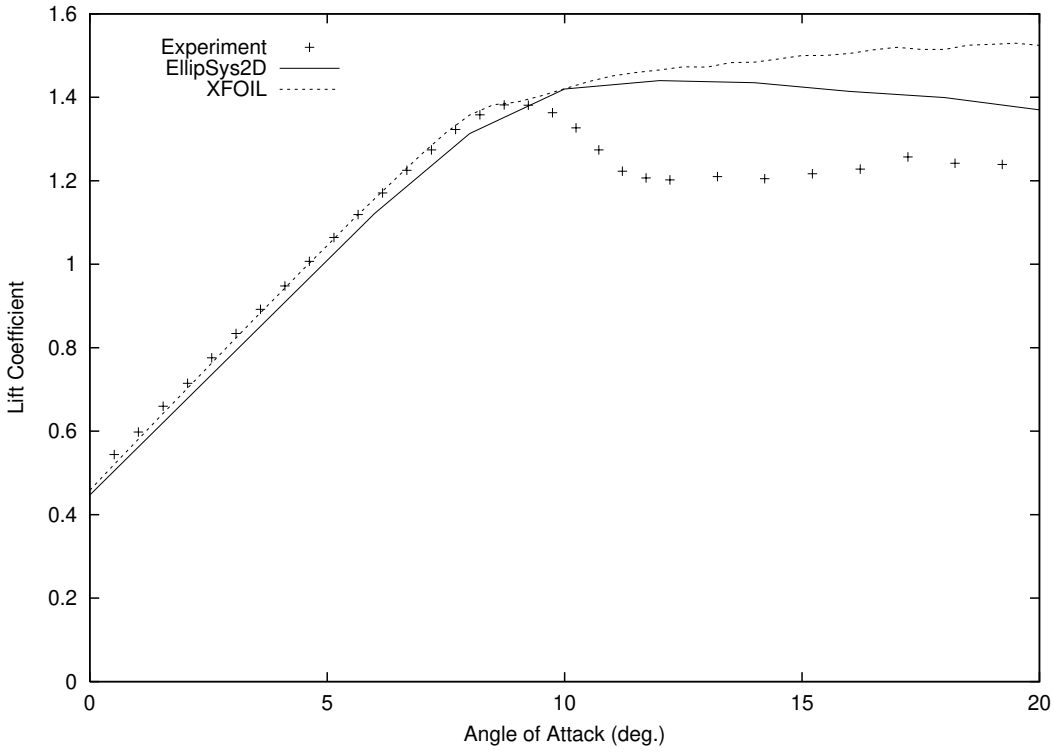

Figure 150. Lift Coefficient Curve (DU 93-W-210, Experiment Delft University of Technology)

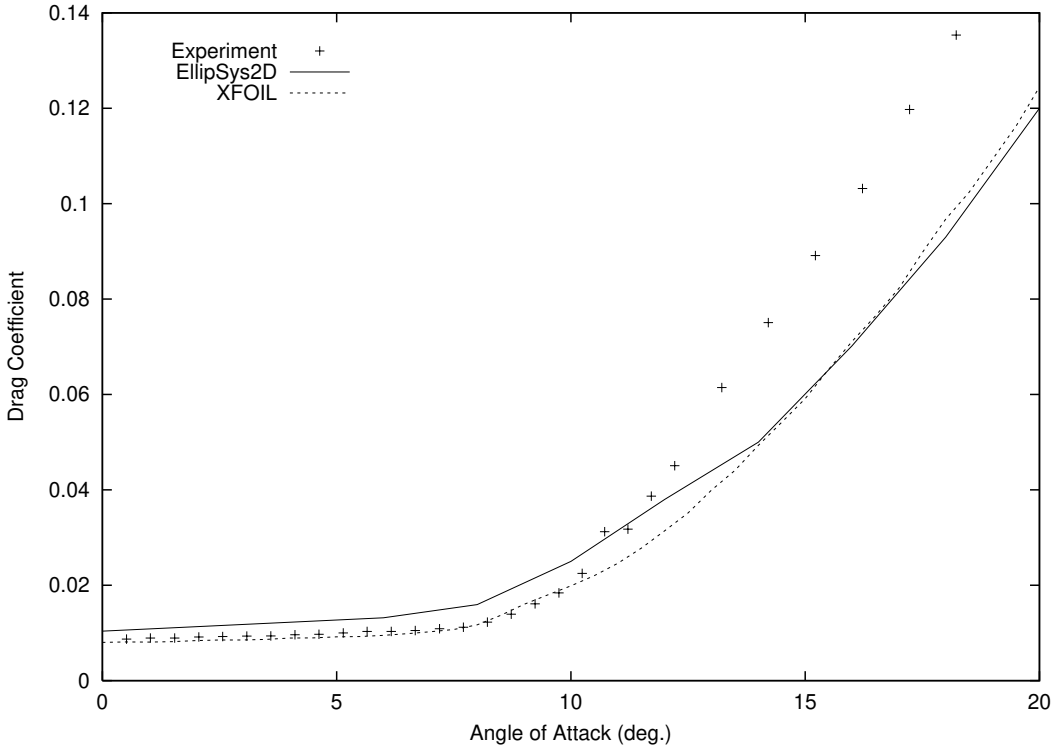

Figure 151. Drag Coefficient Curve (DU 93-W-210, Experiment Delft University of Technology)

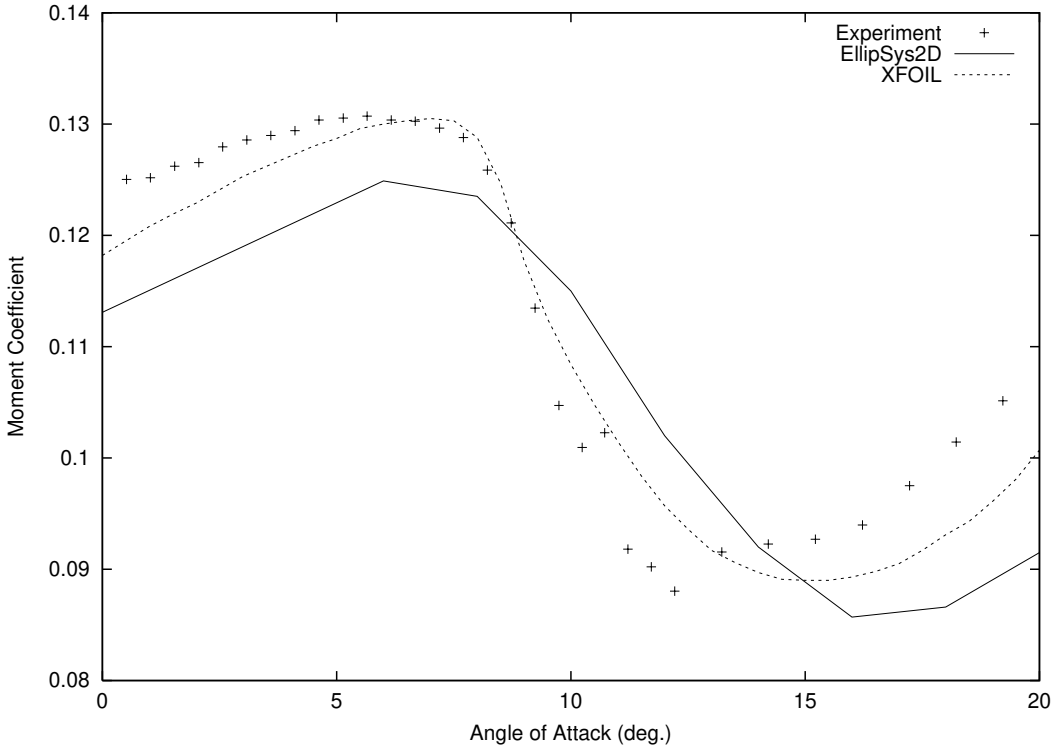

Figure 152. Pitching Moment Coefficient Curve (DU 93-W-210, Experiment Delft University of Technology)

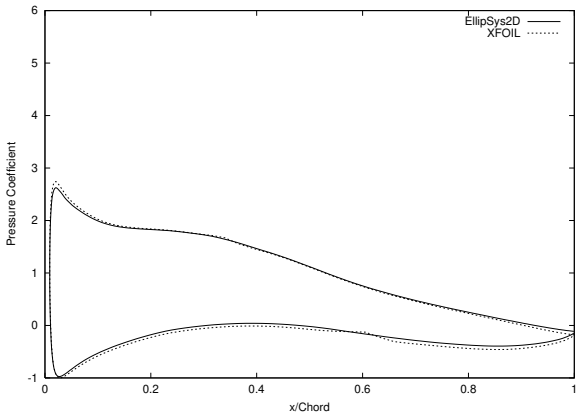

(a) $\alpha = 8.0^o$

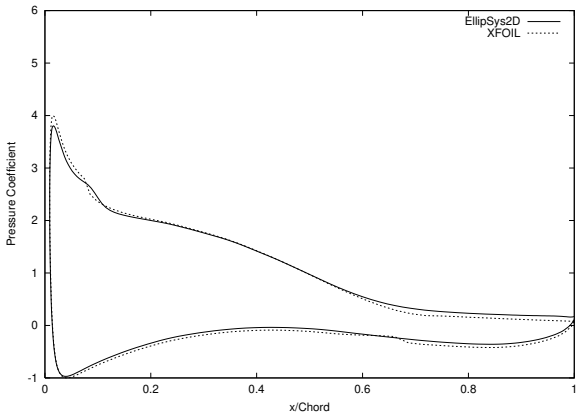

(b) $\alpha = 12.0^o$

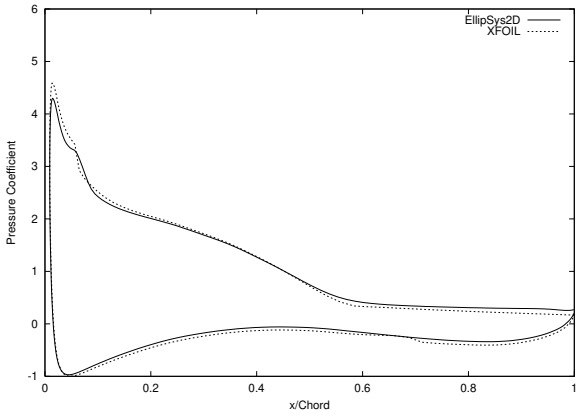

(c) $\alpha = 14.0^o$

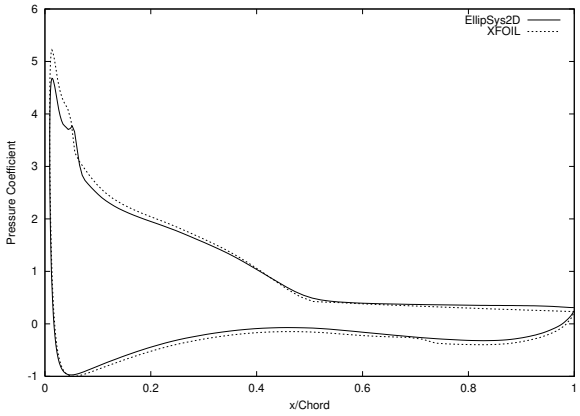

(d) $\alpha = 16.0^o$

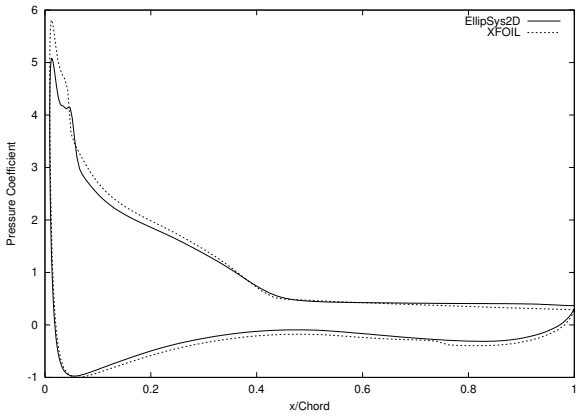

(e) $\alpha = 18.0^o$

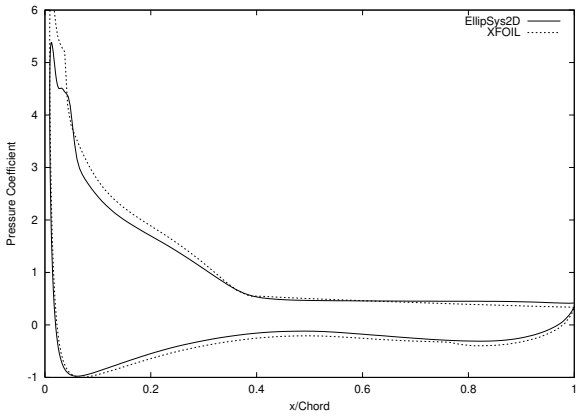

(f) $\alpha = 20.0^o$

Figure 153. Pressure Coefficient Distributions (DU 93-W-210)

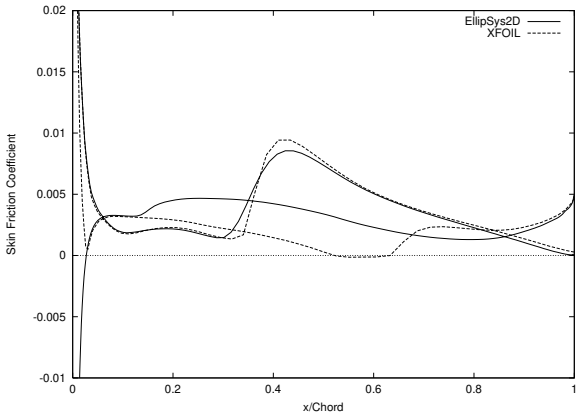

(a) $\alpha = 8.0^o$

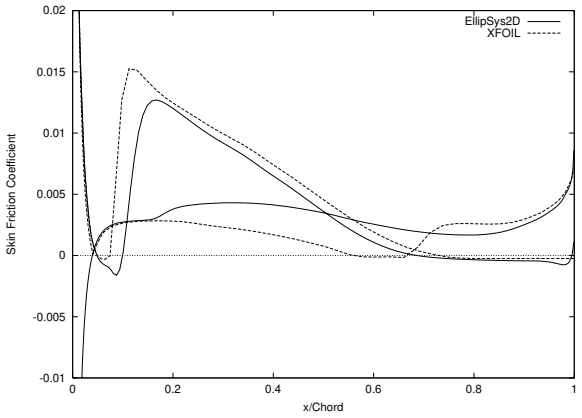

(b) $\alpha = 12.0^o$

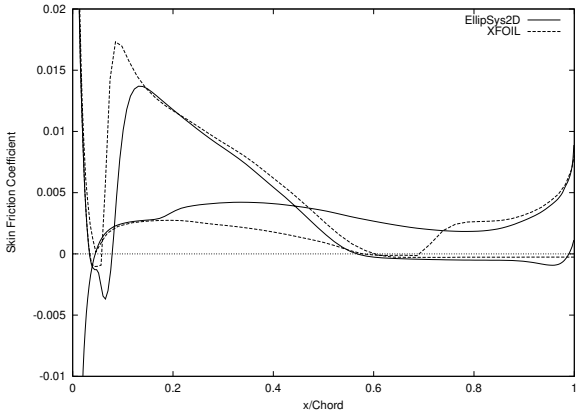

(c) $\alpha = 14.0^o$

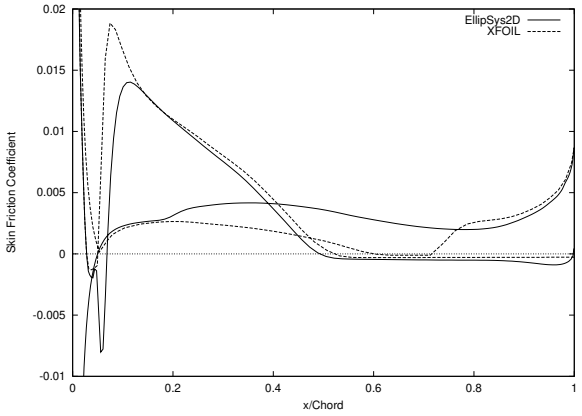

(d) $\alpha = 16.0^o$

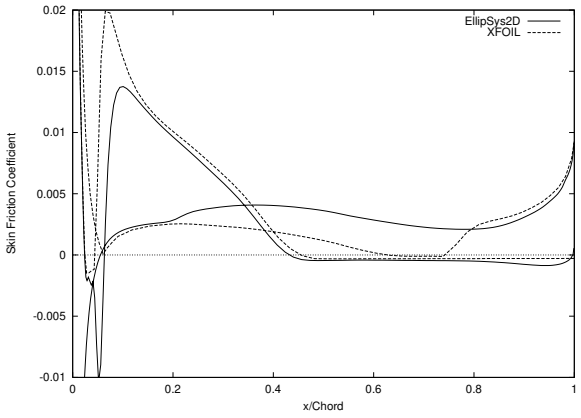

(e) $\alpha = 18.0^o$

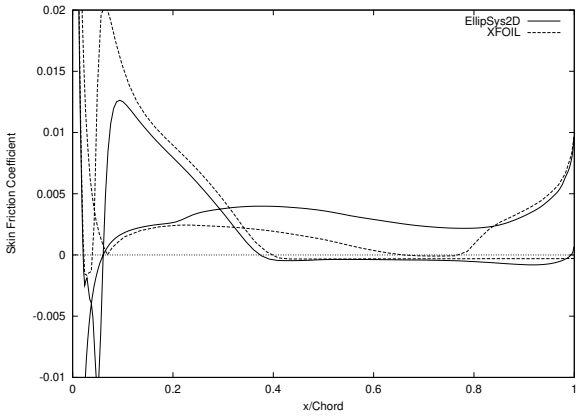

(f) $\alpha = 20.0^o$

Figure 154. Skin Friction Coefficient Distributions (DU 93-W-210)

11 A-Airfoil

The A-Airfoil was chosen as a test case for validating several numerical codes by the partners of the ECARP project [14]. Experiments were carried out in the F1 and F2 wind tunnels at ONERA/FAUGA. The Reynolds number of the experiment was $Re = 2.1 \times 10^6$.

11.1 Method

The C-mesh used for the computation had 384 cells in the direction along the airfoil, 256 of them being on the airfoil, and 64 cells in the direction away from the airfoil. The non-dimensional height of the cell at the airfoil was 1×10^{-5}.

The computations were performed with the SUDS-scheme for the convective terms, and the $k - \omega$ SST turbulence model by Menter [16] for the turbulent viscosity.

The analysis of the measurements shows that the transition on the upper side of the airfoil occured at a fixed location $x/Chord = 0.12$. Therefore, the transition was also fixed in the computations. On the lower side, the transition was fixed both in the experiment and the computations at $x/Chord = 0.3$.

11.2 Results

There was a good agreement between the experiment and the computations in the linear region. Higher maximum lift was predicted by the computations. XFOIL exhibits a strange and unexplainable behavior for a small range of angles of attack before stall.

A-Airfoil

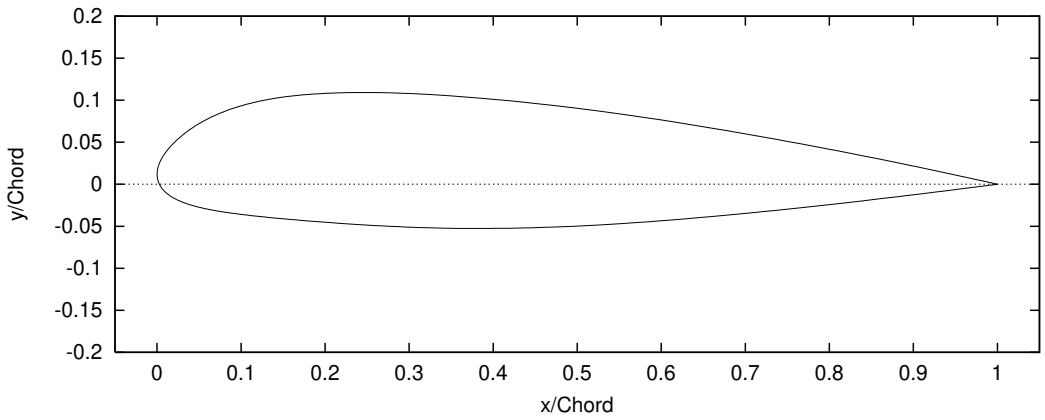

Figure 155. A-Airfoil

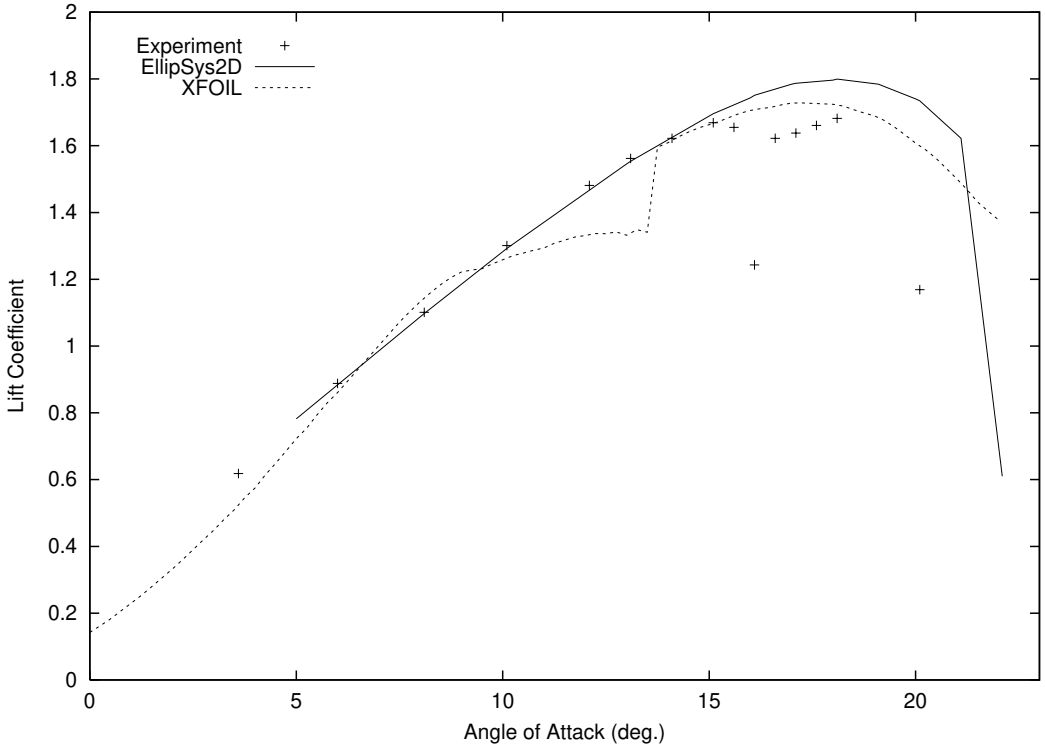

Figure 156. Lift Coefficient Curve (A-Airfoil, Experiment [14])

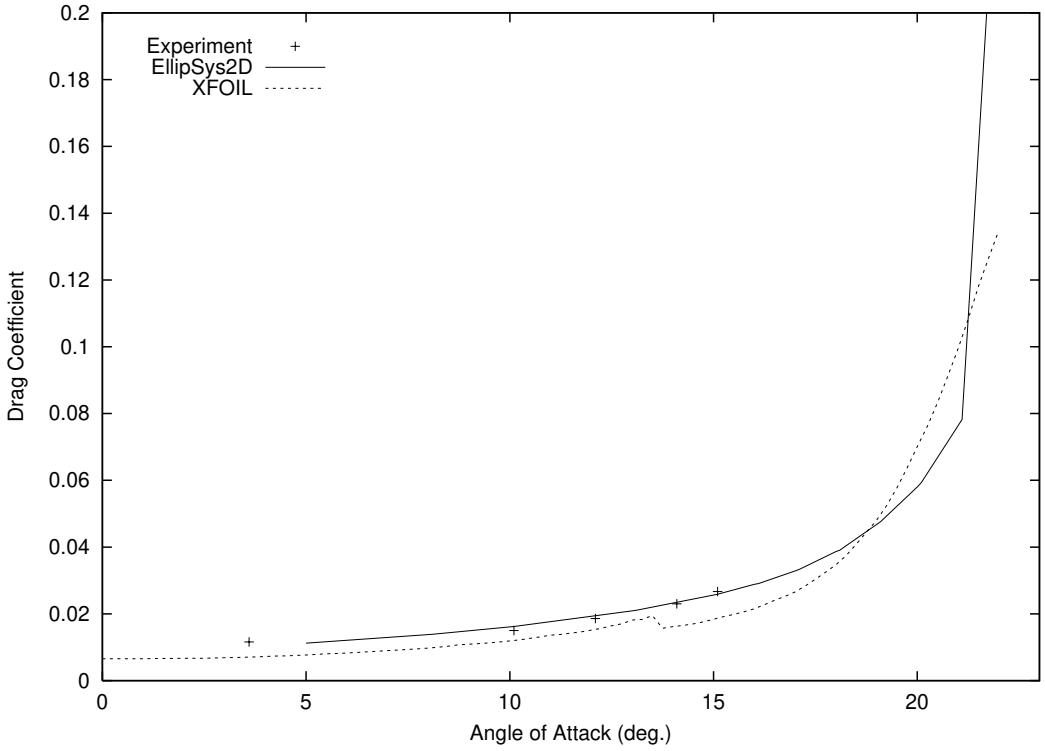

Figure 157. Drag Coefficient Curve (A-Airfoil, Experiment [14])

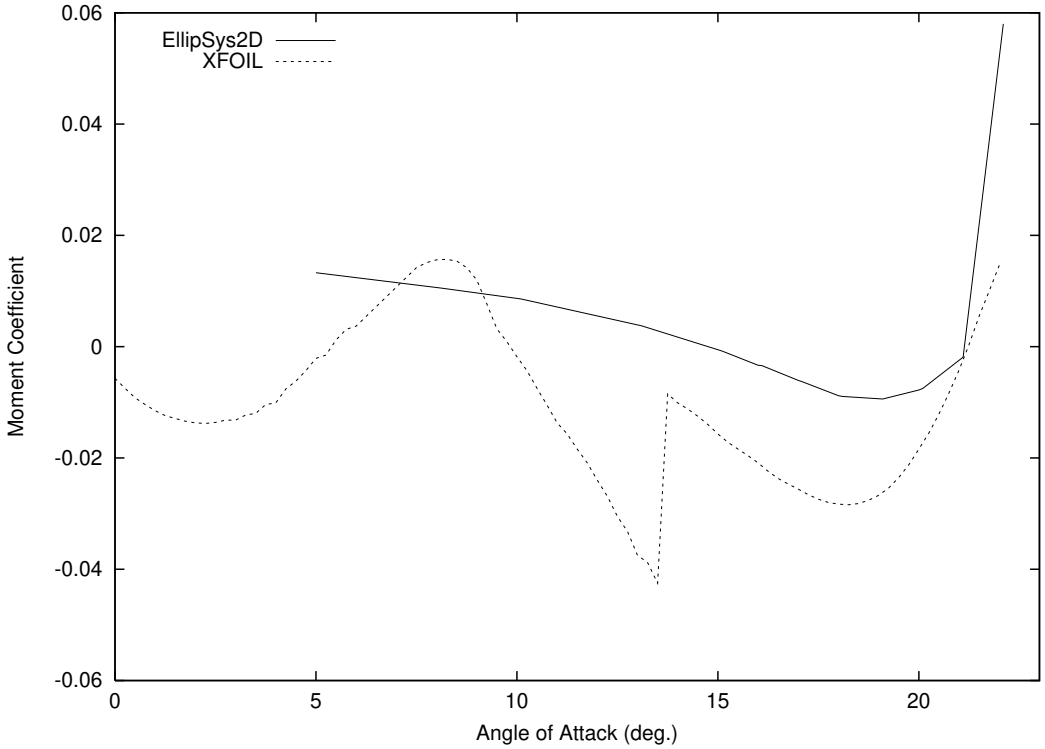

Figure 158. Pitching Moment Coefficient Curve (A-Airfoil)

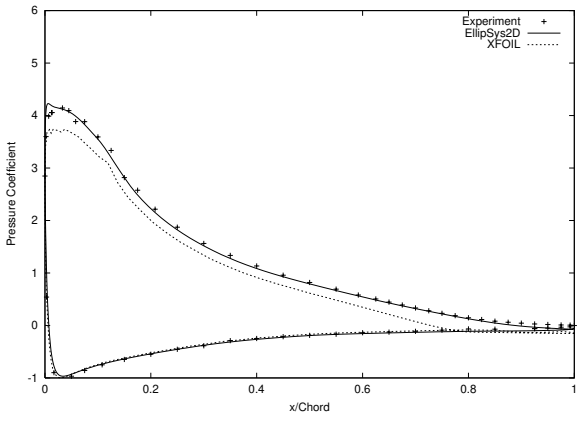

(a) $\alpha = 13.1^o$

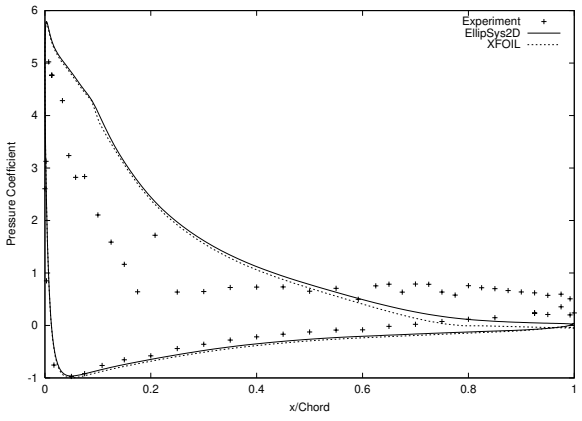

(b) $\alpha = 16.1^o$

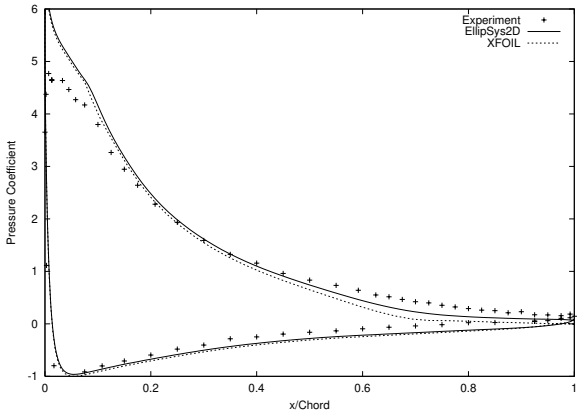

(c) $\alpha = 17.1^o$

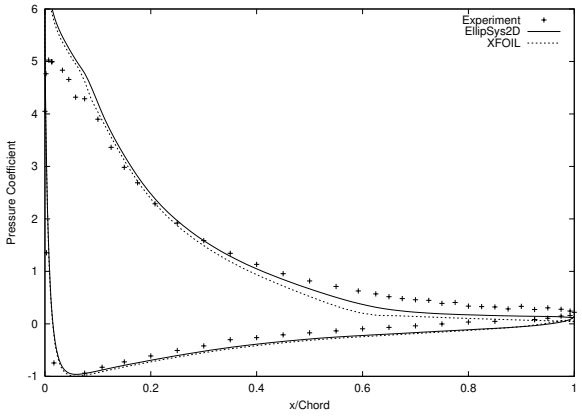

(d) $\alpha = 18.1^o$

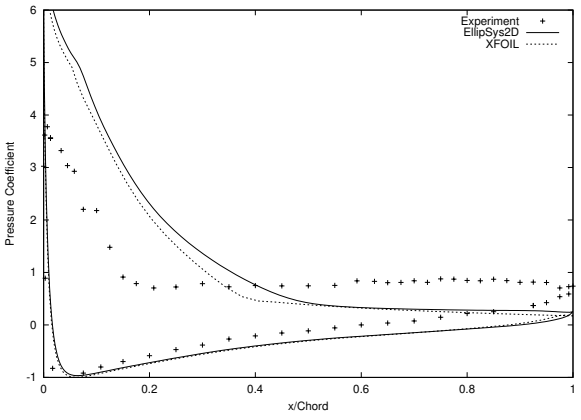

(e) $\alpha = 20.1^o$

Figure 159. Pressure Coefficient Distributions (A-Airfoil, Experiment [14])

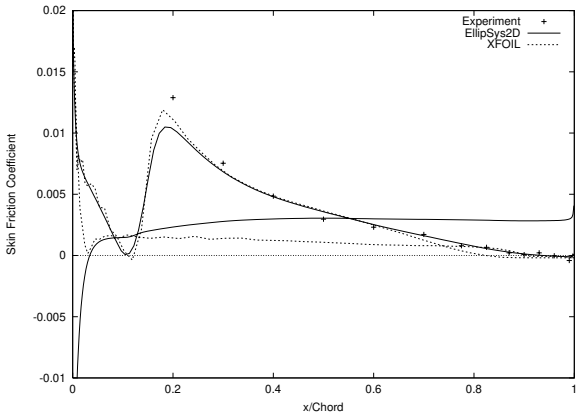

(a) $\alpha = 13.0^o$

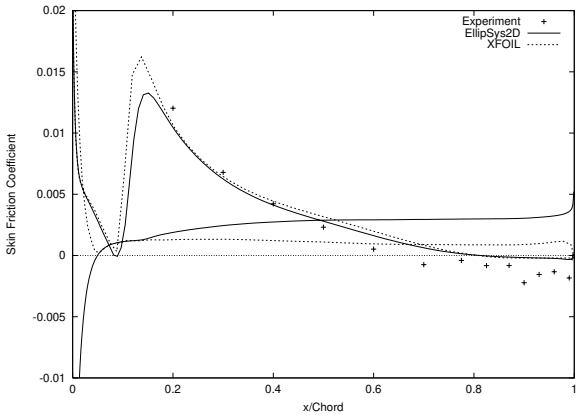

(b) $\alpha = 16.0^o$

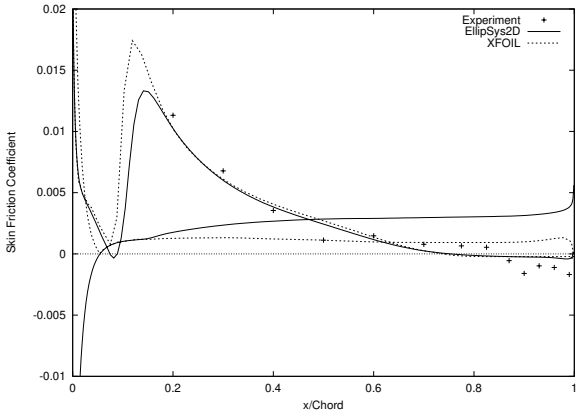

(c) $\alpha = 17.0^o$

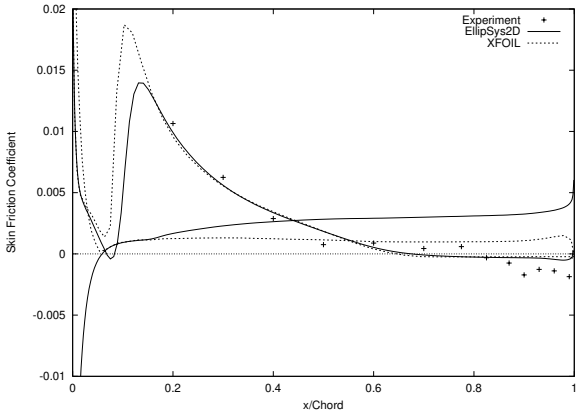

(d) $\alpha = 18.0^o$

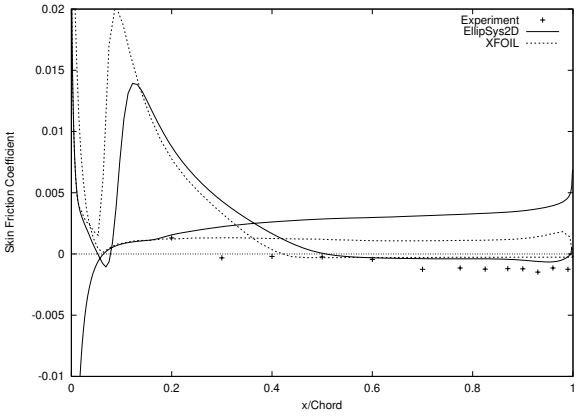

(e) $\alpha = 20.0^o$

Figure 160. Skin Friction Coefficient Distributions (A-Airfoil, Experiment [14])

12 Analysis of the Collected Results

In this section, an analysis of the data that have been collected for the numerous airfoils is attempted. The main objective is to be able to evaluate a priori how good the numerical code EllipSys2D will perform for a given airfoil.

Firstly, quantitative values assessing the agreement between experimental data and computational results from EllipSys2D are calculated. Secondly, airfoils for which the numerical code can be considered as performing well and those for which it performs poorly are sorted with the help of those values. Finally, some conclusions can be drawn concerning the ability of the numerical code EllipSys2D to simulate the flow around certain types of airfoils. These conclusions can give some hints for the design of future airfoils, as far as the numerical code EllipSys2D may be involved as a tool in the design process; but also to a greater extent as they can reveal characteristic facts about the actual flow.

12.1 Quantitative criteria

Quantitative values measuring the discrepancies between experimental data and computational results for each airfoil are gathered in Table 1, p.127. For each airfoil, the following four criterion-values are computed:

1. The difference of lift between experiment and computations averaged over the linear region, expressed in percentage relatively to the maximum experimental lift coefficient, is calculated.
2. The angle of attack for which stall occurs is considered. The angle for which a maximum of lift coefficient is first reached is reported. Then, the difference between the experimental and the computational values is evaluated in percentage relatively to the corresponding experimental angle (Note that in this case, the maximum lift location is searched close after the linear region, even if the lift coefficient grows again after stall, as it can be the case for some experiments).
3. The difference of maximum lift at the previously detected two points is evaluated in percentage relatively to the experimental maximum lift.
4. The maximum difference of lift (at a given angle of attack) in the stalled region is expressed in percentage relatively to the maximum experimental lift.

It should be noted that, when both fully turbulent computations and simulations with transition model were available, the latter ones were used for calculating these four values.

12.2 Classifying the airfoils

In this second step of the analysis, the airfoils for which the results obtained with EllipSys2D are in good agreement with the experimental data are first collected. Then the airfoils for which results are in large disagreement with the experiments are collected.

To select the airfoils that perform well, the three following conditions using the previously computed criterion-values are evaluated:

- The first criterion-value is below 5%

- The second criterion-value is below 12%
- The third or fourth criterion-value is below 20%

The airfoils that fulfil all these criteria are considered to be the ones that perform well. Note that the first condition is assumed to be satisfied for all the NACA airfoils in section 2 (see the comments in section 2.2). The limiting percentages have been chosen in order to make a clear distinction between the airfoils. At the same time, the limits are considered to be sensible as for the respective importance of the several criteria. These airfoils can be roughly classified from the best one to the worst one as:

1) FX66-S196-V1
2) NACA 63-215
3) NACA 63-415
4) NACA 63-215(V)
5) NACA 63-415(V)
6) NACA 63-218
7) NACA 63-418
8) NACA FFA-W3-241
9) S814

They are depicted in Fig.161. Note that the NACA 64-415 and NACA 65-415 airfoils have not been included even though they fulfil the above criteria. It was considered that they would not significantly improve the amount of data involved with airfoils from the NACA wing section family that have been already selected for the next step of the analysis.

The airfoils that perform poorly are selected next. They are defined to be the ones for which strictly more than two of the following conditions are satisfied:

- The first criterion-value is over 5%
- The second criterion-value is over 12%
- The third criterion-value is over 20%
- The fourth criterion-value is over 20%

These airfoils can be roughly classified from the worst one to the best one as:

1) NACA 63-430(V)
2) FFA-W3-211 (Fixed Tr.)
3) RISØ-A1-21
4) NACA 65-421
5) NACA 64-421
6) NACA 63-221

They are depicted in Fig.162.

12.3 Interpretation of the selected airfoils data

It is now attempted to correlate some characteristics of the previously selected airfoils with the quality of the results.

It would be interesting to relate the performance of the code to purely geometrical characteristics of the airfoils. Therefore, both the maximum relative thickness and the maximum curvature near the leading edge of the selected airfoils are reported in Table 2, p.127. The curvatures of the airfoils surfaces in the vicinity of the leading edge are plotted on Figs.163(a) and 163(b). It can be concluded that poorly-performing airfoils are somewhat thicker than well-performing airfoils, whereas the latter ones have a rather more curved leading edge. However, these conclusions highlight a general tendency, but these are not clearly decisive factors.

Some others factors which are related to the flowfield itself are then reported: the pressure center location (Figs.164 and 165), the transition point location (Fig.166), and the trailing edge separation point location (Fig.167). Once again, there is no very clear difference between the well- and poorly-performing airfoils that can lead to conclusive results. Nevertheless, as it can be seen by comparing the experimental results of Fig.165(a) to those of Fig. 165(b), it is quite clear that the poorly-performing airfoils have a tendency to stall earlier (approximately around an angle of attack of 10^o) than the well-performing ones (which stall around 15^o).

Moreover, two important features of the poorly-performing airfoils can be brought out by having an overview of the collected results of the previous sections. Firstly, stall is often numerically predicted at higher angles of attack than in the experiments. Secondly, the predicted lift in the post-stall region is always higher than the experimental lift. In other respects, it is well know that transition is a decisive factor for stall occurence, as well as lift prediction. This issue is then investigated further in the following section.

12.4 Study of the transition and stall behaviors

In this section, except otherwise specified, numerical results obtained with transition modelling are considered only. Remind that the transition model by Michel [17] was used throughout this report, whenever a transition model was used.

At first, a noticeable feature for some of the poorly-performing airfoils is the evolution of the skin friction coefficient on the suction side of the airfoil shortly after the leading edge. As it can be seen for the numerical results obtained with the NACA 63-430(V) airfoil (see Fig.82, p.62), the transition occurs quite far downstream from the leading edge. Even if no direct experimental evidence about the transition point location is available, it could be deduced that the transition actually arises very early after the leading edge [10]. Indeed, the experimental pressure coefficient distributions (Fig.81, p.61) exhibit an irregular pattern in this area which indicates that transition may actually occur at this place. This assertion is reinforced by the fact that fully turbulent simulations exhibit pressure coefficient distributions in closer agreement with the experimental data.

Even more characteristic is the behavior of the skin friction coefficient on the suction side of the RISØ-A1-21 airfoil on Fig.94(d), p.71. As it can be seen, after the sharp leading edge peak followed further downstream by a slowly increasing phase, the skin friction starts to slowly decrease again before transition occurs, consequently triggering a second more abrupt increasing phase. Once again, it is believed that transition occurs in the experiment just after the leading edge.

It must be reminded that a sharp leading edge suction peak is commonly used in airfoil design in order to trigger transition close to the leading edge of the airfoil. Indeed, the subsequent pressure increase thickens rapidly the laminar boundary layer which becomes unstable, thereby triggering transition towards a turbulent boundary layer. A closer study of the transition model behavior in this region has shown that this leading edge suction peak was not enough to trigger transition in the computation.

Let us remind as well that the Michel transition model is based on the laminar boundary layer thickness development. Transition is predicted when this thickness reaches a critical level which is empirically defined beforehand. Note that it is tuned to fit experimental results obtained with a flat plate without any streamwise pressure gradient.

Moreover, further downstream this suction peak, the numerical solution method predicts a relatively slow growth of the laminar boundary layer. As a consequence, the transition model fails to predict the correct transition point location. Transition is delayed far downstream on the suction side. The reason could also be

that the empirical critical value is not well tuned for that experimental airfoil configuration. But a more likely explanation for this phenomenon is to be found again in the pressure distribution. For all the poorly-performing airfoils (see for example Fig.93(d), p.70), a rather flat (or completely flat) pressure plateau can be observed downstream the sharp suction peak on the suction side. This contributes to generate an adverse pressure gradient effect that is unfavourable for laminar boundary layer thickness growth, consequently delaying transition in the model as explained earlier.

These conclusions are assessed by performing the following test. In order to artificially accelerate the growth of the laminar boundary layer perceived by the transition model, the critical value of the boundary layer thickness triggering transition was multiplicated by a factor of 0.8. This factor was chosen in order to locate the transition point at an approximately correct location for one of the poorly-performing airfoils (namely the RISØ-A1-21 airfoil). This scale factor was then kept the same for all other computations presented herein. In the remaining of this section, the computational results obtained with this 'scaled' transition model are compared with the original ones, both for poorly- and well-performing airfoils.

(a) Poorly-performing airfoils

First, results obtained with poorly performing airfoils are presented. Three airfoils are considered: NACA 63-430(V), RISØ-A1-21 and NACA 63-221. The other ones are not considered for the following reasons. The FFA-W3-211 airfoil with fixed transition does obviously not involve the transition model (However, the poor agreement in this case can be explained by the fact that, in the experiment, transition is triggered by rough tapes attached on the airfoil. As a consequence, it can have side-effects that cannot be predict by simply switching on the turbulence model at this very location in the computation. More precisely, these tapes generate a relatively high level of turbulence). The NACA 64-421 and NACA 65-421 present a continual growth of the lift even after stall that is originating from another physical phenomenon than transition, that cannot be explained with the present experimental data. For the sake of simplicity when interpretating the results, they are not included here.

The results obtained for the NACA 63-430(V) are presented on Fig.168. As it can be seen, the scaled transition model exhibits pressure coefficient distributions, as well as lift and drag coefficients, closer to the experimental values. On the skin friction coefficient distributions, it is clear that transition arises earlier with the scaled model. However, it appears on the experimental pressure coefficient distributions that transition occurs even earlier. This explains why the new results do not perfectly match the experimental ones.

The results for the RISØ-A1-21 airfoil are presented next on Fig.169. Conclusions that can be drawn are the same as previously, except that the transition location is now even better predicted with the scaled transition model, yielding to even better agreement with the experimental data (The scaled model was indeed calibrated to this airfoil).

Finally, the lift and drag coefficients obtained for the NACA 63-221 airfoil are depicted on Fig.170. The influence of the transition model is quite small in this case, however, the results are slightly improved in the region close to stall. Moreover, it can be noted that the maximum lift peak at stall which is observed with the original transition model is smoothed out with the scaled model.

(b) Well-performing airfoils

Results obtained with some of the well-performing airfoils are now presented. It must be noted that the FX66-S196-V1 airfoil is not considered. Indeed, it is a

so-called laminar airfoil that has been designed such that the flowfield remains laminar on a large part of the suction side before transition to turbulence occurs. It might be the reason why the results obtained with the original Michel transition model are so close to experimental results. In other words, the adverse pressure gradient effect is delaying transition both in the experiment and in the computations. The following airfoils are considered instead: NACA 63-415, NACA 63-415(V) and FFA-W3-241.

The lift and drag coefficients obtained for the NACA 63-415 and NACA 63-415(V) are presented on Figs.171 and 172, respectively. As it can be seen, there is almost no difference between the original and the scaled transition models. However, both are in good agreement with the experimental data. This good agreement also means that the transition model has a minor influence for those airfoils.

The results obtained with the FFA-W3-241 airfoil are depicted on Fig.173. In this case, even if the airfoil was originally considered as performing well, the results are further improved with the scaled transition model. Again, it is due to a better prediction of the transition location by the numerical model, as it can be seen by looking at the pressure coefficient and the skin friction distributions.

12.5 Conclusions regarding the numerical code performances and airfoil design

It has been shown above that the transition model can have a great impact when simulating the flowfield around some of the considered airfoils, namely those that are sensitive to the transition point location.

This suggests at first that the experimental conditions that can influence the transition point location, such as background turbulence level or roughness of the airfoil surface, should be taken into account when performing these simulations. However, it would require much more sophisticated transition models that would need some input data describing more precisely the experimental conditions. As a result, those models would be less general, and probably very difficult to develop with a sensible theory based on the physics of the transition.

In order to keep the transition models that already exist, and which are performing well in a wide range of cases, any airfoil design process that uses these models should be such that it remains within this favourable range of cases. As a consequence, the design algorithm should include requirements preventing from deviating from the conditions where the model that is used is performing well. As it has been shown previously (as far as the Michel transition model is concerned), if the airfoil is designed such that transition should be triggered by a sharp leading edge suction peak, which the numerical model might not be able to capture, the subsequent boundary layer should be allowed to grow relatively fast on the suction side of the airfoil downstream the leading edge suction peak, so that transition will not be artificially delayed. In other words, relatively flat pressure plateaux should be avoided in this area.

Airfoil Name	Average Lift Difference in Linear Region	Maximum Lift Location Difference	Maximum Lift Difference	Maximum Lift Difference in Stall
NACA 63-215	6.4 %	5.9 %	5.0 %	6.4 %
NACA 63-218	3.8 %	13.3 %	12.2 %	19.8 %
NACA 63-221	3.5 %	25.3 %	22.6 %	23.5 %
NACA 63-415	0.0 %	6.0 %	5.2 %	9.1 %
NACA 63-418	5.1 %	6.6 %	16.2 %	17.6 %
NACA 63-421	2.3 %	17.8 %	15.0 %	19.5 %
NACA 64-415	2.0 %	5.5 %	4.1 %	4.0 %
NACA 64-421	2.5 %	27.9 %	23.3 %	23.3 %
NACA 65-415	7.0 %	4.1 %	4.9 %	10.5 %
NACA 65-421	9.1 %	109.5 %	37.4 %	19.2 %
NACA 63-215(V)	0.7 %	11.2 %	1.5 %	11.0 %
NACA 63-415(V)	2.3 %	7.8 %	10.7 %	11.4 %
NACA 63-430(V)	21.5 %	3.7 %	27.5 %	40.6 %
RISO-A1-18	2.1 %	18.8 %	14.2 %	24.1 %
RISO-A1-21	0.0 %	20.5 %	21.4 %	40.0 %
RISO-A1-24	1.6 %	34.4 %	18.5 %	38.5 %
FFA-W3-211 (Fixed Tr.)	0.0 %	43.5 %	24.8 %	32.0 %
FFA-W3-211 (Free Tr.)	1.3 %	18.9 %	9.5 %	16.2 %
FFA-W3-241	0.0 %	0.0 %	12.4 %	24.8 %
FFA-W3-301	4.8 %	86.2 %	63.5 %	86.5 %
S809	0.0 %	29.9 %	10.5 %	12.9 %
S814	2.1 %	11.8 %	15.3 %	27.8 %
FX66-S196-V1	1.2 %	3.0 %	1.8 %	3.6 %
DU 91-W2-250	2.5 %	16.7 %	7.6 %	21.5 %
DU 93-W-210	2.6 %	35.7 %	3.9 %	17.0 %
A-Airfoil	0.0 %	20.0 %	8.1 %	8.8 %

Table 1. Criteria for Evaluating Agreements and Discrepancies between Experiments and Computations

	Airfoil Maximum Thickness	Leading Edge Maximum Curvature
Well-performing airfoils		
FX66-S196-V1	19 %	50.0
NACA 63-215	15 %	37.1
NACA 63-415	15 %	41.8
NACA 63-218	18 %	28.8
NACA 63-418	18 %	32.4
FFA-W3-241	24 %	16.5
S814	24 %	21.8
Poorly-performing airfoils		
NACA 63-430	30 %	11.2
FFA-W3-211	21 %	24.7
RISO-A1-21	24 %	31.8
NACA 65-421	21 %	27.1
NACA 64-421	21 %	24.1
NACA 63-221	21 %	23.2

Table 2. Selected Airfoils Geometrical Parameters

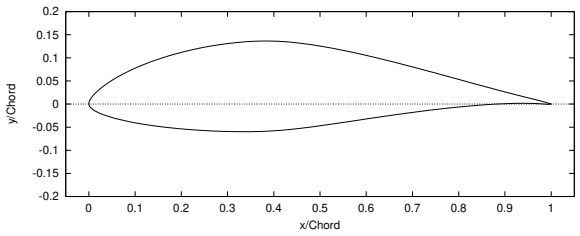

(a) FX66-S196-V1 Airfoil

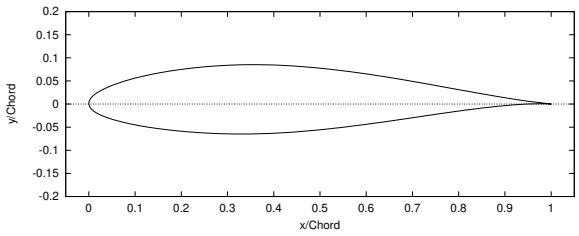

(b) NACA 63-215 Airfoil

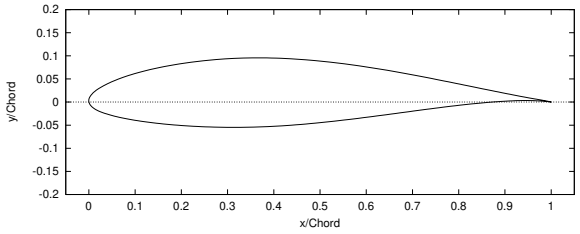

(c) NACA 63-415 Airfoil

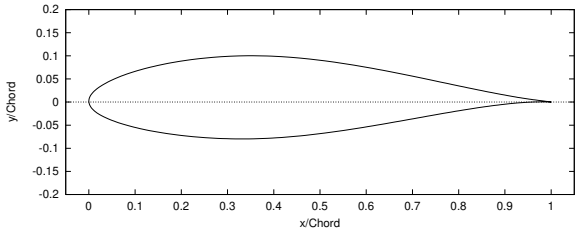

(d) NACA 63-218 Airfoil

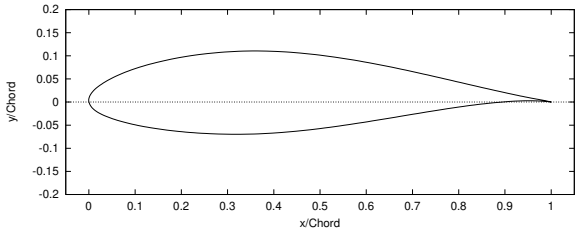

(e) NACA 63-418 Airfoil

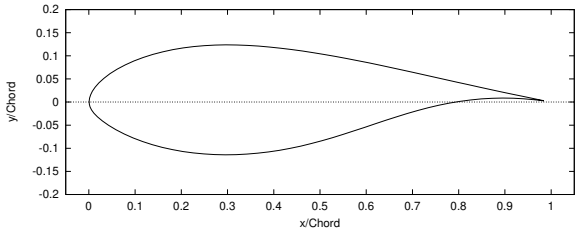

(f) FFA-W3-241 Airfoil

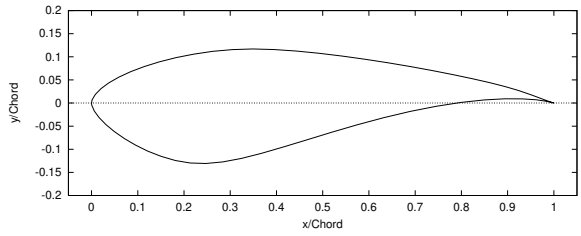

(g) S814 Airfoil

Figure 161. Airfoils With Good Experiment/Computation Agreement

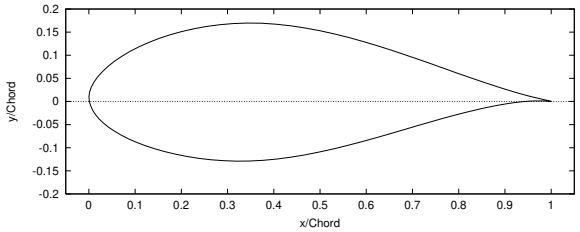

(a) NACA 63-430 Airfoil

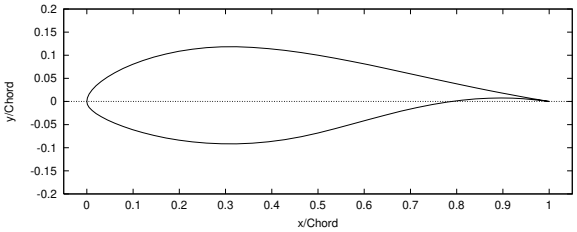

(b) FFA-W3-211 Airfoil

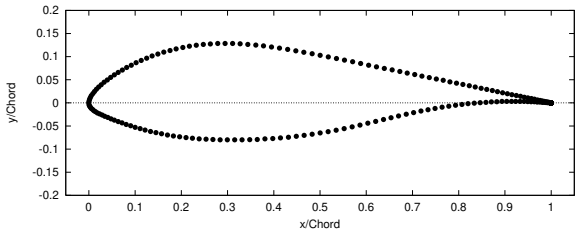

(c) RISO-A1-21 Airfoil

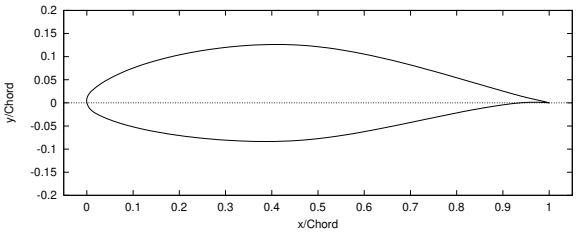

(d) NACA 65-421 Airfoil

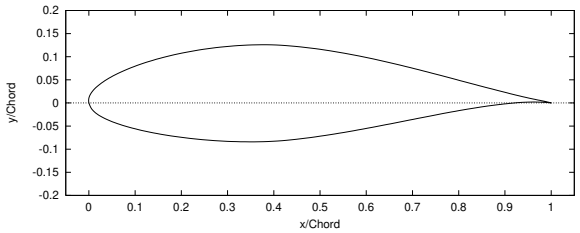

(e) NACA 64-421 Airfoil

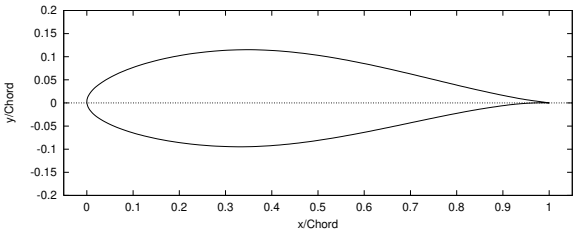

(f) NACA 63-221 Airfoil

Figure 162. Airfoils With Large Experiment/Computation Disagreement

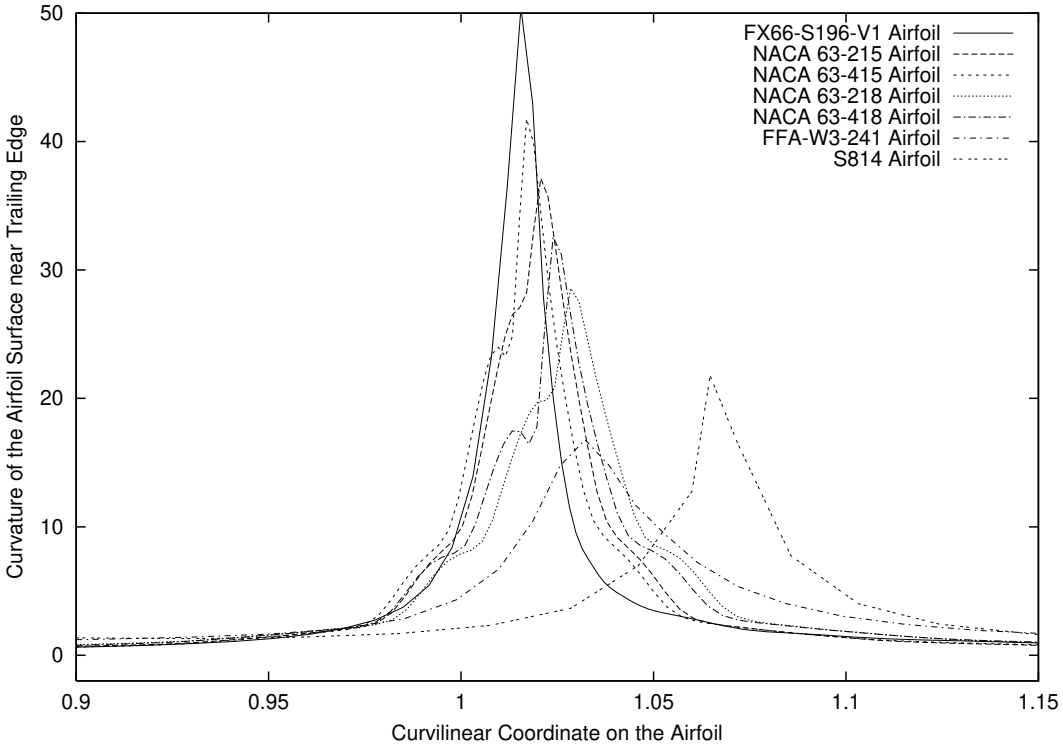

(a) 'Well-Performing' Airfoils

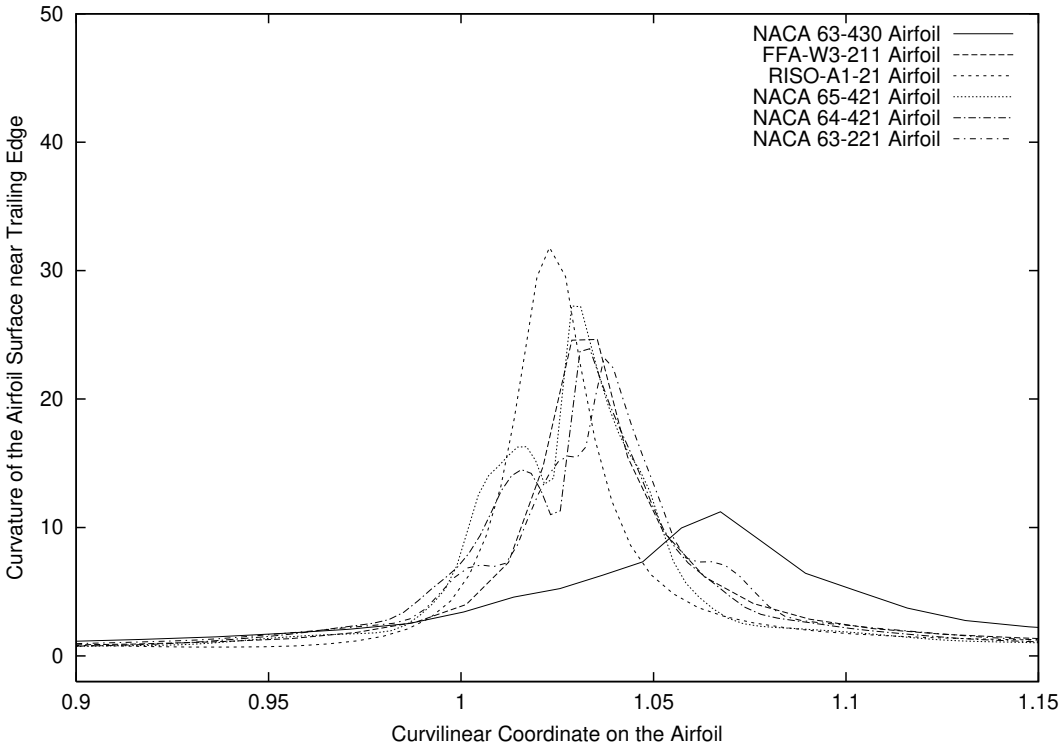

(b) 'Poorly-Performing' Airfoils

Figure 163. Surface Curvature Near Leading Edge for the Selected Airfoils

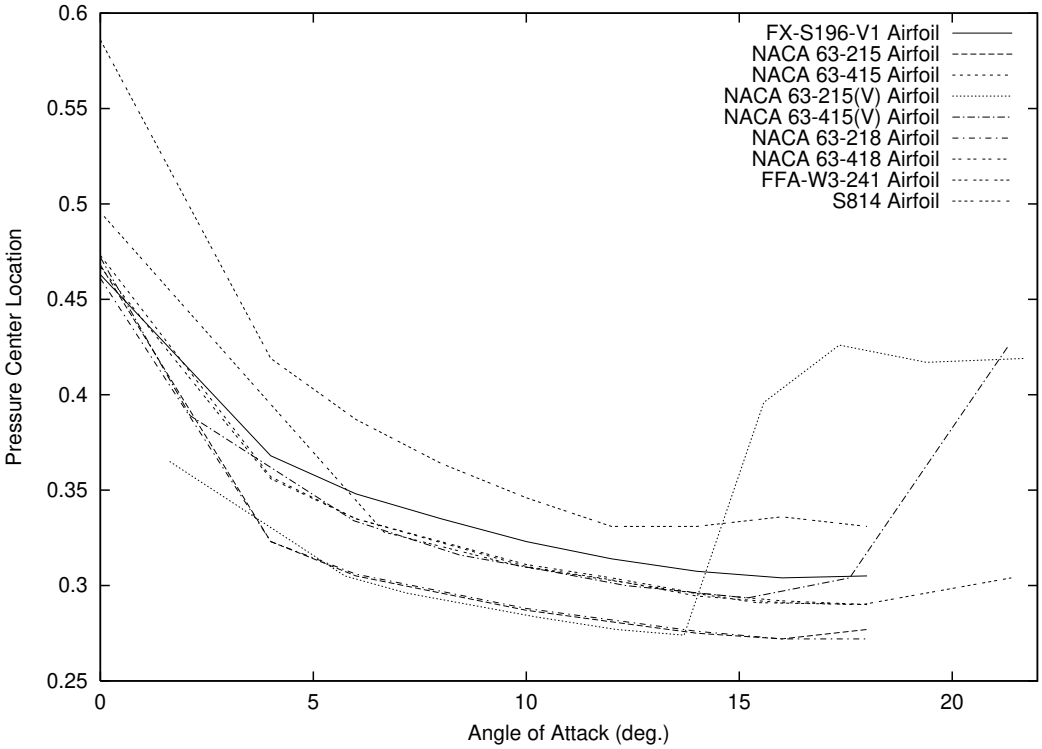

(a) 'Well-Performing' Airfoils

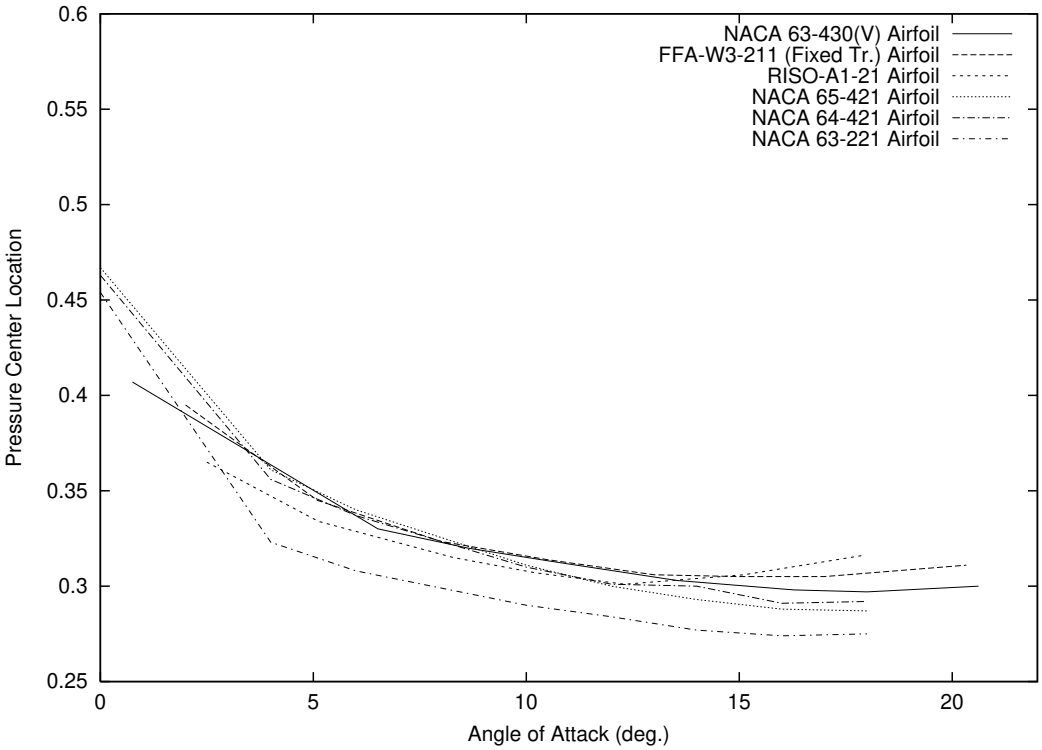

(b) 'Poorly-Performing' Airfoils

Figure 164. Pressure Center Location for the Selected Airfoils

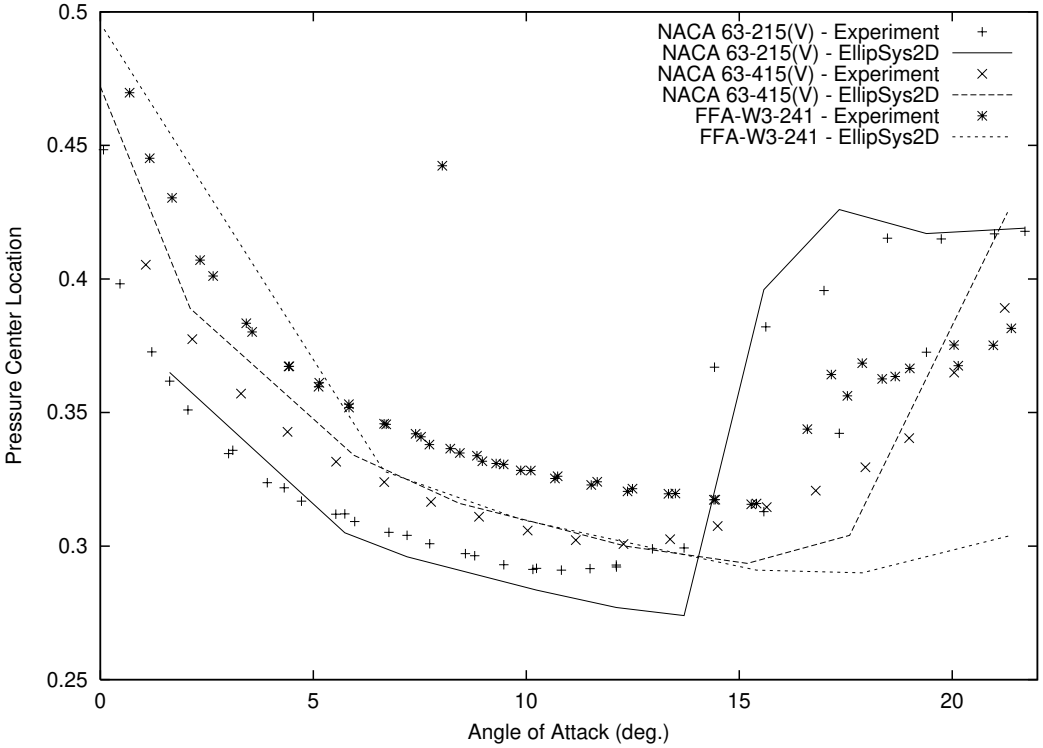

(a) 'Well-Performing' Airfoils

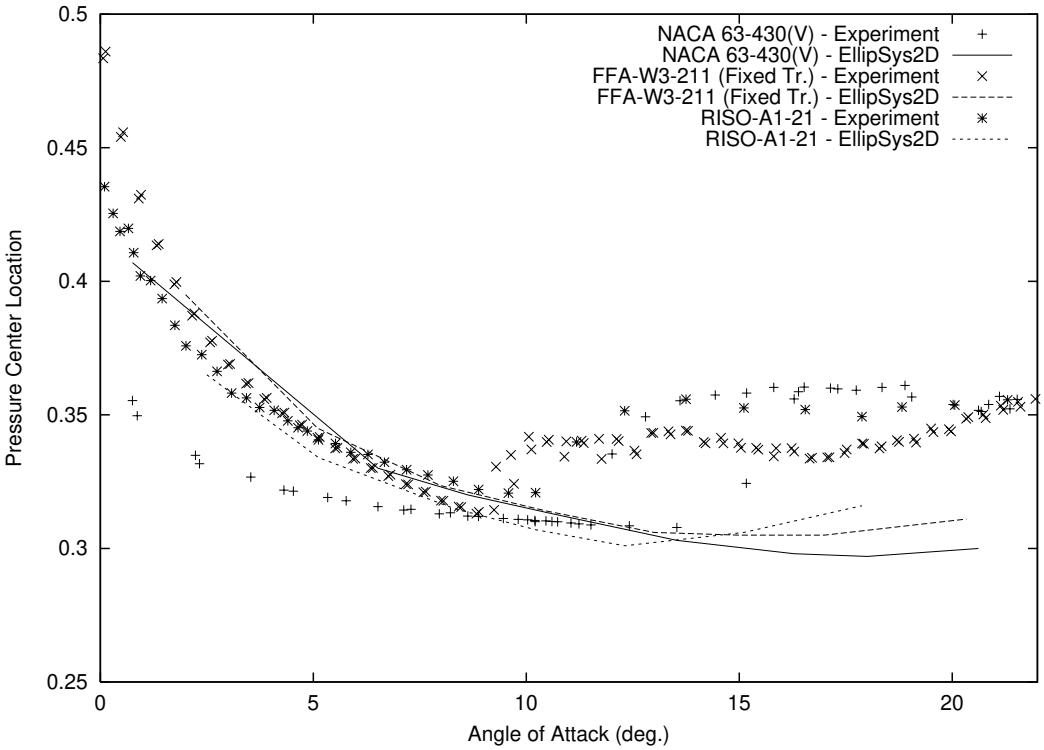

(b) 'Poorly-Performing' Airfoils

Figure 165. Pressure Center Location for the Selected Airfoils (Experimental and Computational Results)

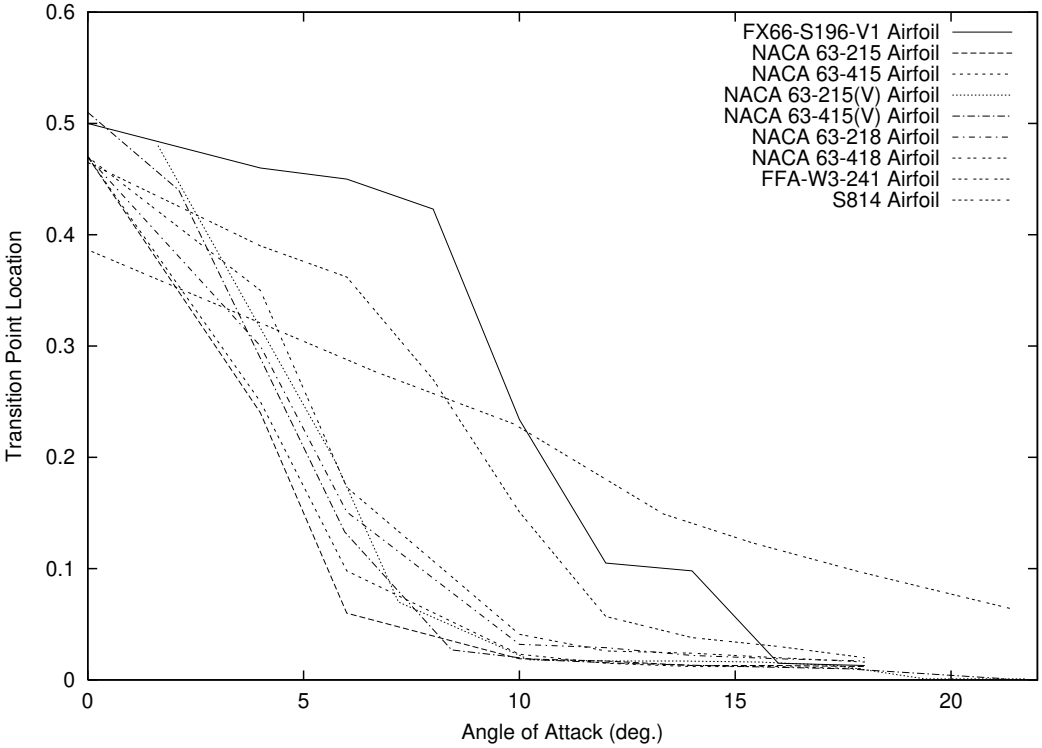

(a) 'Well-Performing' Airfoils

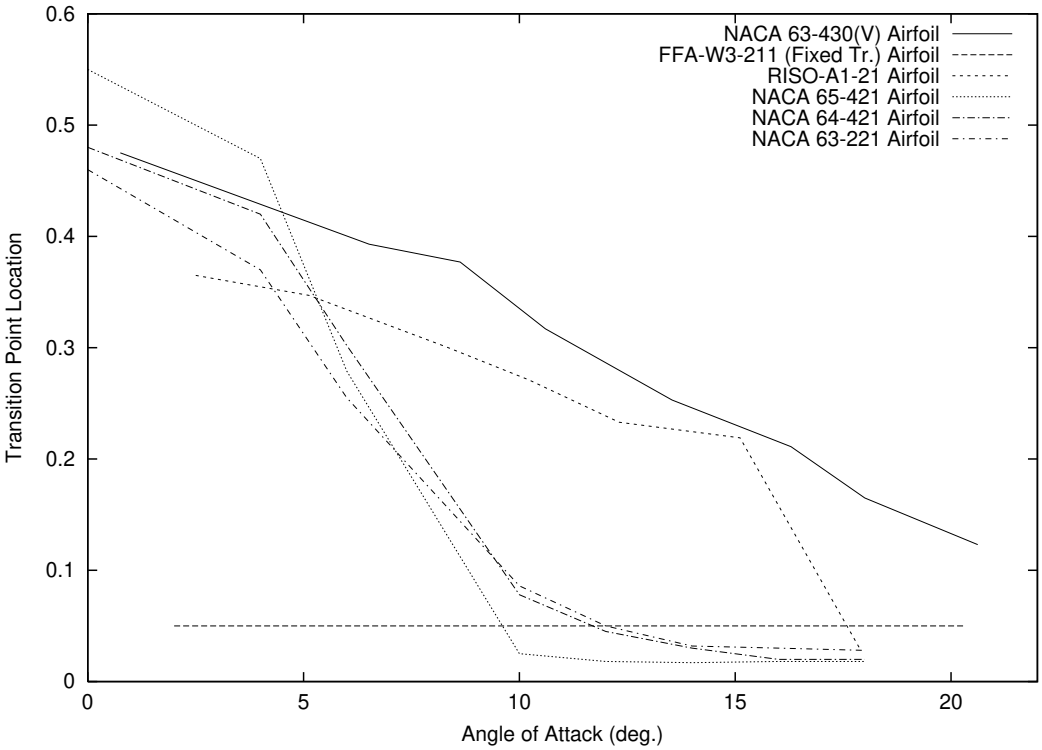

(b) 'Poorly-Performing' Airfoils

Figure 166. Transition Point Location for the Selected Airfoils

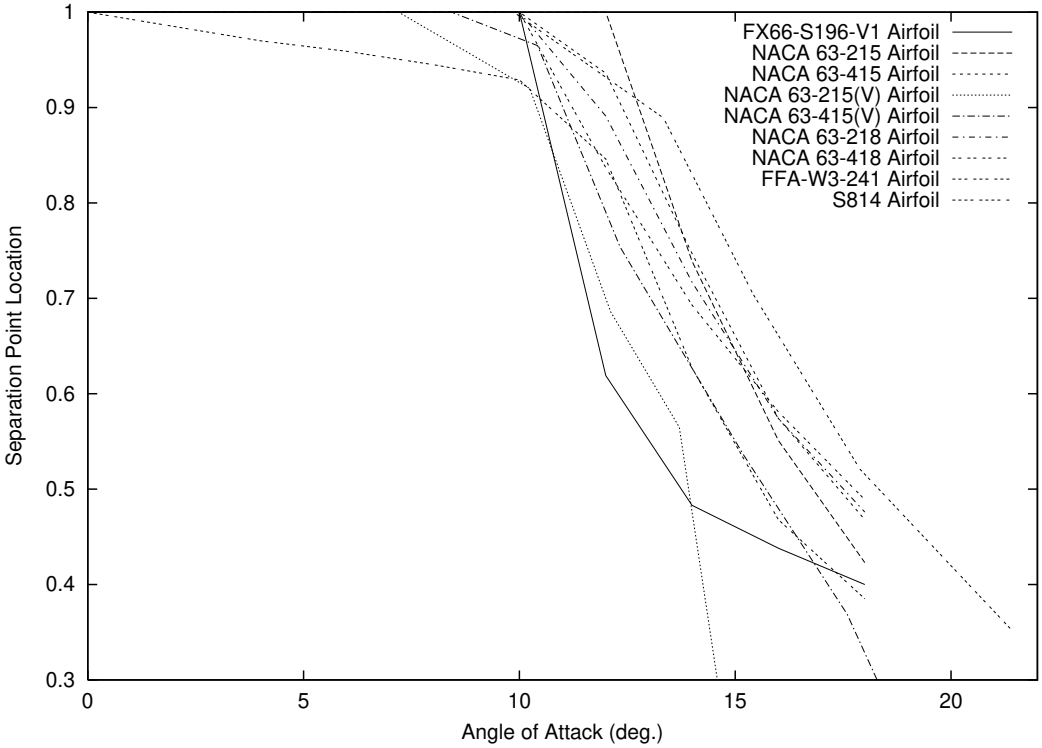

(a) 'Well-Performing' Airfoils

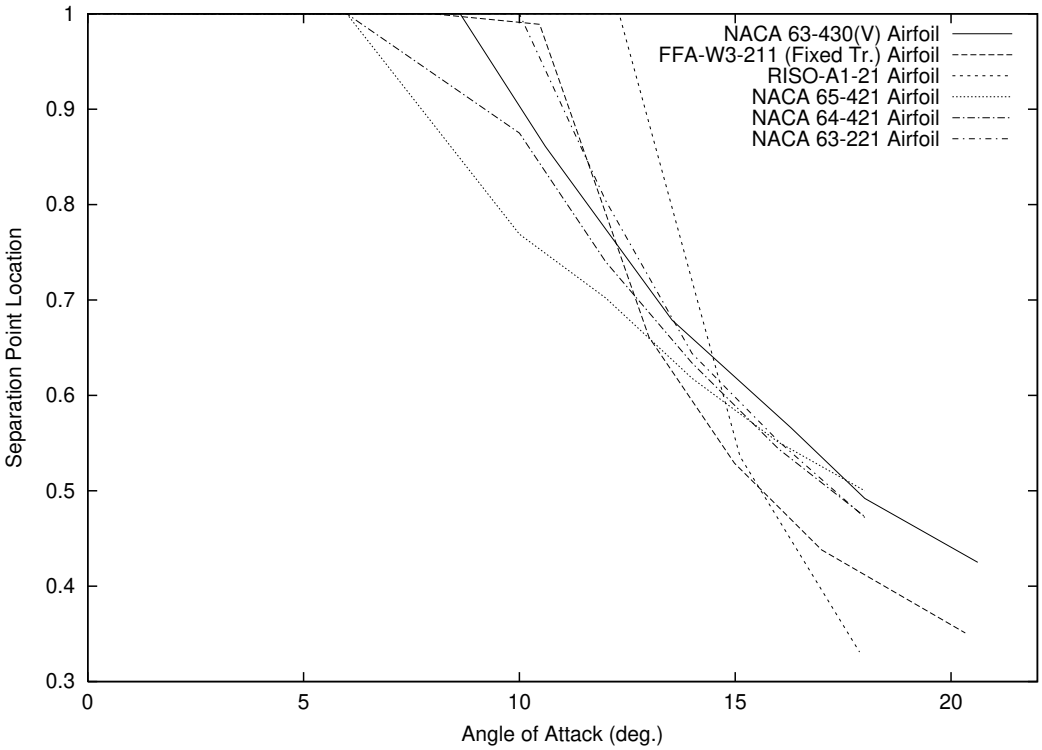

(b) 'Poorly-Performing' Airfoils

Figure 167. Separation Point Location for the Selected Airfoils

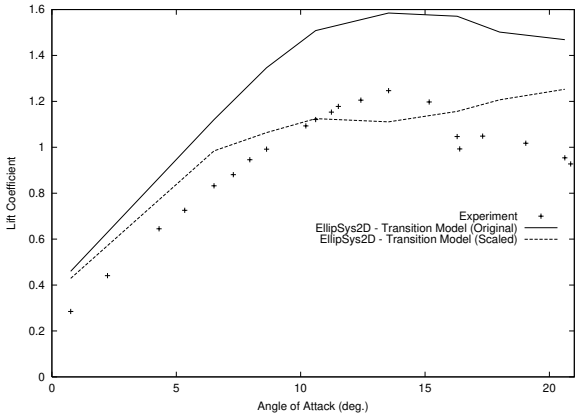

(a) Lift Coefficient

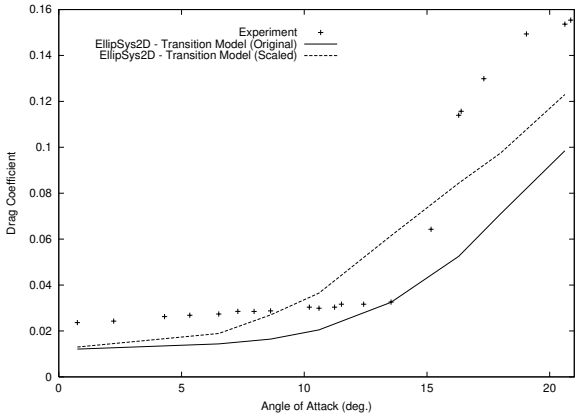

(b) Drag Coefficient

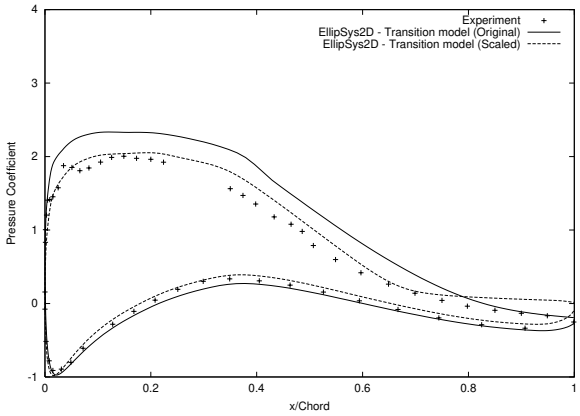

(c) Pressure Coefficient - $\alpha = 8.628^o$

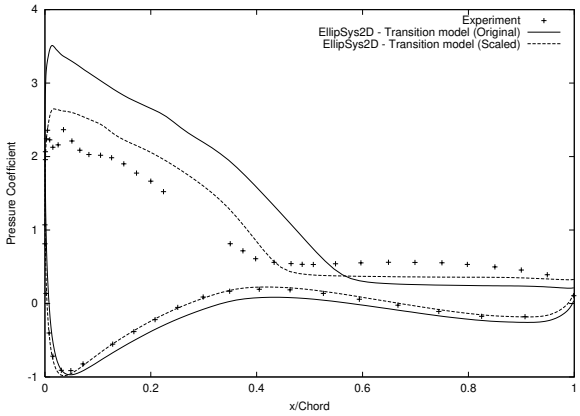

(d) Pressure Coefficient - $\alpha = 16.29^o$

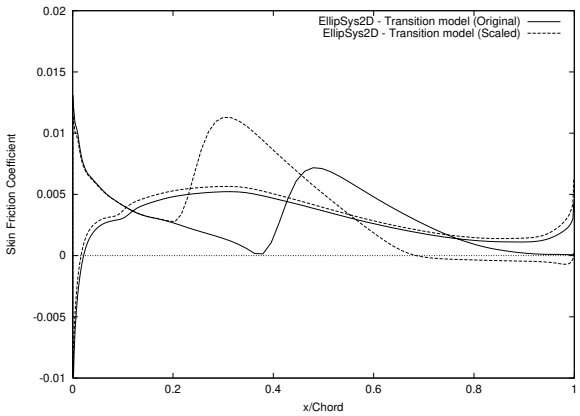

(e) Skin Friction Coefficient - $\alpha = 8.628^o$

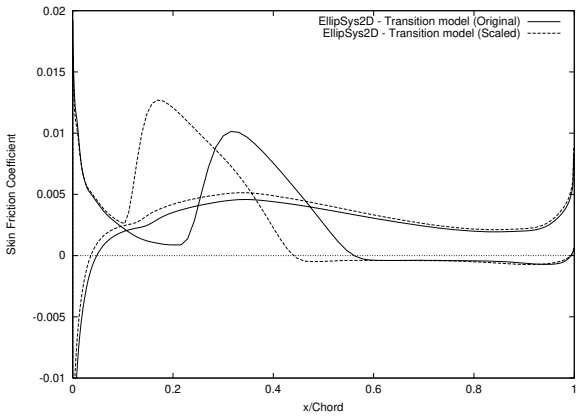

(f) Skin Friction Coefficient - $\alpha = 16.29^o$

Figure 168. Comparison of Original and Scaled Michel Transition Model (NACA 63-430(V), Experiment [10])

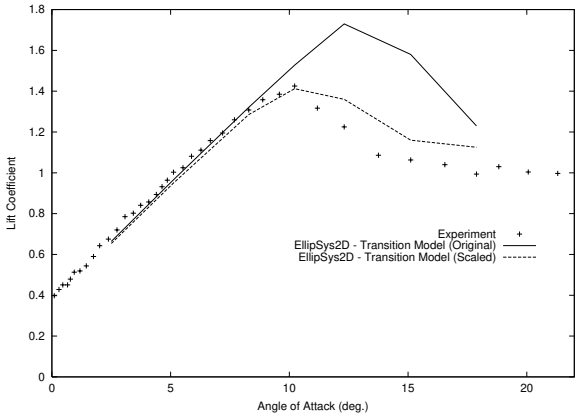

(a) Lift Coefficient

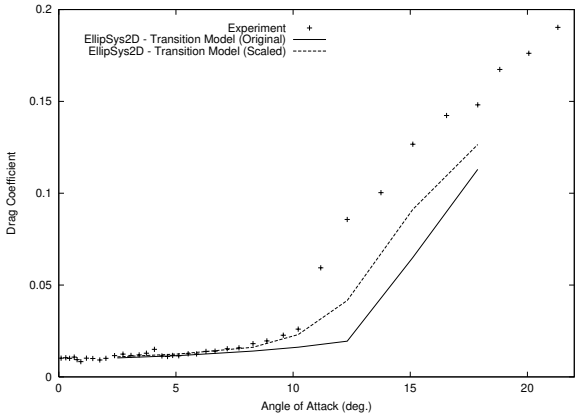

(b) Drag Coefficient

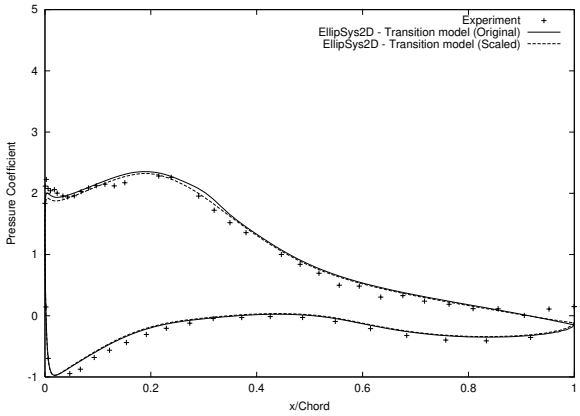

(c) Pressure Coefficient - $\alpha = 8.69^o$

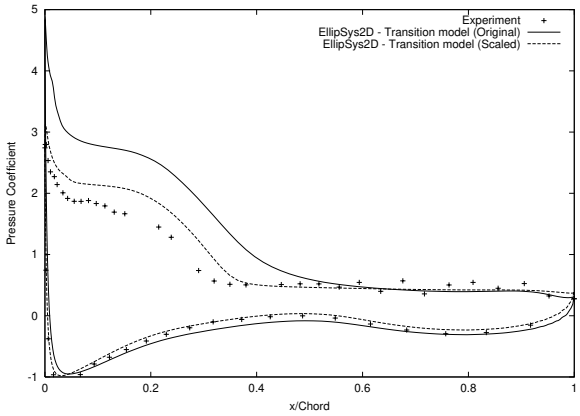

(d) Pressure Coefficient - $\alpha = 15.11^o$

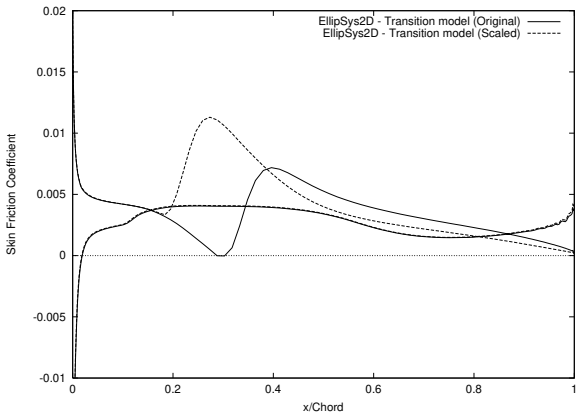

(e) Skin Friction Coefficient - $\alpha = 8.69^o$

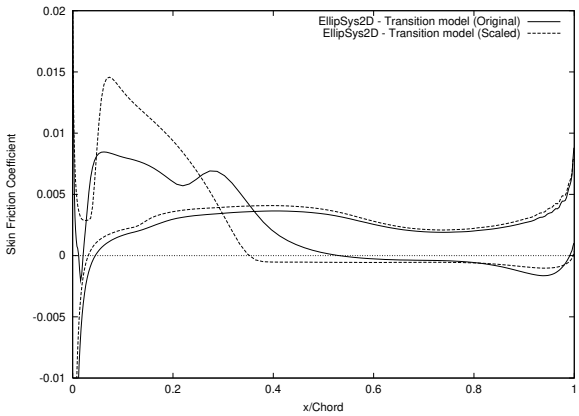

(f) Skin Friction Coefficient - $\alpha = 15.11^o$

Figure 169. Comparison of Original and Scaled Michel Transition Model (RISØ-A1-21, Experiment [13])

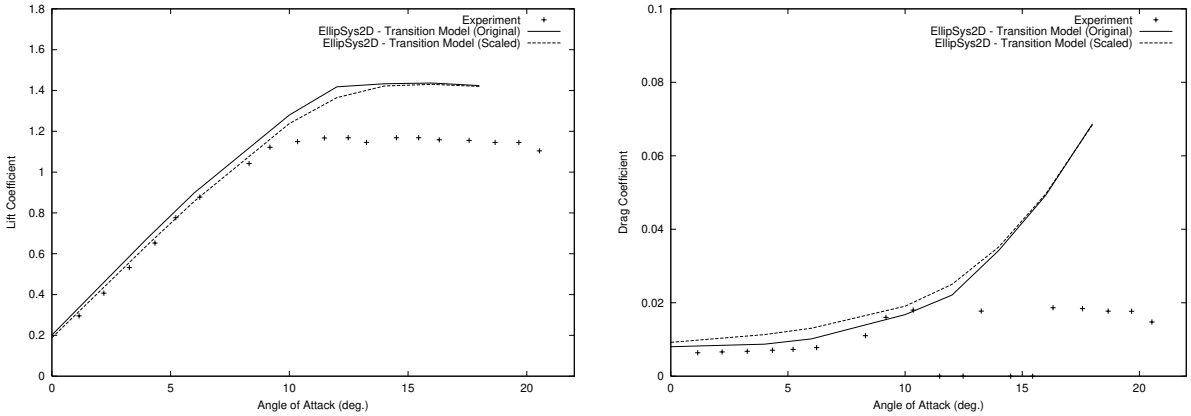

(a) Lift Coefficient (b) Drag Coefficient

Figure 170. Comparison of Original and Scaled Michel Transition Model (NACA 63-221, Experiment [1])

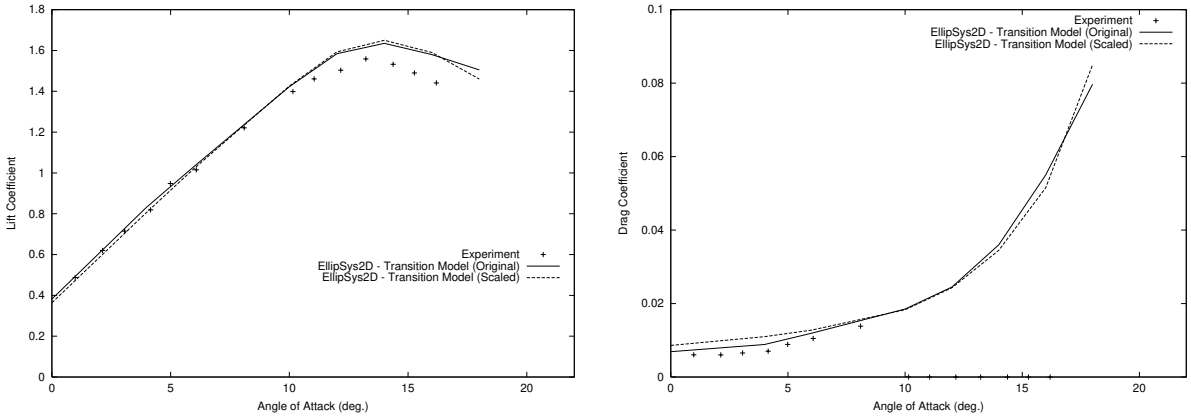

(a) Lift Coefficient (b) Drag Coefficient

Figure 171. Comparison of Original and Scaled Michel Transition Model (NACA 63-415, Experiment [1])

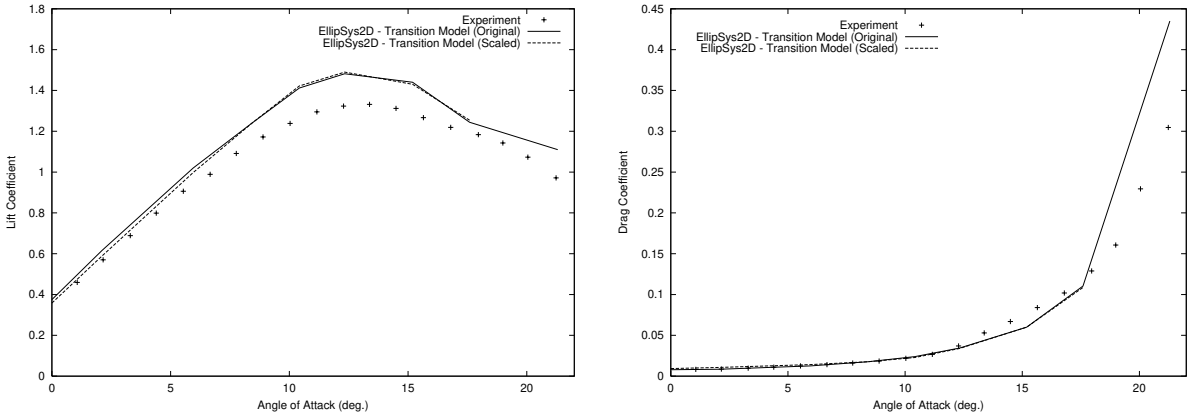

(a) Lift Coefficient (b) Drag Coefficient

Figure 172. Comparison of Original and Scaled Michel Transition Model (NACA 63-415(V), Experiment [11])

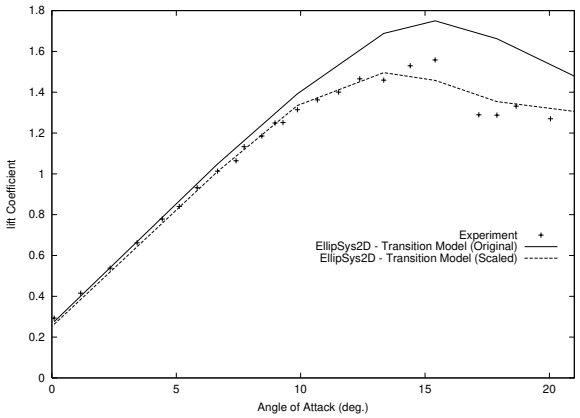

(a) Lift Coefficient

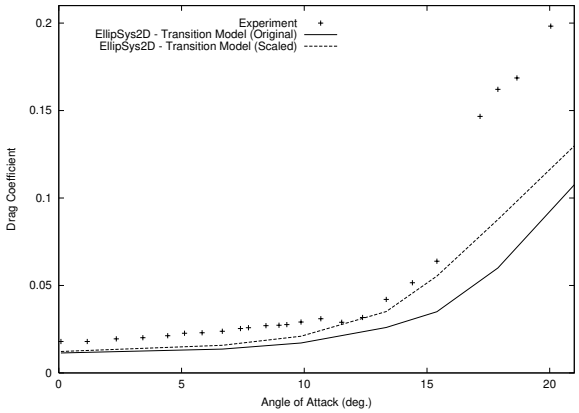

(b) Drag Coefficient

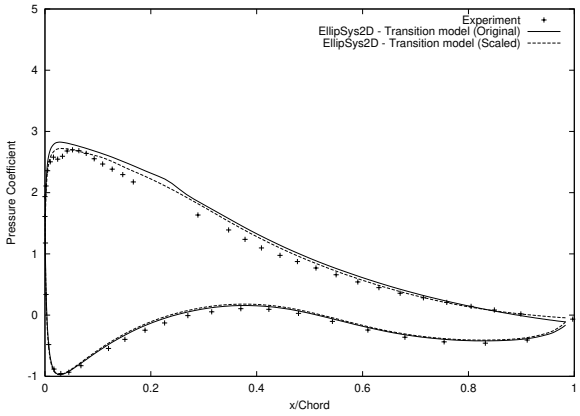

(c) Pressure Coefficient - $\alpha = 9.869^o$

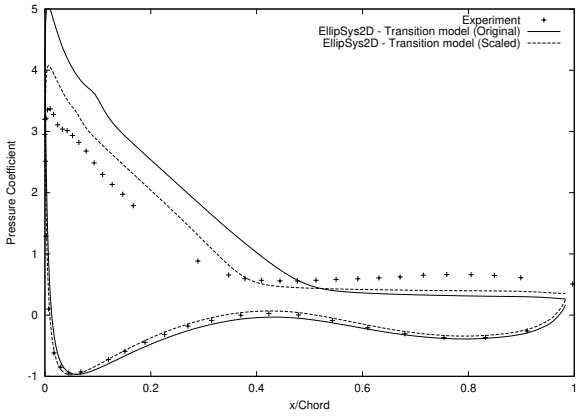

(d) Pressure Coefficient - $\alpha = 17.888^o$

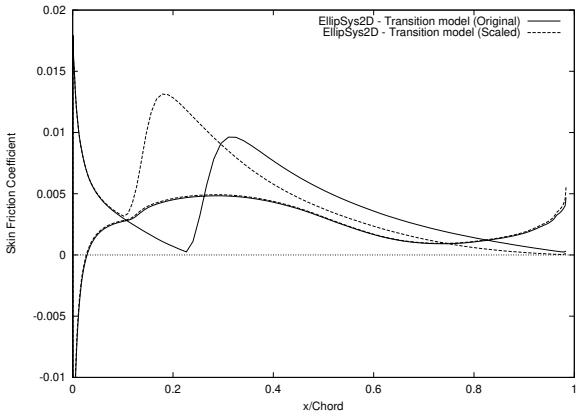

(e) Skin Friction Coefficient - $\alpha = 9.869^o$

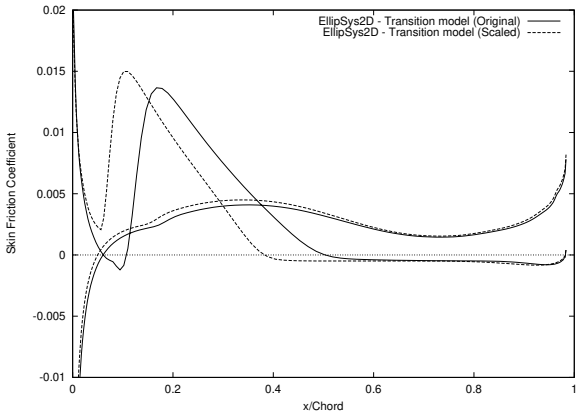

(f) Skin Friction Coefficient - $\alpha = 17.888^o$

Figure 173. Comparison of Original and Scaled Michel Transition Model (FFA-W3-241, Experiment [10])

13 Conclusion

A wide range of airfoils has been simulated with the computational code EllipSys2D. Computational results have been compared with available experimental data and the panel method based code XFOIL.

The collected results have been analysed with the aim of defining some criteria characterizing the ability of the numerical code to match the experimental data. It seems more difficult to simulate relatively thick airfoils. However, transition modelling has been found to have a great impact on the results for certain types of airfoils. The causes of the discrepancies between computational and experimental results that originate from the Michel transition model have been identified. The discrepancies result from the combination of two factors. Firstly, the transition model usually fails to predict transition in the sharp leading edge suction peak region as it happens in the experiments for airfoils that have been designed in that way. Secondly, the subsequent zero or low pressure gradient on the suction side of the airfoil worsens the situation by delaying transition predicted by the model even further.

Some advices have then been given on how to elaborate an airfoil design process using these computational models such that these discrepancies can be avoided. In order to control the transition point location, the sharp leading edge suction peak seems necessary. However airfoils could be designed such that, if transition is not detected by the model in the suction peak, the laminar boundary layer would anyway continue to grow downstream in order to rapidly trigger transition.

APPENDICES

A LS(1)-0413 and LS(1)-0417 Airfoils

The LS(1)-0413 and LS(1)-0417 airfoils were developped at NASA for general aviation applications [15]. They were equipped and measured in the Laminar Wind Tunnel at the Institut für Aerodynamik und Gasdynamik of the Stuttgart University [3]. The Reynold number of the experiments that are considered was $Re = 1.5 \times 10^6$.

A.1 Method

The C-meshes used for the computations had 384 cells in the direction along the airfoil, 256 of them being on the airfoil, and 64 cells in the direction away from the airfoil. The non-dimensional height of the cell at the airfoil was 1×10^{-5}.

The computations were performed with the SUDS-scheme for the convective terms, the $k-\omega$ SST turbulence model by Menter [16] for the turbulent viscosity, and the transition model by Michel [17], together with the empirical function given by Chen and Thyson [8] for modelling the turbulence intermittency. Numerical results were obtained with stationary computations.

A.2 Results

Experimental and computational results were in better agreement for the LS(1)-0413 airfoil. Moreover, for this airfoil, it seems that the transitional effects are less sensitive. Indeed, the experiments with smooth or rough airfoils gave roughly similar results, even after stall. Similarly, computations with transition model and fully turbulent computations gave also close results.

As for the LS(1)-0417 airfoil, computations predicted a higher lift than in the experiments in the linear region. Moreover these discrepancies increase as stall approaches.

LS(1)-0413

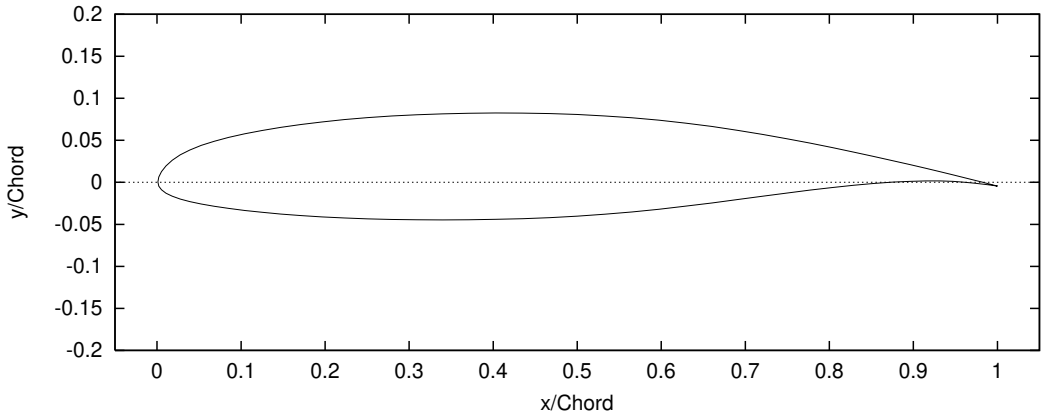

Figure 174. LS(1)-0413 Airfoil

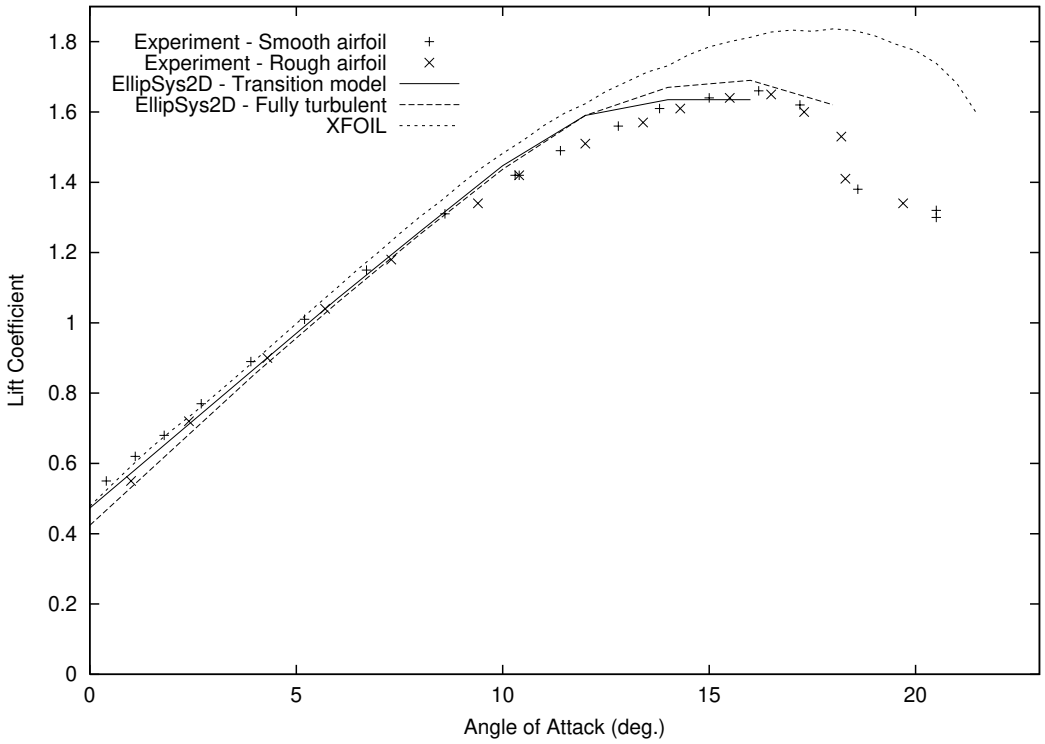

Figure 175. Lift Coefficient Curve (LS(1)-0413, Experiment [3])

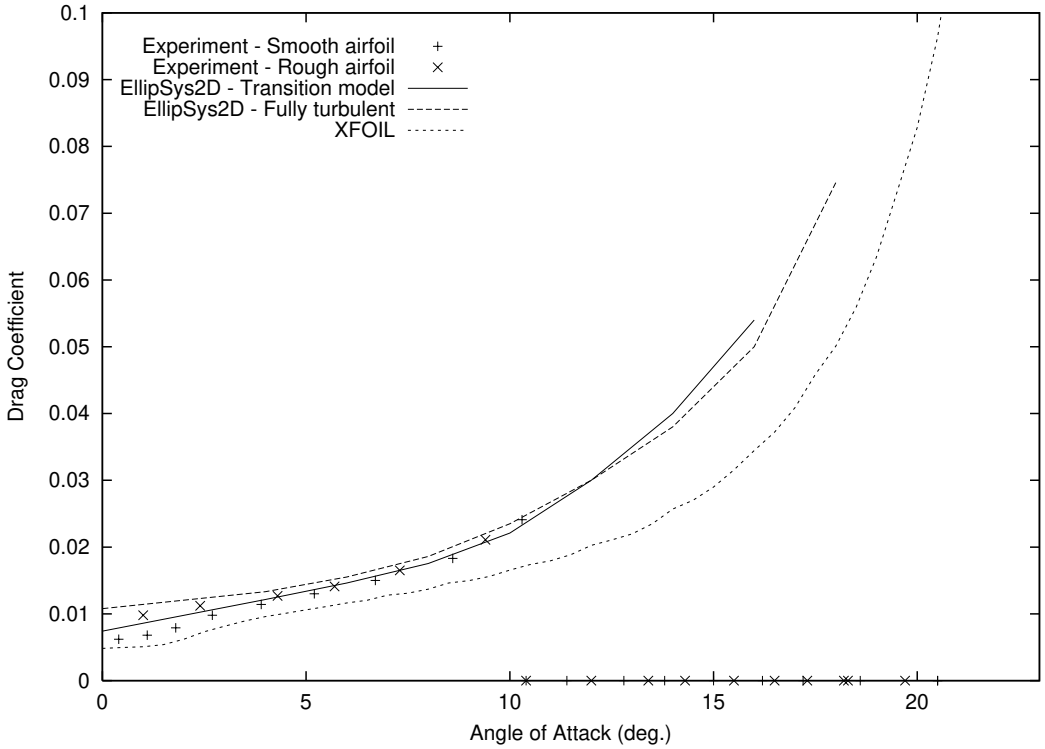

Figure 176. Drag Coefficient Curve (LS(1)-0413, Experiment [3])

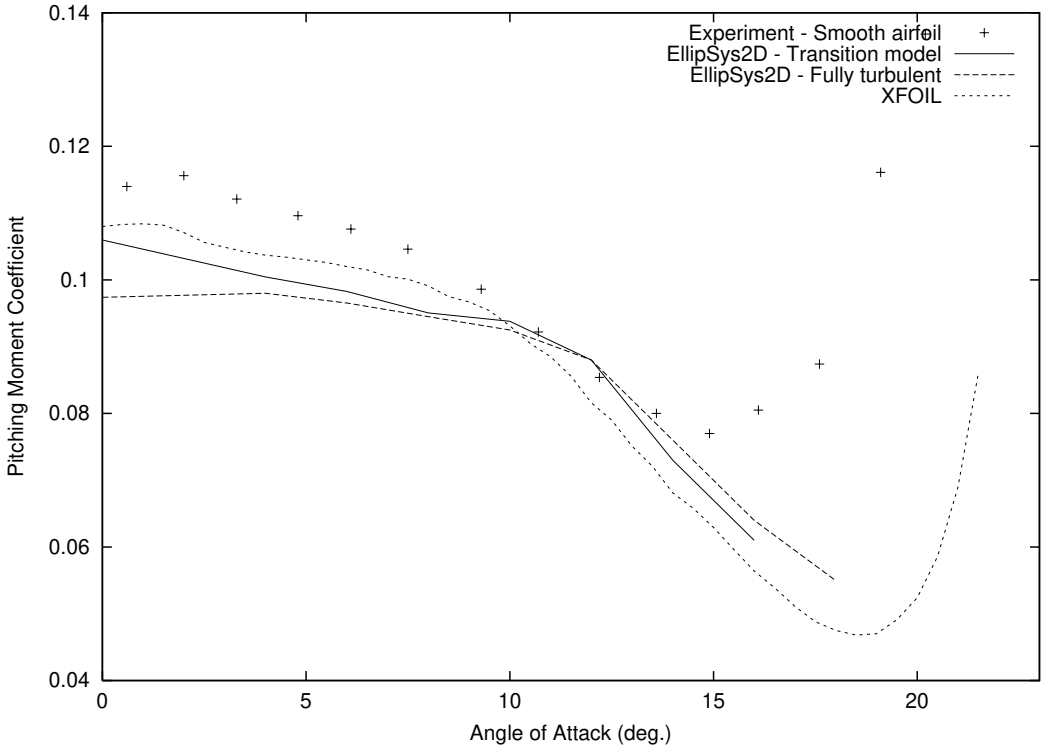

Figure 177. Pitching Moment Coefficient Curve (LS(1)-0413, Experiment [3])

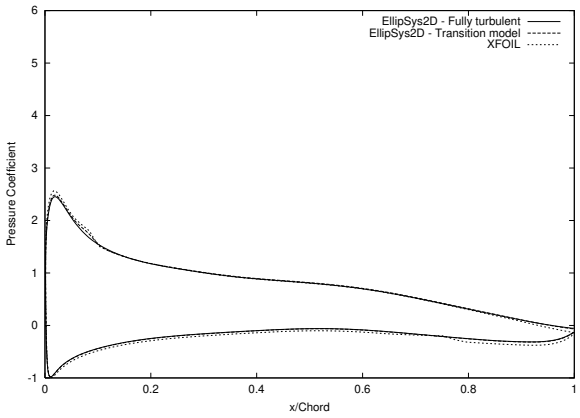

(a) $\alpha = 6.0^o$

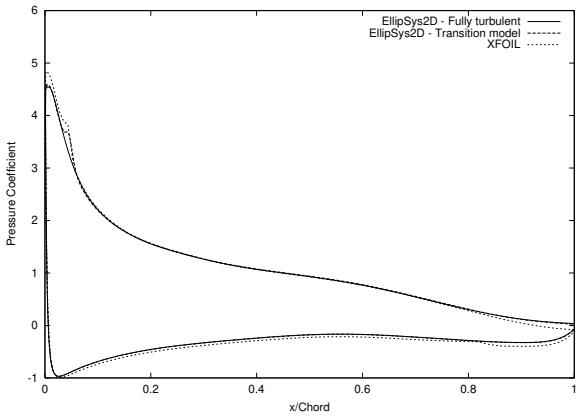

(b) $\alpha = 10.0^o$

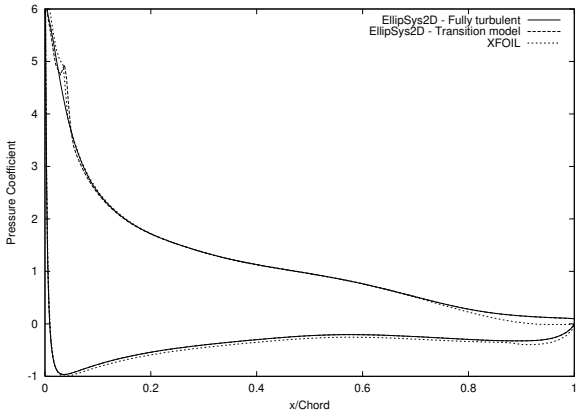

(c) $\alpha = 12.0^o$

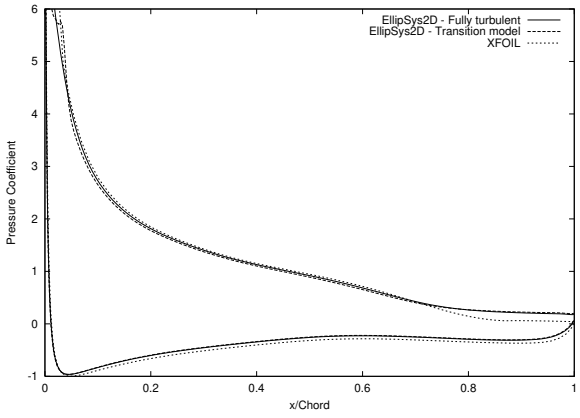

(d) $\alpha = 14.0^o$

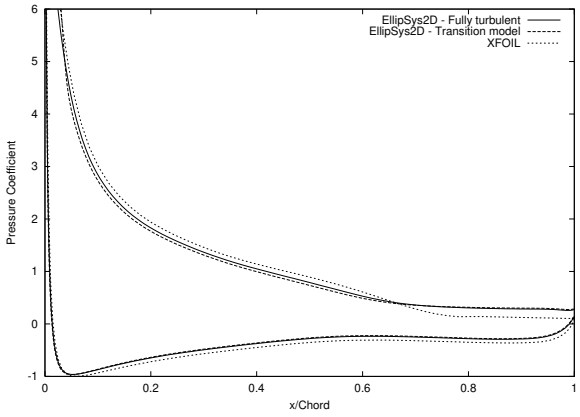

(e) $\alpha = 16.0^o$

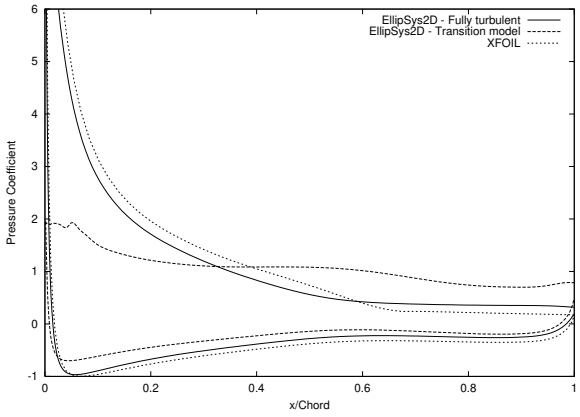

(f) $\alpha = 18.0^o$

Figure 178. Pressure Coefficient Distributions (LS(1)-0413)

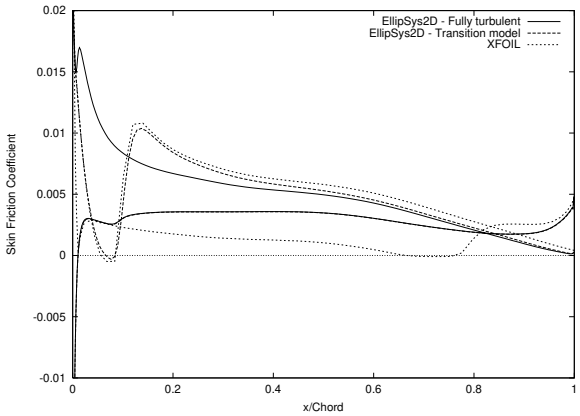

(a) $\alpha = 6.0^o$

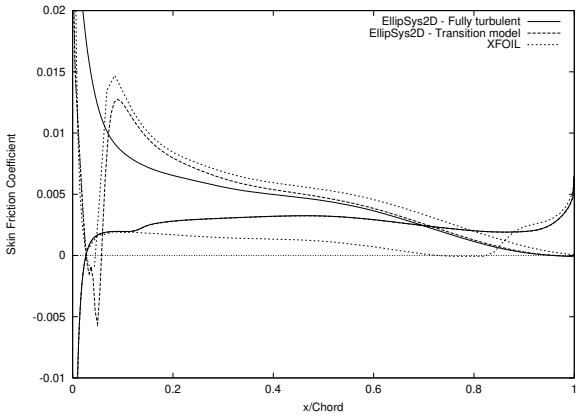

(b) $\alpha = 10.0^o$

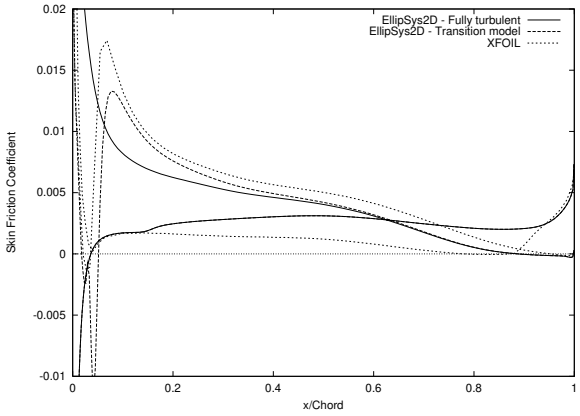

(c) $\alpha = 12.0^o$

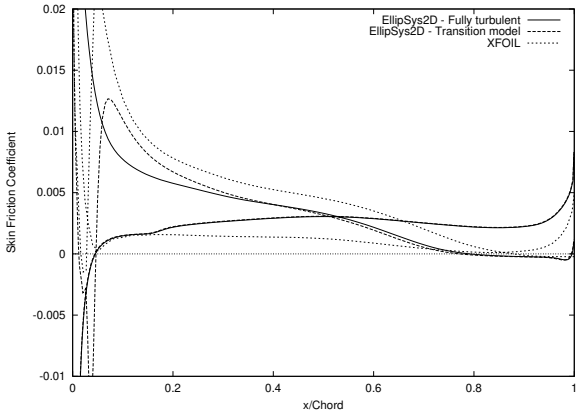

(d) $\alpha = 14.0^o$

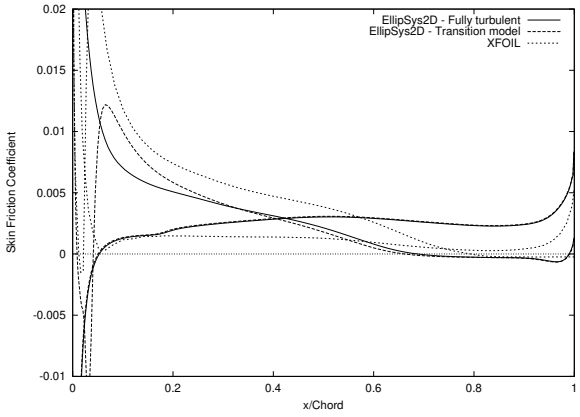

(e) $\alpha = 16.0^o$

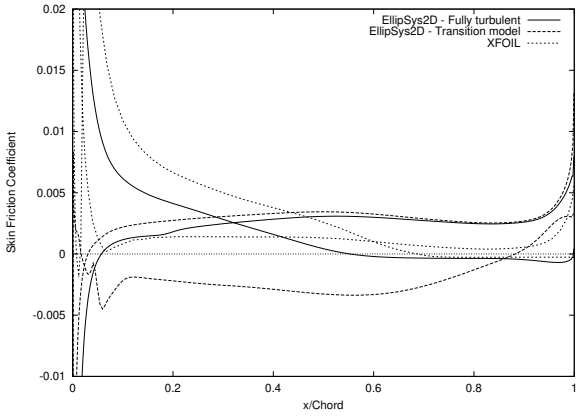

(f) $\alpha = 18.0^o$

Figure 179. Skin Friction Coefficient Distributions (LS(1)-0413)

LS(1)-0417

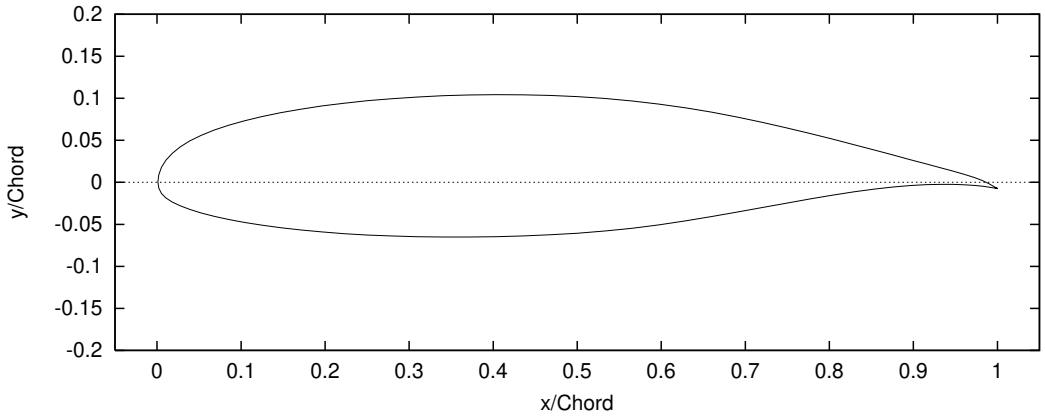

Figure 180. LS(1)-0417 Airfoil

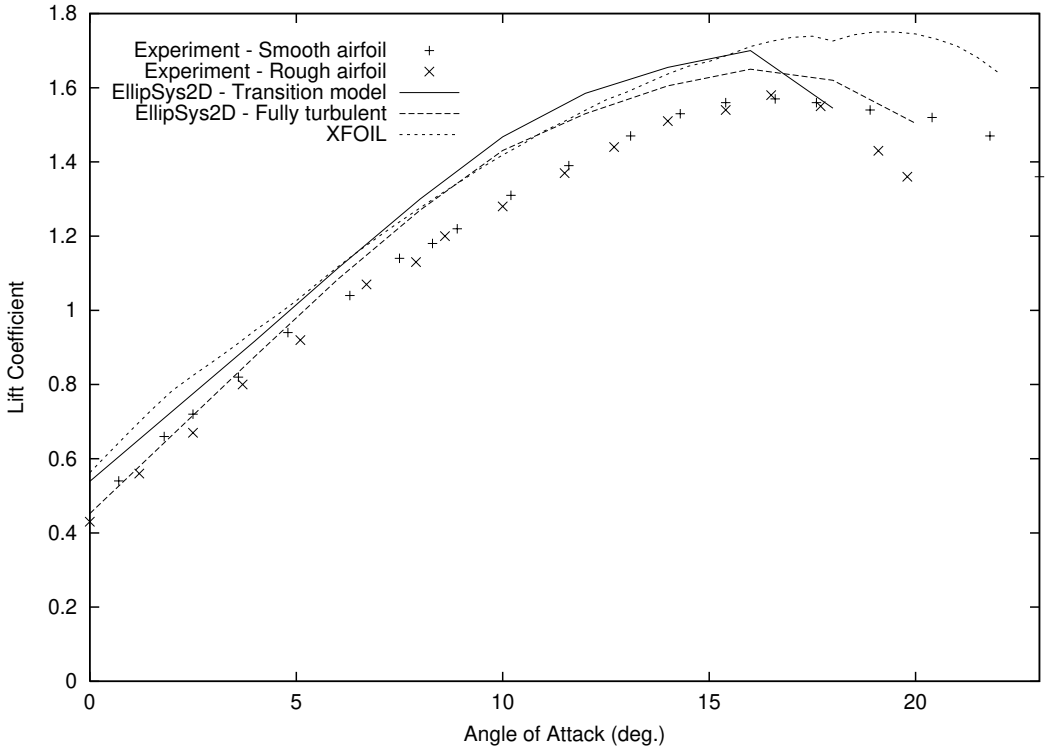

Figure 181. Lift Coefficient Curve (LS(1)-0417, Experiment [3])

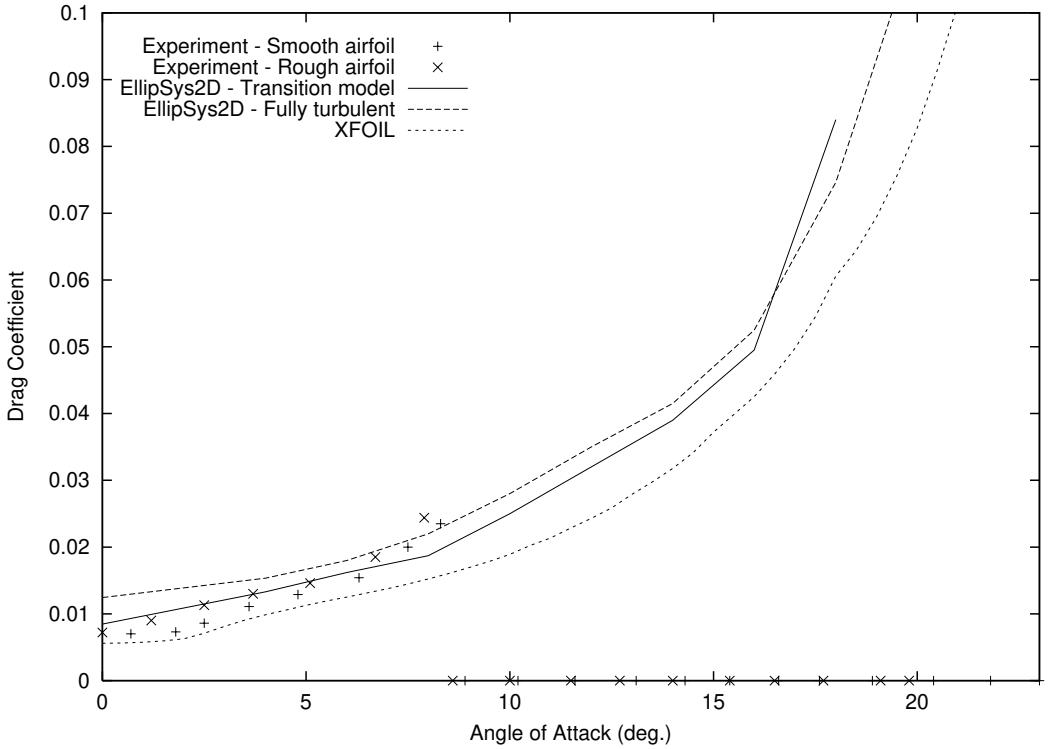

Figure 182. Drag Coefficient Curve (LS(1)-0417, Experiment [3])

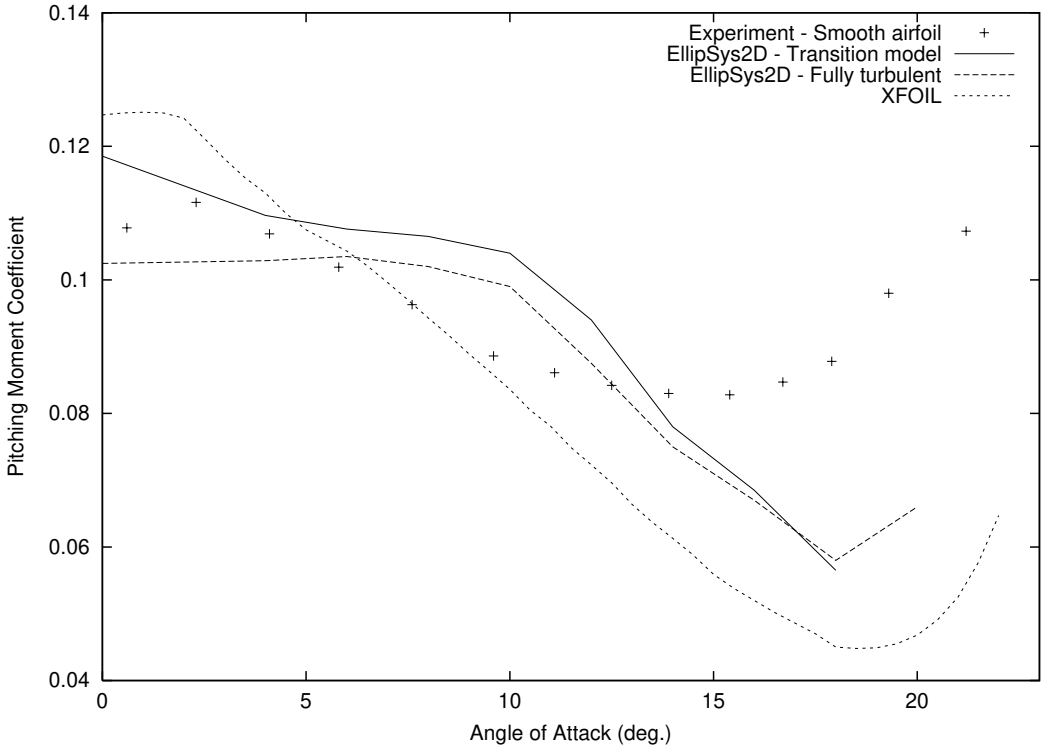

Figure 183. Pitching Moment Coefficient Curve (LS(1)-0417, Experiment [3])

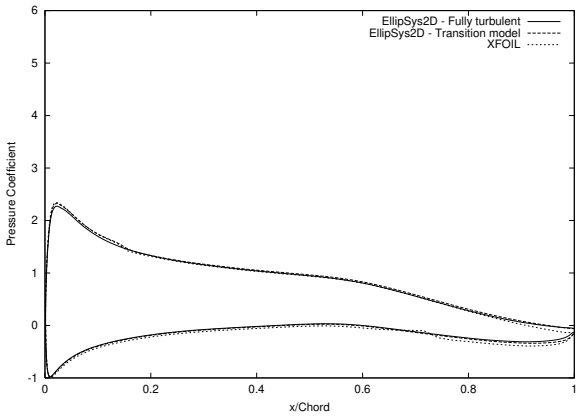

(a) $\alpha = 6.0^o$

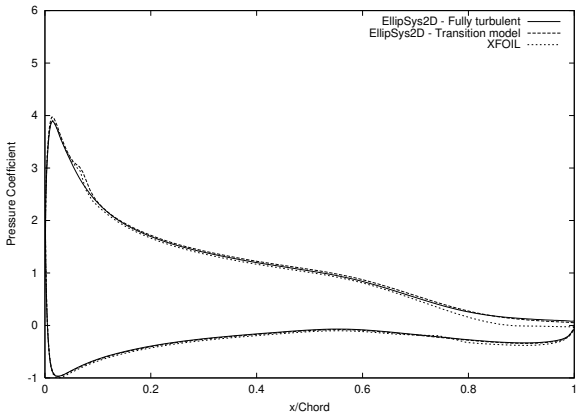

(b) $\alpha = 10.0^o$

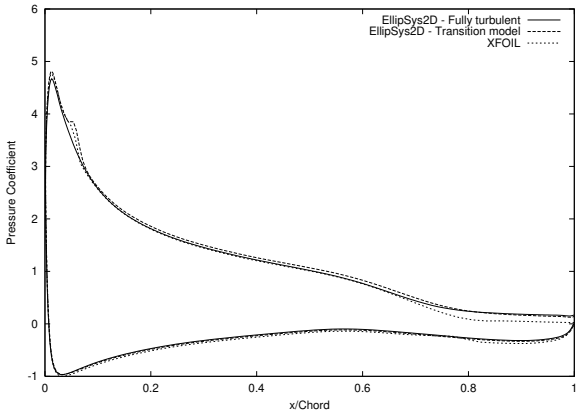

(c) $\alpha = 12.0^o$

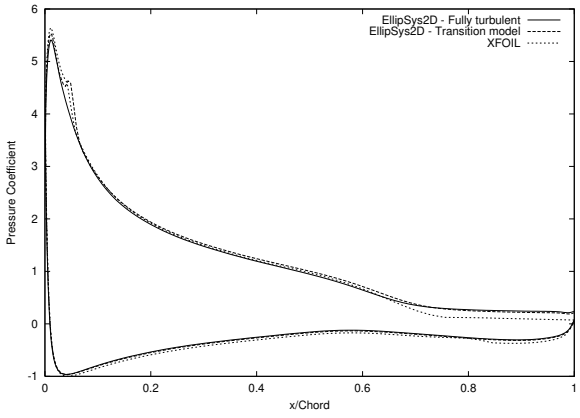

(d) $\alpha = 14.0^o$

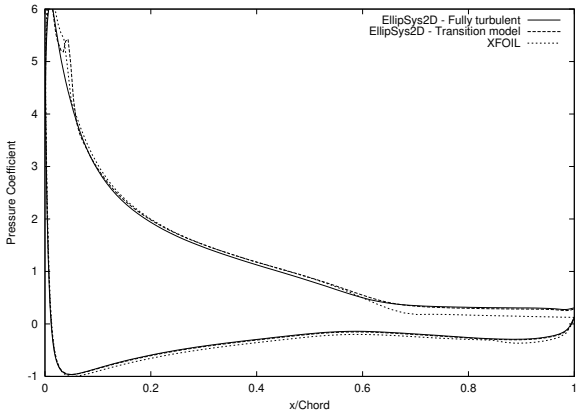

(e) $\alpha = 16.0^o$

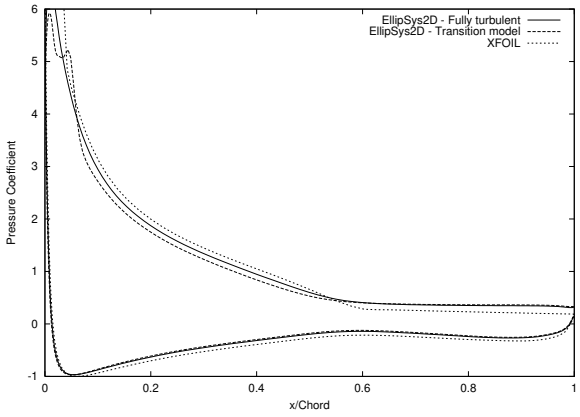

(f) $\alpha = 18.0^o$

Figure 184. Pressure Coefficient Distributions (LS(1)-0417)

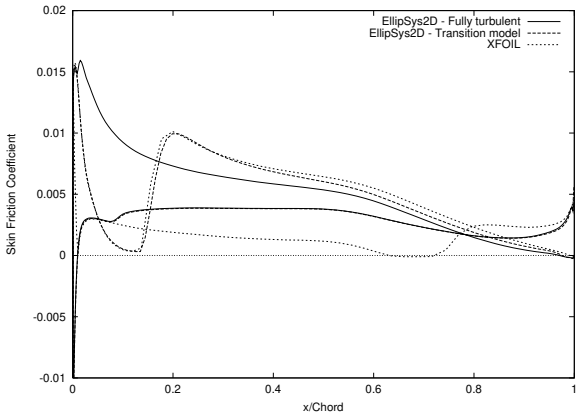

(a) $\alpha = 6.0^o$

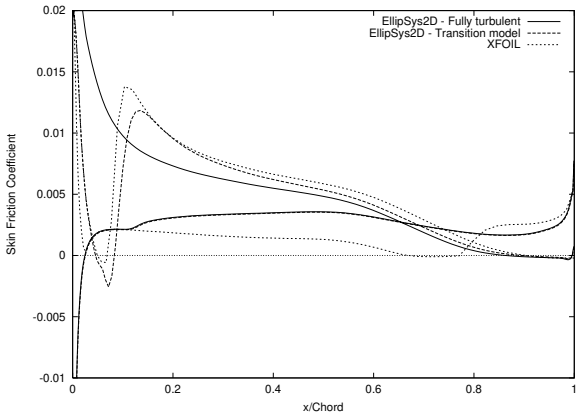

(b) $\alpha = 10.0^o$

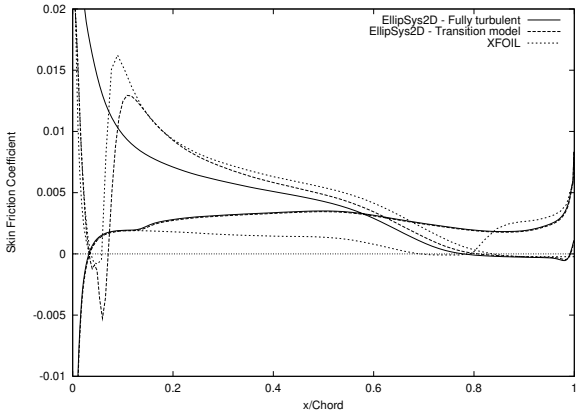

(c) $\alpha = 12.0^o$

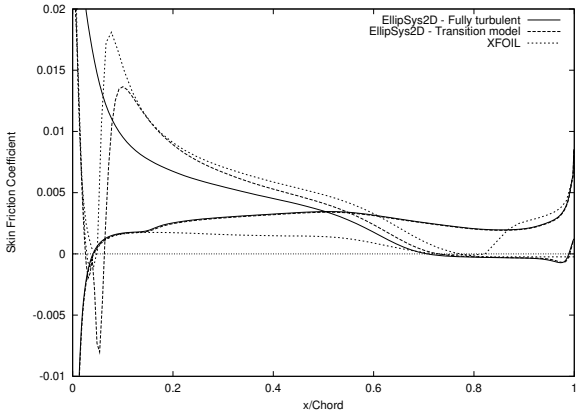

(d) $\alpha = 14.0^o$

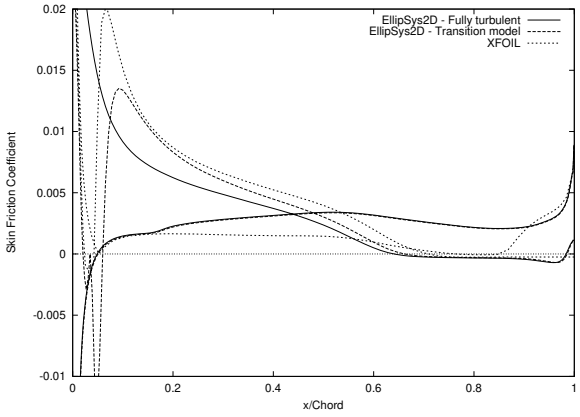

(e) $\alpha = 16.0^o$

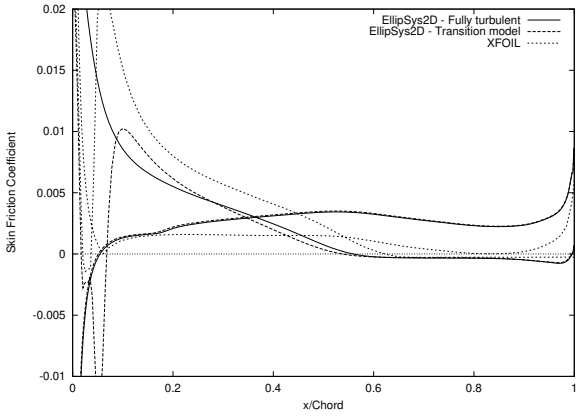

(f) $\alpha = 18.0^o$

Figure 185. Skin Friction Coefficient Distributions (LS(1)-0417)

References

[1] I.H. Abbott and A.E. von Doenhoff, *Theory of Wing Sections*, Dover Publications, Inc., New York, 1959.

[2] D. Althaus and F.X. Wortmann, *Stuttgarter Profilkatalog 1. Technical Report*, Vieweg, Braunschweig, 1981.

[3] D. Althaus, *Niedriggechwinddigkeitsprofile*, Vieweg, Braunschweig, 1996.

[4] C. Bak, P. Fuglsang, J. Johansen and I. Antoniou, Wind Tunnel Tests of the NACA 63-415 and a Modified NACA 63-415 Airfoil, *Risø-R-1193(EN)*, Risø National Laboratory, Denmark, December 2000.

[5] A. Björck, Coordinates and Calculations for the FFA-W1-xxx, FFA-W2-xxx and FFA-W3-xxx Series of Airfoils for Horizontal Axis Wind Turbine, *FFA TN 1990-15*, Flygtekniska Försöksanstalten, Sweden, 1990.

[6] A. Björck, 2D Airfoil Wind Tunnel Test at Stall, *Proceedings of IEA* 7^{th} *Symposium on Aerodynamics of Wind Turbines*, Technical University of Denmark, Denmark, November 1993.

[7] A. Björck, A Guide to Data Files from Wind Tunnel Test of a FFA-W3-211 Airfoil at FFA, *FFA-V-019*, Flygtekniska Försöksanstalten, Sweden, 1996.

[8] K.K. Chen and N.A. Thyson, Extensions of Emmons Spot Theory to Flows on Blunt Bodies, *AIAA Journal*, **9**, No.5, 1971.

[9] M. Drela, XFOIL: An Analysis and Design System for Low Reynolds Number Airfoils, *Conference on Low Reynolds Number Airfoil Aerodynamics*, University of Notre Dame, June 1989.

[10] P. Fuglsang, I. Antoniou, K.S. Dahl and H.A. Madsen, Tunnel Tests of the FFA-W3-241, FFA-W3-301 and NACA 63-430 Airfoils, *Risø-R-1041(EN)*, Risø National Laboratory, Denmark, December 1998.

[11] P. Fuglsang, I. Antoniou, N.N. Sørensen and H.Aa. Madsen, Validation of a Wind Tunnel Testing Facility for Blade Surface Pressure Measurements, *Risø-R-981(EN)*, Risø National Laboratory, Denmark.

[12] P. Fuglsang and K.S. Dahl, Design of the New Risø-A1 Airfoil Family for Wind Turbines, *Proceedings of EWEC'99 Conference*, Nice, France, 1999.

[13] P. Fuglsang, K.S. Dahl and I. Antoniou, Wind Tunnel Tests of the Risø-A1-18, Risø-A1-21 and Risø-A1-24 Airfoils, *Risø-R-1112(EN)*, Risø National Laboratory, Denmark, June 1999.

[14] "ECARP – European Computational Aerodynamics Research Project: Validation of CFD codes and Assessment of Turbulence Models", *Notes on Numerical Fluid Mechanics*, edited by W. Haase, E. Chaput, E. Elsholz, M.A. Leschziner and U.R. Müller, Vol.58, Vieweg Verlag, 1997.

[15] R.J. McGhee and W.D. Beasley, Low-Speed Aerodynamic Characteristics of a 17-Percent Thick Airfoil Section Designed for General Aviation Applications, *NASA TN D-7428*, 1973.

[16] F.R. Menter, Zonal Two-Equations $k-\omega$ Turbulence Models for Aerodynamic Flows, *AIAA Paper 93-2906*, 1993.

[17] R. Michel, Etude de la transition sur les profils d'aile ; Etablissement d'un critère de détermination du point de transition et calcul de la trainée de profil incompressible, *Tech. Report 1/1578A*, ONERA, France, 1951.

[18] J.A. Michelsen, Basis3D - A Platform for Development of Multiblock PDE Solvers, Tech. Report, Technical University of Denmark, AFM 92-05, 1992.

[19] J.A. Michelsen, Block Structured Multigrid Solution of 2D and 3D Elliptic PDE's, Tech. Report, Technical University of Denmark, AFM 94-06, 1994.

[20] D.M. Somers, Design and Experimental Results for the S809 Airfoil, *Technical Report NREL/SR-440-6918*, National Renewable Energy Laboratory, Colorado, USA, January 1997.

[21] D.M. Somers, Design and Experimental Results for the S814 Airfoil, *Technical Report NREL/SR-440-6919*, National Renewable Energy Laboratory, Colorado, USA, January 1997.

[22] N.N. Sørensen, General Purpose Flow Solver Applied to Flow over Hills, Tech. Report, Risø National Laboratory, Roskilde, Denmark, PhD Thesis, Risø-R-827(EN), June 1995.

[23] N.N. Sørensen, HypGrid2D - a 2D Mesh Generator, Tech. Report, Risø National Laboratory, Roskilde, Denmark, Risø-R-1035(EN), March 1998.

[24] W.A. Timmer, The Design and Testing of Airfoil DU 91-W2-250, *Sixth IEA Symposium on the Aerodynamics of Wind Turbines*, Petten, The Netherlands, November 1992.

[25] W.A. Timmer and R.P.J.O.M. van Rooy, Wind Tunnel Results for a 25% Thick Wind Turbine Blade Airfoil, *European Community Wind Energy Conference*, 8-12 march, 1993, Lübeck-Travemünde, Germany.

[26] A.E. von Doenhoff and F.T. Abbott, The Langley Two-dimensional Low-turbulence Pressure Tunnel, NACA TN No.1283, 1947.

Bibliographic Data Sheet **Risø–R–1280(EN)**

Title and author(s)

Wind Turbine Airfoil Catalogue

Franck Bertagnolio, Niels Sørensen, Jeppe Johansen and Peter Fuglsang

ISBN
87–550–2910–8
87–550–2911–6(Internet)

ISSN
0106–2840

Dept. or group
Aeroelastic Design
Wind Energy Department

Date
August 2001

Groups own reg. number(s)

Project/contract No.

Pages	Tables	Illustrations	References
152	2	185	26

Abstract (Max. 2000 char.)

The aim of this work is two-sided. Firstly, experimental results obtained for numerous sets of airfoil measurements (mainly intended for wind turbine applications) are collected and compared with computational results from the 2D Navier-Stokes solver EllipSys2D, as well as results from the panel method code XFOIL. Secondly, we are interested in validating the code EllipSys2D and finding out for which airfoils it does not perform well compared to the experiments, as well as why, when it does so. The airfoils are classified according to the agreement between the numerical results and experimental data. A study correlating the available data and this classification is performed. It is found that transition modelling is to a large extent responsible for the poor quality of the computational results for most of the considered airfoils. The transition model mechanism that leads to these discrepancies is identified. Some advices are given for elaborating future airfoil design processes that would involve the numerical code EllipSys2D in particular, and transition modelling in general.

Descriptors INIS/EDB

AERODYNAMICS; AIRFOILS; COMPUTATIONAL FLUID DYNAMICS; E CODES; NAVIER-STOKES EQUATIONS; TURBINE BLADES; TURBULENT FLOW; TWO-DIMENSIONAL CALCULATIONS; VISCOUS FLOW; WIND TUNNELS; WIND TURBINES

Available on request from:
Information Service Department, Risø National Laboratory
(Afdelingen for Informationsservice, Forskningscenter Risø)
P.O. Box 49, DK–4000 Roskilde, Denmark
Phone (+45) 46 77 46 77, ext. 4004/4005 · Fax (+45) 46 77 4013